Characterization of Derived Angle-of-Attack and Flight Path Angle Algorithms for General Aviation Platforms

December 2019

Final Report

U.S. Department of Transportation
Federal Aviation Administration

NOTICE

This document is disseminated under the sponsorship of the U.S. Department of Transportation in the interest of information exchange. The U.S. Government assumes no liability for the contents or use thereof. The U.S. Government does not endorse products or manufacturers. Trade or manufacturers' names appear herein solely because they are considered essential to the objective of this report. The findings and conclusions in this report are those of the author(s) and do not necessarily represent the views of the funding agency. This document does not constitute FAA policy. Consult the FAA sponsoring organization listed on the Technical Documentation page as to its use.

This report is available at the Federal Aviation Administration William J. Hughes Technical Center's Full-Text Technical Reports page: actlibrary.tc.faa.gov in Adobe Acrobat portable document format (PDF).

1. Report No.	2. Government Accession No.	3. Recipient's Catalog No.
DOT/FAA/TC-18/48		

4. Title and Subtitle	5. Report Date
CHARACTERIZATION OF DERIVED ANGLE-OF-ATTACK AND FLIGHT PATH ANGLE ALGORITHMS FOR GENERAL AVIATION PLATFORMS	December 2019
	6. Performing Organization Code

7. Author(s)	8. Performing Organization Report No.
John Valasek, Joshua Harris Texas A&M University Seth Young, Shawn Pruchnicki, Matthew McCrink, James Gregory The Ohio State University	

9. Performing Organization Name and Address	10. Work Unit No. (TRAIS)
	11. Contract or Grant No.

12. Sponsoring Agency Name and Address	13. Type of Report and Period Covered
Federal Aviation Administration Small Airplane Standards Branch FAA Central Office 901 Locust St Kansas City, MO 64106	Final Report
	14. Sponsoring Agency Code
	AIR-690

15. Supplementary Notes

The FAA William J. Hughes Technical Center Aviation Research Division COR was Robert J. McGuire.
Notes by Sponsor (Dave Sizoo, FAA Flight Test Pilot, FAA Aircraft Certification, Small Airplane Standards Branch, Policy and Innovation Division)
Derived AOA:
This research effort is one element of a larger portfolio of angle of attack research projects. The spectrum of Angle of Attack research was specifically programmed in a coherent landscape to develop FAA policy for incorporating Angle of Attack in General Aviation. See Non Required Safety Enhancing Equipment (NORSEE) Policy PS-AIR-21.8-1602 dated 3/31/16. See also FAA News Release from FAA Administrator and the Secretary of Transportation titled "FAA Clears Path for Installation of Angle of Attack Indicators in Small Aircraft dated Feb 5 2014. Original Memo AIR 100-14-110-PM01.

Other FAA sponsored projects from this office on angle of attack include
1) performance characterization of all commercially available low cost AOA sensor. These sensors were installed, calibrated, and flown with an air data system truth source on Cirrus SR-22 aircraft and the SF-50 Vision Jet. (Performed by Skyward Bound)
2) wind tunnel testing of differential pressure based sensors costing in the $100s range (Performed by Dave Rodgers and Flight Level Engineering)
3) Flight Test of Derived AOA algorithms (Performed by Adaptive Aerospace)
4) Best Practices for designing AOA displays (Performed by FAA CAMI Civil Aerospace Medical Institue) Dr Dennis Beringer)

The portfolio of FAA sponsored research was complementary with work done in the GA JSC (General Aviation Joint Steering Committee) in Loss of Control Working Group 1 and 2. Specifically, the work supported Safety Enhancements and Policy integration between FAA Flight Standards and Aircraft Certification. Furthermore, this work addressed the NTSB's Top Ten Most Wanted List topic: Aircraft Loss of Control.

As discussed at the NTSB's aircraft Loss of control forum on April 24, 2018, angle of attack is not the silver bullet that will prevent loss of control. However, awareness of angle of attack is central to maintaining aircraft control. This was highlighted in a specific AIAA invited session on angle of attack and Co-chaired with Texas A&M in June of 2017. Papers were presented on AOA research ranging from simple display of AOA in the cockpit, to the appropriate use of AOA as an input to envelope protection and fly by wire systems. The appropriate integration of AOA is crucial to flight safety. In this regard refer to additional complementary research sponsored by the Small Airplane Standards branch relating to Run Time Assurance and dynamic consistency checks of AOA signals with vehicle performance.

Other related printed magazine articles relevant to AOA research are found here: FAA Safety Briefing Magazine, May/June 2014 by Dave Sizoo: AOA More than Just a Display: Real World Uses for Angle of Attack.
FAA.gov/news/safety_briefing/2024/media/MayJun2014.pdf. Article was originally published in august of 2012 in Alaska "Transponder" Safety Magazine.

Technical Report Documentation Page (continued)

16. Abstract

Proper exploitation of derived angle-of-attack and sideslip angle from low-cost Attitude Heading Reference System (AHRS) sensors found in general aviation aircraft is a candidate solution for improving flight safety. This approach uses equations for angle-of-attack and sideslip angle that are solved onboard in real-time, using state data and information provided by AHRS sensors. These equations are a function of vehicle parameters and stability and control derivatives, in addition to the angular displacement and angular rate sensor outputs. This work evaluates the feasibility of derived angle-of-attack and sideslip angle for general aviation for use cases of pilot displays, envelope protection, and fly-by-wire flight control systems. The aircraft considered are Part 23 aircraft. Standard angle-of-attack and sideslip angle equations are implemented in a nonlinear six degree-of-freedom simulation model of the Cessna 172, and the AHRS is modeled on a generic type found in general aviation aircraft. The Cessna 172 simulator is flown by evaluation pilots for the purpose of recording pilot input commands during the approach and landing flight phase. The pilot inputs are then used in a non-real-time Monte Carlo flight simulation of the Cessna 172 that evaluates the effect of modeling uncertainties and sensor noise on derived angle-of-attack and sideslip angle. Monte Carlo cases of 10,000 and 100,000 runs are evaluated. Results presented in the report show the allowable bounds on aircraft model parameter uncertainties, such as stability and control derivatives, in addition to sensor noise levels, which produce usable derived angle-of-attack and sideslip angle values from low-cost AHRS sensors. It is expected that these results will be used for recommended minimum performance standards for the algorithm and AHRS devices, in addition to the criteria for each use case when using AHRS that can be coded into a standard or a circular.

17. Key Words	18. Distribution Statement
Angle of attack, Aerodynamic modeling, Sideslip angle, Monte Carlo analysis	This document is available to the U.S. public through the National Technical Information Service (NTIS), Springfield, Virginia 22161. This document is also available from the Federal Aviation Administration William J. Hughes Technical Center at actlibrary.tc.faa.gov.

19. Security Classif. (of this report)	20. Security Classif. (of this page)	21. No. of Pages	22. Price
Unclassified	Unclassified	144	

Form DOT F 1700.7 (8-72) Reproduction of completed page authorized

TABLE OF CONTENTS

LIST OF FIGURES

LIST OF TABLES

LIST OF ACRONYMS

6DOF	Six degrees-of-freedom
AFPC	Augmented flight path control
AGL	Above ground level
AHRS	Attitude heading reference system
AoA	Angle of attack
Beta	Sideslip angle
CFD	Computational fluid dynamics
CFR	Code of Federal Regulations
COTS	Commercial off-the-shelf
DATCOM	USAF Data Compendium
GA	General aviation
INS	Inertial navigation systems
RMS	Root mean square
S&C	Stability and control

EXECUTIVE SUMMARY

This report presents the results of a 14-month investigation by Texas A&M University and The Ohio State University on various commercial-off-the-shelf (COTS) attitude heading reference system (AHRS) component characteristics that affect the usability of derived angle-of-attack (AoA) solutions. The investigation was conducted using Monte Carlo and real-time piloted simulations in the Engineering Flight Simulator at Texas A&M University. The technical objective was to evaluate derived AoA and sideslip angle (beta) algorithms using low-cost AHRS systems found in general aviation (GA) aircraft. The derived AoA algorithm was evaluated for three use cases. The first, and most stringent, is for augmented flight path control (AFPC) systems; the second is an envelope-protection system; and the third is as a display of information to the pilot. These cases are presented in order of tolerance required for success. It is expected that the result of this work will be a model for informing the recommended minimum performance standards for the algorithm and AHRS device, and will determine error threshold criteria for each use case. Further studies will use this data to develop codified AHRS standards and advisory circulars. The aircraft considered were piston single-engine Title 14 Code of Federal Regulations (CFR) Part 23 category small aircraft, such as the Cessna 172. The COTS AHRS considered are typically found in these aircraft systems, specifically those by Garmin and Aspen.

Results presented in this report demonstrate that a basic equation set for derived AoA and beta using unfiltered input signals is capable of generating useful threshold levels for the three use cases outlined above. The specific derived AoA and beta algorithm used requires estimates for six aerodynamic parameters unique to each aircraft. Monte Carlo simulations revealed that accurate initial estimates of the aerodynamic parameters are essential to produce meaningful derived AoA and beta estimates. The most sensitive aerodynamic parameter was the aircraft lift curve slope, C_{L_α}. A fixed value of C_{L_α} results in high derived AoA uncertainty and therefore may need to be scheduled based on the derived AoA itself, although the performance of this approach has not been evaluated. However, reasonable first-order C_{L_α} estimates can be determined using basic Class I analytical methods such as the USAF Data Compendium (DATCOM), and to even higher accuracy from wind tunnel testing or computational fluid dynamics (CFD). Considering the three use cases, first-order modeling of the aerodynamic parameters results in algorithm uncertainty sufficient to violate the AFPC tolerances. However, the same uncertainty does not violate the envelope-protection and pilot-display thresholds. In this work, only the AFPC case results in a failure unless the acceptable error threshold is increased.

Derived beta estimates are more sensitive to aerodynamic parameter estimates than the derived AoA. Specifically, there appears to be a direct correlation between the side-force/sideslip derivative, C_{y_β}, and the resulting derived beta estimates. However, the other five stability and control (S&C) derivatives used in the derived AoA and beta algorithm are shown to have no correlation between their variations and the resulting maximum and root mean square (RMS) errors. Introduction of AHRS sensor noise results in errors similar to those encountered in modeling the aerodynamic derivatives. Derived AoA and beta estimates are found to be relatively sensitive to the AHRS angular rate and acceleration sensor noise. A low level of sensor noise does not violate the envelope-protection threshold for AoA or beta, but it violates the AFPC threshold on 85% of 10,000 Monte Carlo runs. Medium noise levels violated the envelope-protection

tolerance and sideslip tolerance on every run, and high noise violated the display threshold on 55% of 10,000 Monte Carlo runs.

1. INTRODUCTION

This report details work conducted by Texas A&M University and The Ohio State University from August 1, 2015–October 31, 2016 on Phase I of this project. All work was performed in the Vehicle Systems & Control Laboratory located in the Aerospace Engineering Department at Texas A&M University, and at The Ohio State University and associated industry partners.

The technical objective of the proposed effort was to exploit derived angle-of-attack (AoA) and flightpath angles (gamma) from low-cost attitude heading reference system (AHRS) commercial-off-the-shelf (COTS) systems found in GA aircraft. The feasibility of derived angle-of-attack (AoA) was evaluated for use cases of displays, envelope protection, and fly-by-wire flight-control systems. It is expected the results of this work will be 1) recommended minimum performance standards for the algorithm and AHRS device, and 2) the criteria for each use case when using AHRS that can be codified into a standard or a circular. The aircraft considered were piston single-engine 14 CFR Part 23 category small, bizjet, and hybrid concepts, such as Cessna 172, Cirrus SR22, Cessna Corvalis, and Lancair Columbia 350. The COTS AHRS evaluated were those typically found in these aircraft systems, specifically those by Garmin and Aspen.

The work sought to understand how various COTS AHRS component characteristics affected the usability of derived AoA solutions by conducting a simulation study to investigate:

·   Sensor accuracy
·   Dynamic response
·   Error analysis
·   Sensitivity analysis of derived AoA equations
·   Parameters
·   GPS update rate
·   Vertical airmass motion (steady-state and gust)

The test plan and schedule is found in appendix A. Note that only the six cases of Maneuver Set 1: Power Approach: 70 KIAS, 1000 feet above ground level (AGL) were conducted and are addressed in this report.

2. MODELING

2.1 SIMULATIONS

Two flight-simulation packages were used in this work. The commercial X-Plane® flight simulator by Laminar Research was used to generate pilot inputs (see section 2.2) in the Texas A&M University Engineering Flight Simulator, but was not used for Monte Carlo simulations because of a lack of batch capability and concerns over the fidelity of the blade-element theory-based aerodynamics model. The default X-Plane Cessna 172 was the aircraft model used.

The open-source JSBSim simulation software, a nonlinear, six degrees-of-freedom (6DOF) flight simulation using traditional S&C derivative-based aerodynamic modeling, was also used [1]. The S&C derivatives in JSBSim were obtained via a combination of analytical methods (e.g., United

States Air Force Data Compendium or DATCOM), computational methods such as computational fluid dynamics (CFD), and experimental wind-tunnel tests. JSBSim is capable of both real-time and batch simulation, and is scriptable via the eXtensible Markup Language. JSBSim's Cessna 172R model was used for the batch Monte Carlo simulations. A description of the lift and sideforce models of the JSBSim 172R is presented in section 2.3.2.

2.2 PILOT-INPUT MODELING

The pilot inputs used in all simulations consisted of elevator, aileron, rudder, and throttle commands obtained from piloted simulation in a fixed-base, real-time, nonlinear, 6DOF flight simulator using the X-Plane® flight-simulation software (see figure 1). The simulated flight was a left approach to landing at Easterwood Airport (KCLL), consisting of a turn from downwind onto base and then onto final. This was conducted with zero winds and turbulence. The flight condition was $V_{CAS} = 90\,kts$ at 1347 ft, which is approximately the pattern altitude at KCLL. The X-Plane® pilot inputs were recorded to file as normalized values in the closed interval $[-1,1]$, with the ± 1 endpoints corresponding to the actuator position limits.

For the Monte Carlo batch simulations, the aircraft was initially trimmed at the specified flight condition using JSBSim's trim algorithm and was then subjected to the input time histories from the piloted simulation, which were treated as perturbations from the trim-control deflections. JSBSim rescaled the normalized control inputs into the range defined by actuator position limits of the aircraft model, which avoided any incompatibilities between the actuator models of the two simulations.

Figure 1. Texas A&M University engineering flight simulator

Two flight conditions were modeled. The first was the piloted simulation-approach flight condition, from which a 50-second time period was used. Figure 2 shows the control inputs used in the batch simulations for this flight condition. The corresponding 3-D trajectory of this segment is shown in figure 3. This trajectory was used for Monte Carlo cases 1–12, which are presented in detail in section 3.

The second flight condition was trimmed flight with the same initial conditions ($V_{CAS} = 90 \text{ kts}$ at 1347 ft, $\alpha_1 = 2.6°$) but with the aircraft subjected to short-duration doublet inputs on each control. This second flight condition was added to examine the effect of different control time histories on the derived aerodynamic angle calculation. Figure 4 shows the control inputs used in the batch simulations for this flight condition. A 3-D trajectory resulting from these inputs is shown in figure 5. This flight condition was used for Monte Carlo cases 13–16.
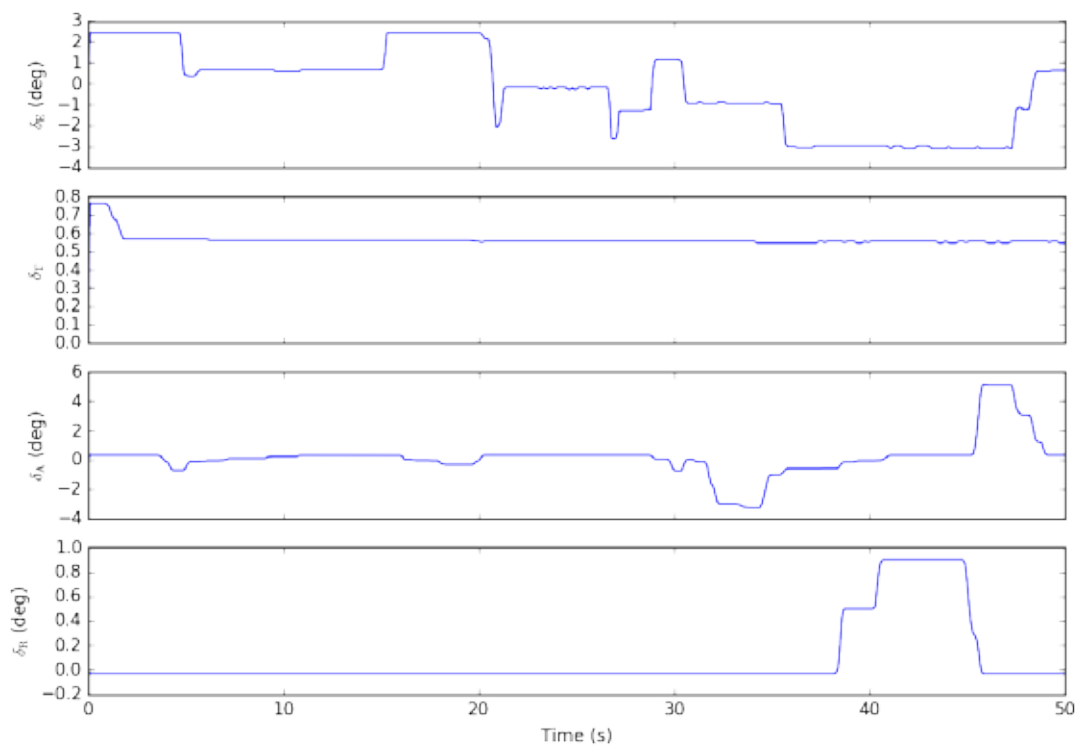
Figure 2. Recorded piloted simulation control inputs for approach flight condition
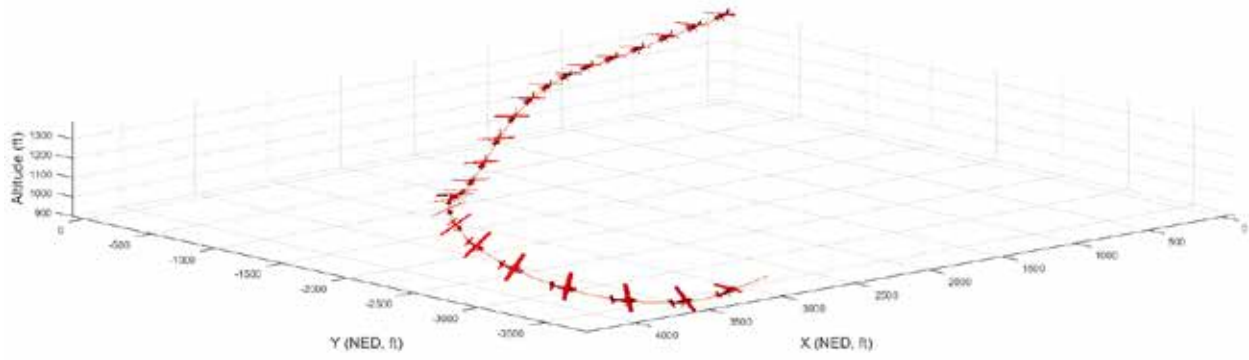
Figure 3. 3-D flight path from recorded approach trajectory
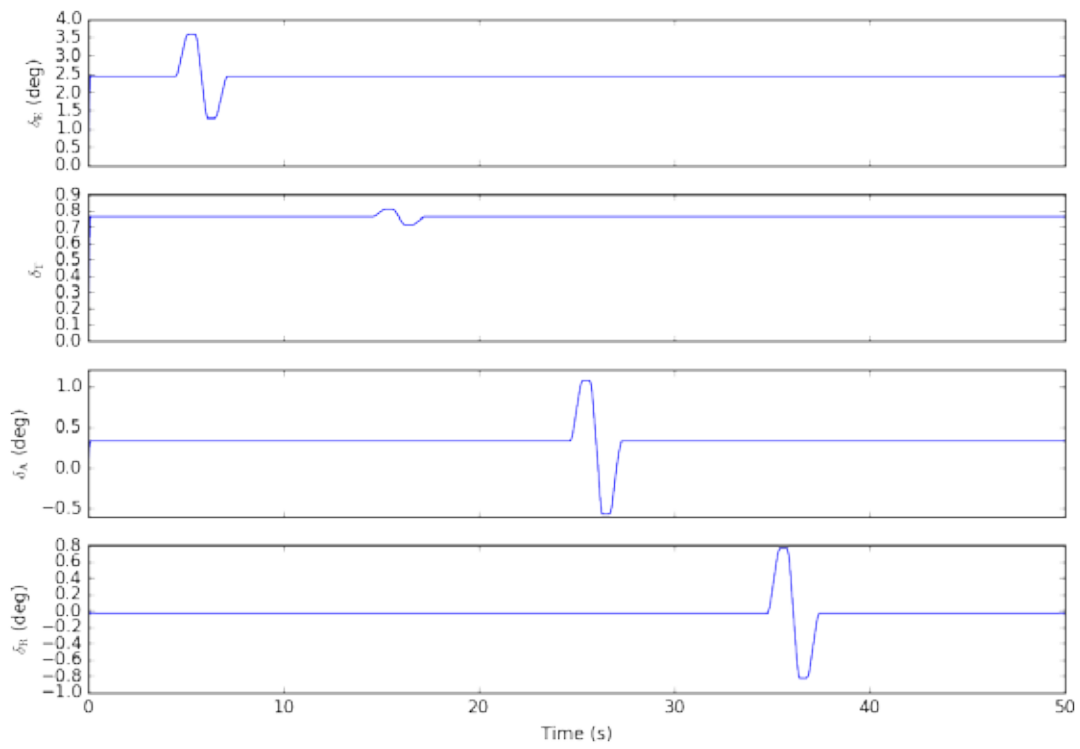
Figure 4. Doublet control input time histories
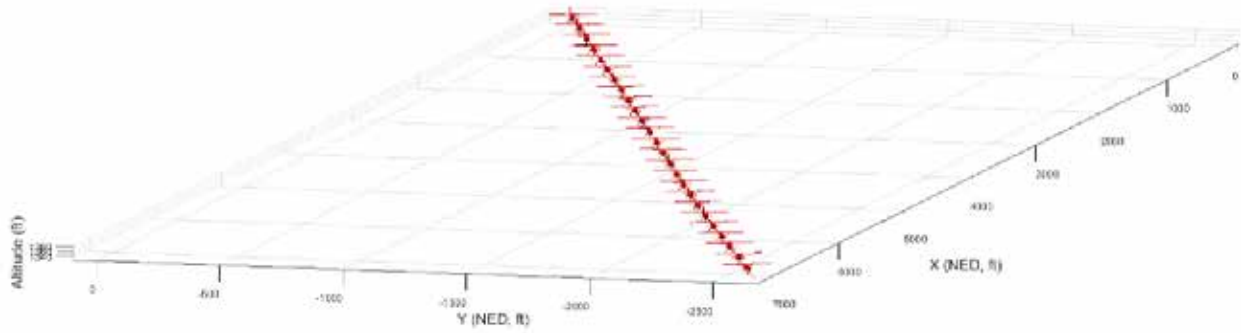
Figure 5. 3-D trajectory resulting from doublet control inputs

2.3 AERODYNAMIC MODELING

2.3.1 DATCOM Model

Several of the Monte Carlo cases were run with varying S&C derivatives to determine the effect of modeling errors. The random variables for the stability derivatives are calculated as:

$$\tilde{C}_X = \mathcal{N}\left(C_X, |\Delta C_X \cdot C_X|^2\right) \tag{1}$$

where C_X is an arbitrary S&C derivative and $\mathcal{N}(\mu, \sigma^2)$ is a standard normal distribution with mean μ and variance σ^2. Three methods are typically used for determining values for S&C derivatives. Analytical methods such as DATCOM [2] require the least amount of data and are easy to determine, but they are the least accurate. Wind-tunnel testing provides medium accuracy but requires large and mature amounts of data and is relatively expensive. Flight testing provides the highest accuracy but is also the most expensive method. Analytic stability derivatives tend to be available in the open literature, whereas values from wind-tunnel testing and flight testing are usually proprietary and not available to researchers. The uncertainties used for this work were determined analytically using DATCOM methods and represent the largest expected uncertainties in each derivative when using analytical modeling methods. It is important to note that the derivative values shown in table 1 are based on presumed modeling errors, not actual variations encountered during flight.

**Table 1. Parameter uncertainties and nominal values for derived
AoA/sideslip angle calculations**

S&C Derivative	Nominal Value (1/rad)	Uncertainty (%)	Standard Deviation (1/rad)
C_{L_α}	4.41	5	0.2205
C_{L_q}	3.9	20	0.78
$C_{L_{\delta_E}}$	0.43	10	0.043
C_{y_β}	-0.393	20	0.0786
C_{y_p}	-0.075	50	0.0375
C_{y_r}	0.214	50	0.107
$C_{y_{\delta_A}}$	0	N/A	N/A
$C_{y_{\delta_R}}$	0.187	10	0.0187

These values are based on modeling errors for DATCOM-based methods for estimating S&C derivatives. These values can be considered a medium level of parameter uncertainty.

2.3.2 JSBSim Nonlinear Model

This section briefly describes the nonlinear aerodynamic model used by JSBSim for the Cessna 172.

2.3.2.1 Lift Equation

The lift equation for the Cessna 172R in JSBSim can be modeled as:

$$L = \left(C_L(\alpha) + C_{L_{\dot\alpha}}\dot\alpha + C_{L_q}q + \Delta C_L(\delta_F) + C_{L_{\delta_E}}\delta_E \right)\bar{q}S \tag{2}$$

where $\Delta C_L(\alpha)$ is the increment in lift coefficient due to AoA, $C_{L_{\dot\alpha}}$ is the effect of AOA rate on lift coefficient, C_{L_q} is the lift pitch damping derivative, $\Delta C_L(\delta_F)$ is the increment in lift coefficient due to flap deflection δ_F, and $C_{L_{\delta_E}}$ is the elevator effectiveness. Note that the above equation is a simplification of the actual model, which also takes ground effect and a stall hysteresis into account for the $\Delta C_L(\alpha)$ and $\Delta C_L(\delta_F)$ terms.

2.3.2.1.1 Lift Curve Slope

JSBSim models the lift curve slope (C_{L_α}) as a lookup table as a function of the AoA and a stall hysteresis. Ignoring the stall effect, the contribution to lift due to AoA can be modeled as:

$$\Delta C_L(\alpha) = \left(C_{L_{\alpha=0}} + C_{L_\alpha}(\alpha) \cdot \alpha \right)\bar{q}S \tag{3}$$

where $C_{L_{\alpha=0}}$ is the zero AoA contribution to the lift coefficient, and $C_{L_\alpha}(\alpha)$ is the lift curve slope as a function of AoA. JSBSim lift curve slope as a function of AoA is shown in Figure 6.
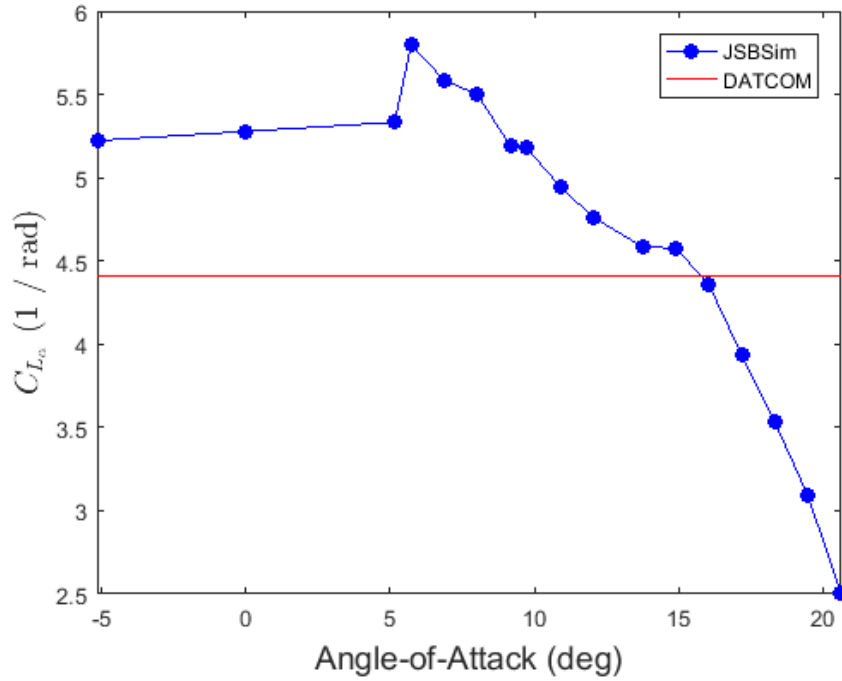
Figure 6. JSBSim lift curve slope as a function of AoA

2.3.2.1.2 Angle-of-Attack Rate Derivative

JSBSim uses a constant value of 1.7 1/rad for the derivative $C_{L_{\dot\alpha}}$.

2.3.2.1.3 Pitch Damping Derivative

JSBSim uses the same static value for C_{L_q} as the DATCOM model, 3.9 1/rad.

2.3.2.1.4 Flap Effectiveness

JSBSim has a nonlinear lookup table for the effect of flap deflection on the lift coefficient.

2.3.2.1.5 Elevator Effectiveness

JSBSim uses a constant value of 0.3470 1/rad for the derivative $C_{L_{\delta_E}}$.

2.3.2.2 Sideforce Equation

The sideforce equation has the following component build up in the Cessna 172R model:

$$Y = \left(C_{y_\beta}(\beta) \cdot \beta + C_{y_p}p + C_{y_r}r + C_{y_{\delta_A}}\delta_A + C_{y_{\delta_R}}\delta_R \right) \bar{q}S \qquad (4)$$

In the above equation, $C_{y_\beta}(\beta)$ is the sideforce due to sideslip as a function of sideslip, C_{y_p} is the effect of roll rate on the sideforce, C_{y_r} is the effect of yaw rate, $C_{y_{\delta_A}}$ is the aileron effectiveness, and $C_{y_{\delta_R}}$ is the rudder effectiveness. The term $C_{y_\beta}(\beta) \cdot \beta$ modeled as a lookup table, but is effectively a constant C_{y_β} multiplied by the sideslip angle. All of the modeling terms can be represented as constant values. Table 2 is a listing of the sideforce model parameters.

Table 2. JSBSim sideforce S&C derivatives

S&C Derivative	JSBSim Value (1/rad)
C_{y_β}	-0.3095
C_{y_p}	-0.0370
C_{y_r}	0.2100
$C_{y_{\delta_A}}$	-0.0500
$C_{y_{\delta_R}}$	0.0980

2.4 MODIFIED Z-SCORE

The modified z-score [3] is introduced as a metric to calculate how "close" an uncertain parameter lies to the nominal value (e.g., a z-score of two indicates that, on average, the parameter value is approximately two standard deviations from the mean). The modified z-score, subsequently simply referred to as the z-score, differs from the z-score in that the z-score is a statistic based on the entire population, rather than a sample. The z-score is calculated as:

$$z_i = \frac{x_i - \mu}{\sigma} = \frac{C_{X_{random_i}} - C_{X_{nominal}}}{\Delta C_X \cdot C_{X_{nominal}}} \text{ for } i = 1 \dots N \tag{5}$$

Note that the DATCOM values are used as the nominal value for the algorithm, as they provide an example of a non-proprietary aerodynamic model available to system developers.

2.5 SENSOR MODELING

The attitude heading and reference systems and inertial navigation systems (INS) commonly use an inertial measurement unit (IMU) and external aiding sensors (GPS, barometer, magnetometer) for aircraft state estimation [4, 5]. For the purposes of testing the derived AoA algorithms proposed in this work, the quality of the IMU and aiding sensors was varied to investigate the influence of sensor capability on the resulting derived AoA. The IMU consists of three orthogonal gyroscopes and accelerometers. The quality of the IMU is typically couched in terms of the bias stability of the gyroscopes and scale factor/orthogonality of the accelerometer triad [6]. The attitude fusion algorithms are a level above the IMU and do not directly affect the derived AoA estimates. Ignoring the sensor fusion algorithms drastically reduces the complexity of developing minimum operational performance standards for derived AoA estimation techniques. Whereas the fused sensor estimates are not directly applicable to this work, the raw sensor data furnished by the IMU

are applicable. In this manner, the quality of the IMU will directly affect the derived AoA estimates. The degree to which the IMU errors couple to AoA errors can best be investigated using Monte-Carlo-type simulations. This simulation methodology allows for mapping sensor statistical noise characteristics through the derived AoA algorithms and providing AoA error bounds directly traceable to the IMU. The specific sensors and corresponding noise characteristics are given in tables 3–4.

Table 3. Gyroscope performance data

Manufacturer	Axes	Full scale range (deg/s)	Bias stability (deg/hr)	Resolution (deg/s/bit)	Noise density (deg/s/√Hz)	Total error (deg/s)
Silicon Sensing CMS390	1	300	10.0	0.005	0.0055	1.5
VTI SCC1300	1	300	12.0	0.056	0.014	5.0
InvenSense MPU-9150	3	500	20.0-50.0	0.030	0.065	15.0

Table 4. Accelerometer performance data

Manufacturer	Axes	Full scale range (g)	Bias stability (mg)	Total error (mg)	Resolution (mg/bit)	Noise density (mg/√Hz)
Silicon Sensing CMS390	2	±2.5/10	30.0	±13.0	0.08	1.0
VTI SCC-1300	3	±6	70.0	±40.0	1.5	5.0
InvenSense MPU-9150	3	±2/4/8/16	103.0	±150.0 (4g mode)	0.4	4.0

Additional state estimates for fused datasets are also provided. These estimates cover any cases in which airspeed data are not available. In this case, the GPS/INS-furnished ground speed may be used, albeit in error. These additional sensor characteristics can provide further insight into the sensitivity of the derived AoA algorithms. The provided data correspond to IMU data typical of commercially available AHRS and INS systems [7–9]. Table 5 gives GPS-specific errors common to single-band, low-cost devices. Table 6 gives the fused state errors. Sensor fusion is accomplished using an error-state Kalman filter [10]. This filter topology is common in INS applications using higher performance IMUs. The fused state estimate errors in table 6 correspond to:

1.   No sensor noise—testing performance of EKF only.
2.   Aiding sensor noise only—GPS errors, as per table 5.
3.   Remaining corresponds to GPS and specific sensor errors outlined in tables 3–4.

Table 5. GPS noise characteristics

Noise component	Noise estimate
Position	± 0.7 m static, *x-y* ± 2.5 m dynamic, *x-y* ± 2.5 m static, *z* ± 5 m dynamic, *z*
Velocity	± 0.5 m/s static, *x-y* ± 1.5 m/s dynamic, *x-y* ± 2.5 m/s static, *z* ± 5 m/s dynamic, *z*

Table 6. Fused sensor state estimates (3σ)

Manufacturer	RMS angular error (±deg)	RMS velocity error (±m/s)	RMS position error (±m)
No noise	1.738e-2	0.389	0.422
Aiding sensor noise only	0.265	0.413	0.491
CMS390 noise	0.315	0.413	0.496
VTI SCC1300 noise	0.542	0.546	0.634
InvenSense MPU-9150 noise	0.790	0.796	0.924

The sensor noise components presented in tables 3–6 can be interpreted in the following ways. The bias terms represent fixed quantities typically subtracted after an appropriate turn-on time. The gyroscope bias stability represents the integrated effect of Schott and flicker noise on the derived attitude estimates. The noise density represents the effect of noise as a function of sampling rate. Typically, higher sampling rates diminish the noise magnitude in a manner similar to successive averaging. The total error statistics represent the combined effect of bias, noise, and manufacturing tolerances. This statistic represents the worst-case scenario and helps classify the sensors into quality categories. The aiding sensor statistics follow the same trends, with similar bias and noise statistics. The fused state estimates in table 6 can be used in place of proprietary AHRS and INS algorithms used in commercial devices. These estimates are well documented and match the reported performance of many commercial devices [10].

Notes:

1. The total gyroscope error in table 3 included the effects of turn-on bias. In practice, this was removed by averaging once the device had stabilized after powering on.
2. The noise statistics for the IMU sensors were determined via an Allan variance analysis [2, 3].
3. The GPS sensor was an Ublox NEO-7m, sampled at 4 Hz. WAAS- (Wide Area Augmentation System-) enabled aircraft GPS systems can typically achieve better performance (approximately half the error).
4. All data are presented in [8].

2.6 DERIVED AERODYNAMIC ANGLE ALGORITHMS

For the Monte Carlo runs, the "basic" equation for derived AoA was used [11]. This approach solved the component buildup of the lift equation for AoA:

$$\hat{\alpha} = \frac{-\left(C_{L_1} + C_{L_q}\frac{q\bar{c}}{2V_T} + C_{L_{\delta_E}}\delta_E\right)\frac{\bar{q}S}{W} - n_z}{C_{L_\alpha}\frac{\bar{q}S}{W} + n_x} \tag{6}$$

Similarly, the side force equation is solved for the sideslip angle [11]:

$$\hat{\beta} = \frac{n_y\frac{W}{\bar{q}S} - C_{y_p}\frac{pb}{2V_T} - C_{y_r}\frac{rb}{2V_T} - C_{y_{\delta_A}}\delta_A - C_{y_{\delta_R}}\delta_R}{C_{y_\beta}} \tag{7}$$

True values for the measured values (e.g., V_T, n_x, n_y, n_z, p, q, r, δ_A, δ_E, δ_R) were used for calculations. AoA and sideslip-angle calculations used measurements at 10 Hz for all values.

2.7 ERROR METRICS

Two types of errors were used to quantify the algorithm performance. They are described in sections 2.7.1 and 2.7.2.

2.7.1 Maximum Absolute Error

The maximum absolute error was calculated as:

$$e_{max} := \left|\max_i(\xi_i - \hat{\xi}_i)\right| \tag{8}$$

where ξ_i is the i-th value of an angle ξ, one of either α or β. The hat indicates an estimated/derived value.

2.7.2 Root Mean Square Error

The RMS error was calculated as:

$$e_{rms} := \sqrt{\frac{1}{N}\sum_{i=1}^{N}(\xi_i - \hat{\xi}_i)^2}, \tag{9}$$

The RMS error was a better measure of the average error over the time period compared to the maximum error.

2.8 ERROR THRESHOLDS

Three levels of error tolerances were set:

1.   Error for pilot display: **2**°
2.   Error for envelope protection: **1**°
3.   Error for an AFPC: **0.5**°

Pilot display entailed the display of the AoA and sideslip angle via an indexer or numeric readout. Envelope protection consisted of a flight-control system designed to limit pilot inputs to prevent exceedance of the safe-flight envelope of the aircraft. Finally, AFPC was a digital fly-by-wire system. The error values chosen for each of these systems was determined based on engineering and pilot judgment. The maximum absolute error was used to determine exceedance of these thresholds because these are the current (instantaneous) values that the pilot/flight control system uses.

3. MONTE CARLO RESULTS

3.1 CASE 1: UNCERTAIN S&C DERIVATIVES, 1000 RUNS

3.1.1 Overview

Figure 7 plots histograms of the absolute error for the AoA and sideslip angle for Case 1, which included 1000 Monte Carlo runs.
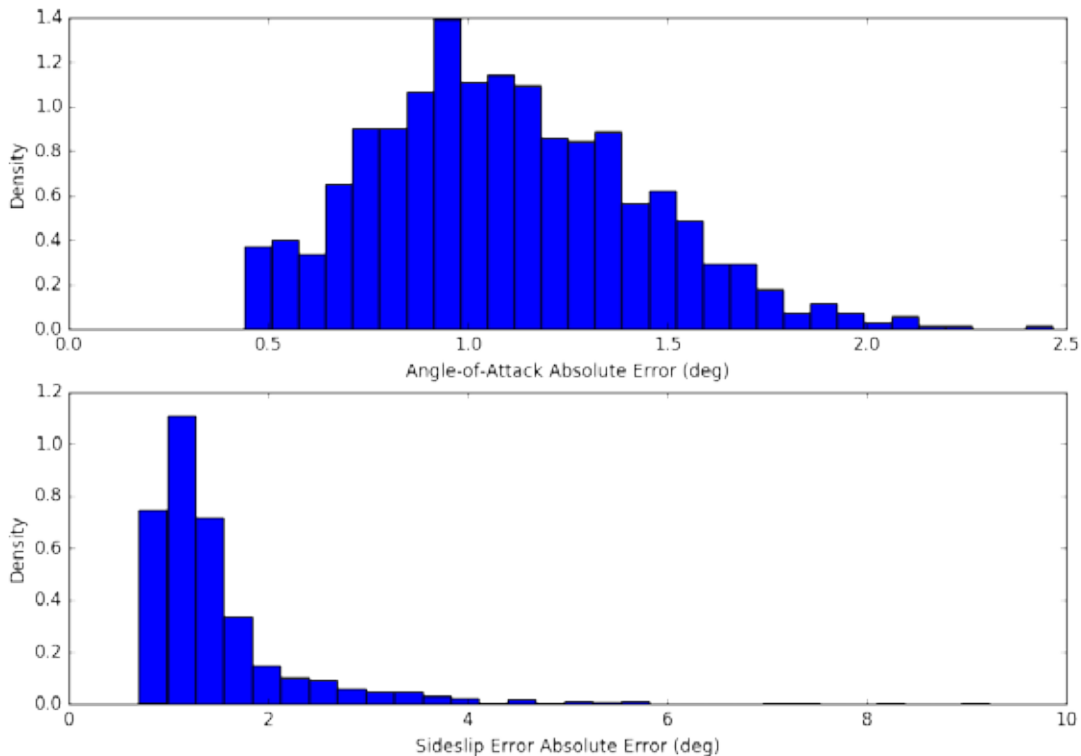
Figure 7. Case 1 error histograms

Figure 8 plots the histograms of the RMS errors for derived AoA and derived sideslip angle. The AoA RMS error distribution is skewed more to the left than the absolute error distribution.
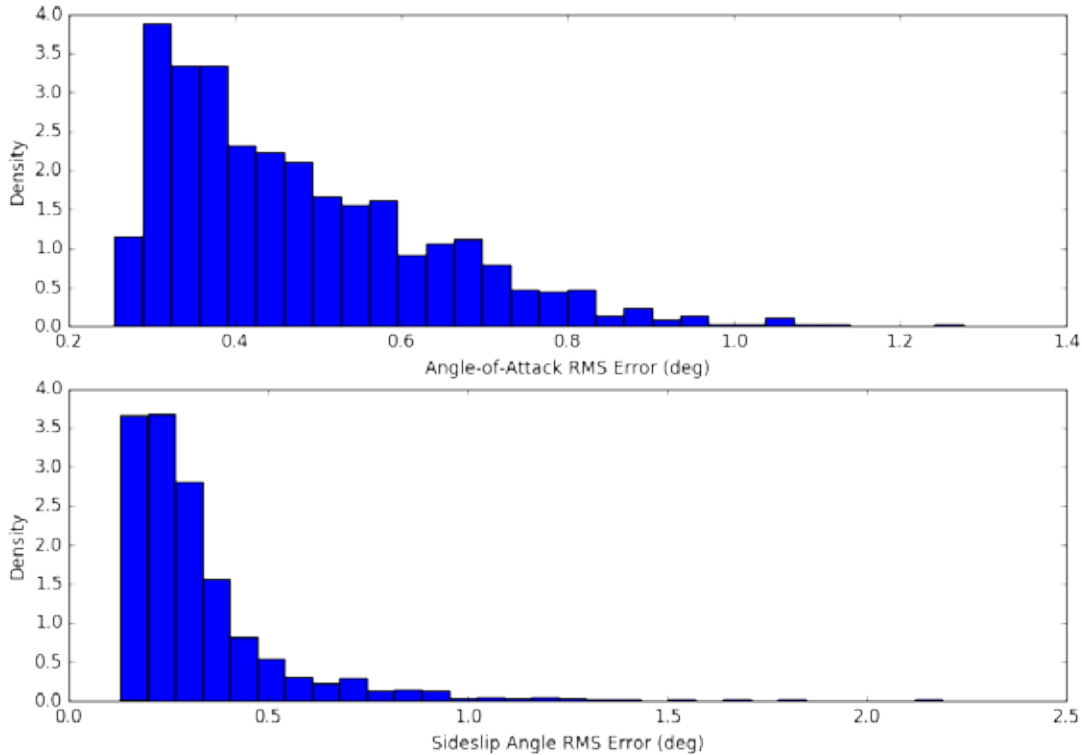
Figure 8. RMS error histograms for Case 1

3.1.2 AoA

For the derived AoA,

- 0.9000 % of runs violated the display tolerance.
- 55.9000 % of runs violated the envelope-protection tolerance.
- 41.1000 % of runs violated the AFPC tolerance.
- 2.1000 % of runs met all tolerances.

Figure 9 is a scatter plot of the C_{L_α} z-scores versus the maximum error in AoA for each iteration of the Monte Carlo runs. These maximum errors were calculated by taking the argument of the maximum absolute value of the AoA errors and then selecting the corresponding signed error value (see equation 3 in section 2.7.1). The maximum signed error was used because the error behavior depended on the sign of the z-score and the magnitude of the error. Figure 9 shows that the magnitude of the error depends on the sign of the z-score. Observing the figure, there appear to be two linear relationships between the z-scores and errors, centered on the area of minimum error. Note that the minimum error values occur at a z-score of approximately 2. This suggests that the DATCOM model C_{L_α} value is approximately 2σ less than the true JSBSim parameter.

Examining Eq. 6, the parameters in the numerator, C_{L_q} and $C_{L_{\delta_E}}$, influence the shape of the result, whereas in the denominator, C_{L_α} acts as a scaling factor for the entire result because, for most situations, $n_x \ll 1$ and $\frac{\bar{q}S}{W}$ is near unity. Note that C_{L_1} is a constant parameter calculated from $C_L = \frac{W}{\bar{q}S}$ in steady-state trimmed flight.
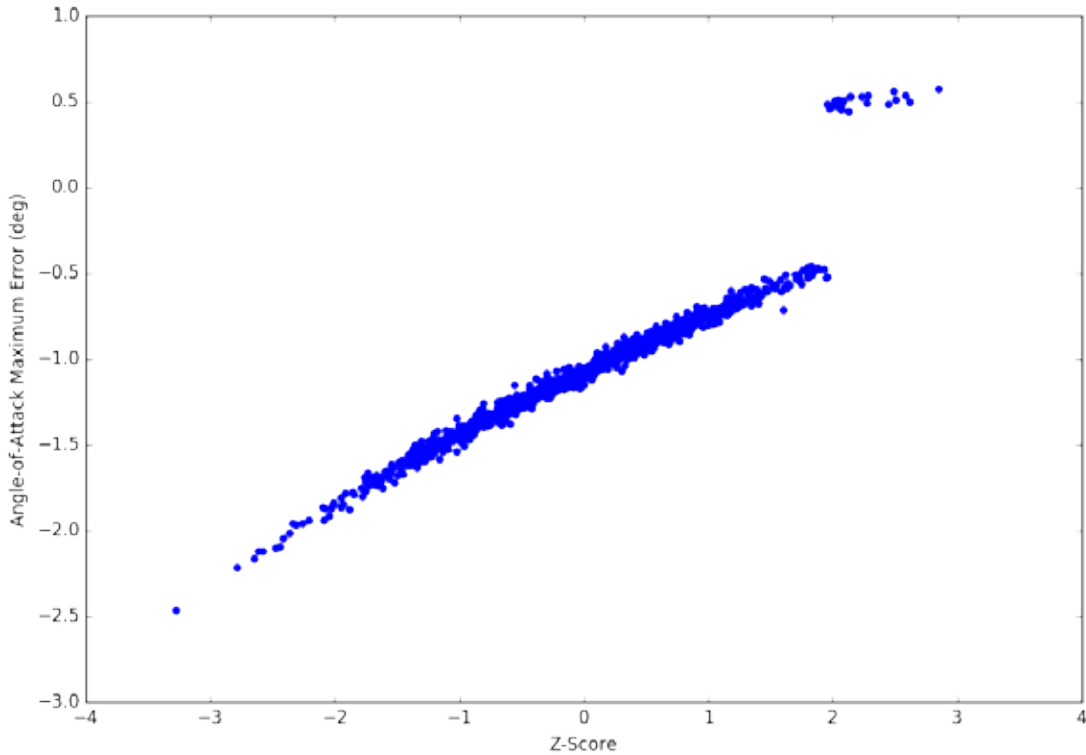
Figure 9. C_{L_α} scatter plot for Case 1

Because the absolute error may not be the best way to show the overall error, figure 10 plots the RMS errors versus the C_{L_α} z-scores. This shows a definite relationship between the variability of the lift curve slope value and the RMS error in derived AoA, and shows a symmetric relationship around the minimum error. Assuming a perfect lift curve slope value, the RMS error should be centered on the 0 z-score value. Here, the RMS error curve suggests that the best results are obtained with lift curve sloped approximately 1.5σ above the DATCOM model.
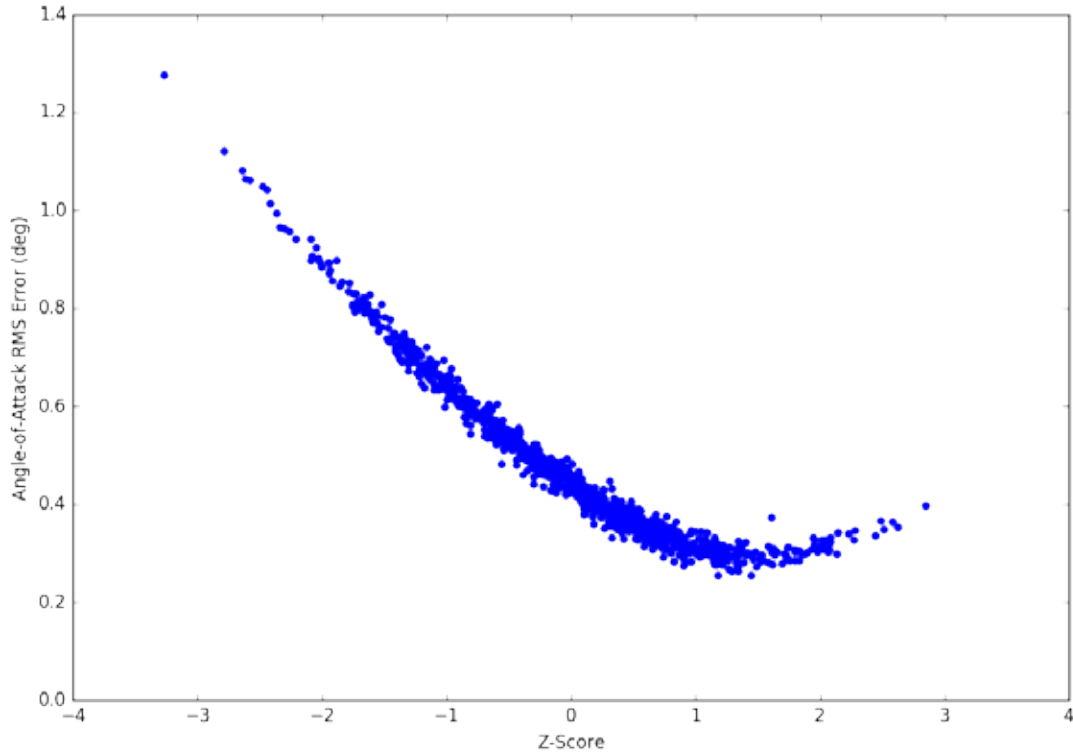
Figure 10. RMS errors vs C_{L_α} z-scores for Case 1

Figure 11 is a scatter plot of the z-scores of the derivative C_{L_q} versus AoA error. There appears to be no correlation between the C_{L_q} modeling errors represented by the z-scores and the resulting error in derived AoA. Furthermore, it does not appear that there is an effect caused by whether the modeled C_{L_q} is above or below the nominal value.
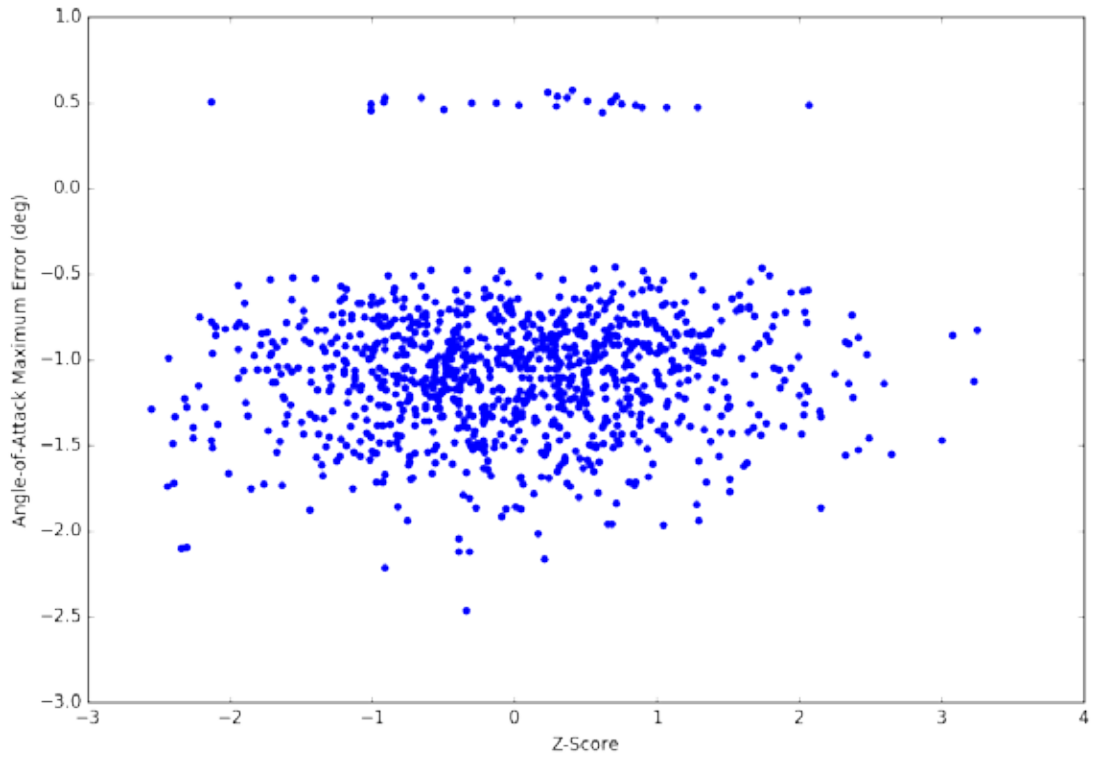
Figure 11. C_{L_q} **scatter plot for Case 1**

Figure 12 plots the RMS error for AoA versus the C_{L_q} z-scores, and clearly shows the lack of correlation between the two variables.
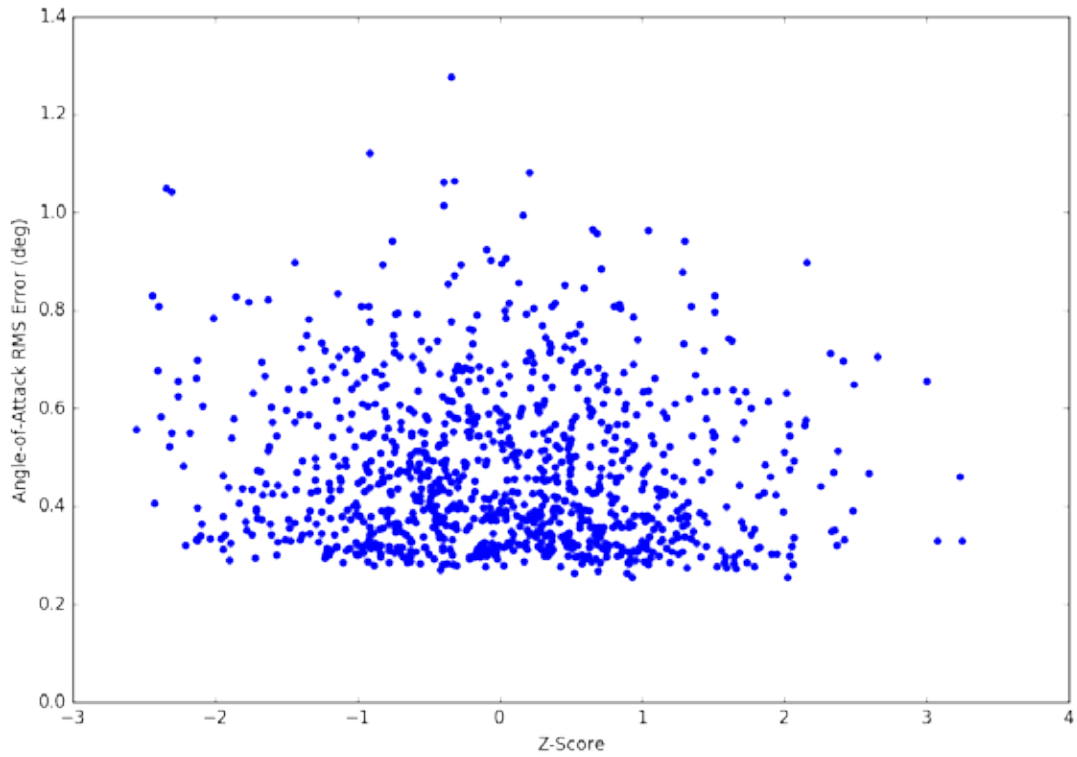
Figure 12. RMS error vs C_{L_q} z-scores for Case 1

Figure 13 plots the variability of the elevator effectiveness, $C_{L_{\delta_E}}$, versus the maximum error in the derived AoA estimate. As with the derivative C_{L_q}, there appears to be no correlation between the two variables.
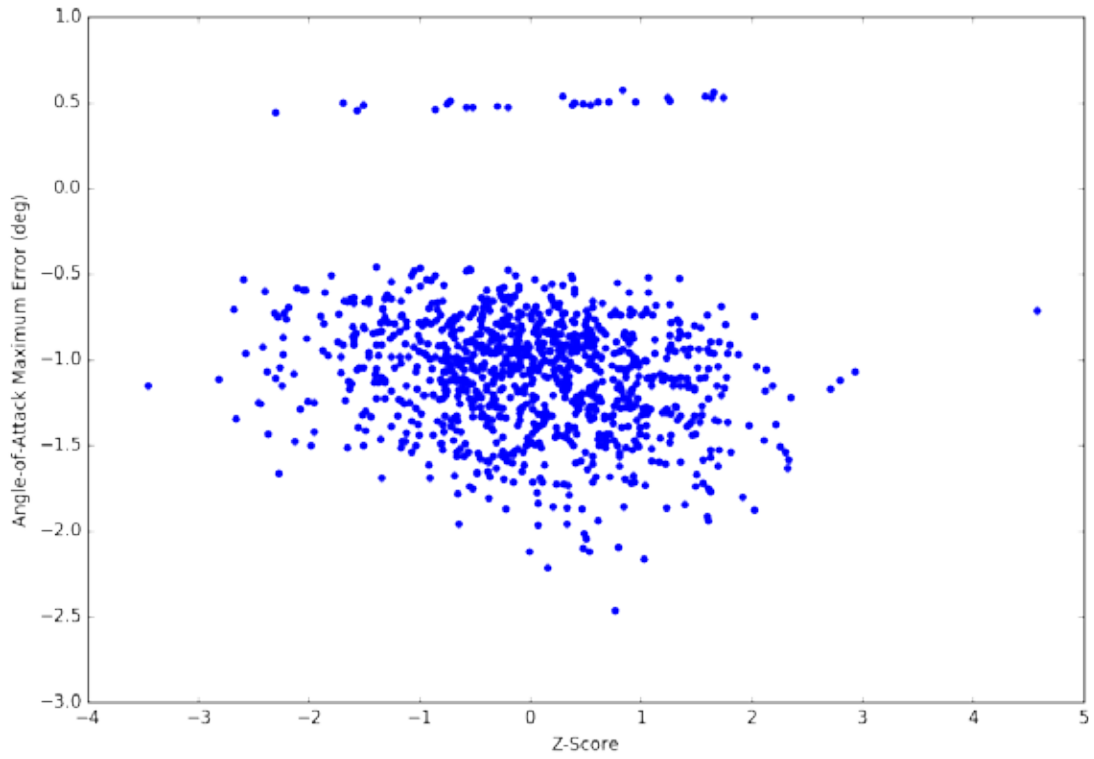
Figure 13. $C_{L_{\delta_E}}$ **scatter plot for Case 1**

Similarly, figure 14 plots the RMS error against the $C_{L_{\delta_E}}$ z-scores, again showing the lack of correlation.
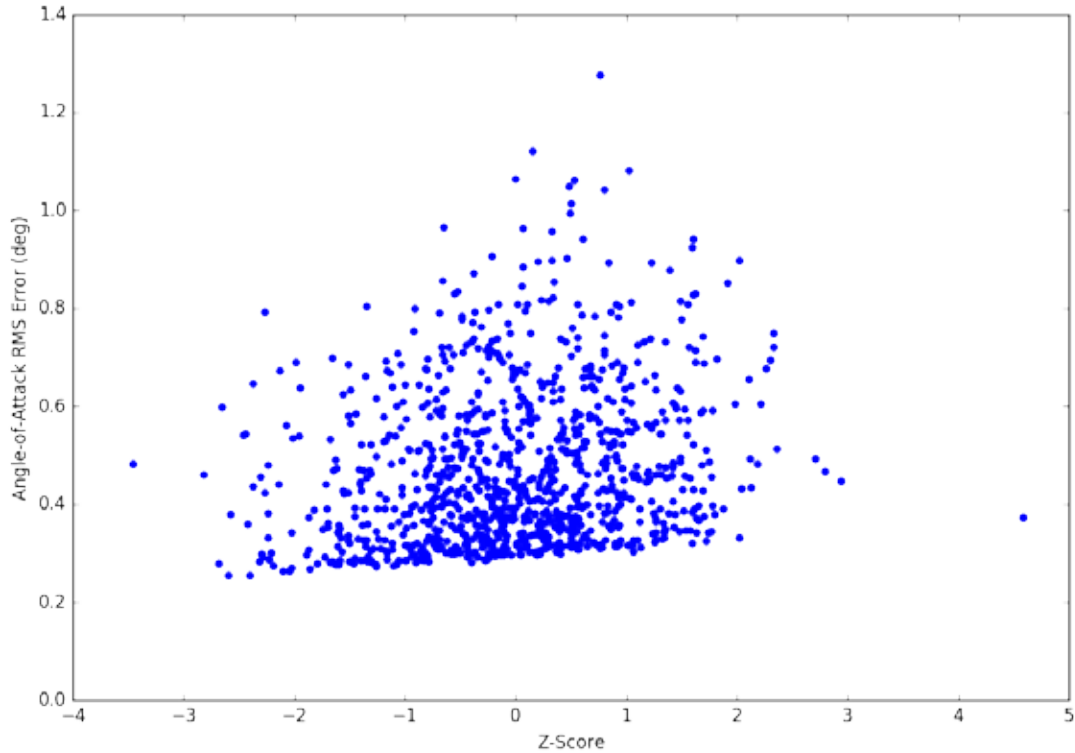
Figure 14. RMS error in derived AoA vs. elevator effectiveness for Case 1

If the C_{L_α} value corresponding to the minimum observed errors is used as the nominal value instead of the DATCOM value, the uncertainties needed to violate the AFPC tolerances are relatively low. The uncertainties needed to violate the envelope-protection tolerance are on average greater than $\pm 2\sigma$, which indicates that in most cases the algorithm will perform satisfactorily in this role with good modeling of the S&C derivatives. It is clear from the results that the accurate modeling of the lift curve slope is paramount for an accurate derived AoA estimate. Fortunately, this is one of the easier terms to determine. However, this is probably insufficient, and stricter tolerances will be needed for use in envelope-protection systems.

3.1.3 Sideslip Angle

For the derived sideslip angle:

·   14.5000 % of runs violated the display tolerance.
·   62.8000 % of runs violated the envelope-protection tolerance.
·   22.7000 % of runs violated the AFPC tolerance.
·   0.0000 % of runs met all tolerances.

Figure 15 plots the derivative C_{y_β}, the effect of the sideslip angle on the sideforce, versus the maximum error in the sideslip angle estimate. Examining the figure, there appears to be a noticeable correlation between the maximum sideslip angle error and the z-score of C_{y_β}. This trend

appears to be symmetric about the horizontal axis, suggesting that the magnitude of the error depends only on the z-score and not the sign of the error.
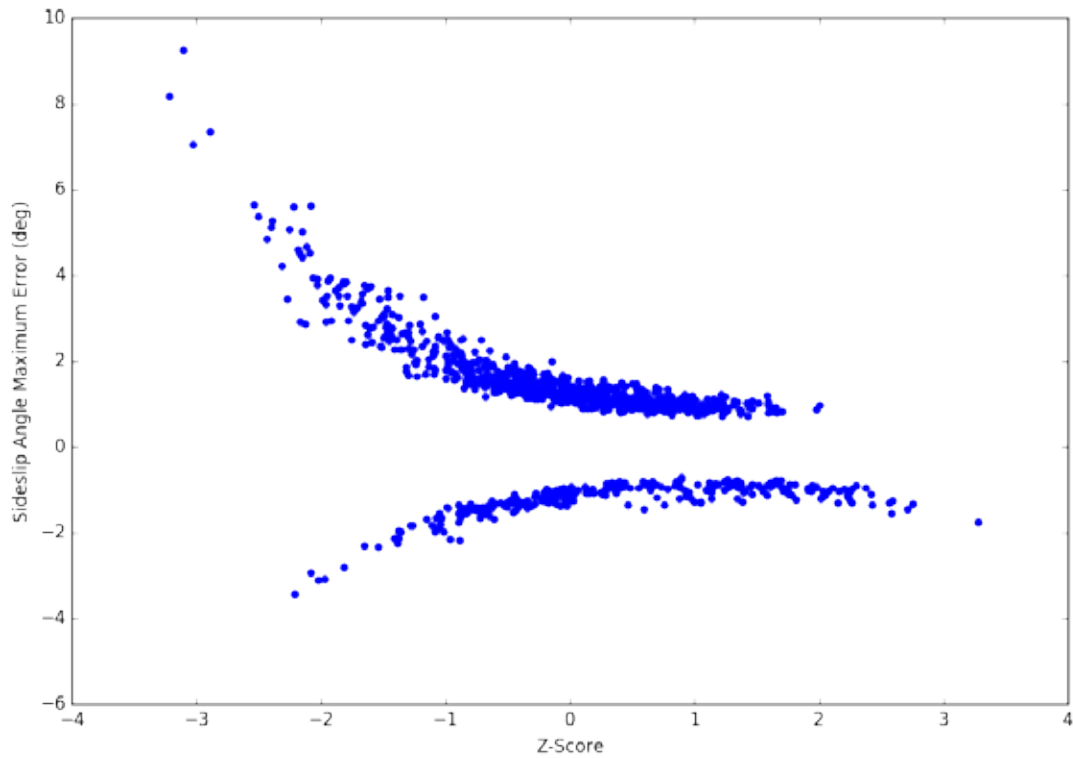
Figure 15. C_{y_β} scatter plot for Case 1

Figure 16 plots the sideslip angle RMS errors against the z-scores of the derivative C_{y_β}, which also clearly shows a relationship between the two parameters. As with figure 15, it appears that the more negative the C_{y_β} z-score, the worse the error in the derived sideslip angle. There are insufficient data to say with certainty, but it appears that the error also increases dramatically at large positive z-scores, as is expected, so that the RMS error versus z-score plot is symmetric.
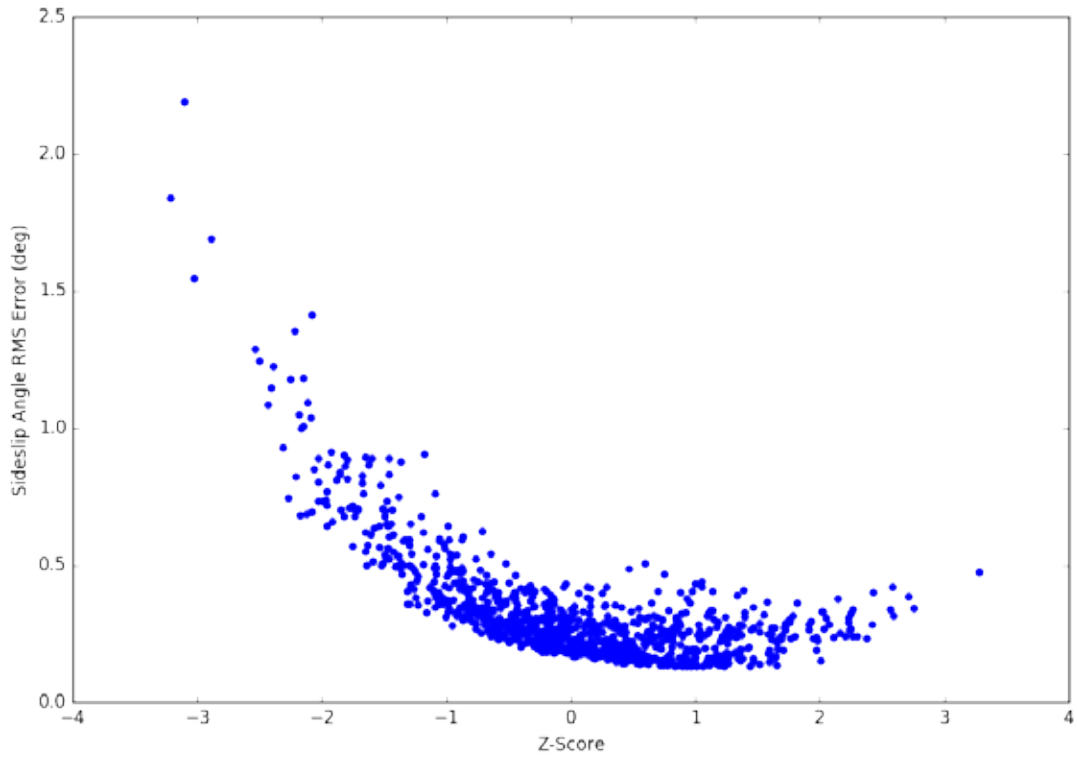
Figure 16. Sideslip angle RMS Error vs C_{y_β} z-scores for Case 1

Figure 17 plots the maximum sideslip estimate error versus the variability of the derivative C_{y_p}, the effect of the roll rate on the side force. There appears to be no correlation between the value of C_{y_p} and the maximum sideslip angle error.
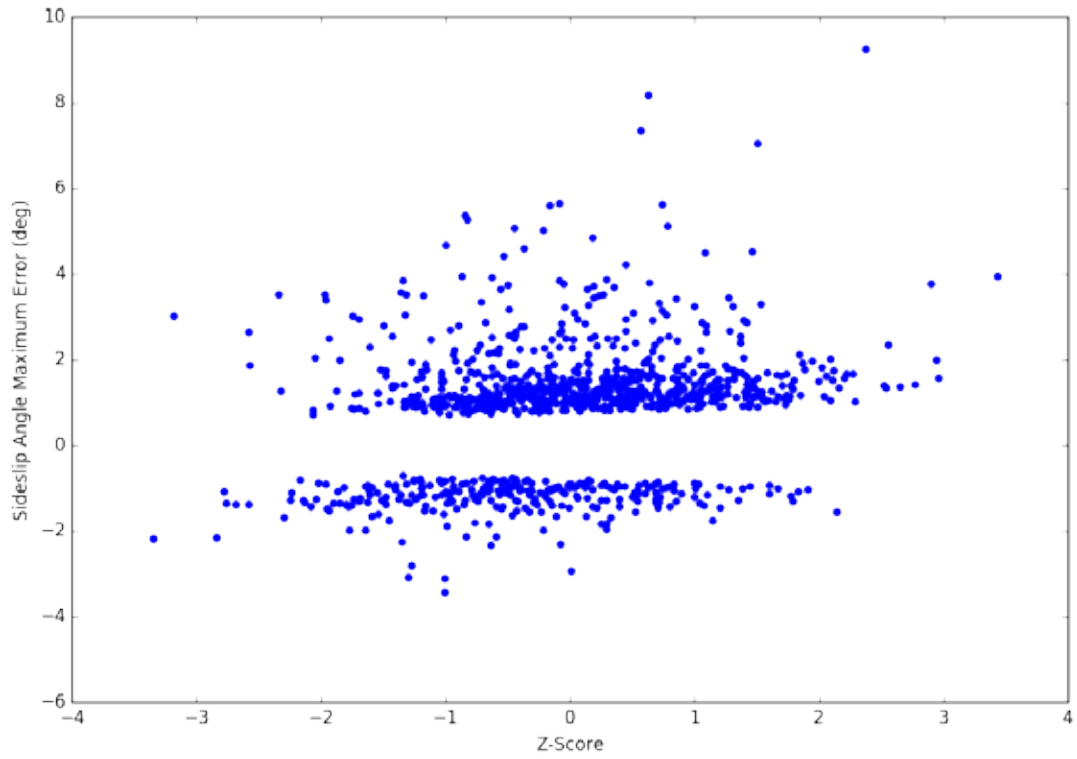
Figure 17. C_{y_p} **scatter plot for Case 1**

This is corroborated by figure 18, which plots the RMS error instead of the maximum error.
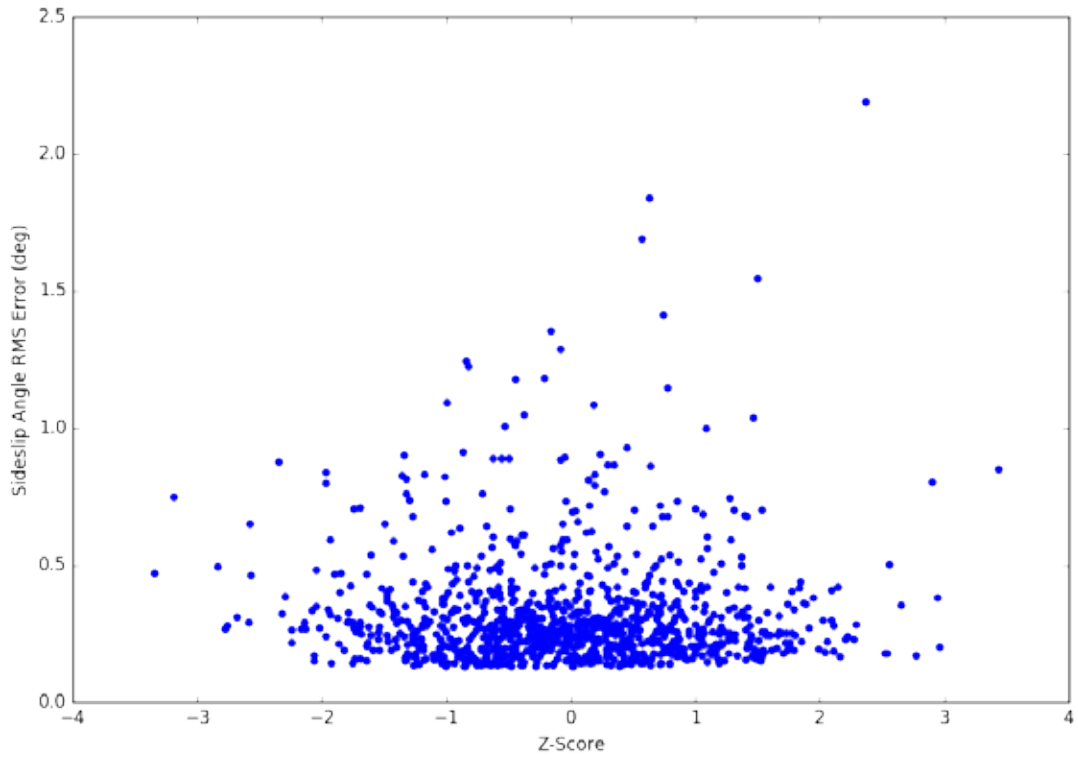
Figure 18. RMS error vs C_{y_p} z-scores for Case 1

Similarly, the maximum sideslip error does not seem to be affected by the variation in the derivative C_{y_r}, as shown in figure 19.
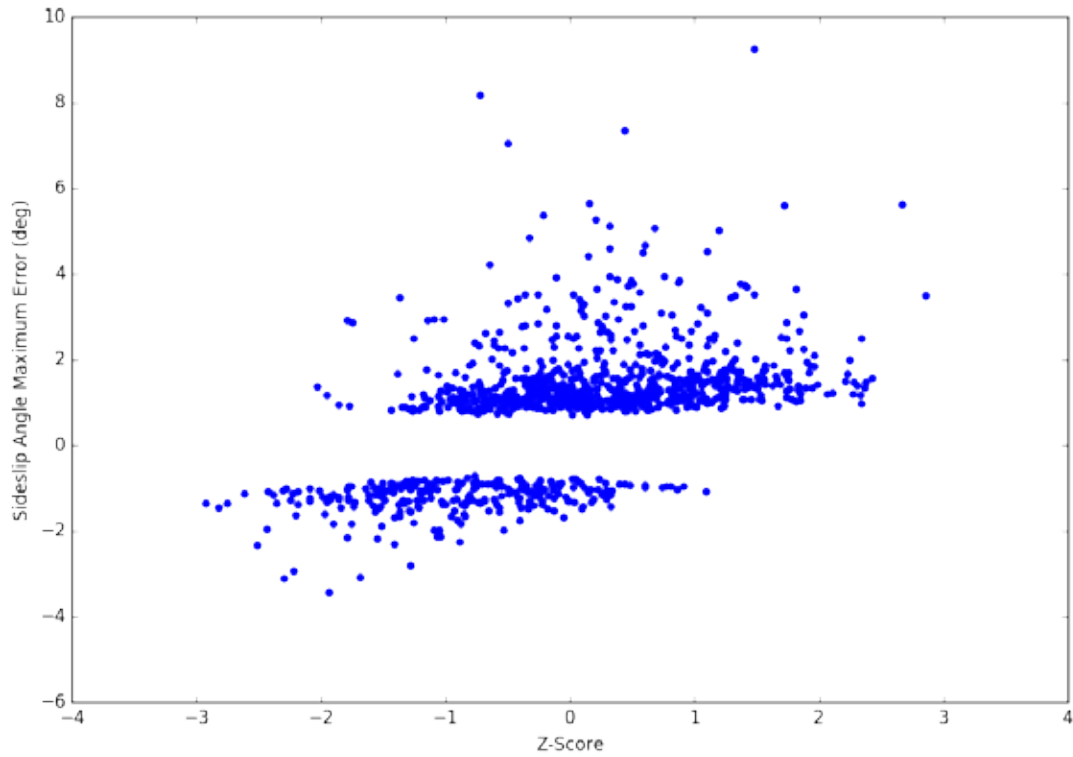
Figure 19. C_{y_r} scatter plot for Case 1

Figure 20 plots RMS error for derived sideslip against the variation of the derivative C_{y_r}. Unlike the absolute error shown in figure 19, there appears to be a slight correlation between the two variables, although the effect is much less than that of C_{y_β}.
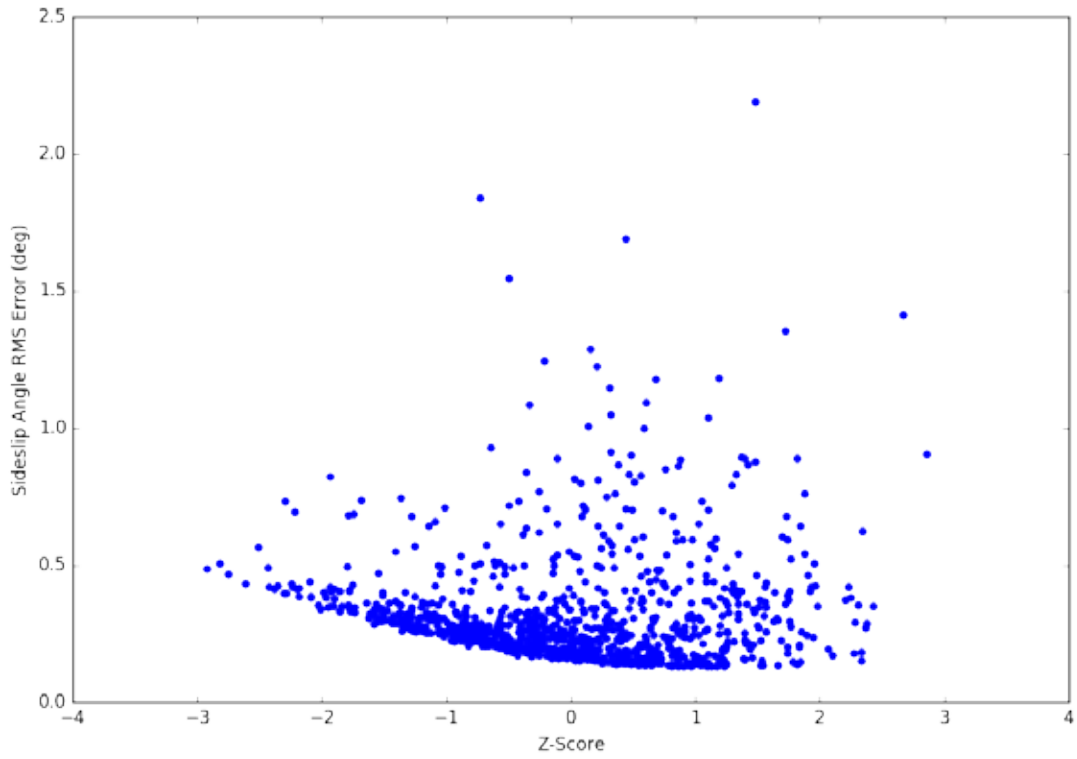
Figure 20. RMS error vs C_{y_r} z-scores for Case 1

Figure 21 plots the maximum sideslip angle errors versus the rudder effectiveness ($C_{y_{\delta_R}}$) and appears to show no correlation between the two.
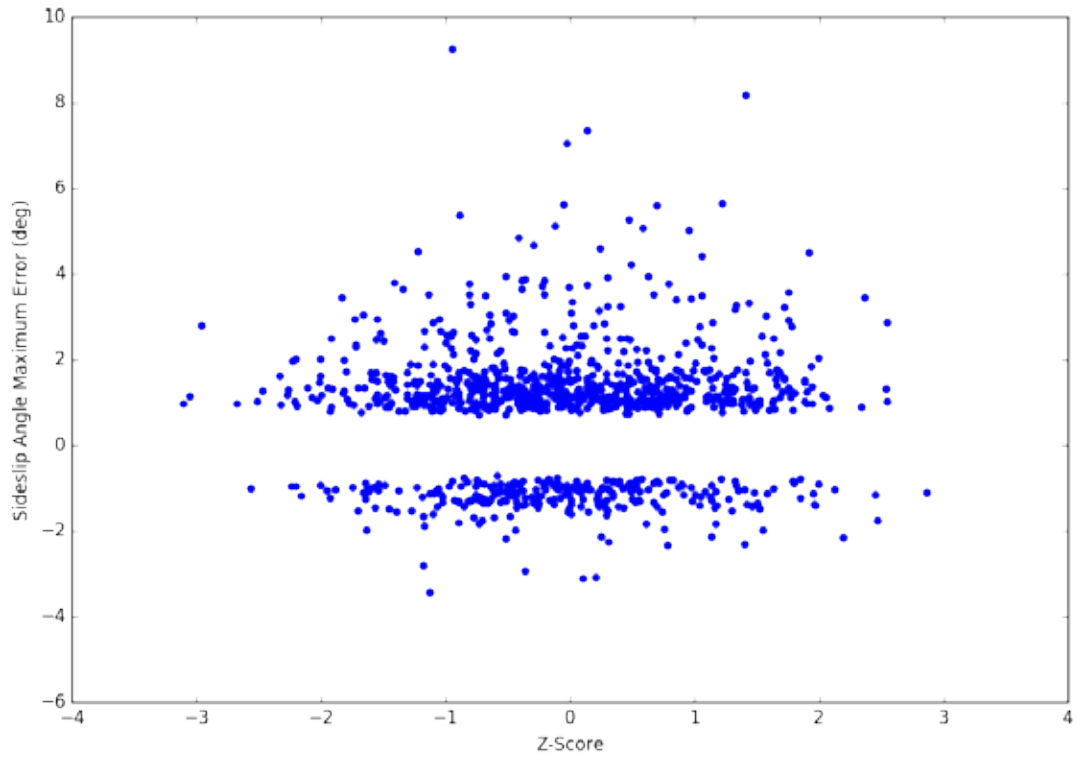
Figure 21. $C_{y_{\delta_R}}$ **scatter plot for Case 1**

The same lack of correlation is seen with the RMS error in figure 22.
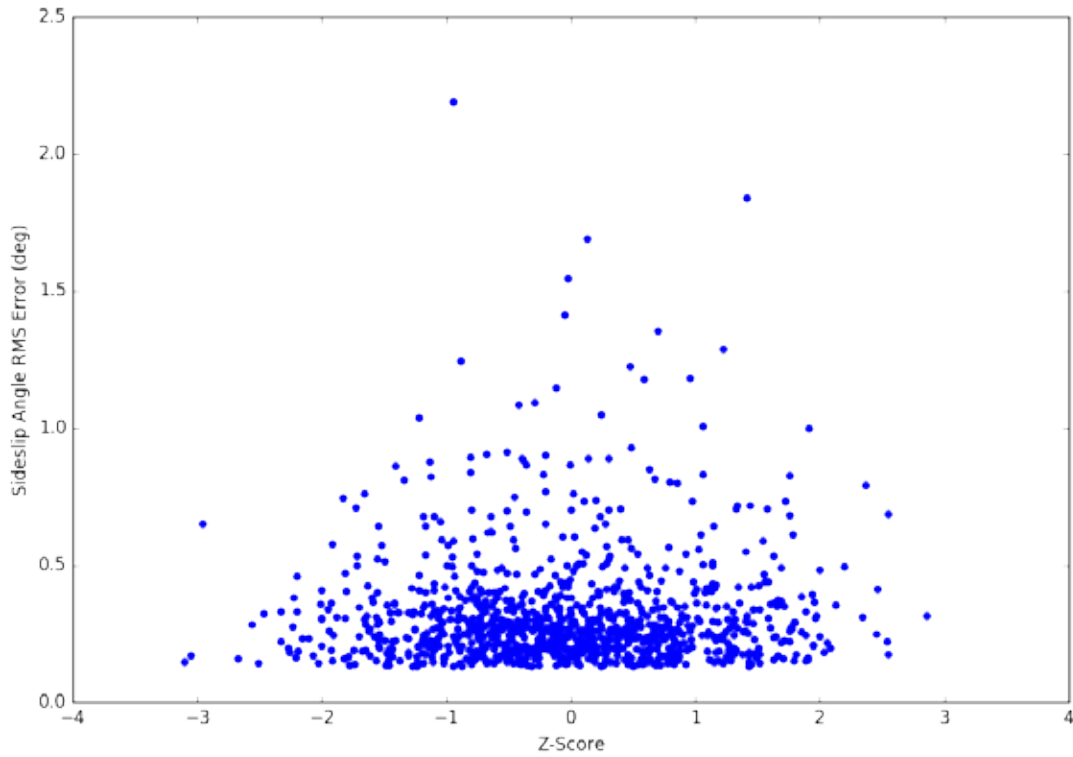
Figure 22. RMS error vs variation of $C_{y_{\delta_R}}$ for Case 1

3.2 CASE 2: UNCERTAIN S&C DERIVATIVES, 10,000 RUNS

3.2.1 Overview

Case 2 ran an order of magnitude more Monte Carlo iterations than Case 1. Figure 23 shows the error histograms for the AoA and sideslip angle absolute errors. Note that the sideslip angle error histogram is skewed by an outlier with a $50°$ maximum error.
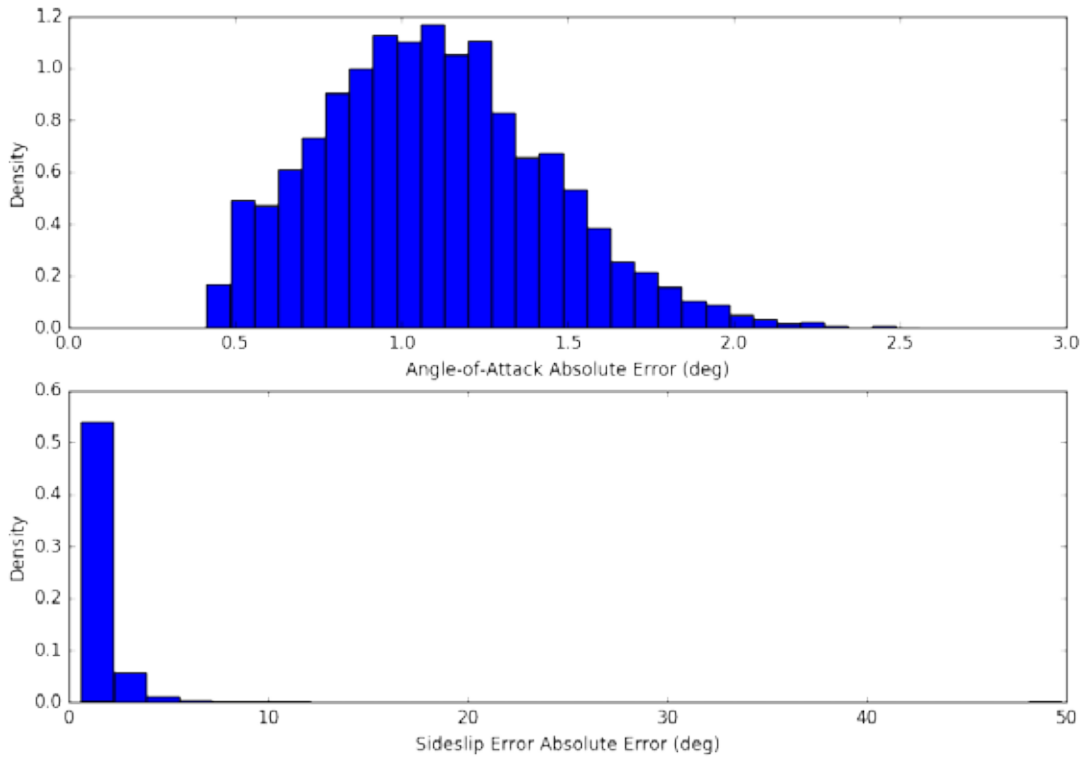
Figure 23. Case 2 error histograms

Similarly, figure 24 plots the RMS error histograms. The sideslip error RMS error histogram shows a similar distribution with the absolute errors. Whereas the AoA is skewed toward lower RMS errors, the absolute AoA errors approximate a normal distribution centered near 1-degree error. Note that the sideslip error histogram is skewed by an outlier to the far right.
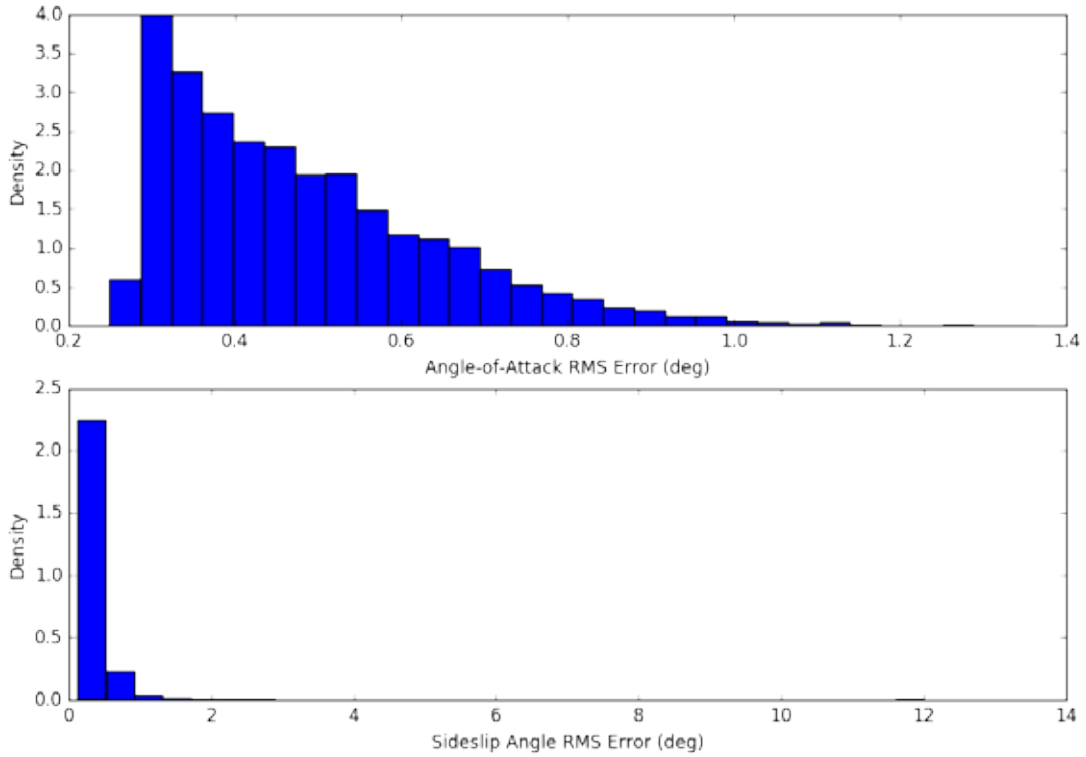
Figure 24. RMS error histograms for Case 2

Because the derivatives C_{L_q}, $C_{L_{\delta_E}}$, C_{y_p}, C_{y_r}, and $C_{y_{\delta_R}}$ continue to appear to have no correlation between their variations and the resulting maximum and RMS errors, only the plots for RMS errors for these parameters are shown in the interests of brevity for the remainder of this report.

3.2.2 Angle-of-Attack

For the derived AoA,

- 0.9500 % of runs violated the display tolerance,
- 58.0900 % of runs violated the envelope-protection tolerance,
- 39.0000 % of runs violated the AFPC tolerance,
- 1.9600 % of runs met all tolerances.

Figures 25–26 show that the relationship between the absolute and RMS errors and the z-scores of C_{L_α} continue as seen in Case 1. Figures 27–28 show the continuing lack of correlation between the parameters C_{L_q} and $C_{L_{\delta_E}}$ with the derived AoA errors.
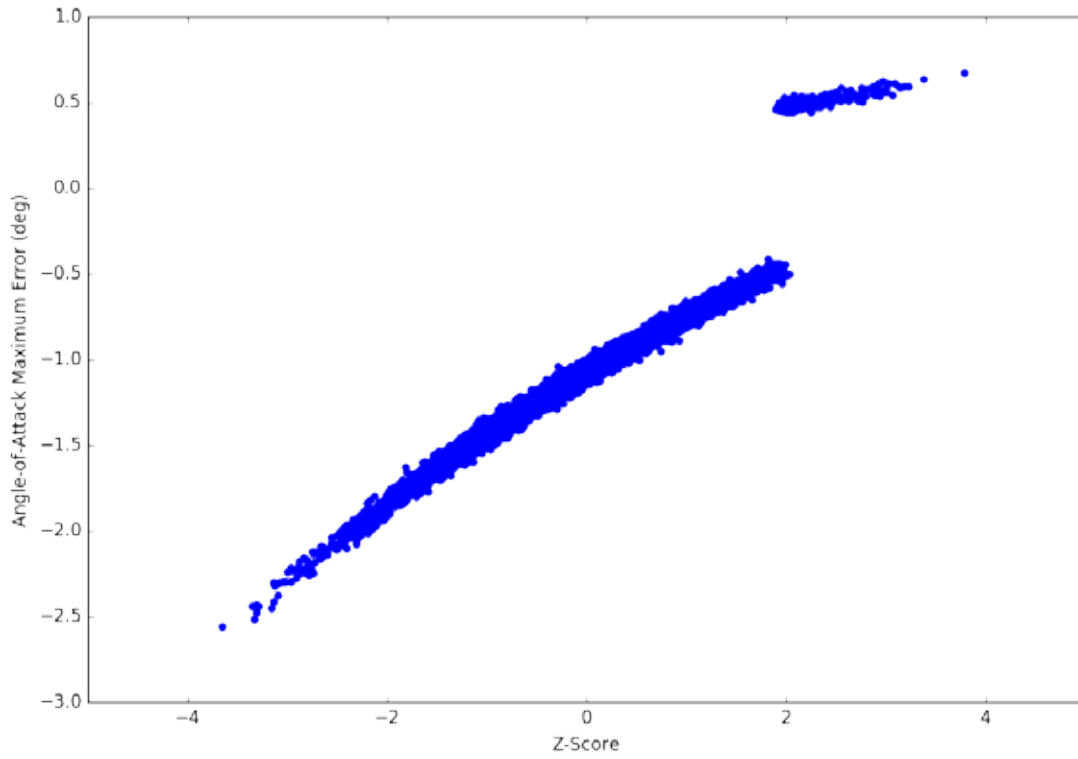
Figure 25. C_{L_α} **scatter plot for Case 2**
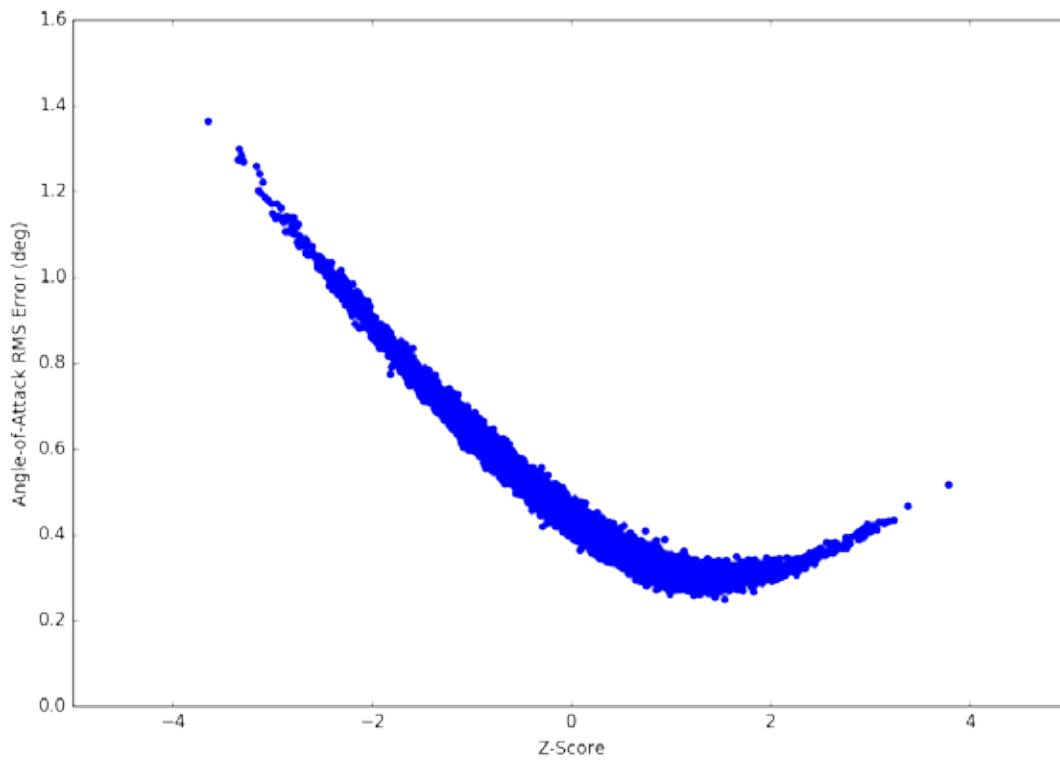
Figure 26. C_{L_α} **RMS error scatter plot for Case 2**
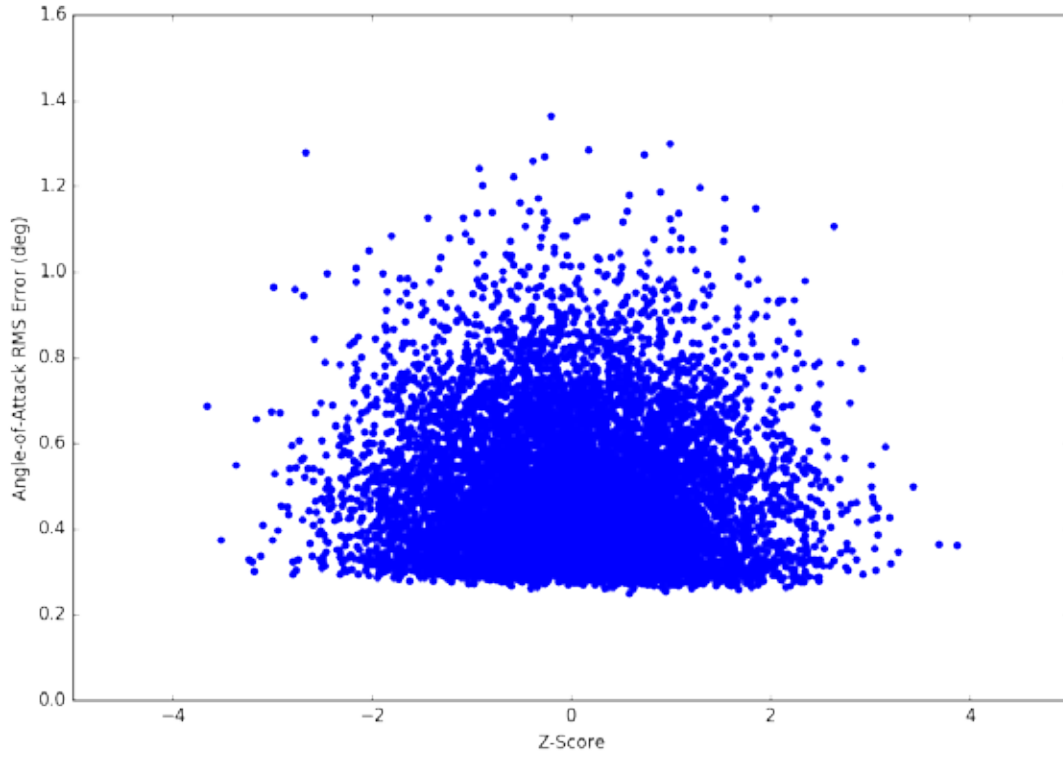
Figure 27. C_{L_q} **RMS error scatter plot for Case 2**
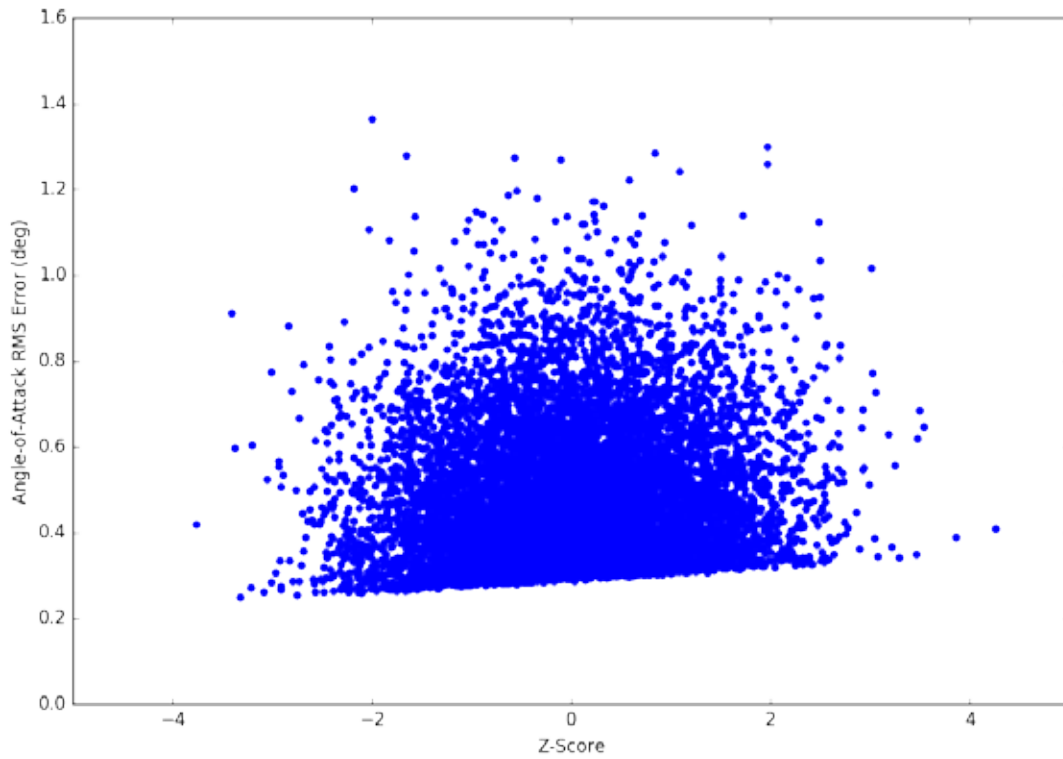
Figure 28. $C_{L_{\delta_E}}$ **RMS error scatter plot for Case 2**

3.2.3 Sideslip Angle

For the derived sideslip angle:

·   15.9400 % of runs violated the display tolerance
·   62.4000 % of runs violated the envelope-protection tolerance.
·   21.6600 % of runs violated the AFPC tolerance.
·   0.0000 % of runs met all tolerances.

Figures 29–33 show the derived sideslip angle results. Figure 29 shows a noticeable correlation between the maximum sideslip angle error and the z-score of C_{y_β}, and the magnitude of the error depends only on the z-score and not the sign of the error. This is a similar but more refined result that was shown for this stability derivative in figure 15, Case 1. Specifically, for Case 2, there are more z-scores between -1 to -3, and there are now many values between -3 to -4. The outlier now lies at -4.5. As shown in figure 15, the trend appears to be symmetric about the horizontal axis, suggesting that the magnitude of the error depends only on the z-score and not the sign of the error. Figure 30 shows the same correlation trend as figure 16, but with the data more refined. Figures 31–33 show the same lack of correlation for these results as in Case 1, but with more data points that populate the trends shown in figures 17–19. The benefit of 10,000 runs versus 1,000 runs is clear, as the established trends are strengthened and less dispersed (i.e., more refined).
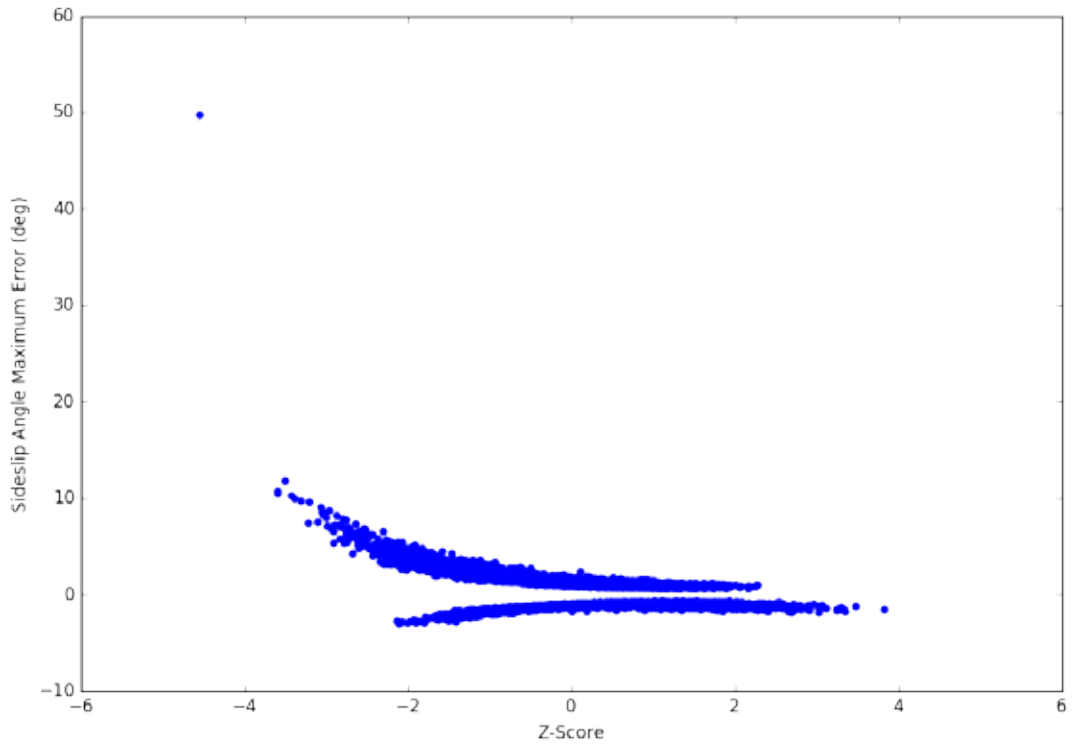
Figure 29. C_{y_β} scatter plot for Case 2
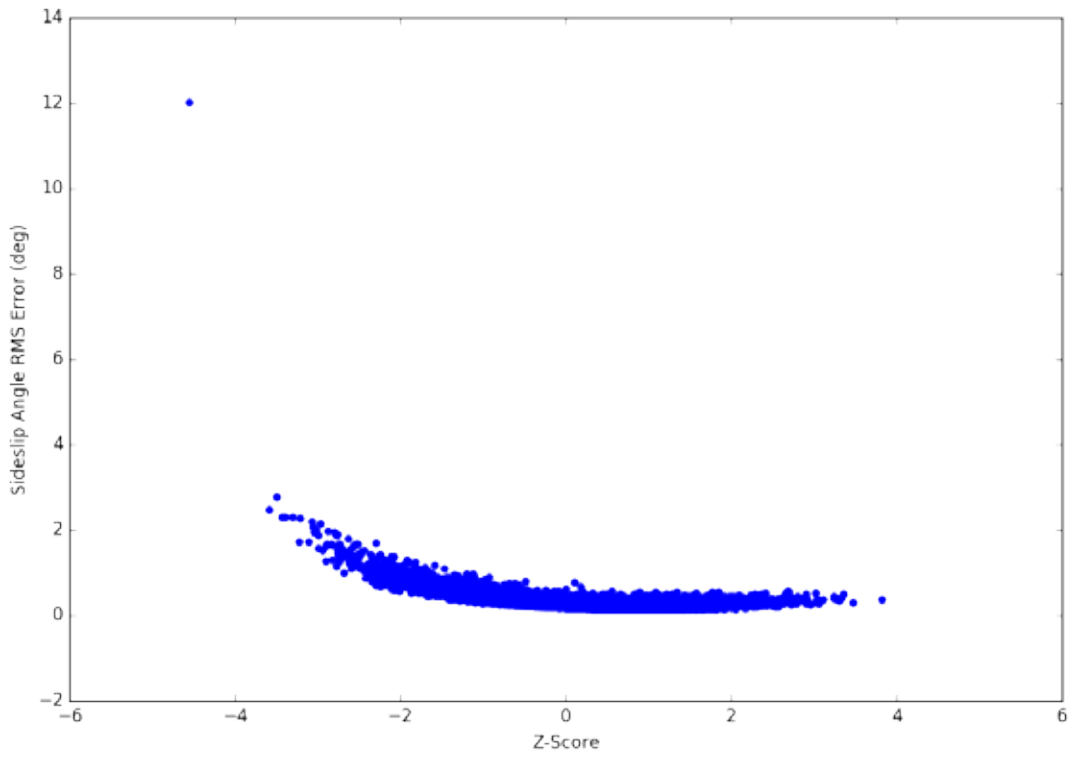
Figure 30. C_{y_β} RMS error scatter plot for Case 2
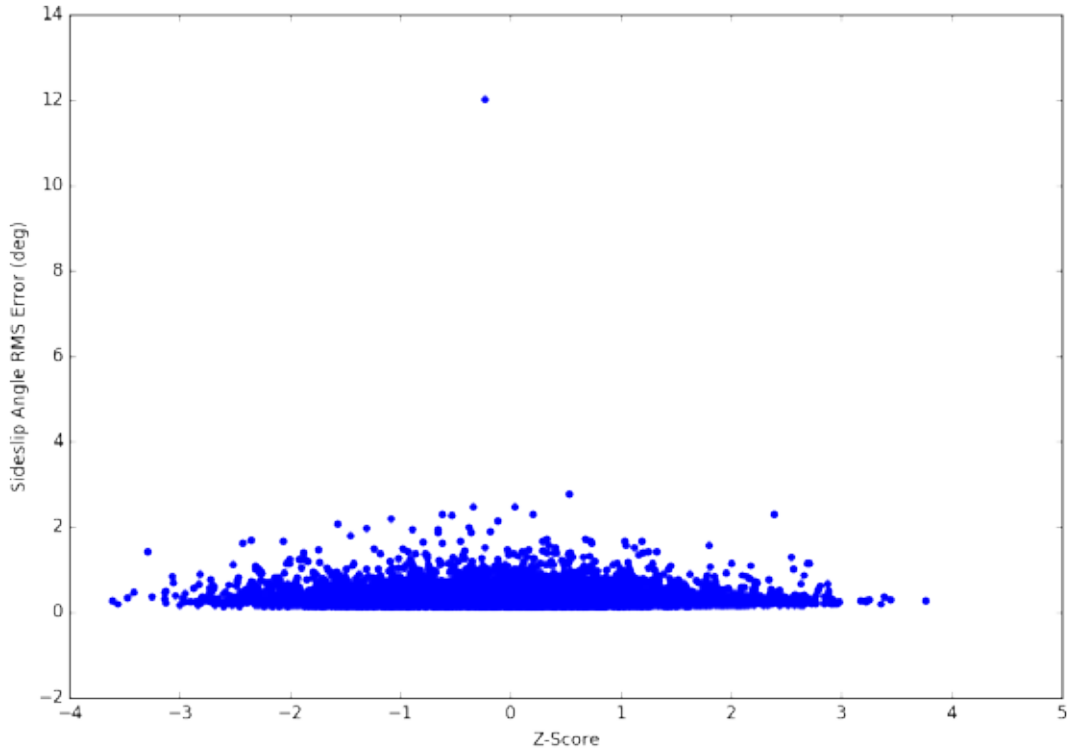
Figure 31. C_{y_p} RMS error scatter plot for Case 2
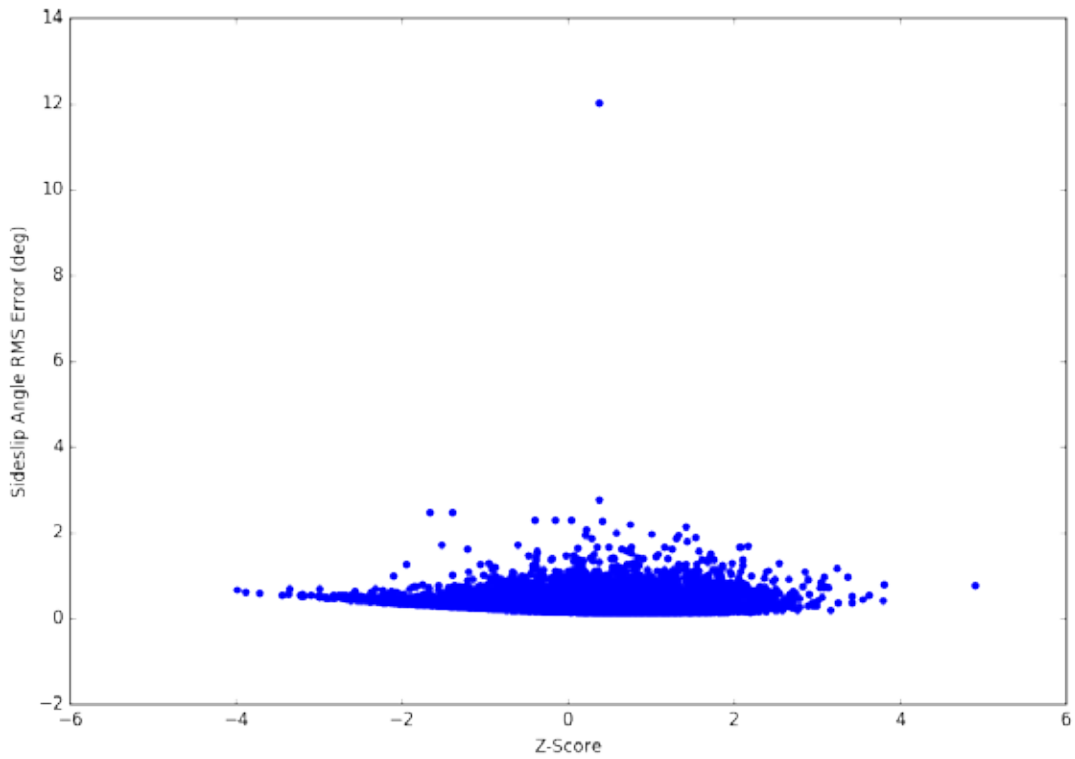
Figure 32. C_{y_r} RMS error scatter plot for Case 2
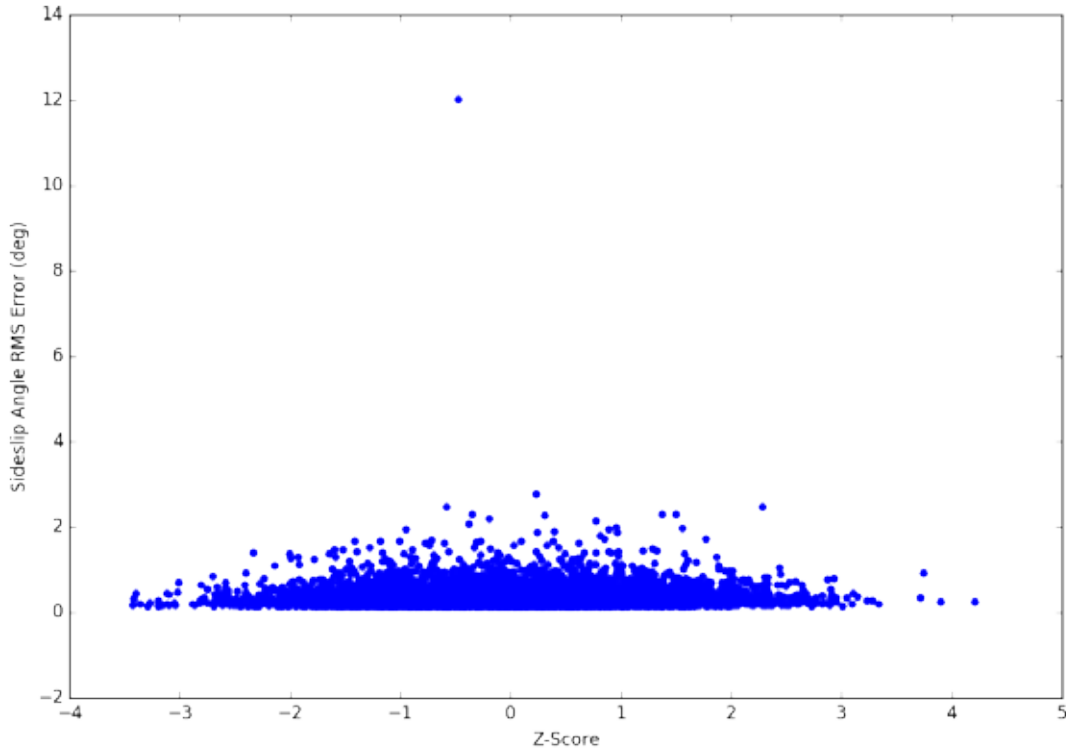
Figure 33. $C_{y_{\delta_R}}$ **RMS error scatter plot for Case 2**

3.3 CASE 3: UNCERTAIN S&C DERIVATIVES, 100,000 RUNS

3.3.1 Overview

Case 3 increased the number of iterations to 100,000. This is one order of magnitude more Monte Carlo iterations than Case 2 and two orders of magnitude more than Case 1. Figure 34 shows the error histograms for the AoA and sideslip angle absolute errors. Note that the sideslip angle error histogram is skewed by an outlier with a $50°$ maximum error. Figure 35 plots the RMS error histograms. The sideslip error RMS error histogram shows a similar distribution with the absolute errors. Corresponding to the result in Case 2, the AoA is skewed toward lower RMS errors, and the absolute AoA errors approximate a normal distribution centered near 1 degree error. Note that the sideslip error histogram is skewed by an outlier to the far right.
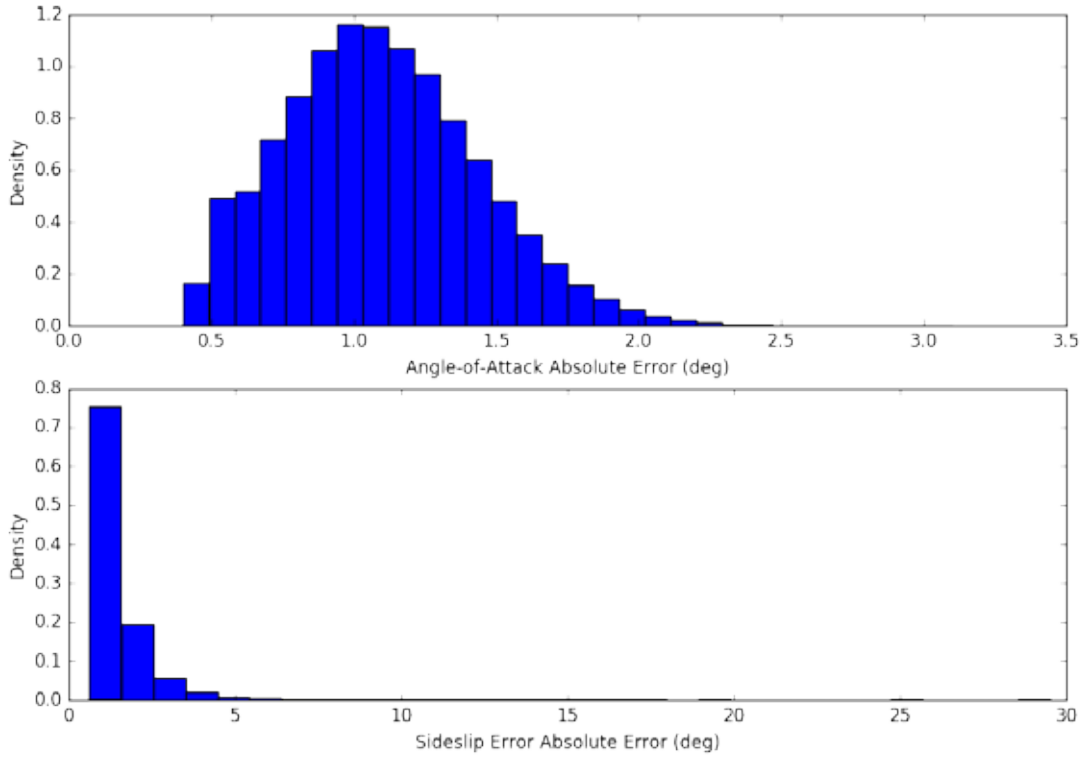
Figure 34. Case 3 error histograms
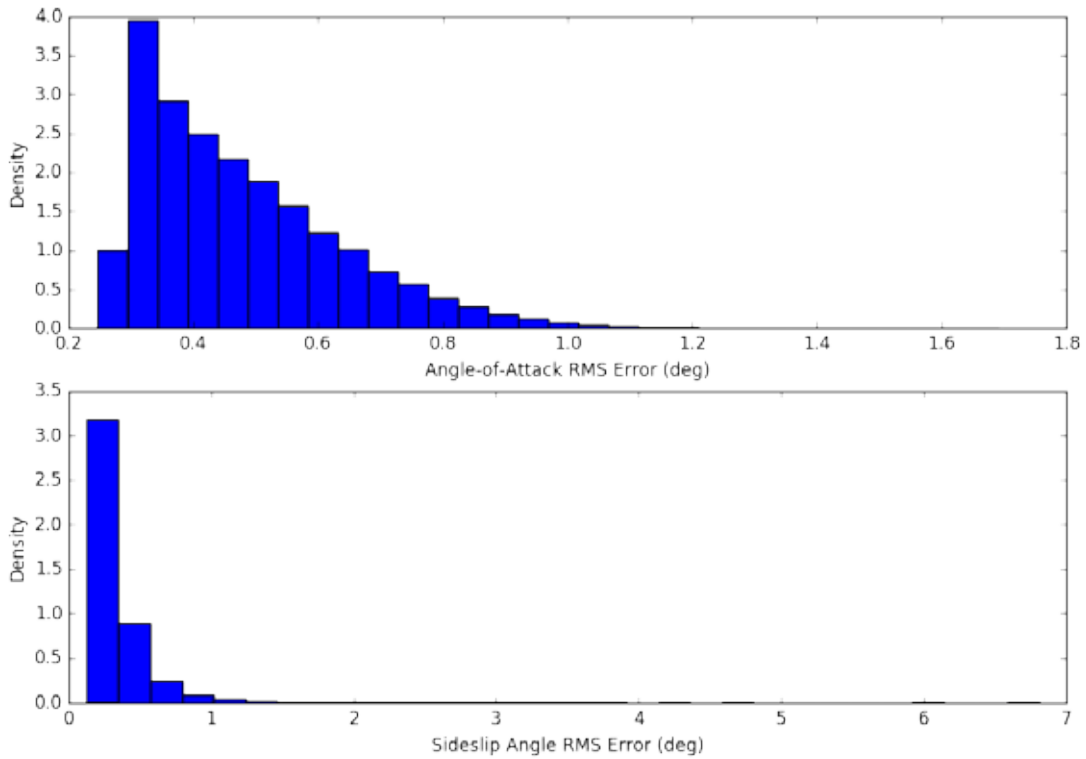
Figure 35. Case 3 RMS error histograms

3.3.2 Angle-of-Attack

For the derived AoA:

- 0.9350 % of runs violated the display tolerance.
- 57.8170 % of runs violated the envelope-protection tolerance.
- 39.3500 % of runs violated the AFPC tolerance.
- 1.8980 % of runs met all tolerances.

As shown in figures 36 and 37, the 100,000 runs confirm the strong correlation trends seen earlier in Cases 1–2, but with more spread in the actual z-score values and a refinement in the values of the maximum errors. Figures 38 and 39 again demonstrate the lack of correlation shown in Cases 1 and 2, but with more refinement.
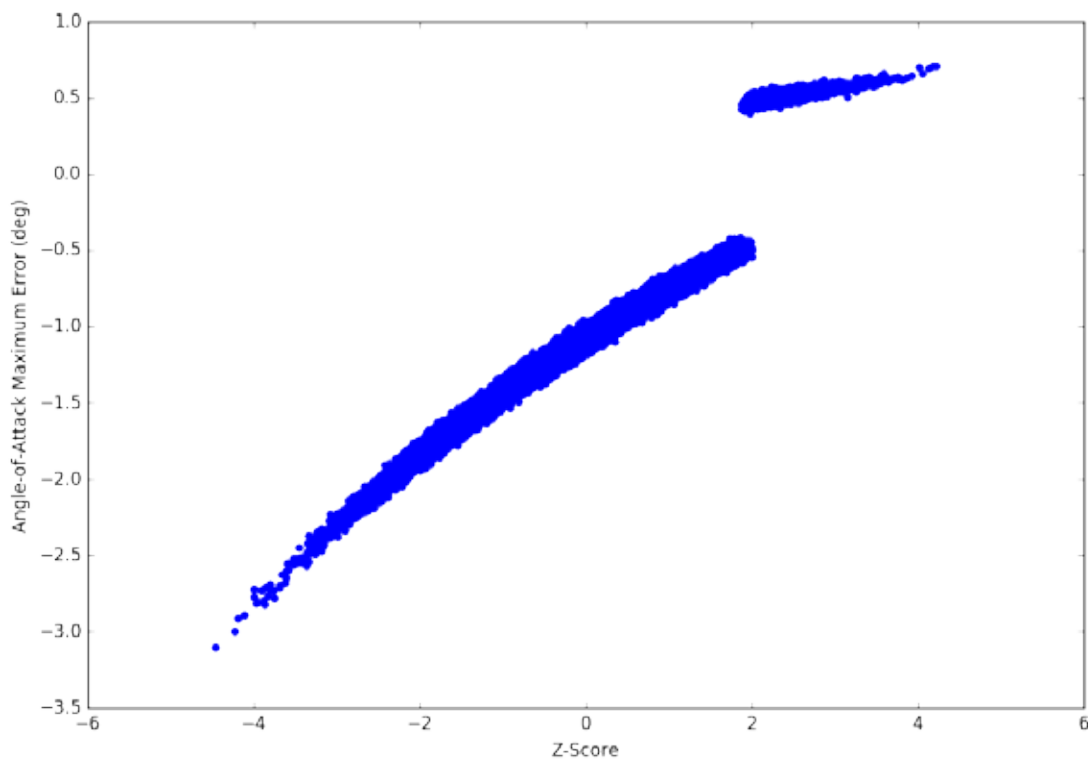
Figure 36. C_{L_α} scatter plot for Case 3
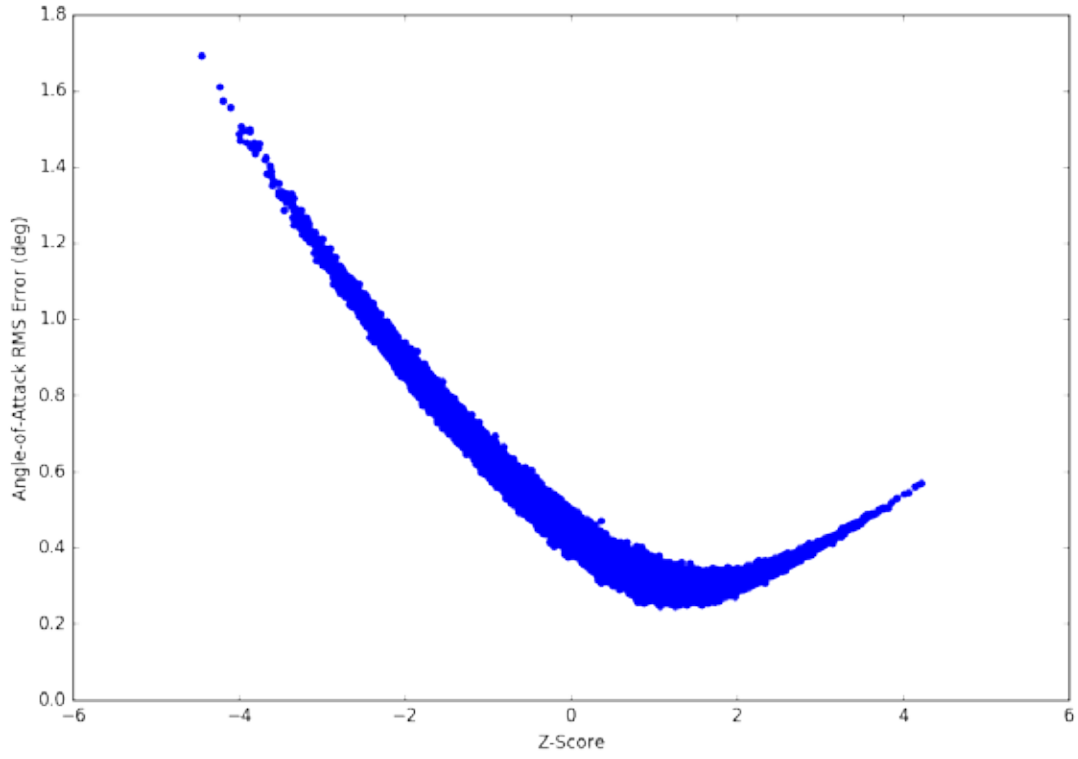
Figure 37. C_{L_α} **RMS error scatter plot for Case 3**
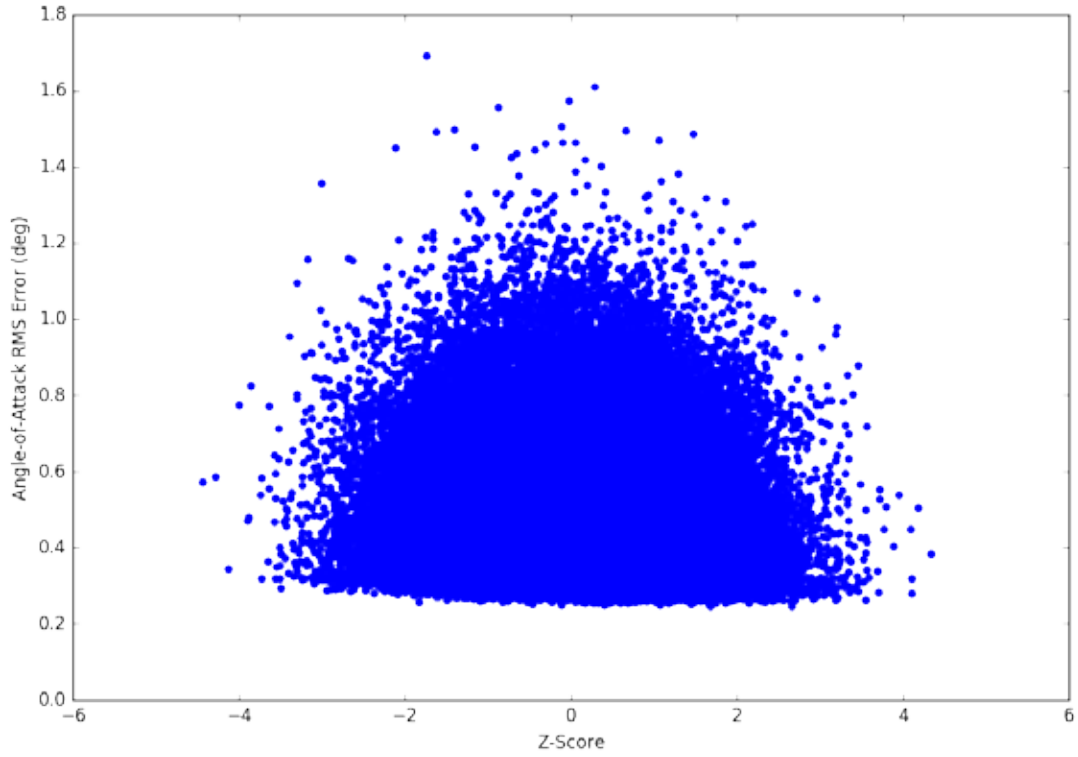
Figure 38. C_{L_q} **RMS error scatter plot for Case 3**
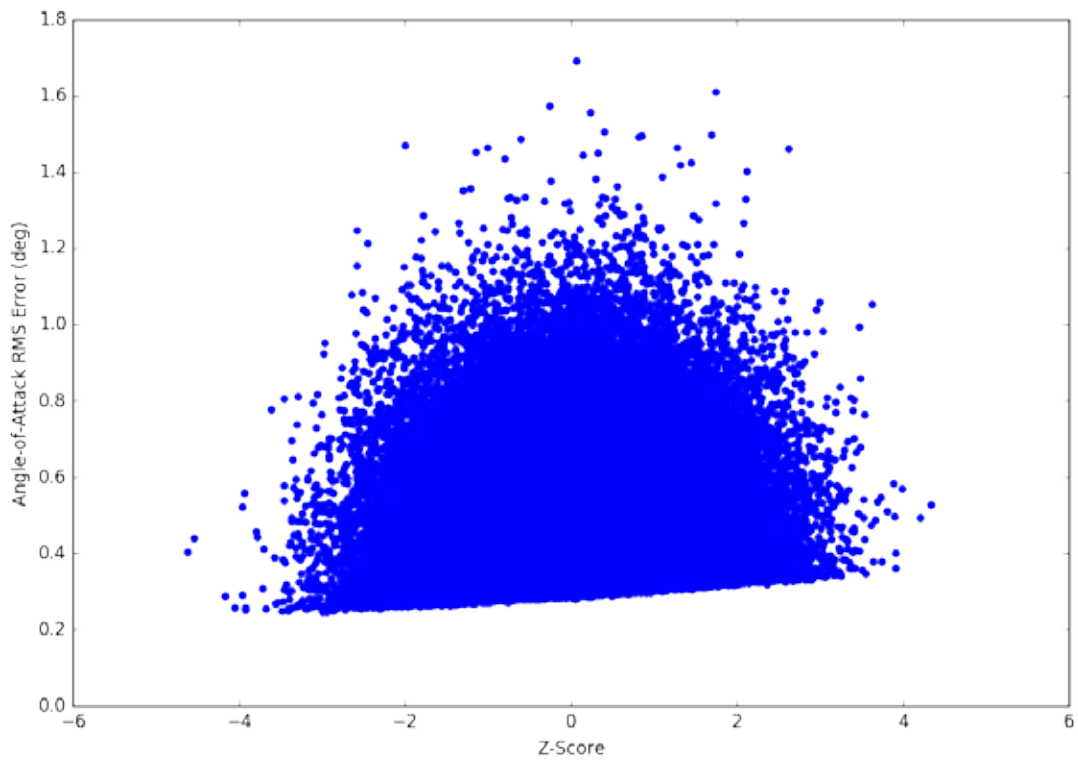
Figure 39. $C_{L_{\delta_E}}$ **RMS error scatter plot for Case 3**

3.3.3 Sideslip Angle

For the derived sideslip angle:

- 15.8120 % of runs violated the display tolerance.
- 62.0670 % of runs violated the envelope-protection tolerance.
- 22.1210 % of runs violated the AFPC tolerance.
- 0.0000 % of runs met all tolerances.

As with the AoA, the sideslip angle results from the 100,000-run case confirms the earlier results shown for Cases 1 and 2 but with more refinement. Figures 40 and 41 display the strong correlation between the maximum sideslip angle error and the z-score of C_{y_β}, and figures 42–44 confirm the lack of correlation shown in Cases 1 and 2.
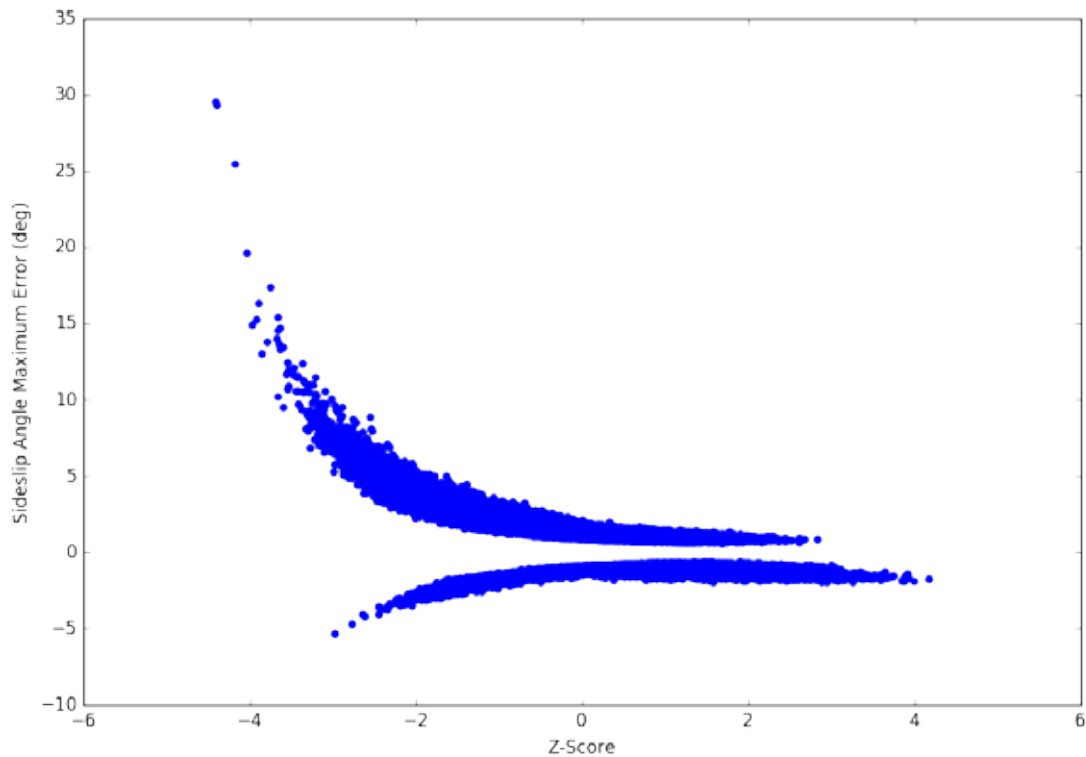
Figure 40. C_{y_β} scatter plot for Case 3
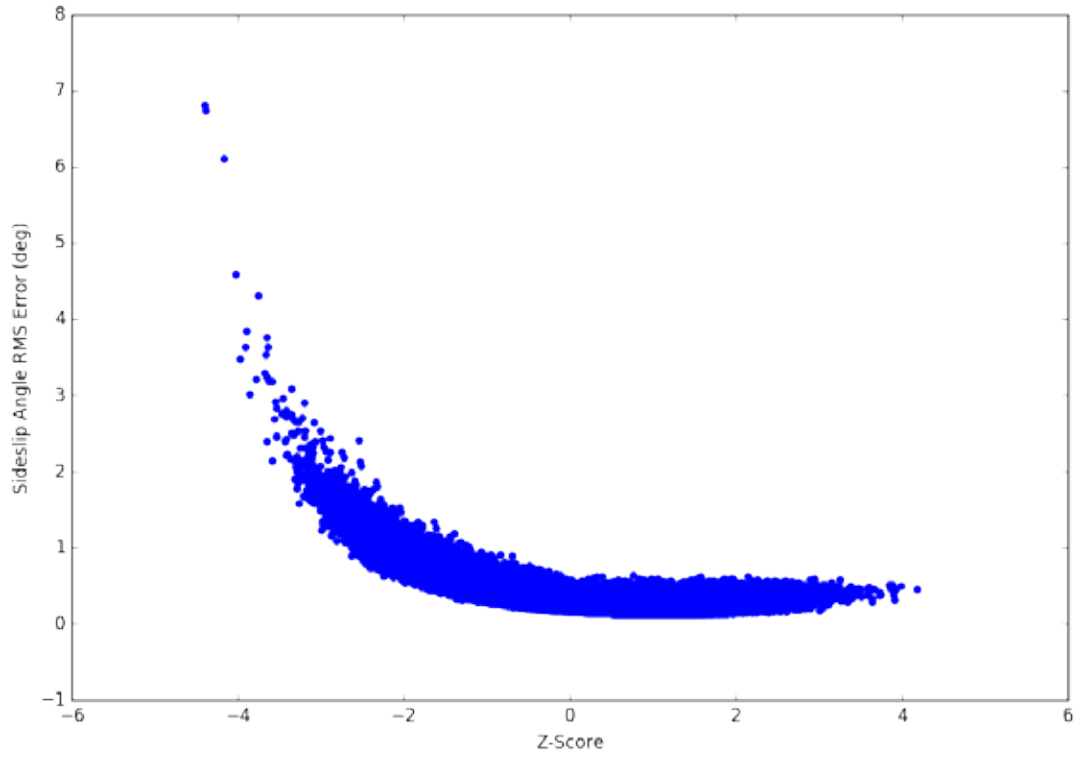
Figure 41. C_{y_β} **scatter plot for Case 3**
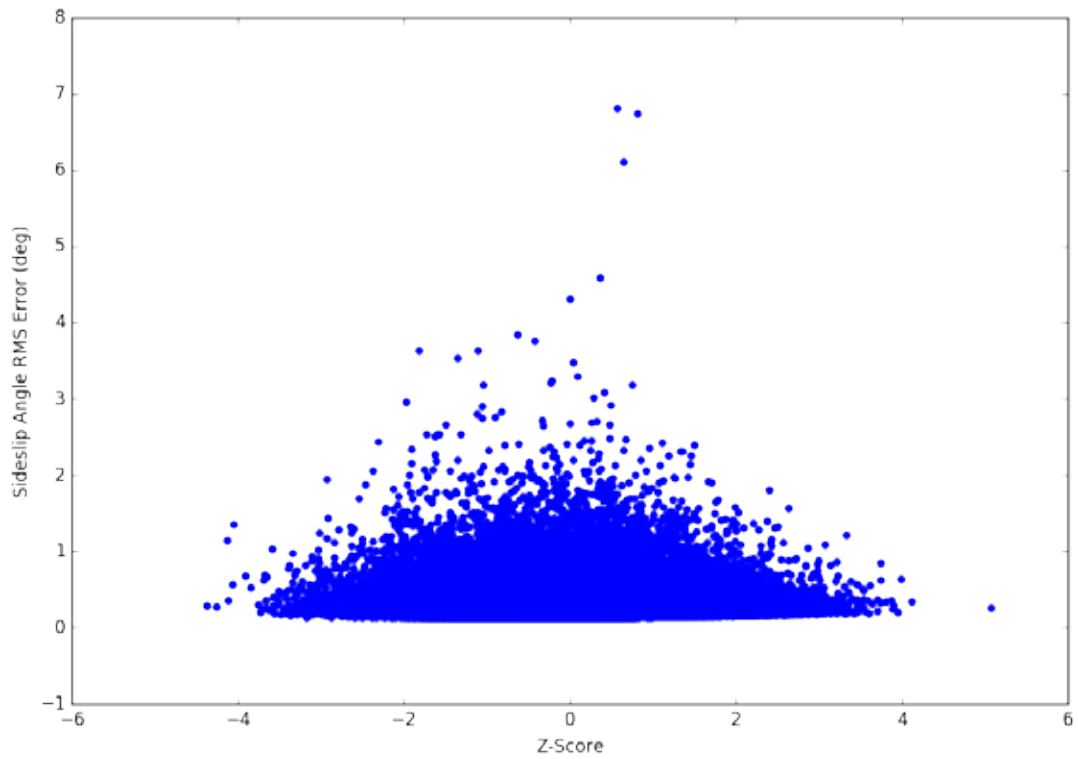
Figure 42. C_{y_p} **RMS error scatter plot for Case 3**
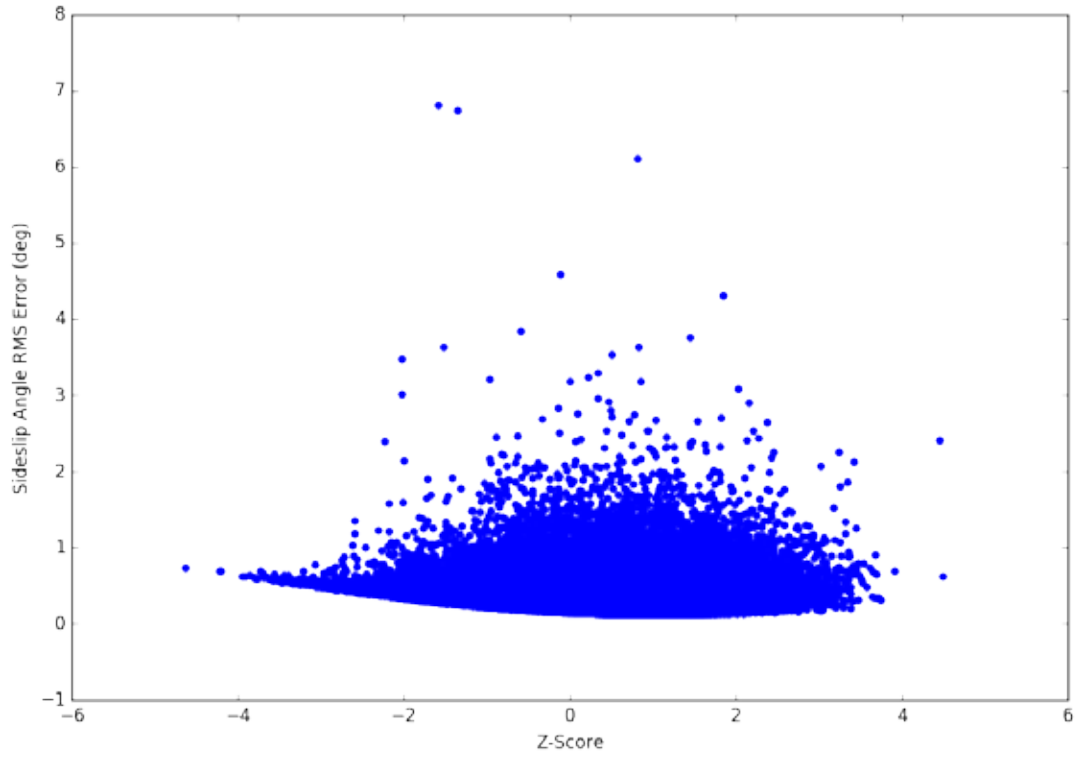
Figure 43. C_{y_r} **RMS error scatter plot for Case 3**
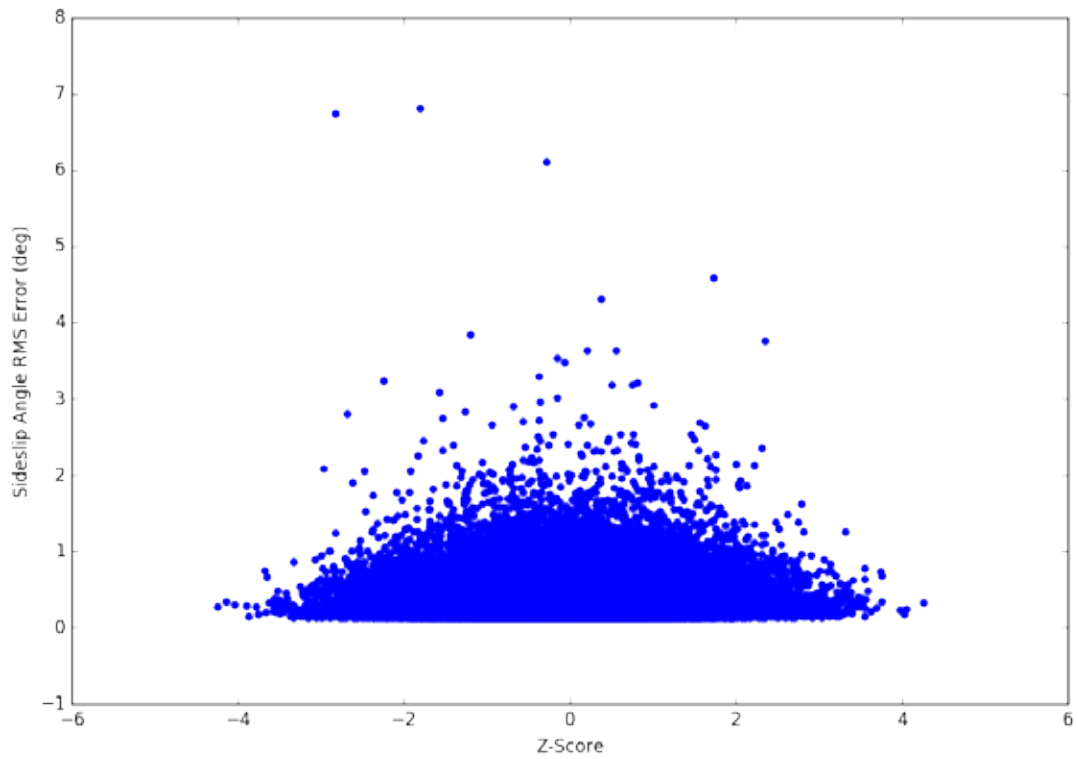
Figure 44. $C_{y_{\delta_R}}$ **RMS error scatter plot for Case 3**

The results for Case 4 through Case 16 follow generally similar trends to those presented above for Cases 1–3. For the sake of brevity, those results are not shown here, but the reader is referred to appendix C for the plots for Cases 4–16.

4. SELECTED RESULTS

This section presents selected figures showing time histories of results for derived AoA and sideslip angle calculations from parts of the Monte Carlo iterations. Note that there is initially an error of ~0.6 degrees at the start of the time histories. This is an artifact of the JSBSim initialization and should be ignored for purposes of algorithm evaluation.

The times when the error thresholds were exceeded are shown in the figure, with green lines indicating the AFPC threshold, maroon lines indicating the envelope-protection threshold, and red lines indicating the pilot-display threshold.

 Because of the similarity of the results, only 10,000 iteration cases are shown.

4.1 NOMINAL CASE

This section plots the derived AoA and sideslip angle for the nominal linear model S&C derivative.

4.1.1 Angle-of-Attack

Figure 45 shows that the nominal model values result in a derived AoA estimate that meets all the tolerances for approximately half of the time period, at which point the AFPC tolerance is exceeded, and then approximately 10 seconds later the envelope-protection tolerance is briefly exceeded. This error is likely because these derivatives are the nominal values for the linear model provided in Airplane Dynamics and Automatic Flight Controls, Part I and not the nominal values for the nonlinear model used by JSBSim. By visual inspection, the derived AoA appears to match the shape of the true AoA but with incorrect scaling. This suggests that C_{L_α} is the cause, as seen in section 3. Furthermore, it appears the DATCOM value is approximately at the 5° AoA mark, at which point it becomes smaller than the true C_{L_α} value, causing a conservative overprediction of the AoA.
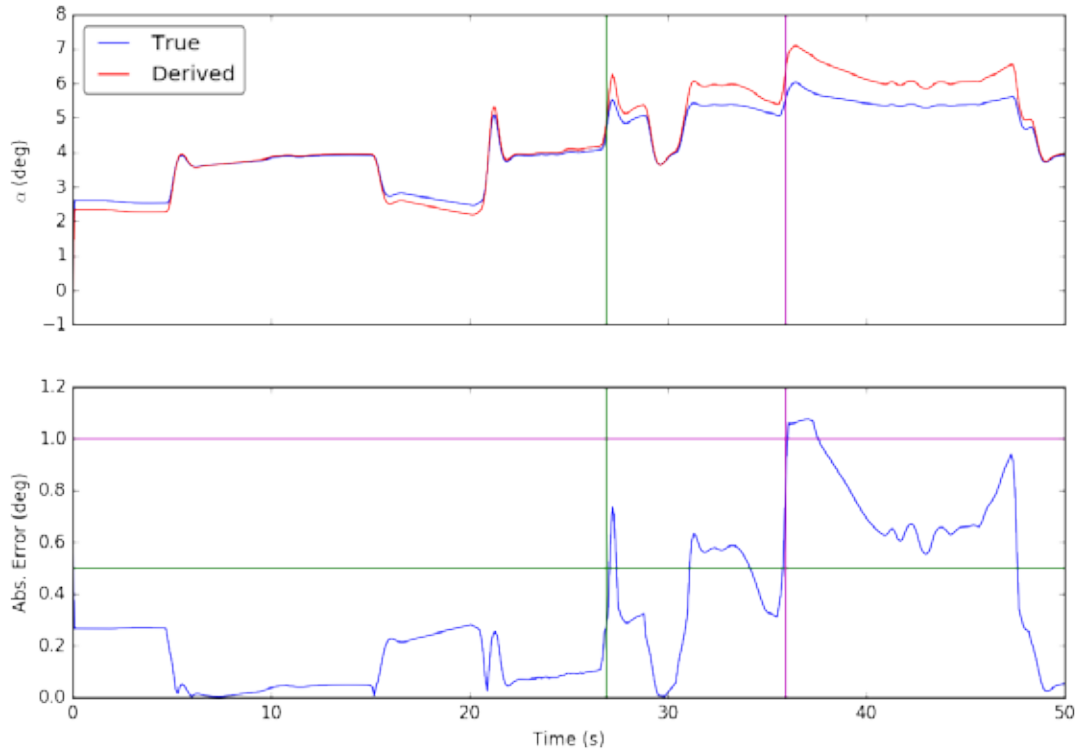
Figure 45. Derived AoA for nominal linear model

4.1.2 Sideslip Angle

Figure 46 plots the derived sideslip angle. Like the derived AoA, the derived sideslip meets all tolerances for a large part of the simulation time. The AFPC tolerance is briefly violated a few times after the 30-second mark, and later the envelope-protection tolerance is violated after the 45-second mark. These exceedance times correspond approximately to changes in, and large values of, the roll and yaw rates (p and r, respectively), as seen in Figure 47, which plots the time histories of the lateral/directional state variables.
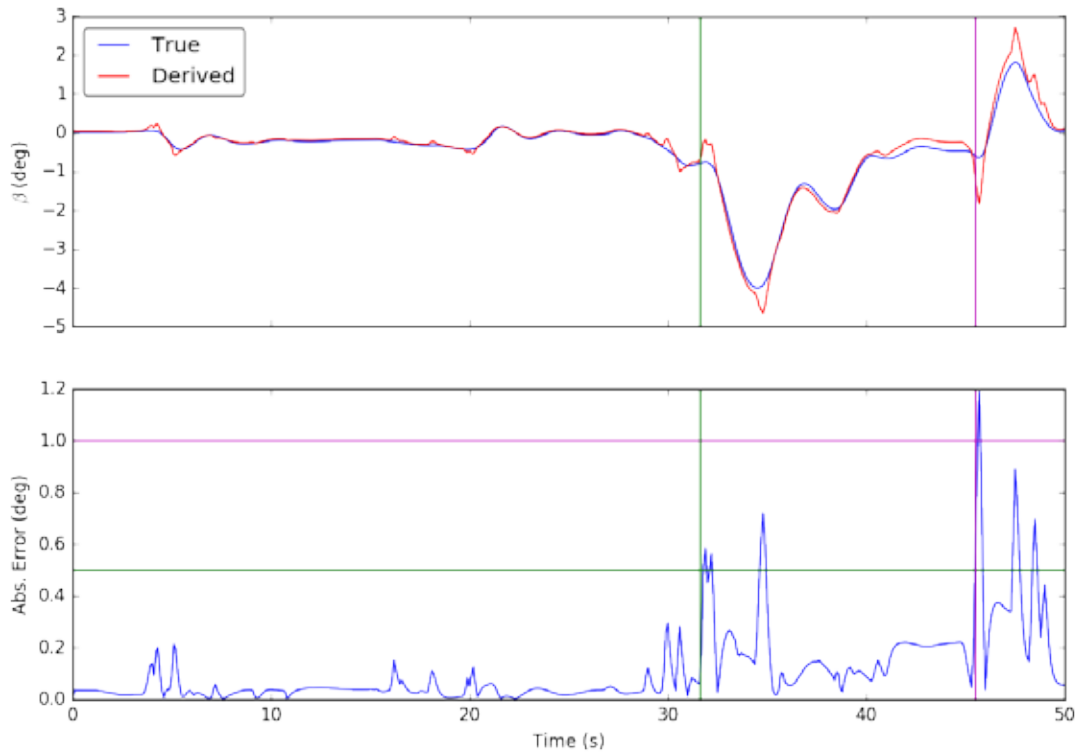
Figure 46. Derived sideslip angle for nominal linear model
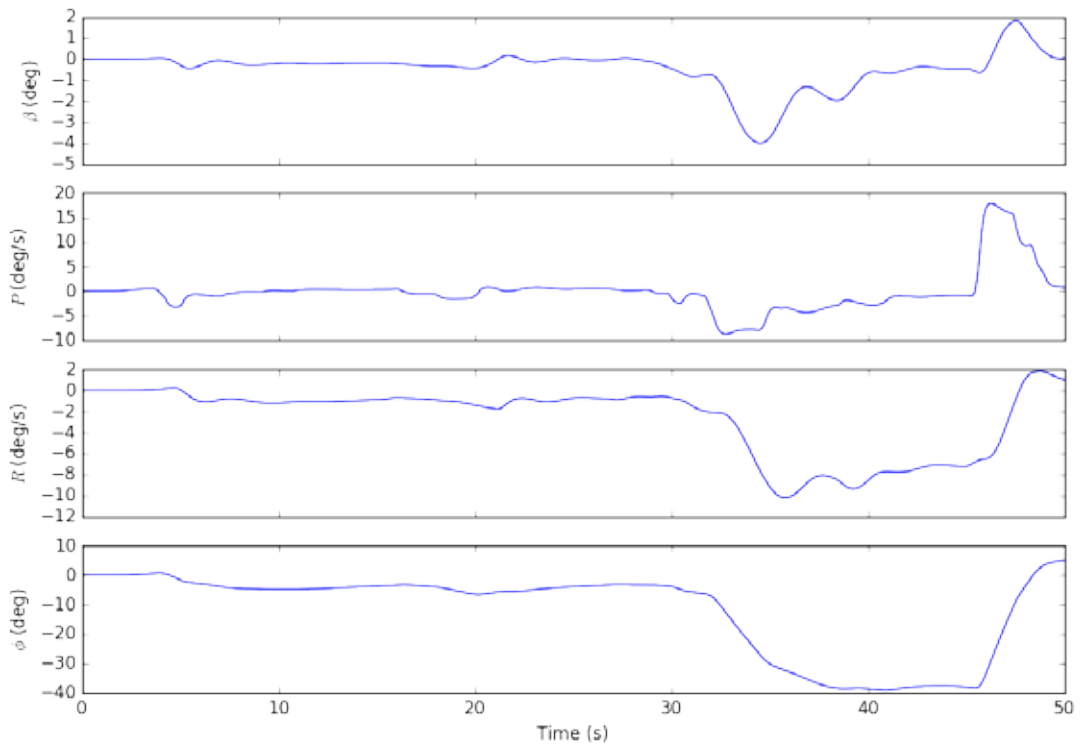
Figure 47. Time histories of lateral/directional state variables

4.2 CASE 1: UNCERTAIN S&C DERIVATIVES, 1000 RUNS

4.2.1 Low-Error Example

4.2.1.1 Angle-of-Attack

Figure 48 plots the derived AoA seen in run 662 of Case 1, which is the best performance shown using the absolute error metric.

Table 7 lists the values for the S&C power derivatives along with their z-scores.

Table 7. Z-scores and S&C derivative values for run 662 of Case 1

S&C Derivative	Z-Score	Value (1/rad)	Nominal Value (1/rad)
C_{L_α}	2.1438	4.8827	4.41
C_{L_q}	-1.3078	2.8799	3.9
$C_{L_{\delta_E}}$	-2.2163	0.3347	0.43
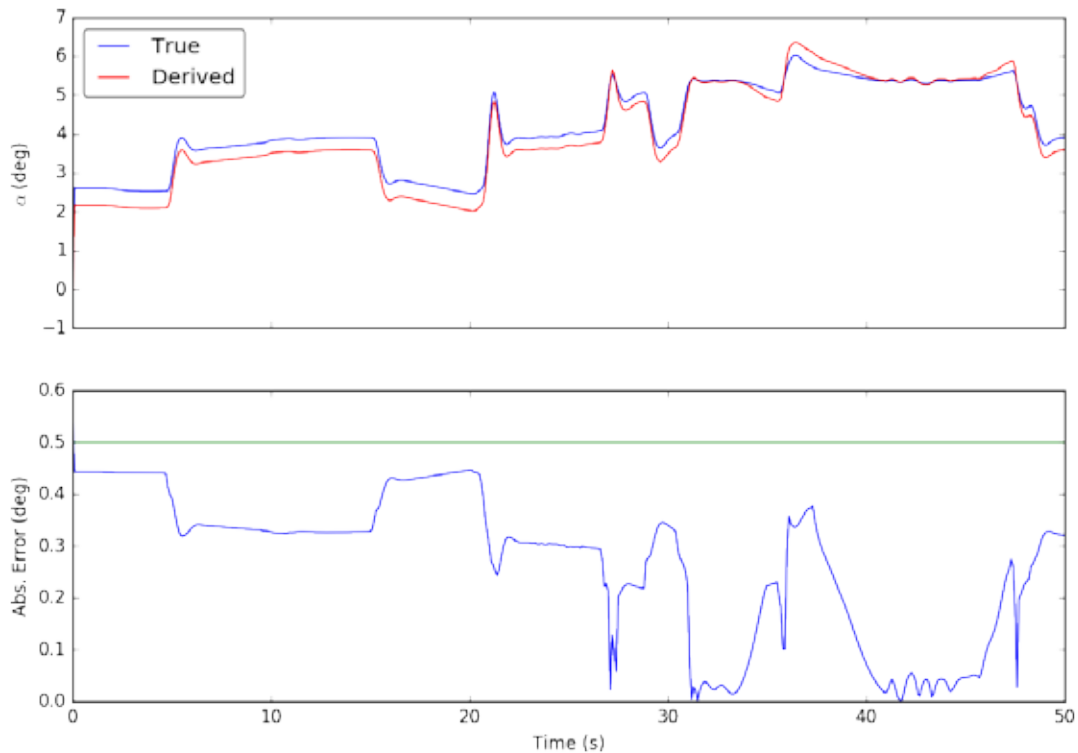
Figure 48. Run 662 of Case 1 derived AoA

46

4.2.1.2 Sideslip Angle

Figure 49 plots the derived sideslip angle seen in run 734 of Case 1. Table 8 lists the values for the S&C power derivatives along with their z-scores.

Table 8. Z-scores and S&C derivative values for run 734 of Case 1

S&C Derivative	Z-Score	Value (1/rad)	Nominal Value (1/rad)
C_{y_β}	-1.5153	-0.5121	-0.393
C_{y_p}	1.7200	-0.0105	-0.075
C_{y_r}	0.2364	0.2392	0.214
$C_{y_{\delta_R}}$	0.8128	0.2022	0.187
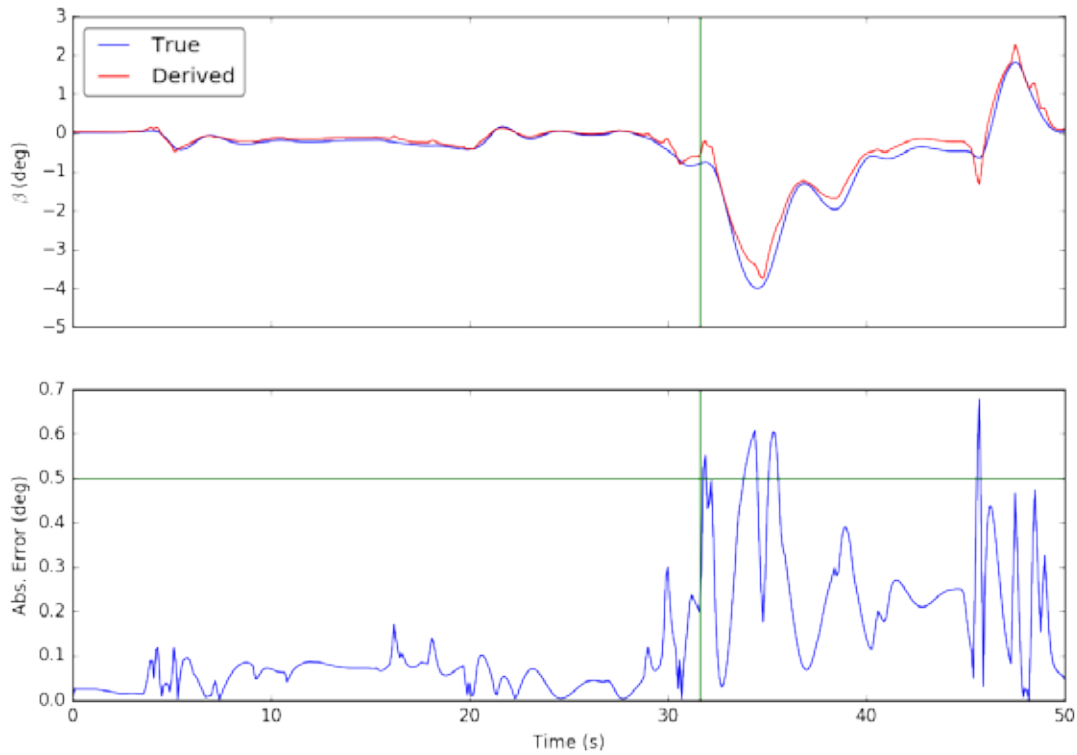
Figure 49. Run 734 of Case 1 derived sideslip angle

4.2.2 High-Error Example

4.2.2.1 Angle-of-Attack

Figure 50 is a time history of the true and derived AoA signals for run 145 of Case 1, with S&C derivatives listed in table 9.

Table 9. Z-scores and S&C derivative values for run 145 of Case 1

S&C Derivative	Z-Score	Value (1/rad)	Nominal Value (1/rad)
C_{L_α}	-2.9696	3.7552	4.41
C_{L_q}	1.0050	4.6839	3.9
$C_{L_{\delta_E}}$	0.1837	0.4379	0.43

Here it is shown that derived AoA is close to the true value near the trim AoA at ~$2.7°$, but it significantly underpredicts the AoA at higher AoA values (e.g., ~$4°$). This run violates all the tolerances by the end of the run but is conservative because it predicts a high AoA earlier than it occurs. The lift curve slope is approximately 3σ below the nominal DATCOM value, which makes this case representative of an unlikely level of modeling error. The pitch-damping derivative and elevator effectiveness are both relatively common values, and the behavior of the derived AoA curve is nearly identical to the true AoA, modulo a scaling factor. This scaling factor is C_{L_α}, which consistently seems to be the most important parameter for accuracy.
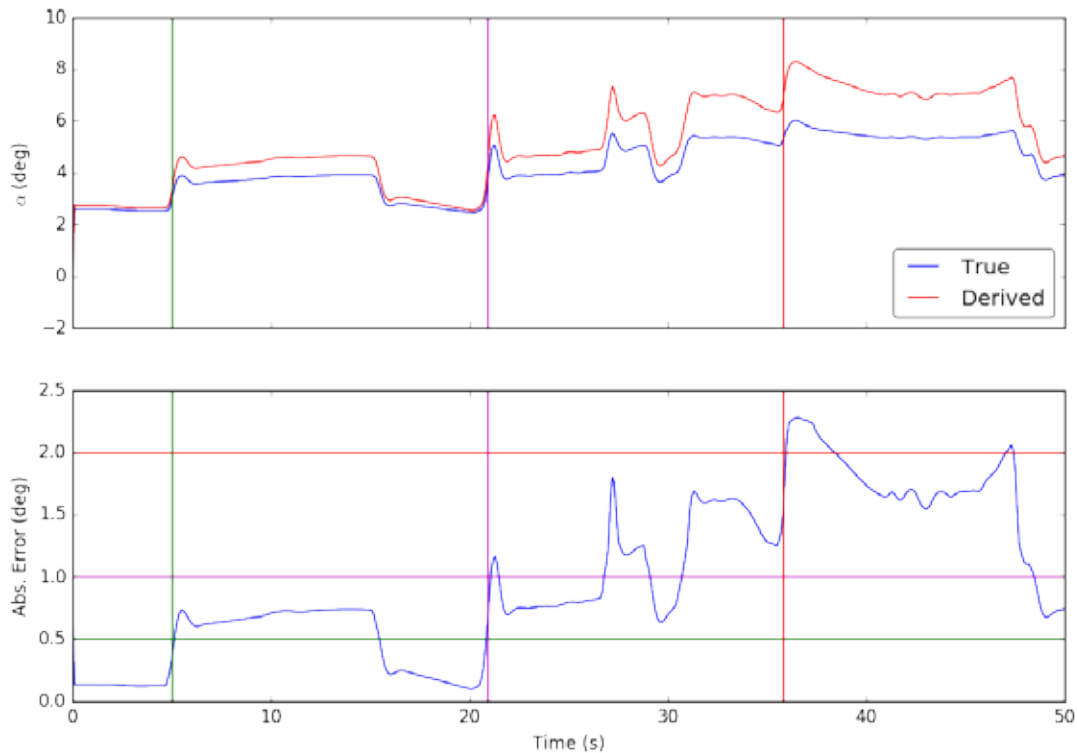
Figure 50. Run 145 of Case 1 derived AoA

4.2.2.2 Sideslip Angle

Figure 51 plots the derived sideslip angle seen in run 652 of Case 1. Table 10 lists the values for the S&C power derivatives along with their z-scores.

Table 10. Z-scores and S&C derivative values for run 652 of Case 1

S&C Derivative	Z-Score	Value (1/rad)	Nominal Value (1/rad)
C_{y_β}	3.2316	-0.1390	-0.393
C_{y_p}	-0.9840	-0.1119	-0.075
C_{y_r}	-1.0832	0.0981	0.214
$C_{y_{\delta_R}}$	-0.9037	0.1701	0.187

Comparing Eqs. (1) and (2), the derivative C_{y_β} appears to have the same scaling effect for the derived sideslip as the derivative C_{L_α} does for the derived AoA. With a $> 3\sigma$ value of C_{y_β}, this effect is seen in the derived sideslip shown in figure 51.
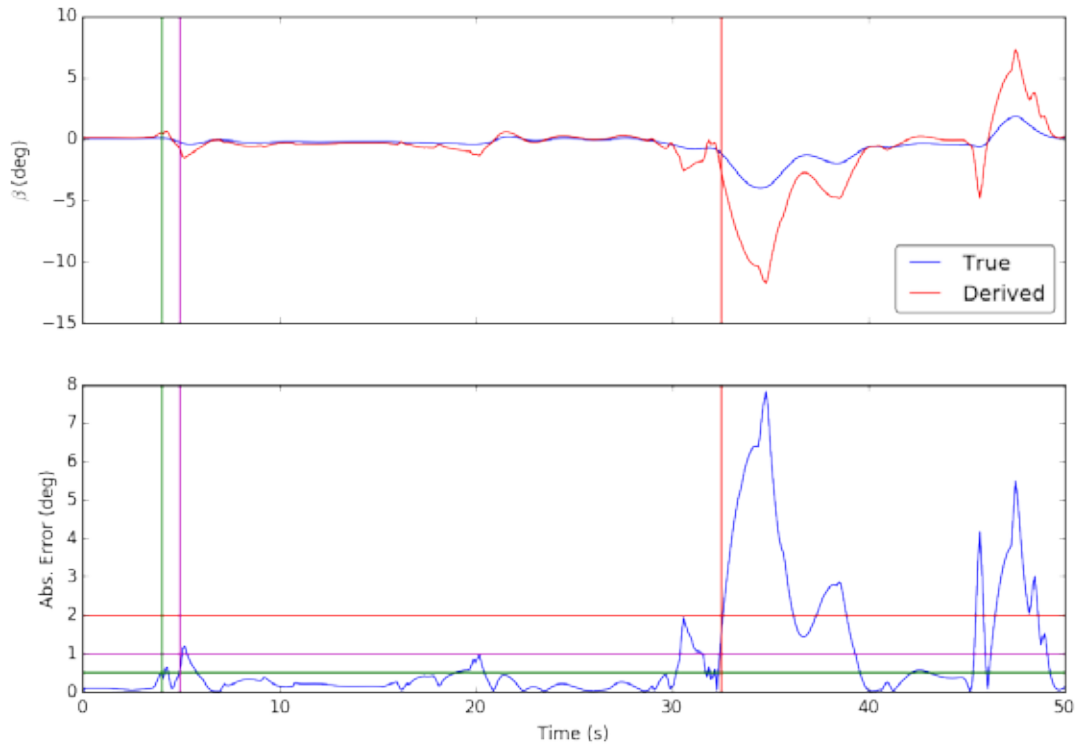
Figure 51. Run 652 of Case 1 derived sideslip angle

4.3 CASE 2: UNCERTAIN S&C DERIVATIVES, 10,000 RUNS

4.3.1 Low-Error Example

4.3.1.1 Angle-of-Attack

Figure 52 plots the derived AoA seen in run 2879 of Case 2. Table 11 lists the values for the S&C power derivatives along with their z-scores.

Table 11. Z-scores and S&C derivative values for Run 2879 of Case 2

S&C Derivative	Z-Score	Value (1/rad)	Nominal Value (1/rad)
C_{L_α}	1.8233	4.8120	4.41
C_{L_q}	1.2415	4.8684	3.9
$C_{L_{\delta_E}}$	-2.9099	0.3049	0.43
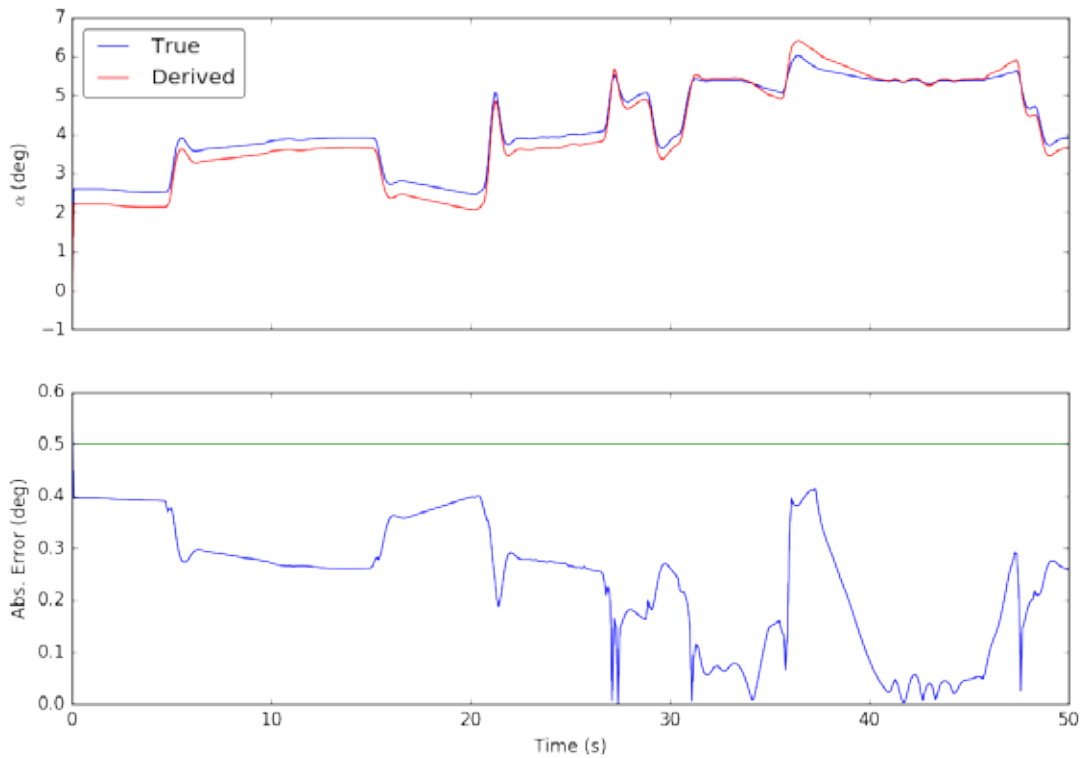
Figure 52. Run 2879 of Case 2 AoA estimate

4.3.1.2 Sideslip Angle

Figure 53 plots the derived sideslip angle seen in run 8736 of Case 2. Table 12 lists the values for the S&C power derivatives along with their z-scores.

Table 12. Z-scores and S&C derivative values for run 8736 of Case 2

S&C Derivative	Z-Score	Value (1/rad)	Nominal Value (1/rad)
C_{y_β}	-2.1648	-0.5632	-0.393
C_{y_p}	3.0014	0.0376	-0.075
C_{y_r}	1.2118	0.3437	0.214
$C_{y_{\delta_R}}$	-1.3800	0.1652	0.187
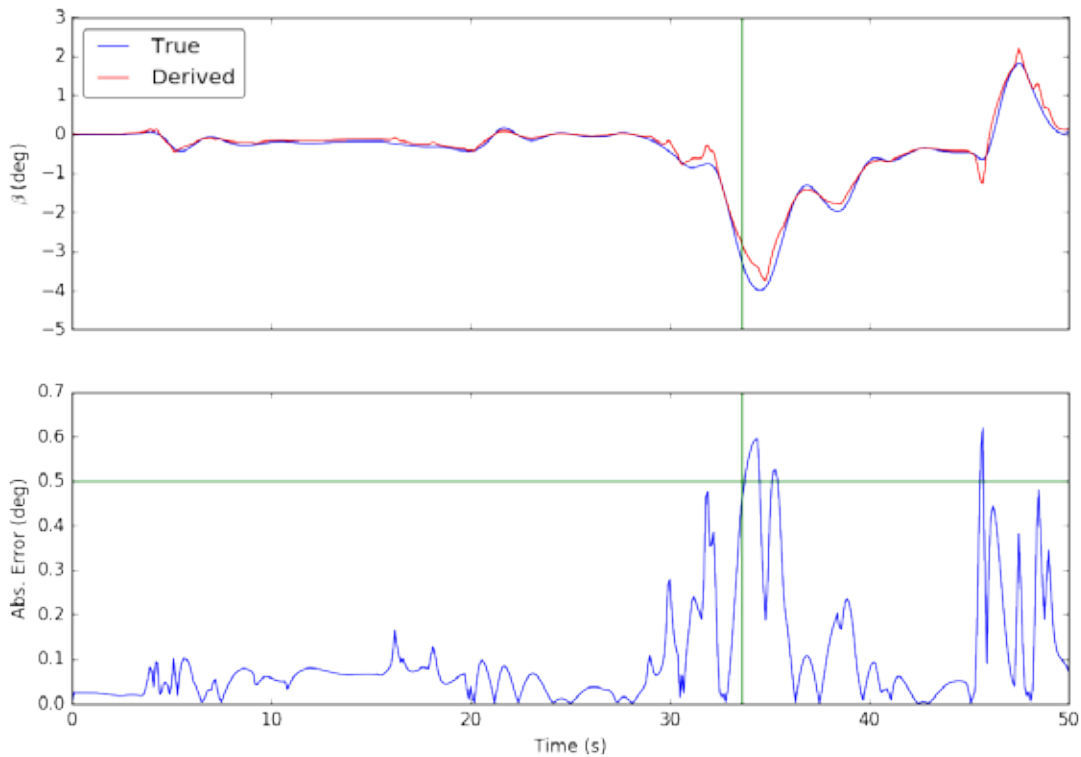
Figure 53. Run 8736 of Case 2 sideslip angle estimate

4.3.2 High-Error Example

4.3.2.1 Angle-of-Attack

Figure 54 plots the derived AoA seen in run 936 of Case 2. Table 13 lists the values for the S&C power derivatives along with their z-scores.

51

Table 13. Z-scores and S&C derivative values for run 936 of Case 2

S&C Derivative	Z-Score	Value (1/rad)	Nominal Value (1/rad)
C_{L_α}	-3.6485	3.6055	4.41
C_{L_q}	-0.2063	3.7391	3.9
$C_{L_{\delta_E}}$	-1.9953	0.3442	0.43
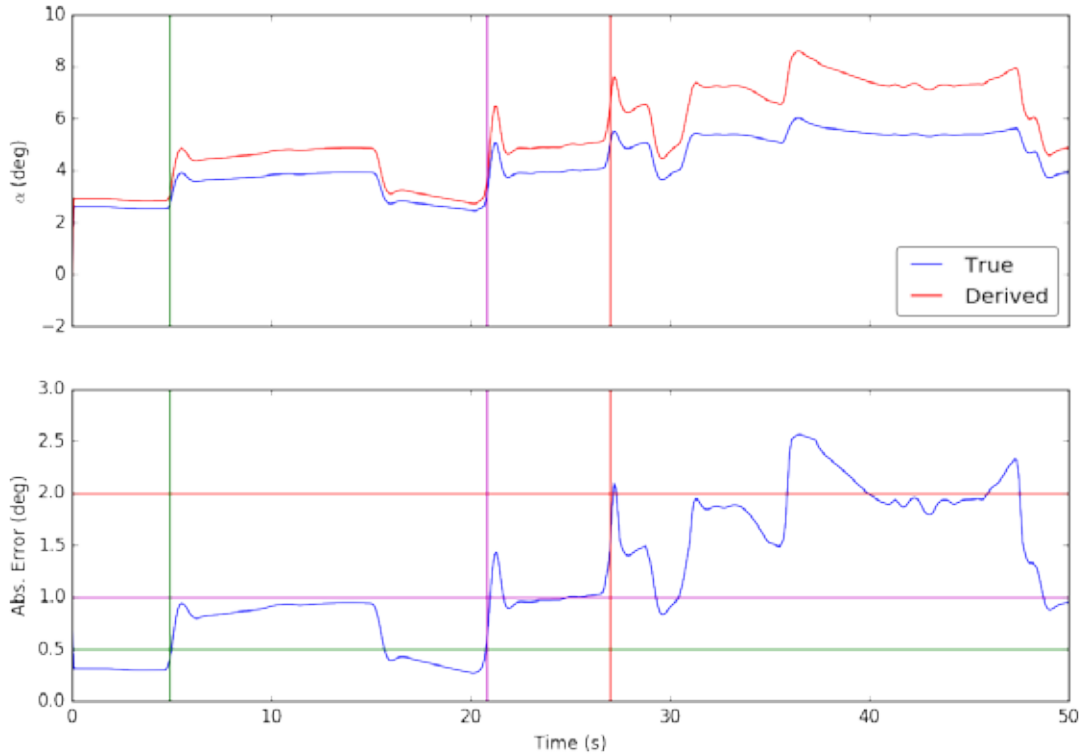
Figure 54. Run 936 of Case 2 AoA estimate

4.3.2.2 Sideslip Angle

Figure 55 plots the derived sideslip angle seen in run 5249 of Case 2. Table 14 lists the values for the S&C power derivatives along with their z-scores.

Table 14. Z-scores and S&C derivative values for run 5249 of Case 2

S&C Derivative	Z-Score	Value (1/rad)	Nominal Value (1/rad)
C_{y_β}	4.5527	-0.0352	-0.393
C_{y_p}	0.2385	-0.0661	-0.075
C_{y_r}	0.3750	0.2541	0.214
$C_{y_{\delta_R}}$	-0.4775	0.1781	0.187
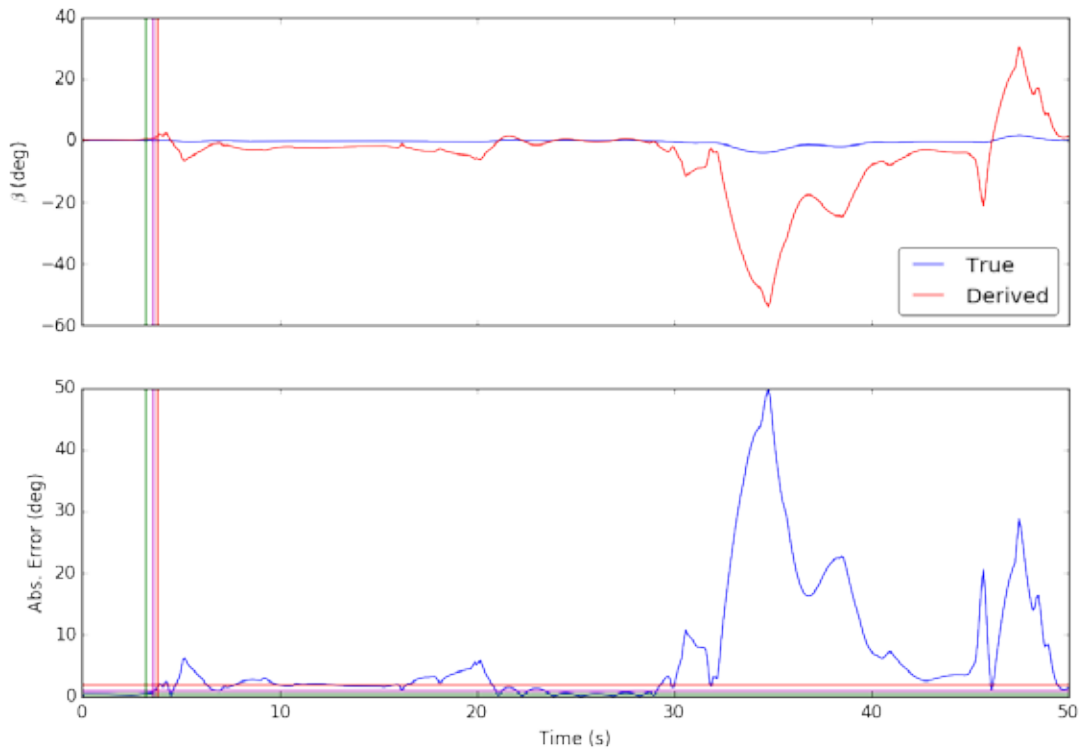
Figure 55. Run 5249 of Case 2 sideslip angle estimate

4.4 CASE 4: LOW SENSOR NOISE, 10,000 RUNS

4.4.1 Low-Error Example

4.4.1.1 Angle-of-Attack

Figure 56 plots the derived AoA seen in run 6822 of Case 4.
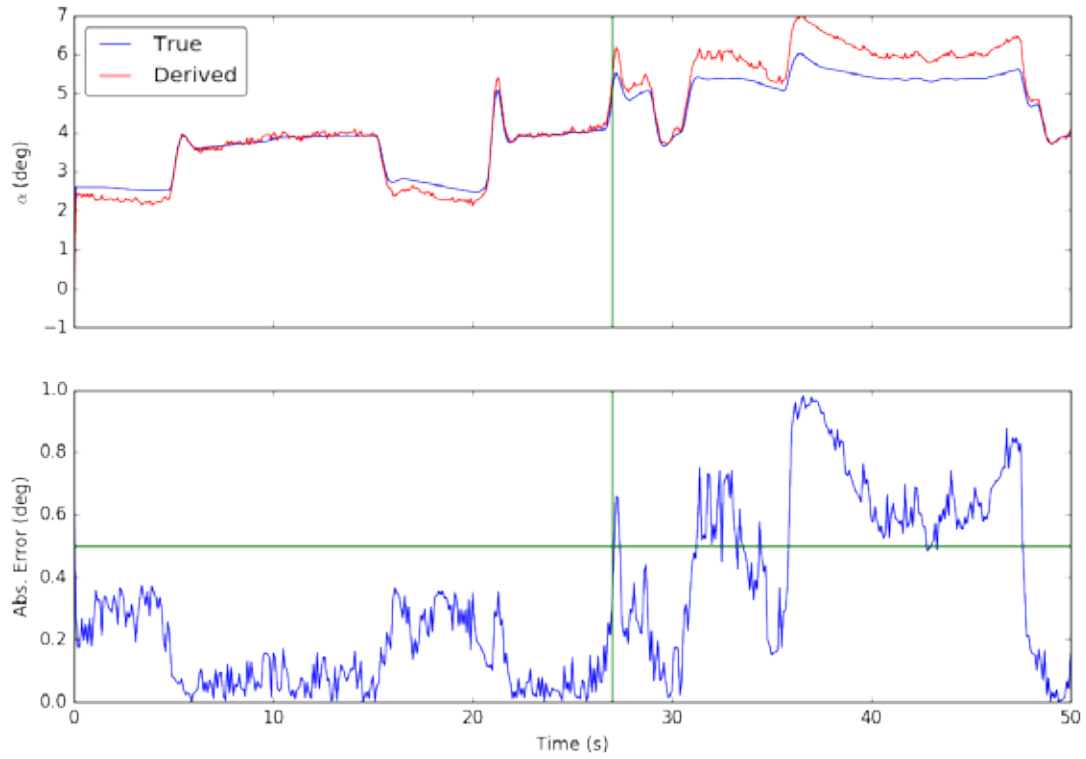
Figure 56. AoA estimate for run 6822 of Case 4

4.4.1.2 Sideslip Angle

Figure 57 plots the derived sideslip angle seen in run 5413 of Case 4.
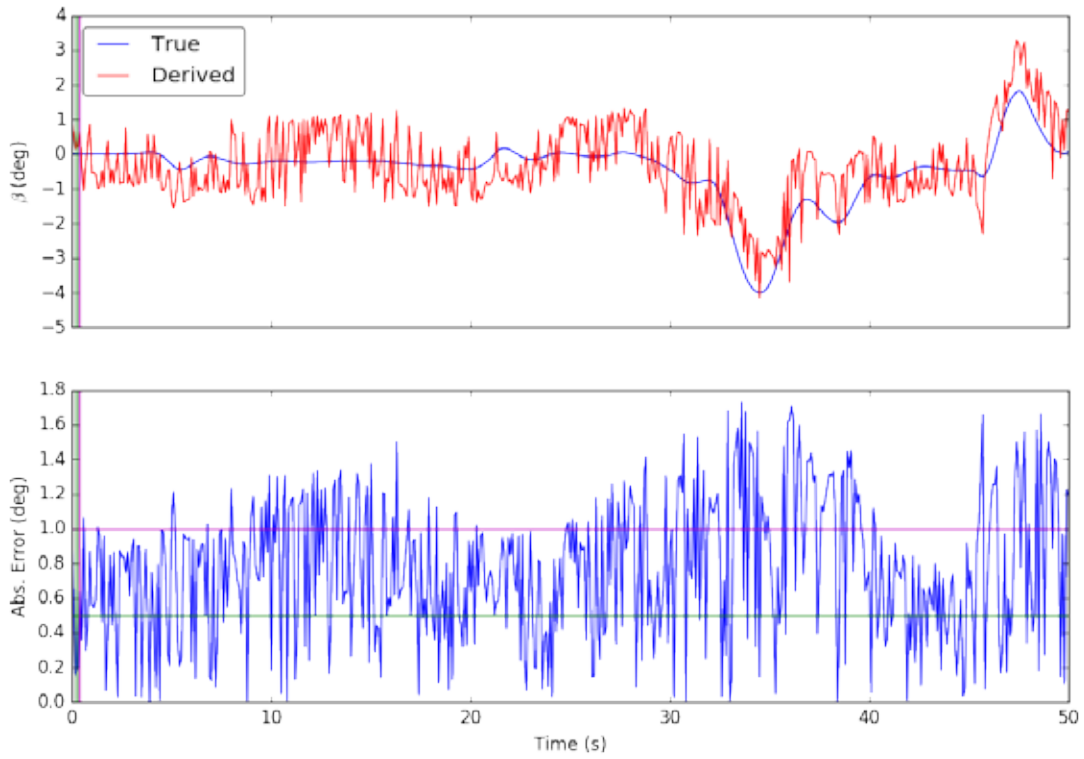
Figure 57. Sideslip angle estimate for run 5413 of Case 4

4.4.2 High-Error Example

4.4.2.1 Angle-of-Attack

Figure 58 plots the derived AoA seen in run 1930 of Case 4.
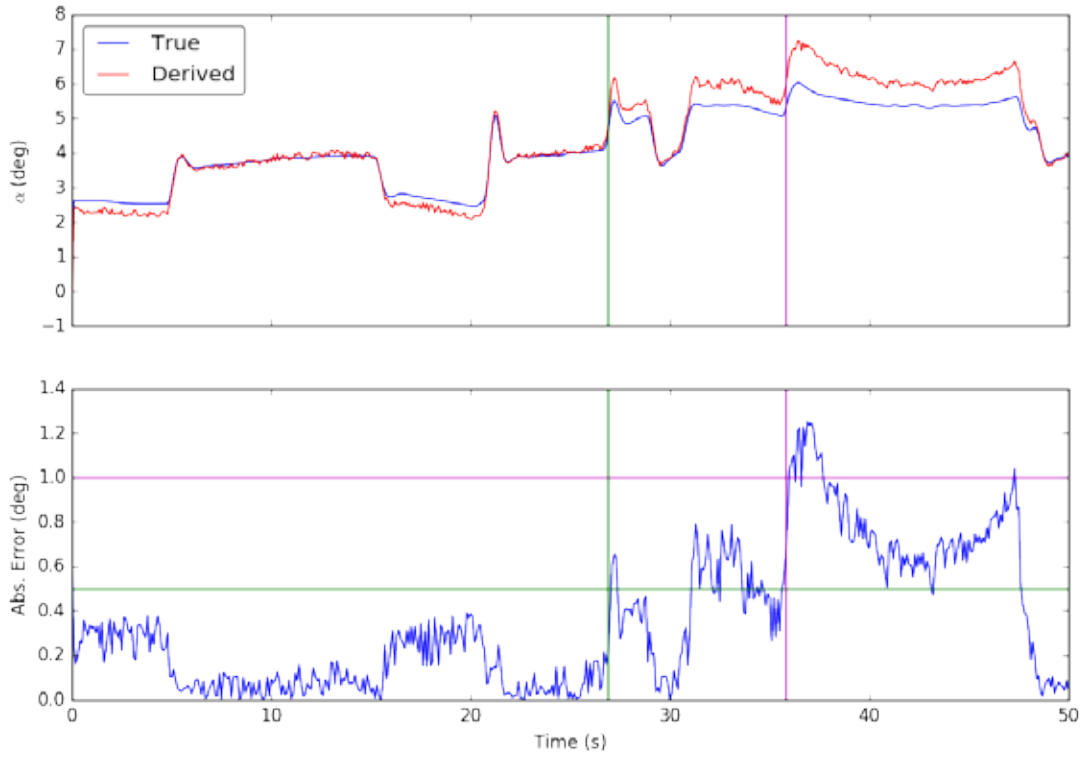
Figure 58. AoA estimate for run 1930 of Case 4

4.4.2.2 Sideslip Angle

Figure 59 plots the derived sideslip angle seen in run 1847 of Case 4.
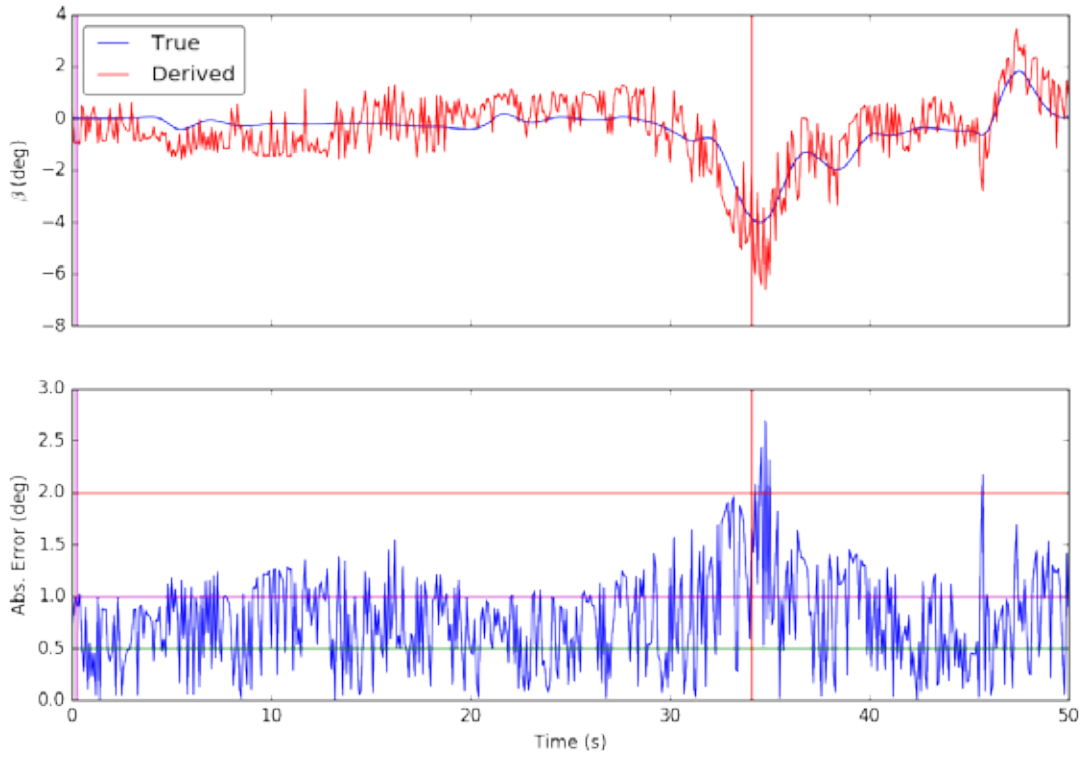
Figure 59. Sideslip angle estimate for run 1847 of Case 4

4.5 CASE 6: MEDIUM SENSOR NOISE, 10,000 RUNS

4.5.1 Low-Error Example

4.5.1.1 Angle-of-Attack

Figure 60 plots the derived AoA seen in run 4651 of Case 6.
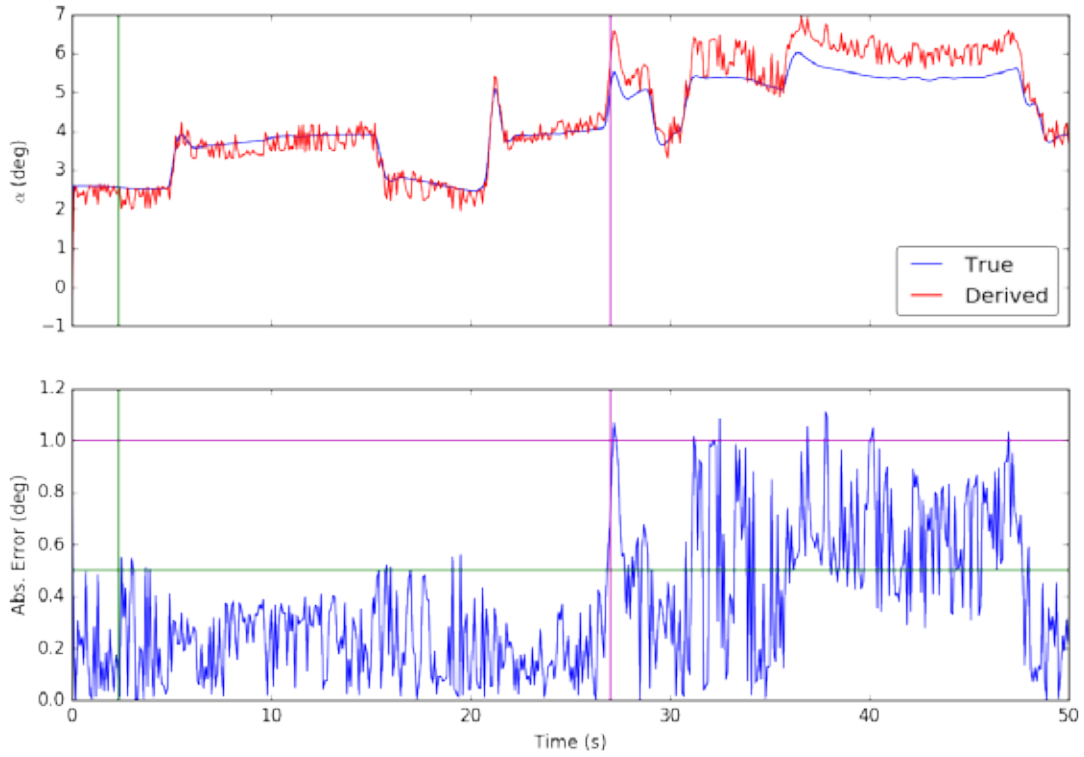
Figure 60. AoA estimate for run 4651 of Case 6

4.5.1.2 Sideslip Angle

Figure 61 plots the derived sideslip angle seen in run 7718 of Case 6.
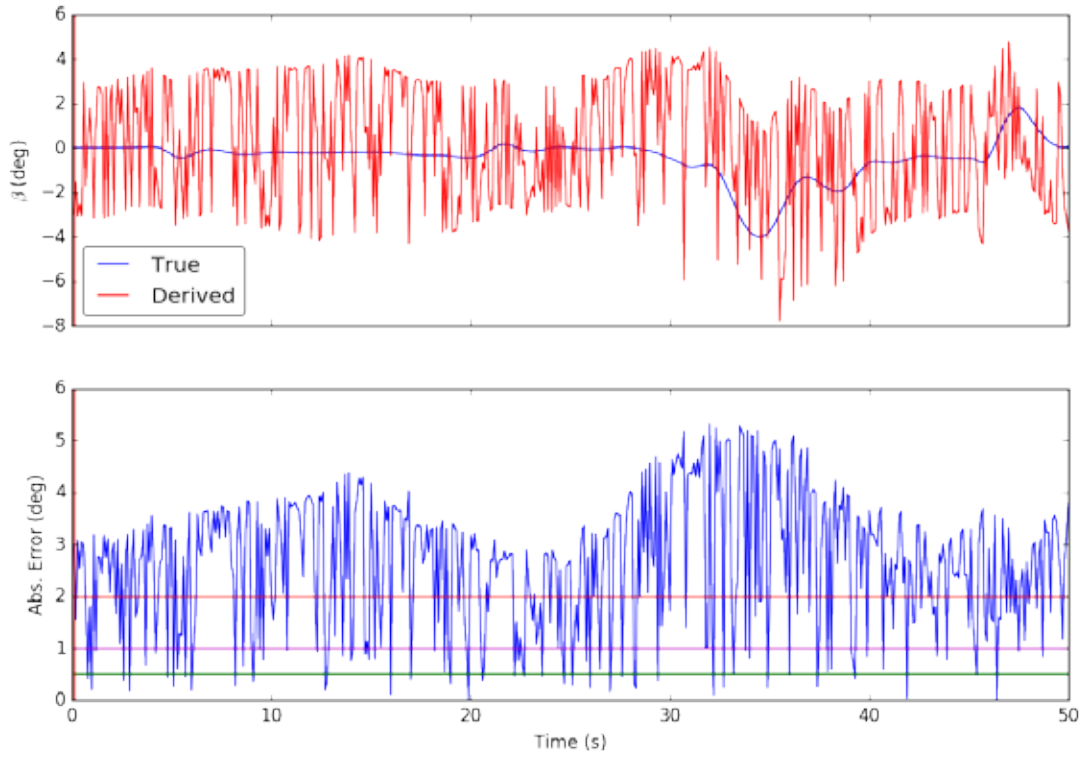
Figure 61. Sideslip angle estimate for run 7718 of Case 6

4.5.2 High-Error Example

4.5.2.1 Angle-of-Attack

Figure 62 plots the derived AoA seen in run 8555 of Case 6.
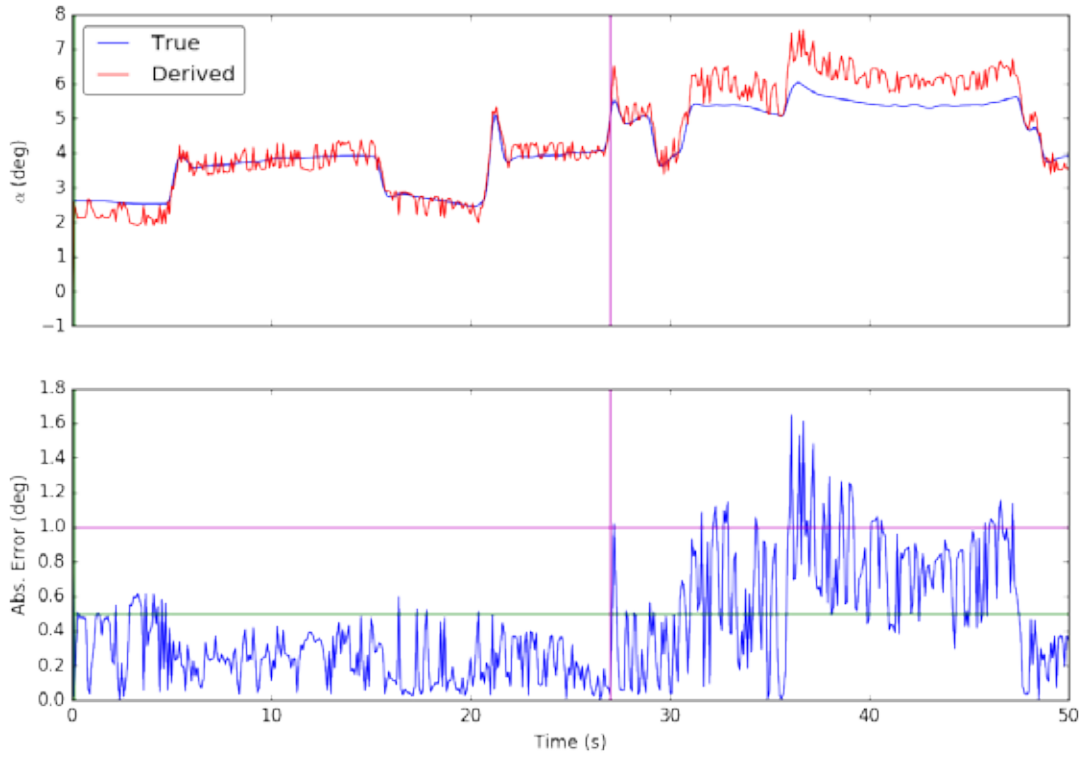
Figure 62. AoA estimate for run 8555 of Case 6

4.5.2.2 Sideslip Angle

Figure 63 plots the derived sideslip angle seen in run 753 of Case 6.
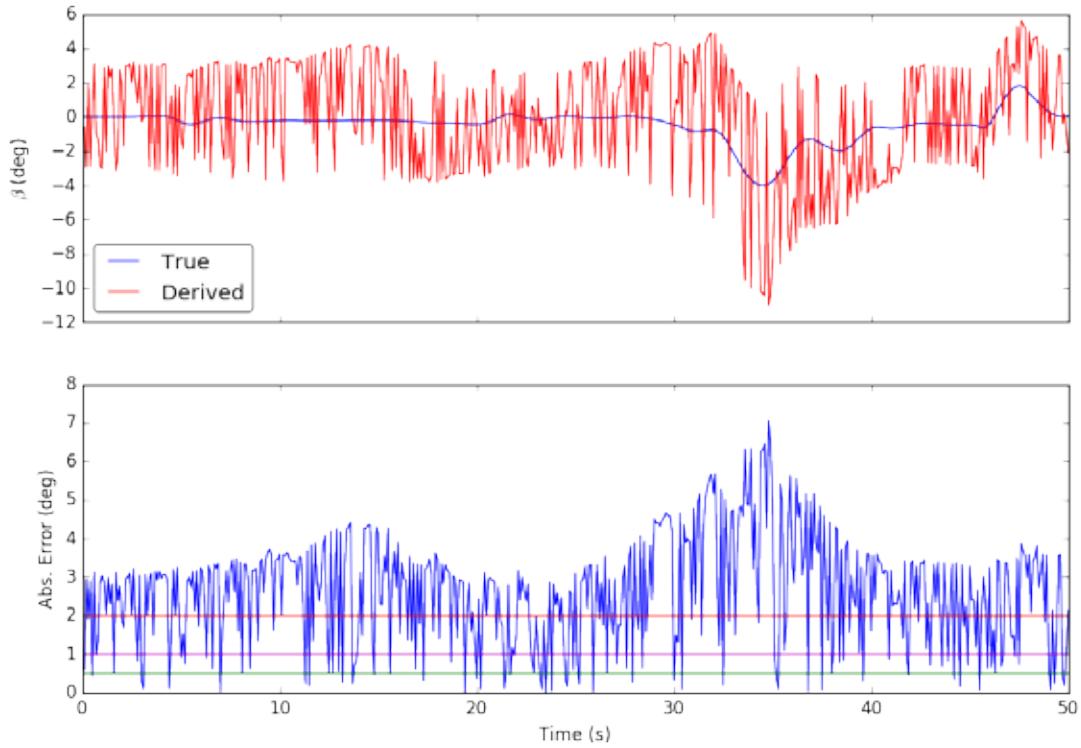
Figure 63. Sideslip angle estimate for run 753 of Case 6

4.6 CASE 8: HIGH SENSOR NOISE, 10,000 RUNS

4.6.1 Low-Error Example

4.6.1.1   Angle-of-Attack

Figure 64 plots the derived AoA seen in run 190 of Case 8.
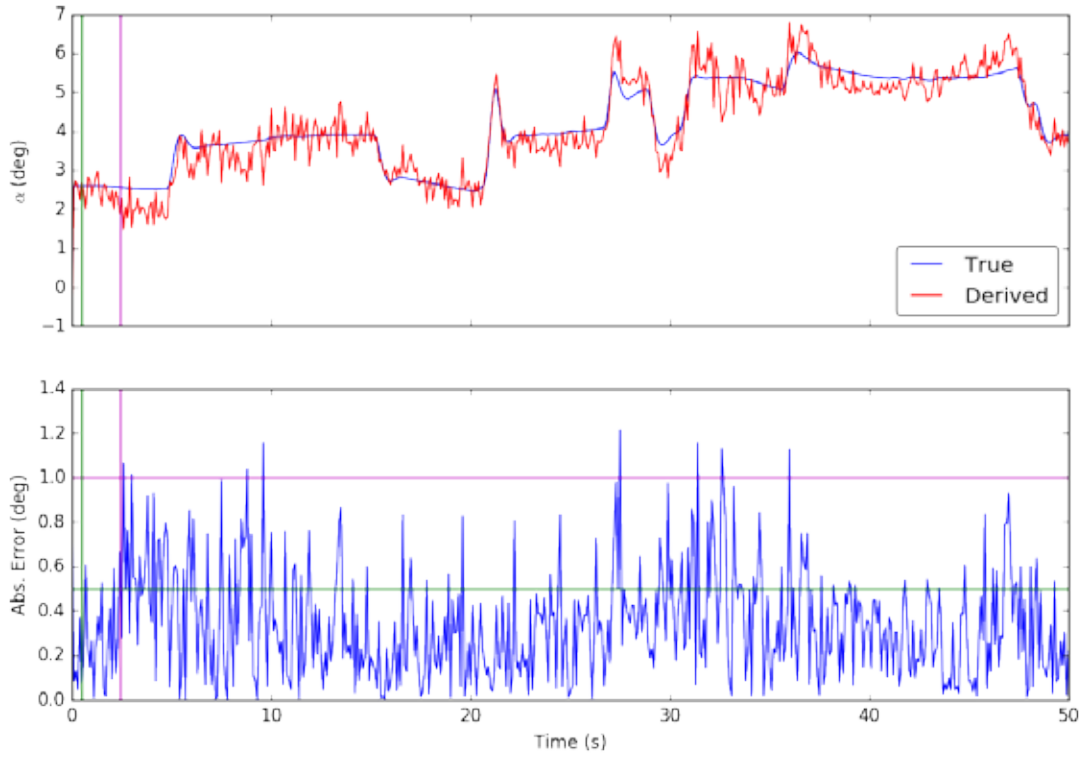
Figure 64. AoA estimate for run 190 of Case 8

4.6.1.2 Sideslip Angle

Figure 65 plots the derived sideslip angle seen in run 3751 of Case 8.
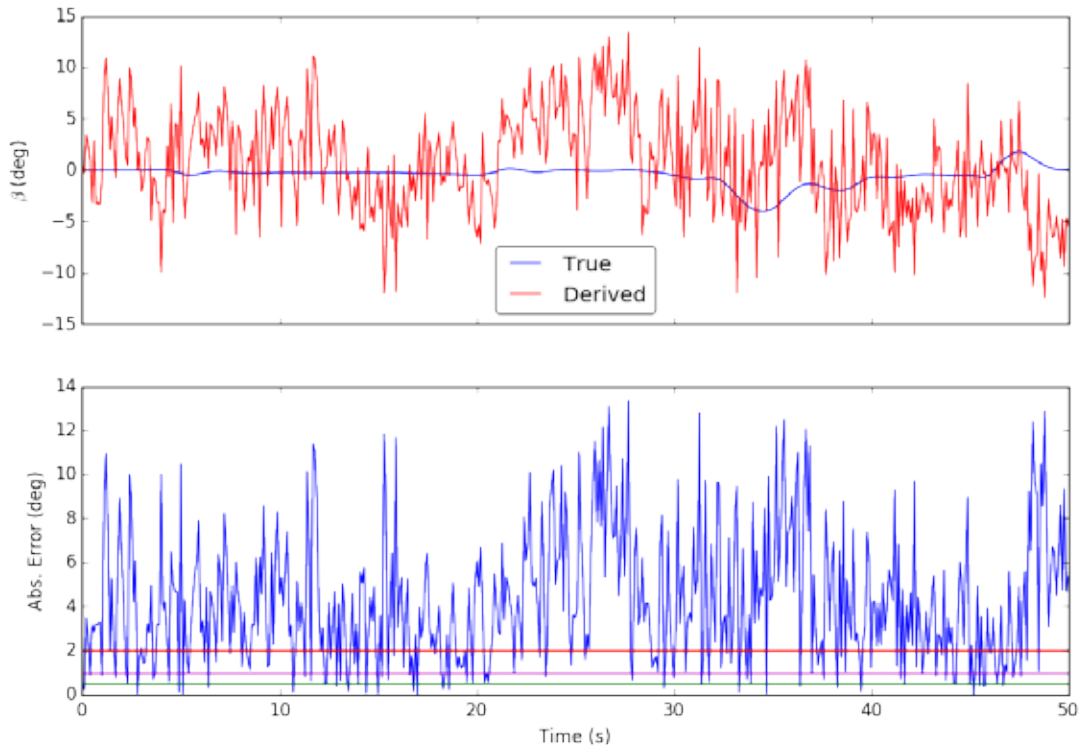
Figure 65. Sideslip angle estimate for run 3751 of Case 8

4.6.2 High-Error Example

4.6.2.1   Angle-of-Attack

Figure 66 plots the derived AoA seen in run 6341 of Case 8.
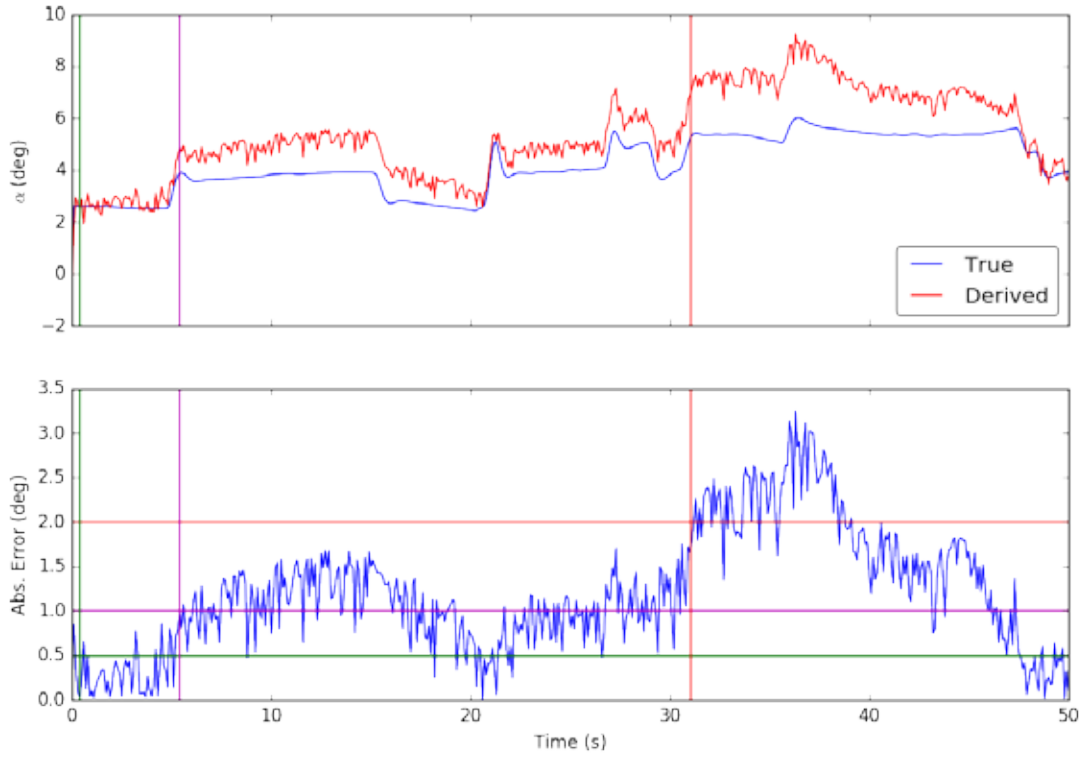
Figure 66. AoA estimate for run 6341 of Case 8

4.6.2.2 Sideslip Angle

Figure 67 plots the derived sideslip angle seen in run 3422 of Case 8.
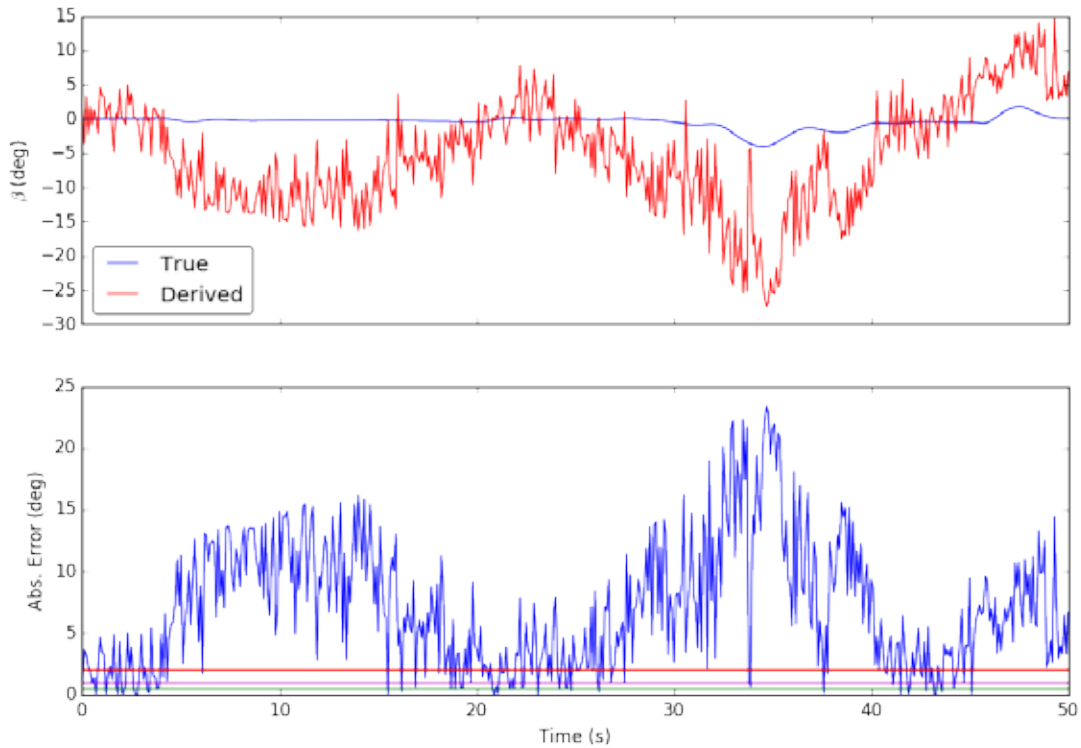
Figure 67. Sideslip angle estimate for run 3422 of Case 8

4.7 CASE 13: DOUBLET INPUTS, UNCERTAIN S&C

4.7.1 Low-Error Example

4.7.1.1 Angle-of-Attack

Figure 68 plots the derived AoA seen in run 4716 of Case 13. Table 15 lists the values for the S&C power derivatives along with their z-scores.

Table 15. Z-scores and S&C derivative values for run 4716 of Case 13

S&C Derivative	Z-Score	Value (1/rad)	Nominal Value (1/rad)
C_{L_α}	0.0475	4.4205	4.41
C_{L_q}	-0.5280	3.4882	3.9
$C_{L_{\delta_E}}$	-0.8780	0.3922	0.43
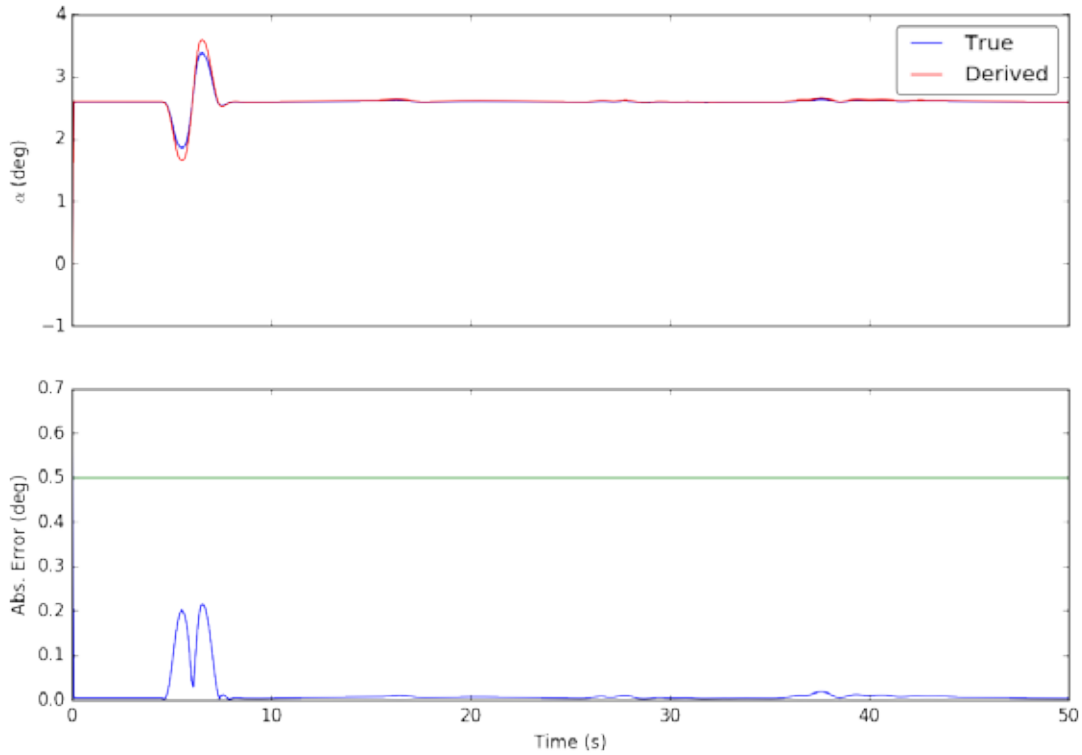
Figure 68. Run 4716 of Case 13 AoA estimate

4.7.1.2 Sideslip Angle

Figure 69 plots the derived sideslip angle seen in run 3770 of Case 13. Table 16 lists the values for the S&C power derivatives along with their z-scores.

Table 16. Z-scores and S&C derivative values for run 3770 of Case 13

S&C Derivative	Z-Score	Value (1/rad)	Nominal Value (1/rad)
C_{y_β}	-0.1470	-0.4046	-0.393
C_{y_p}	0.7173	-0.0481	-0.075
C_{y_r}	-0.4817	0.1625	0.214
$C_{y_{\delta_R}}$	0.9981	0.2057	0.187

66
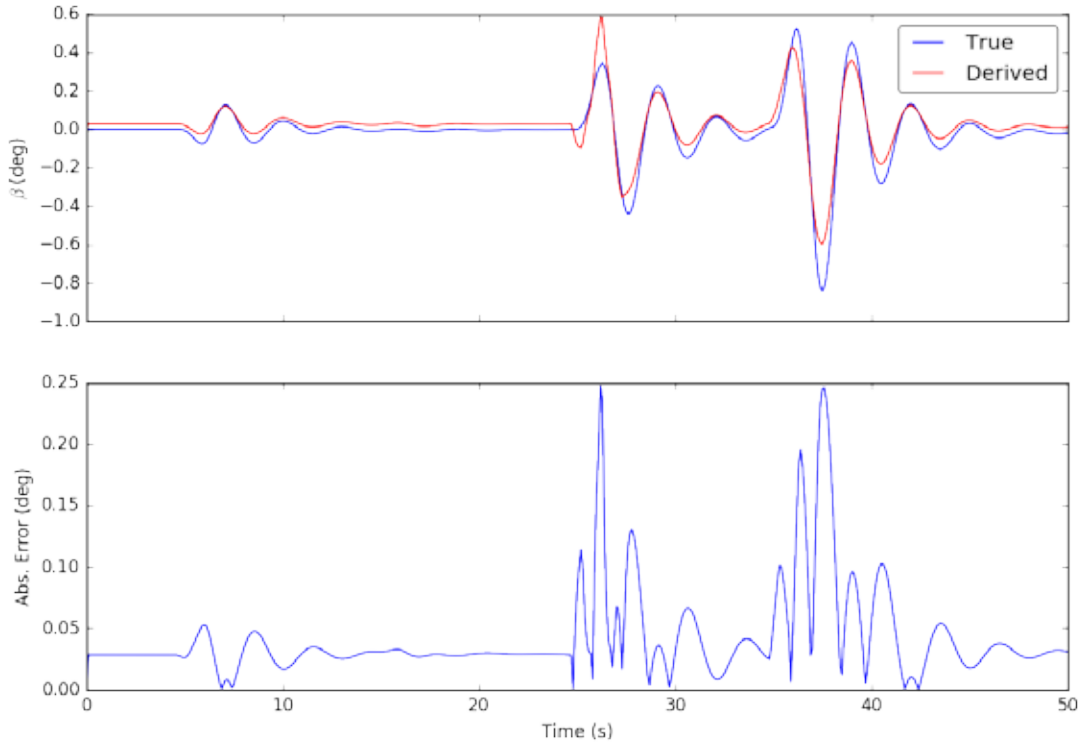
Figure 69. Run 3770 of Case 13 sideslip angle estimate

4.7.2 High-Error Example

4.7.2.1 Angle-of-Attack

Figure 70 plots the derived AoA seen in run 596 of Case 13. Table 17 lists the values for the S&C power derivatives along with their z-scores.

Table 17. Z-scores and S&C derivative values for run 596 of Case 13

S&C Derivative	Z-Score	Value (1/rad)	Nominal Value (1/rad)
C_{L_α}	2.2069	4.8966	4.41
C_{L_q}	0.1391	4.0085	3.9
$C_{L_{\delta_E}}$	-0.1166	0.4250	0.43

67
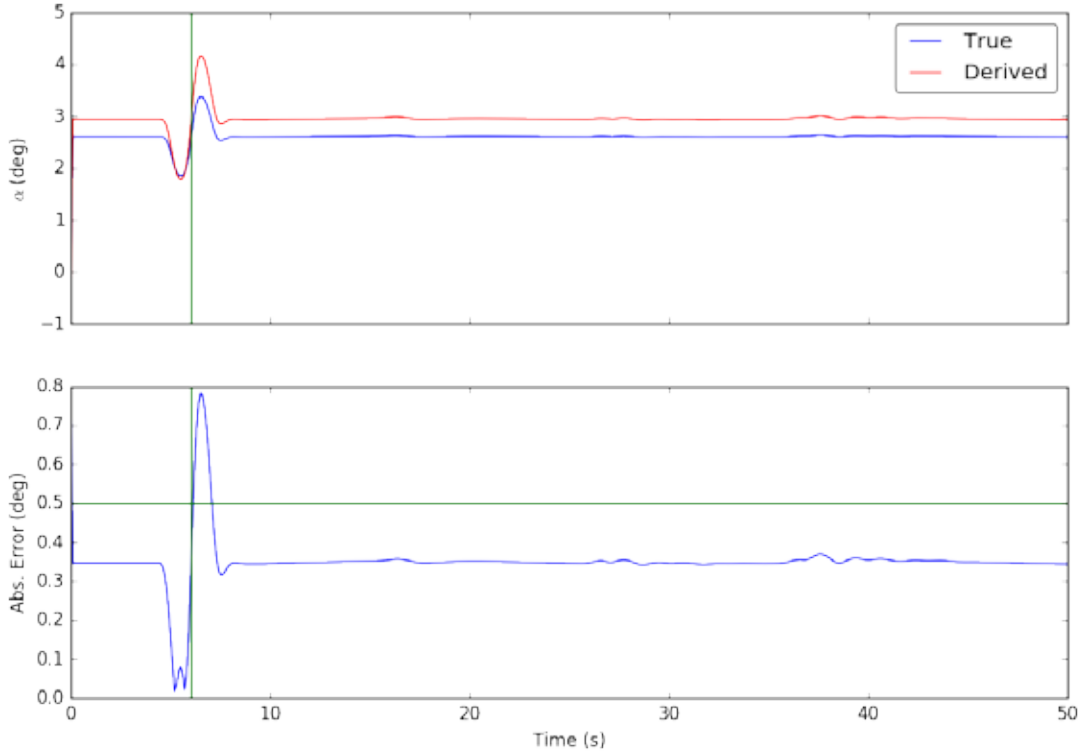
Figure 70. Run 596 of Case 13 AoA estimate

4.7.2.2 Sideslip Angle

Figure 71 plots the derived sideslip angle seen in run 4843 of Case 13. Table 18 lists the values for the S&C power derivatives along with their z-scores.

Table 18. Z-scores and S&C derivative values for run 4843 of Case 13

S&C Derivative	Z-Score	Value (1/rad)	Nominal Value (1/rad)
C_{y_β}	0.7536	-0.3338	-0.393
C_{y_p}	-1.2413	-0.1215	-0.075
C_{y_r}	-0.0554	0.2081	0.214
$C_{y_{\delta_R}}$	0.6956	0.2000	0.187
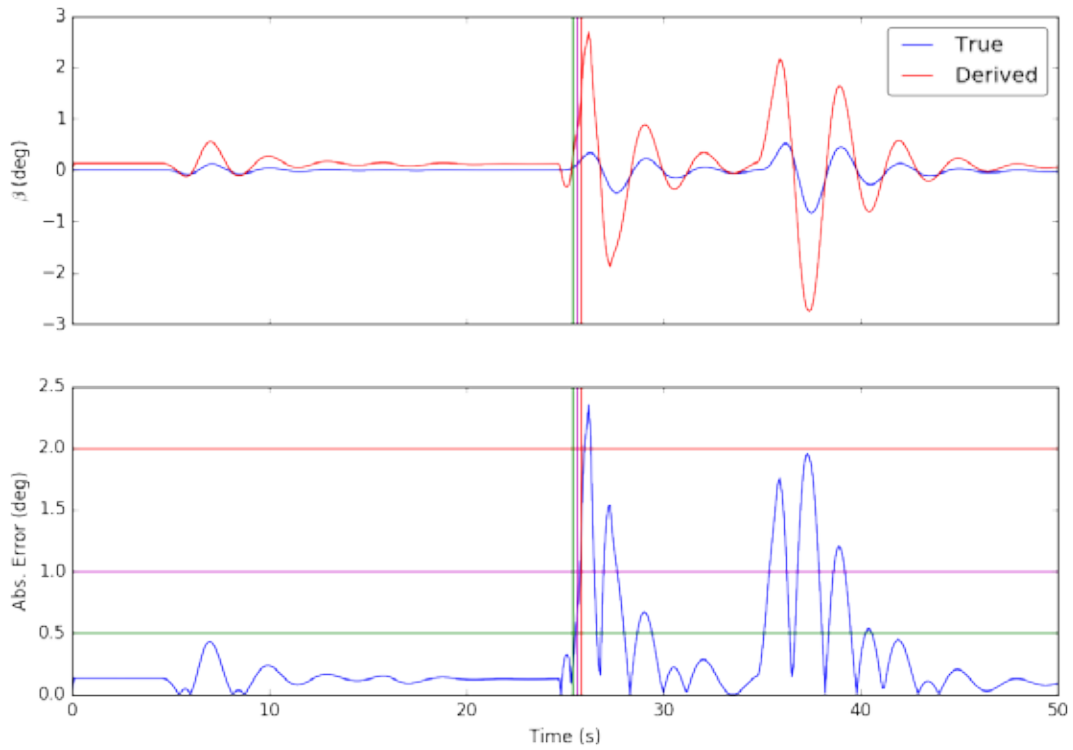
Figure 71. Run 4843 of Case 13 sideslip angle estimate

4.8 CASE 15: DOUBLET INPUTS, MEDIUM SENSOR NOISE

4.8.1 Low-Error Example

4.8.1.1 Angle-of-Attack

Figure 72 plots the derived AoA seen in run 9839 of Case 15.
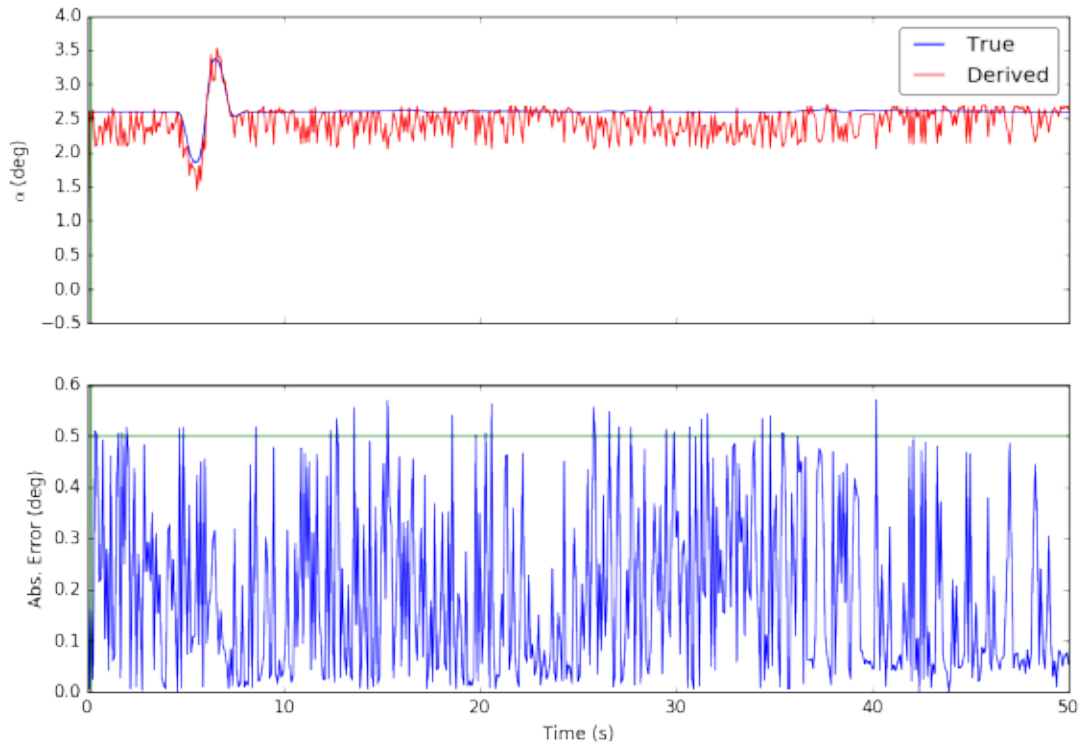
Figure 72. AoA estimate for run 9839 of Case 15

4.8.1.2 Sideslip Angle

Figure 73 plots the derived sideslip angle seen in run 826 of Case 15.
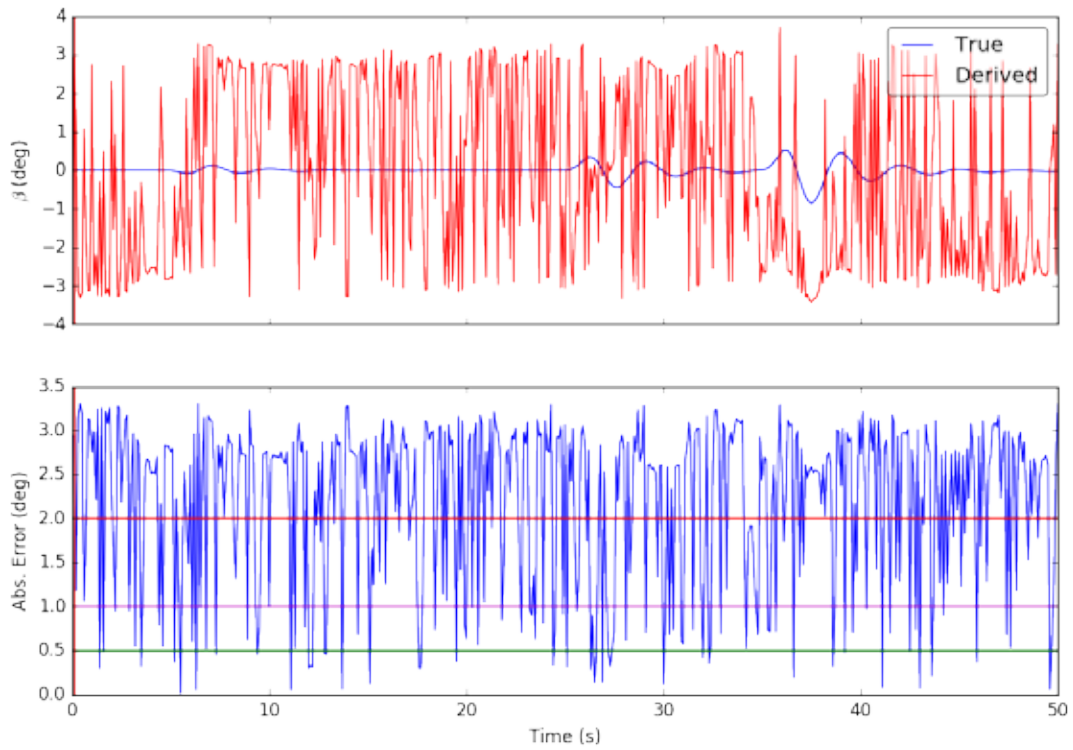
Figure 73. Sideslip angle estimate for run 826 of Case 15

4.8.2 High-Error Example

4.8.2.1 Angle-of-Attack

Figure 74 plots the derived AoA seen in run 5920 of Case 15.
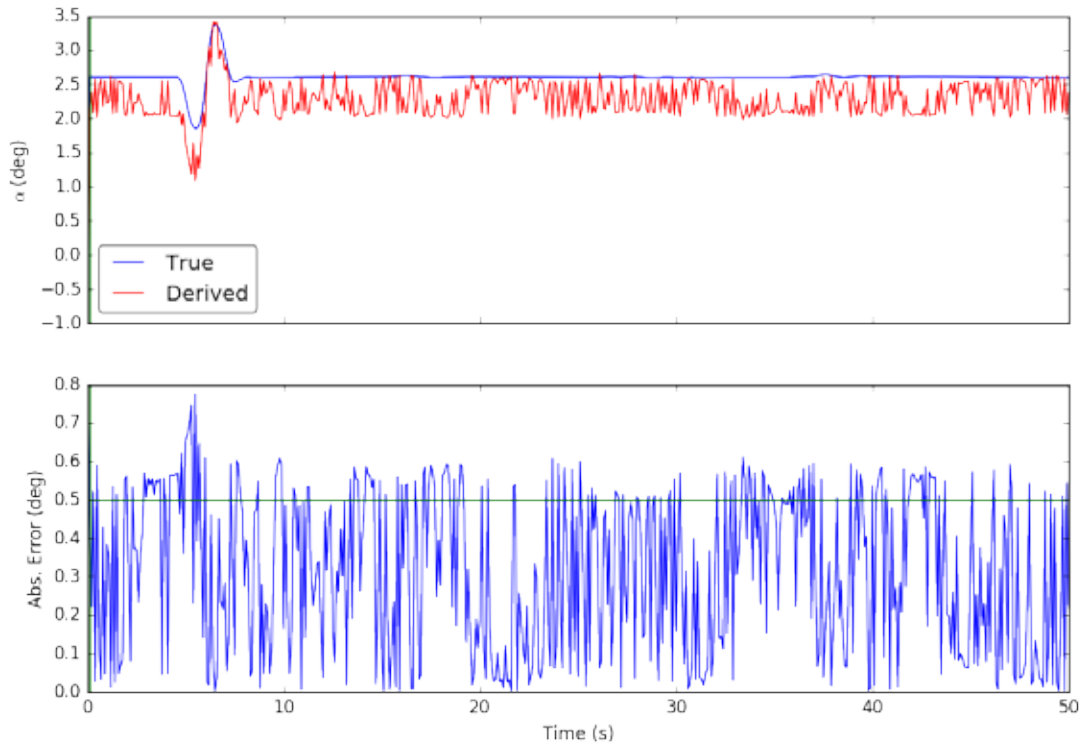
Figure 74. AoA estimate for run 5920 of Case 15

4.8.2.2 Sideslip Angle

Figure 75 plots the derived sideslip angle seen in run 3922 of Case 15.
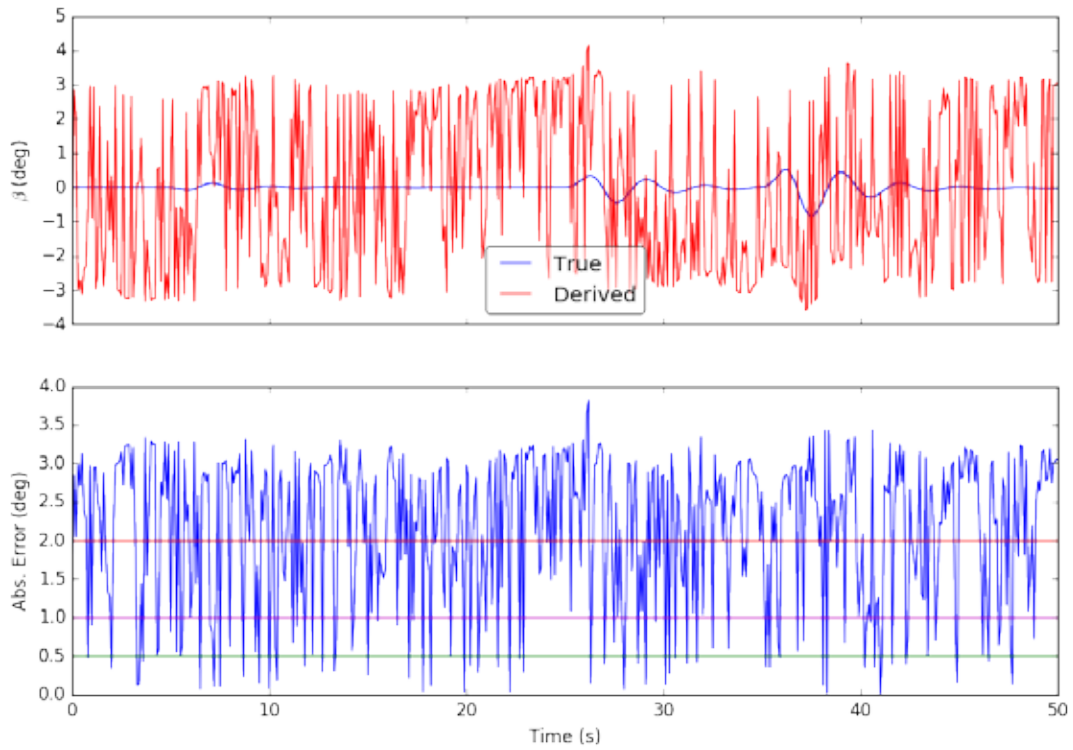
Figure 75. Sideslip angle estimate for run 3922 of Case 15

4.9 CASE 16: DOUBLET INPUTS, HIGH SENSOR NOISE

4.9.1 Low-Error Example

4.9.1.1 Angle-of-Attack

Figure 76 plots the derived AoA seen in run 457 of Case 16.

73
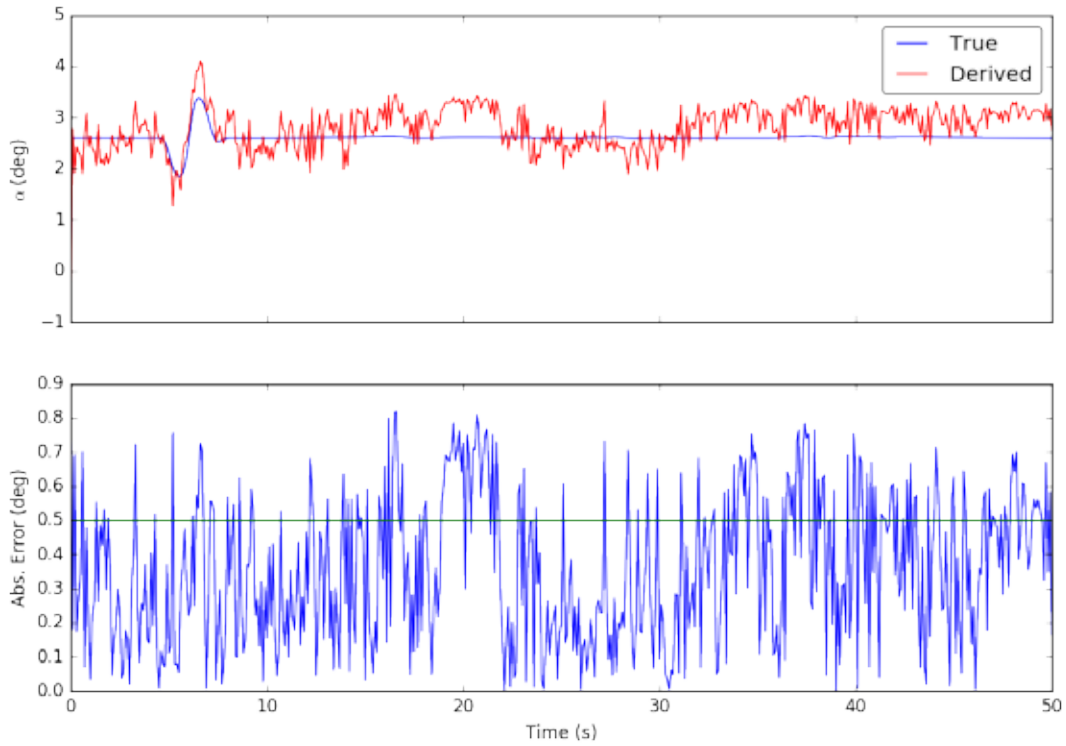
Figure 76. AoA estimate for run 457 of Case 16

<u>4.9.1.2 Sideslip Angle</u>

Figure 77 plots the derived sideslip angle seen in run 8811 of Case 16.
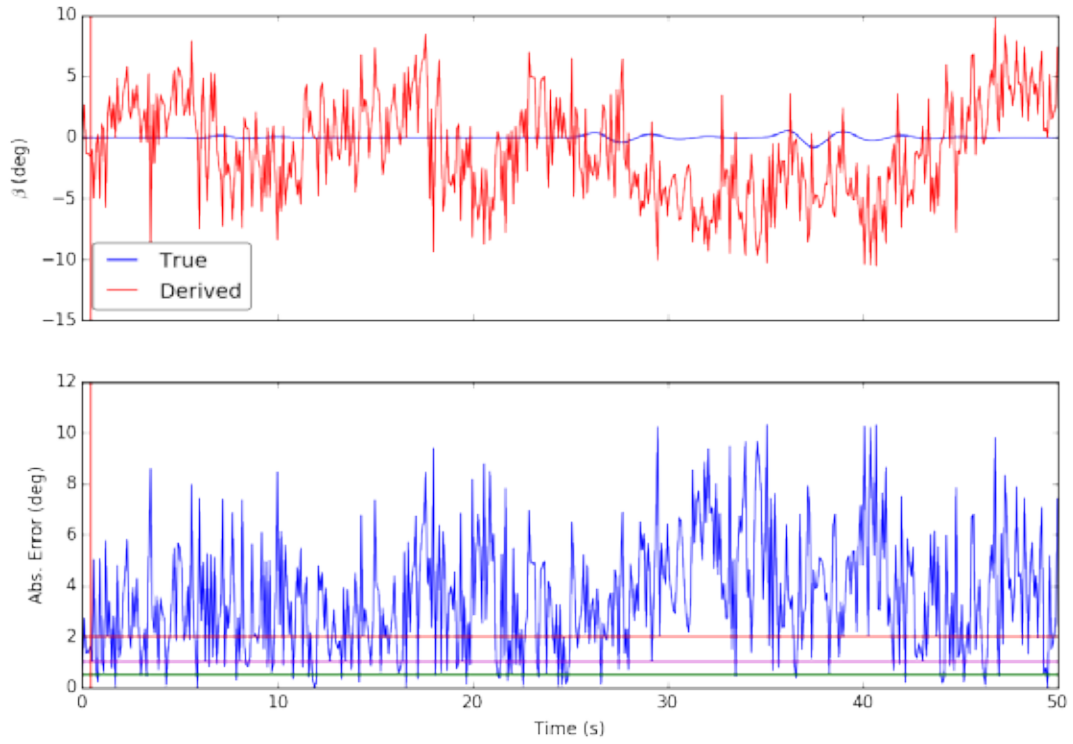
Figure 77. Sideslip angle estimate for run 8811 of Case 16

4.9.2 High-Error Example

4.9.2.1 Angle-of-Attack

Figure 78 plots the derived AoA seen in run 7965 of Case 16.
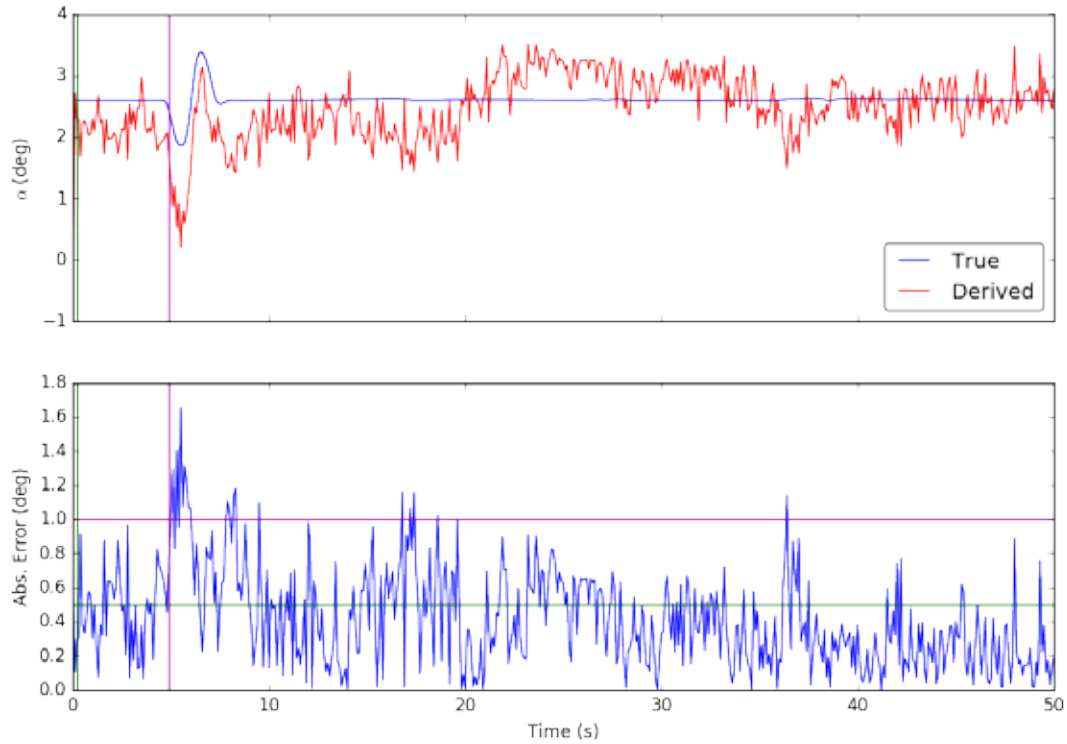
Figure 78. AoA estimate for run 7965 of Case 16

4.9.2.2 Sideslip Angle

Figure 79 plots the derived sideslip angle seen in run 5287 of Case 16.
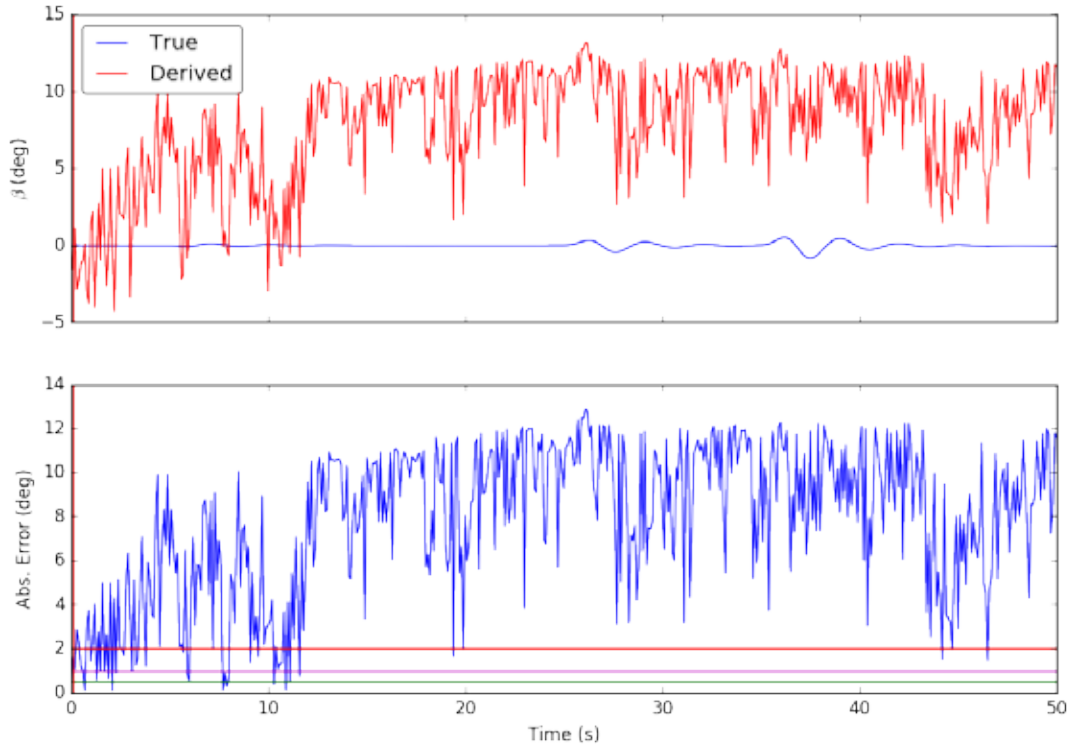
Figure 79. Sideslip angle estimate for run 5287 of Case 16

5. SUMMARY OF RESULTS

5.1 CASES 1–3 EFFECT OF S&C DERIVATIVES—UNCERTAINTY

1. The magnitude of the error greatly depends on the C_{L_α} and C_{y_β} terms. For the derived AoA, the minimum error occurs at a C_{L_α} $1.5\sigma - 2\sigma$ above the DATCOM value, suggesting a difference between the DATCOM and JSBSim models. Because the C_{L_α} and C_{y_β} terms control the scaling of the derived AoA and sideslip, this causes the algorithm to perform worse than expected. However, if the nominal value of the lift curve slope is shifted to the value suggested by the error analysis, the results are as expected. The derived AoA value is extremely sensitive to the lift curve slope, and results suggest that a single value of C_{L_α} is insufficient and that C_{L_α} may need to be scheduled based on the derived AoA itself, although the performance of this approach was not evaluated in this work.
2. For the derived AoA, C_{L_α} values below the nominal value lead to conservative predictions of the derived AoA (i.e., derived AoA is larger than true AoA), and values above the nominal value lead to derived AoA values less than the true AoA.
3. There appears to be no correlation between the C_{L_q} modeling errors represented by the z-scores and the resulting error in derived AoA. Furthermore, it does not appear that there is an effect caused by whether the modeled C_{L_q} is above or below the nominal value. Similar results hold for $C_{L_{\delta_E}}$.

77

4. A low level of modeling error/model uncertainty is sufficient to violate the AFPC tolerances, but the uncertainty needed to violate the envelope-protection and pilot display thresholds tend to be outside the level of modeling error experienced in practice.

5. Considering the derivative C_{y_β}, the effect of the sideslip angle on the sideforce, there appears to be a noticeable correlation between the maximum sideslip angle error and the z-score of C_{y_β}. This trend suggests that the magnitude of the error depends only on the z-score and not the sign of the error. The plot of sideslip angle RMS errors against the z-scores of the derivative C_{y_β} clearly shows a relationship between the two parameters. The more negative the C_{y_β} z-score, the worse the error in the derived sideslip angle.

6. The derivatives C_{L_q}, $C_{L_{\delta_E}}$, C_{y_p}, C_{y_r}, and $C_{y_{\delta_R}}$ are shown to have no correlation between their variations and the resulting maximum and RMS errors in derived AoA and sideslip errors.

7. The 100,000-run case shows similar behavior to the 10,000-run case, suggesting that 10,000 runs are sufficient to verify the algorithm performance.

5.2 CASES 4–9 IMU OUTPUTS—BIAS AND NOISE

1. Cases 4–5 show that the AoA algorithm can be used for envelope protection with the low level of sensor noise because all runs meet the envelope-protection tolerances. Nearly 85% of runs violate the AFPC tolerances for AoA. The performance for sideslip is considerably worse, with all runs violating the envelope-protection tolerances.

2. Cases 6–7 consider a medium level of sensor noise. With this increased noise, the derived AoA violates the envelope-protection tolerances in every run. The sideslip now consistently violates the pilot display tolerances, with errors in the range of 5–7 degrees.

3. Cases 8–9 consider a high level of sensor noise. More than 55% of the AoA runs violate the display tolerance, with the remainder violating the envelope-protection tolerance. The sideslip angle always violates the pilot display tolerances with errors in the range of 6–11 degrees, making it effectively useless.

4. Note that these results are degraded by increased error caused by the C_{L_α} value overpredicting the derived A-A at higher AoA flight phases.

5.3 CASES 10–12 COMBINED S&C DERIVATIVES AND IMU OUTPUTS

1. Case 10 presents low sensor noise with model uncertainty. The combination of the two error sources degrades the performance of the algorithm, with the poorer performance from the sensor noise and the greater variability from the uncertain S&C derivatives. For Case 10, the uncertain S&C derivatives have the dominant effect, with the worst errors resulting from erroneous derivatives. Conclusions from cases 1–3 hold with respect to the effect of the derivative terms. The AoA is usable for pilot display, whereas the sideslip angle violates the loosest tolerance the majority of the time.

2. Case 11 consists of medium sensor noise with uncertain S&C derivatives. Here, the noise terms have more effect, although the uncertain derivatives still dominate. The different S&C derivatives still behave according to the above analysis. The derived AoA is usable for pilot display more than 80% of the time. Derived sideslip now uniformly violates all tolerances.

3.   Case 12 shows the effect of the combination of high sensor noise and uncertain derivatives. The sensor noise now begins to dominate, with the effect of the modeling errors becoming less noticeable in the z-score plots, which become more scattered. This effect is less noticeable on the sideslip angle plots, which better retain their trends. The derived AoA violates the display tolerance in approximately 55% of runs with these conditions.

5.4 CASES 13–16 DOUBLET FLIGHT CONDITIONS

1.   The results from the previous flight condition hold for the doublet flight condition for the case of uncertain S&C derivatives. There is once again a definite relationship between C_{L_α} z-scores and RMS error, which appears to show the same shape as in Case 1, with the difference of being shifted along the z-score axis and the minimum RMS errors occurring at z-scores of approximately -2. This likely is a result of the nominal S&C derivatives from the Roskam text not matching the JSBSim model. Additionally, the AoA values do not change much once the short-period from the elevator doublet finishes, and, therefore, the "nominal" values have a somewhat constant bias for a 40-second period.
2.   The derivatives C_{L_q}, $C_{L_{\delta_E}}$, C_{y_p}, C_{y_r}, and $C_{y_{\delta_R}}$ are shown to have no correlation between their variations and the resulting maximum and RMS errors in derived AoA and sideslip errors. In particular, the derivatives C_{L_q} and $C_{L_{\delta_E}}$ show much less correlation than in the previous flight condition.
3.   The effect of sensor noise matches that of the previous flight condition.

6. RECOMMENDATIONS

The specific recommendations produced by this work are as follows:

1.   The derived AoA and beta analytic and simulation tools developed in this work are sufficient to assess algorithm and sensor performance. Results presented in this report show good agreement with truth models and demonstrate that the modeling errors and sensor errors can be adjusted in a reasonable way to permit evaluation of the results.
2.   Accurate aerodynamic parameters and quantification of sensor noise are essential in bounding the uncertainty in derived AoA and beta. The methods and tools developed for this project allow for this bounding to be evaluated in detail for a variety of aircraft and sensors.
3.   AFPC systems are the most demanding application of the derived AoA and beta algorithms and require the highest fidelity aerodynamic models and sensor data.
4.   The initial algorithm testing and validation work was completed using a limited dataset. Further testing is needed to validate the derived AoA and beta algorithms across a broad range of flight conditions and on aircraft with different performance characteristics.
5.   Additional testing using the methods and tools developed for this project in conjunction with actual flight hardware is required to demonstrate the real-world performance of the algorithms, in the context of unknown aerodynamic and sensor-noise characteristics.
6.   Using the tools and techniques developed in this work with additional testing of the algorithms on different real-world platforms will provide the data necessary to inform future derived AoA and beta standards.

7. REFERENCES

1. Berndt, Jon S., "JSBSim: An Open Source Flight Dynamics Model in C++," AIAA-2004-4923,
    AIAA Modeling and Simulation Technologies Conference and Exhibit, Providence, RI, 16-19
    August 2004.

2. Hoak, D. E., et al., "The USAF Stability and Control DATCOM," Air Force Wright Aeronautical Laboratories, TR-83-3048, Oct. 1960 (Revised 1978).

3. Fisher, Ronald Aylmer (1936). "The Use of Multiple Measurements in Taxonomic Problems".
    Annals of Eugenics. 7: 179. doi:10.1111/j.1469-1809.1936.tb02137.x.

4. Li, W., and Wang, J., "Effective adaptive Kalman filter for MEMS-IMU/magnetometers integrated attitude and heading reference systems," Journal of Navigation, Vol. 66, No. 01, 2013,
    pp. 99-113. doi:10.1017/s0373463312000331

5. Savage, P.G., "Strapdown Inertial Navigation Integration Algorithm Design Part 1: Attitude
    Algorithms," Journal of Guidance, Control, and Dynamics, Vol. 21, No. 1, January 1998, pp. 19-
    28. doi:10.2514/2.4228

6. Rogers, R.M., Applied Mathematics in Integrated Navigation Systems, 3rd ed., American Institute of Aeronautics and Astronautics, Reston, VA, January 2007. doi:10.2514/4.861598

7. Kempe, V., Inertial MEMS principles and practice, Cambridge University Press, Cambridge,
    2011. doi:10.1017/CBO9780511933899

8. Farrell, J., and Barth, M., The Global Positioning System and Inertial Navigation, McGraw-Hill,
    New York, 1999.

9. Bekir, E., Introduction to Modern Navigation Systems, World Scientific, Singapore, 2007. doi:10.1142/6481

10. McCrink, M.H., "Development of Flight-Test Performance Estimation Techniques for Small
    Unmanned Aerial Systems," Dissertation, The Ohio State University, 2015.

11. Myschik, S., Heller, M., Holzapfel, F., and Sachs, G., "Low-Cost Approach Based On

Navigation Data For Determining Angles Of Attack And Sideslip For Small Aircraft," AIAA
2004-5240, AIAA Guidance, Navigation, and Control Conference and Exhibit, Providence, RI
16-19 August 2004.

12.   Heller, M., Myschik, S., Holzapfel, F., and Sachs, G., "Low-Cost Approach Based On Navigation Data For Determining Angles Of Attack And Sideslip For Small Aircraft," AIAA
2003-5777, AIAA Guidance, Navigation, and Control Conference and Exhibit, Austin, TX, 11-14
August 2003.

TEST PLAN AND SCHEDULE

DERIVED ANGLE-OF-ATTACK AND

DERIVED SIDESLIP ANGLE

Version 2

1. Test Objectives

    a. Determine acceptable limiting values of the terms that appear in equations for Derived Angle-of-Attack (AOA) and Derived Sideslip Angle (Beta), to specified accuracies.
    b. Determine both individual limiting values and combinations of limiting values.
    c. Evaluate the effects:

        i. Uncertainty in vehicle dynamics
        ii. Sensor errors and noise
        iii. Atmospheric gust and turbulence

    d. Use the determined limits to specify guidelines and requirements on sensor accuracy for Derived AOA and Derived Beta avionics .

2. Methods

    a. Holzapfel equations for Derived AOA and Derived Beta.
    b. Monte Carlo simulation using a nonlinear model of the aircraft's dynamics.

        i. Use pilot inputs recorded from the Engineering Flight Simulator as the inputs for the simulation runs.
        ii. Vary the items listed in 1 c), individually and in combinations.
        iii. Start with 1000 simulation runs for the Monte Carlo. Modify this value as the analysis progresses.

    c. Flight conditions to be evaluated:

        i. Approach
        ii. Wings-level stall

    d. Aircraft to be evaluated:

        i. Cessna 172
        ii. Adaptive Aerospace aircraft

3.   Test Metrics
      The test metrics are specified values for the acceptable error levels in Derived AOA and
      Derived Beta. The specified values for Derived AOA correspond to use cases as follows:

      a.   Envelope Protection = 1.0 degrees
      b.   Display = 2.0 degrees
      c.   Fly by Wire = 0.5 degrees

      User specified values for Derived Beta have not yet been determined.

4.   Test Matrix
      The test matrix is presented in the Excel file "Test Plan for Monte Carlo Analysis
      Ver3.xlsx."

5.   Schedules

Cirrus Jet

      26–29 August

Monte Carlo

      a)   Stability derivative variations
            29 August–1 September
      b)   Sensor noise variations
            2–6 September
      c)   Combined stability derivative and sensor noise variations
            7–14 September

Final Technical Report

      Provide first draft to sponsor by 23 September

Test and Evaluation Plan for Monte Carlo Analysis of Derived AOA
Version 2.0
21-Aug-16

Aircraft: Cessna 172

Maneuver Set 1: Power Approach: 70 KIAS, 1,000 feet AGL

<u>Series 1</u>

Stability and Control Derivatives - Uncertainty

Case 1: Low
Case 2: Medium
Case 3: High

<u>Series 2</u>

IMU Outputs - Bias and Noise

Case 4: Low
Case 5: Medium
Case 6: High

<u>Series 3</u>

Combined Stability and Control Derivatives + IMU Outputs

Case 7: Low
Case 8: Medium
Case 9: High

Maneuver Set 2: Wings Level Stall: 63 KIAS, 2,000 feet AGL

<u>Series 4</u>

Stability and Control Derivatives - Uncertainty

Case 10: Low
Case 11: Medium
Case 12: High

<u>Series 5</u>

IMU Outputs - Bias and Noise

Case 13: Low
Case 14: Medium
Case 15: High

<u>Series 6</u>

Combined Stability and Control Derivatives + IMU Outputs

Case 16: Low
Case 17: Medium
Case 18: High

APPENDIX C—SUPPORTING FIGURES

C.1 CASE 4: LOW SENSOR NOISE, 10,000 RUNS

C.1.1 OVERVIEW

Case 4 consisted of 10,000 Monte Carlo iterations with noise added to the signals used to calculate the derived AoA and sideslip angle. The characteristics of a low-noise-level sensor package were used.

Figure C-1 plots histograms of the absolute errors for AoA and sideslip angle estimates, whereas figure C-2 plots the histograms for the corresponding RMS errors. In figure C-1, the histograms show a skewed distribution, although the effect is less pronounced on the sideslip angle. The histograms of the RMS errors in figure C-2 are, however, standard normal distributions.
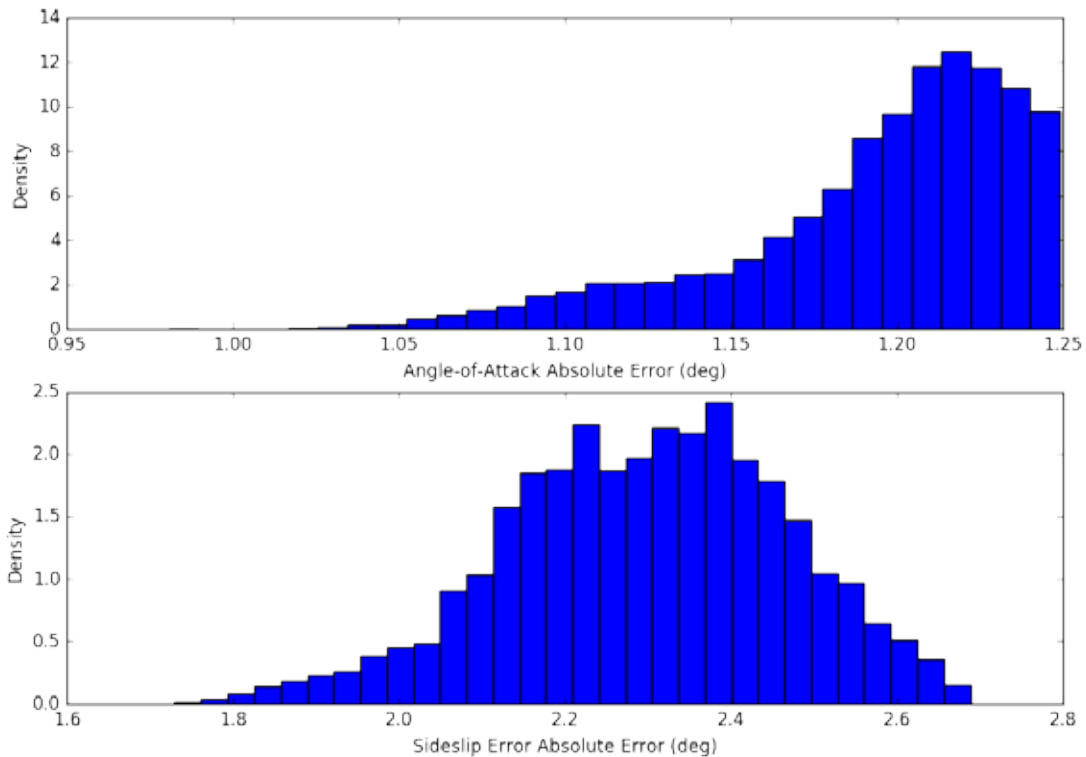
Figure C-1. Error histograms for Case 4
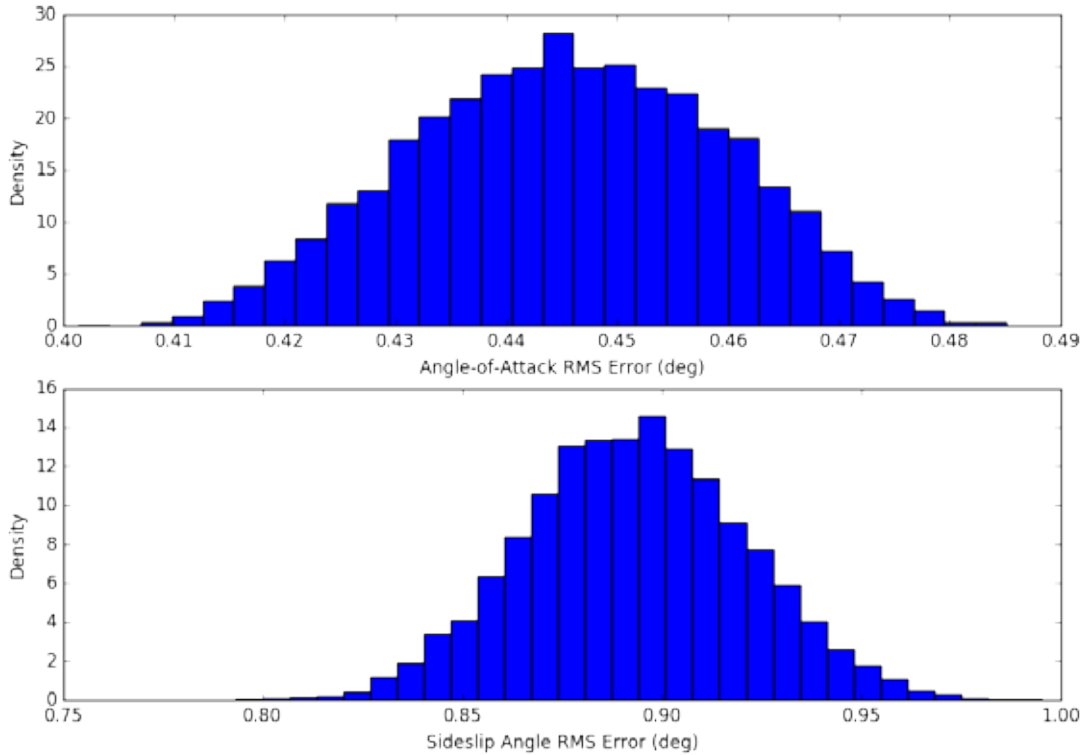
Figure C-2. RMS error histograms for Case 4

C.1.2. ANGLE-OF-ATTACK

For the derived AoA:

·   0.0000 % of runs violated the display tolerance.
·   99.9700 % of runs violated the envelope-protection tolerance.
·   0.0300 % of runs violated the AFPC tolerance.
·   0.0000 % of runs met all tolerances.

C.1.3. SIDESLIP ANGLE

For the derived sideslip angle:

·   95.1800 % of runs violated the display tolerance.
·   14.8200 % of runs violated the envelope-protection tolerance.
·   0.0000 % of runs violated the AFPC tolerance.
·   0.0000 % of runs met all tolerances.

C.2 CASE 5: LOW SENSOR NOISE, 100,000 RUNS

C.2.1 OVERVIEW

Case 5 repeated Case 4 with 100,000 Monte Carlo runs.
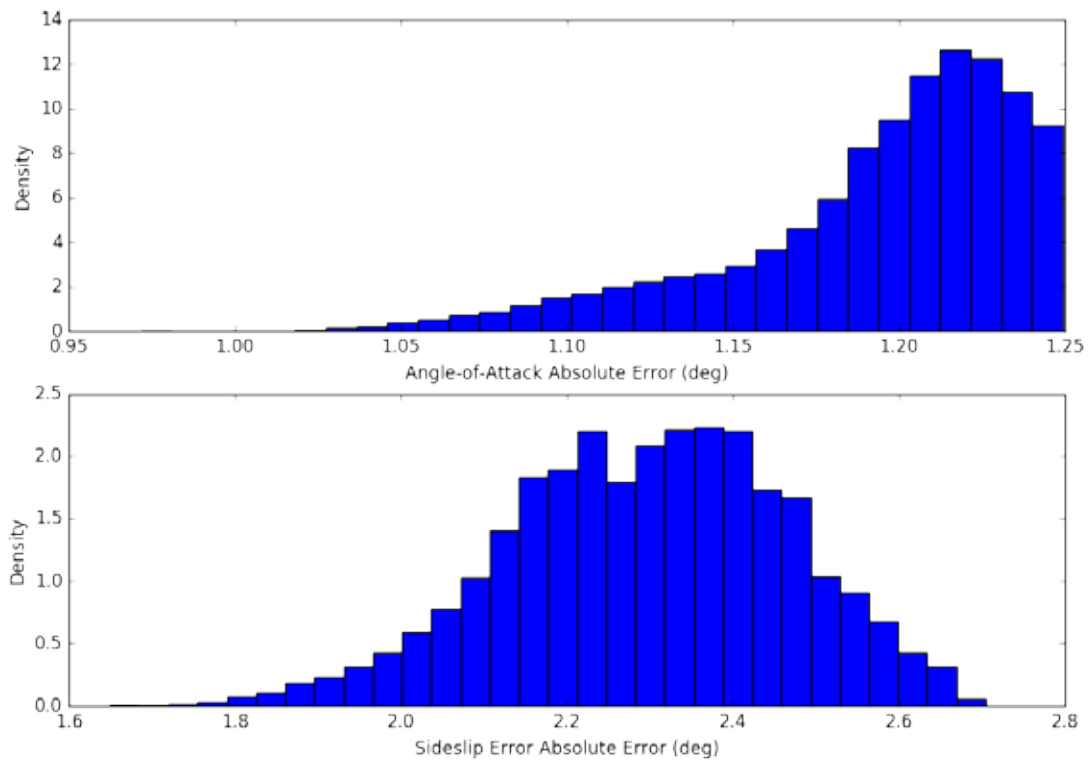
Figure C-3. Error histograms for Case 5
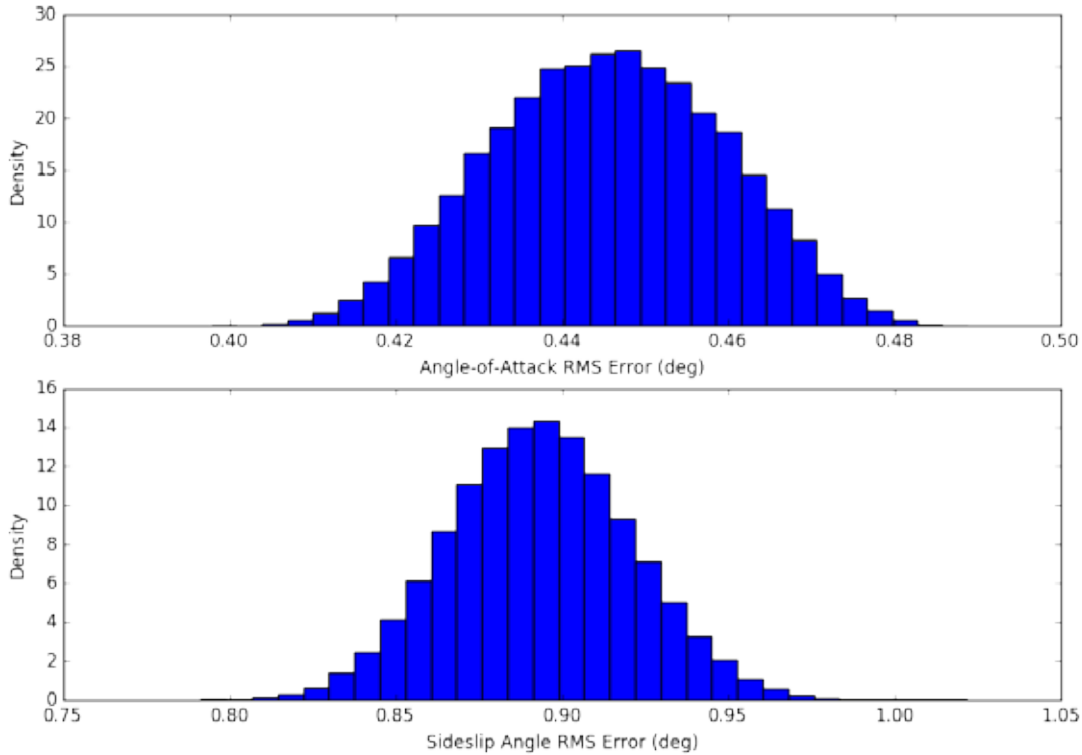
Figure C-4. RMS error histograms for Case 5

C.2.2 ANGLE-OF-ATTACK

For the derived AoA:

·   0.0000 % of runs violated the display tolerance.
·   99.9810 % of runs violated the envelope-protection tolerance.
·   0.0190 % of runs violated the AFPC tolerance.
·   0.0000 % of runs met all tolerances.

C.2.3 SIDESLIP ANGLE

For the derived sideslip angle:

·   95.2590 % of runs violated the display tolerance.
·   4.7410 % of runs violated the envelope-protection tolerance.
·   0.0000 % of runs violated the AFPC tolerance.
·   0.0000 % of runs met all tolerances.

 C.3 CASE 6: MEDIUM SENSOR NOISE, 10,000 RUNS

Case 6 consists of 10,000 Monte Carlo iterations with noise added to the signals used to calculate the derived AOA and sideslip angle. The characteristics of a medium noise level sensor package were used.

C.3.1. OVERVIEW
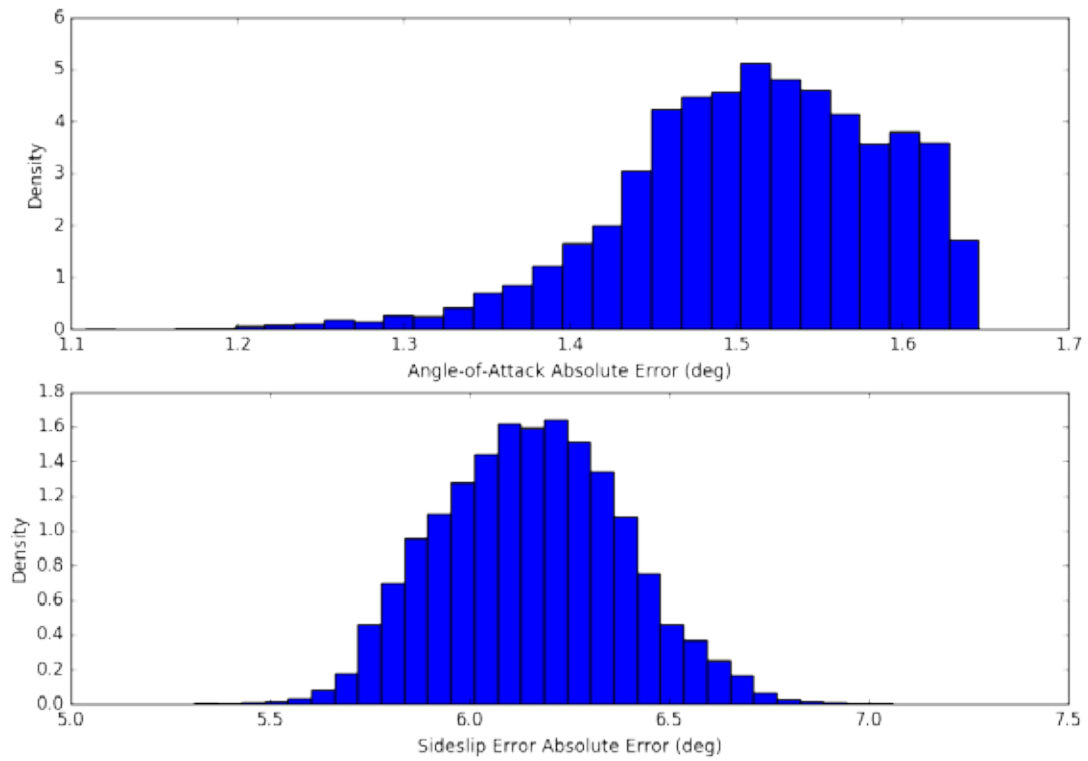
Figure C-5. Error histograms for Case 6
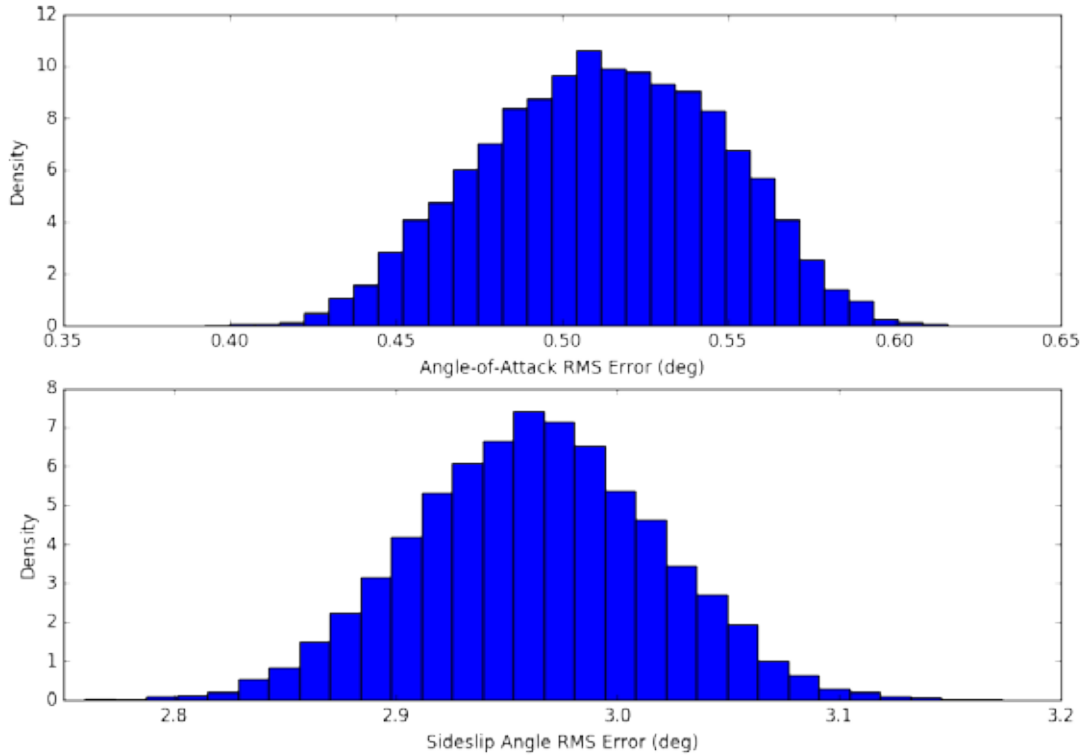
Figure C-6. RMS error histograms for Case 6

C.3.2 ANGLE-OF-ATTACK

For the derived AoA:

- ·   0.0000 % of runs violated the display tolerance.
- ·   100.0000 % of runs violated the envelope-protection tolerance.
- ·   0.0000 % of runs violated the AFPC tolerance.
- ·   0.0000 % of runs met all tolerances.

C.3.3 SIDESLIP ANGLE

For the derived sideslip angle:

- ·   100.0000 % of runs violated the display tolerance.
- ·   0.0000 % of runs violated the envelope-protection tolerance.
- ·   0.0000 % of runs violated the AFPC tolerance.
- ·   0.0000 % of runs met all tolerances.

C.4 CASE 7: MEDIUM SENSOR NOISE, 100,000 RUNS

C.4.1 OVERVIEW

Case 7 repeated Case 6 with 100,000 Monte Carlo iterations.
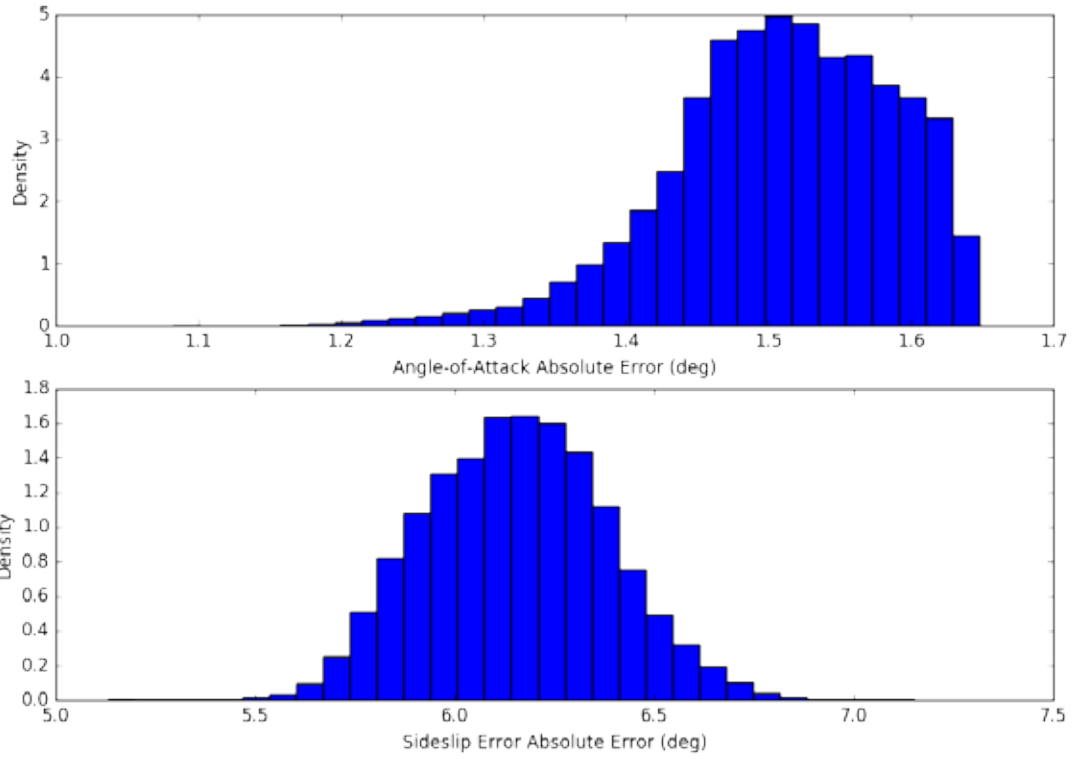
Figure C-7. Error histograms for Case 7
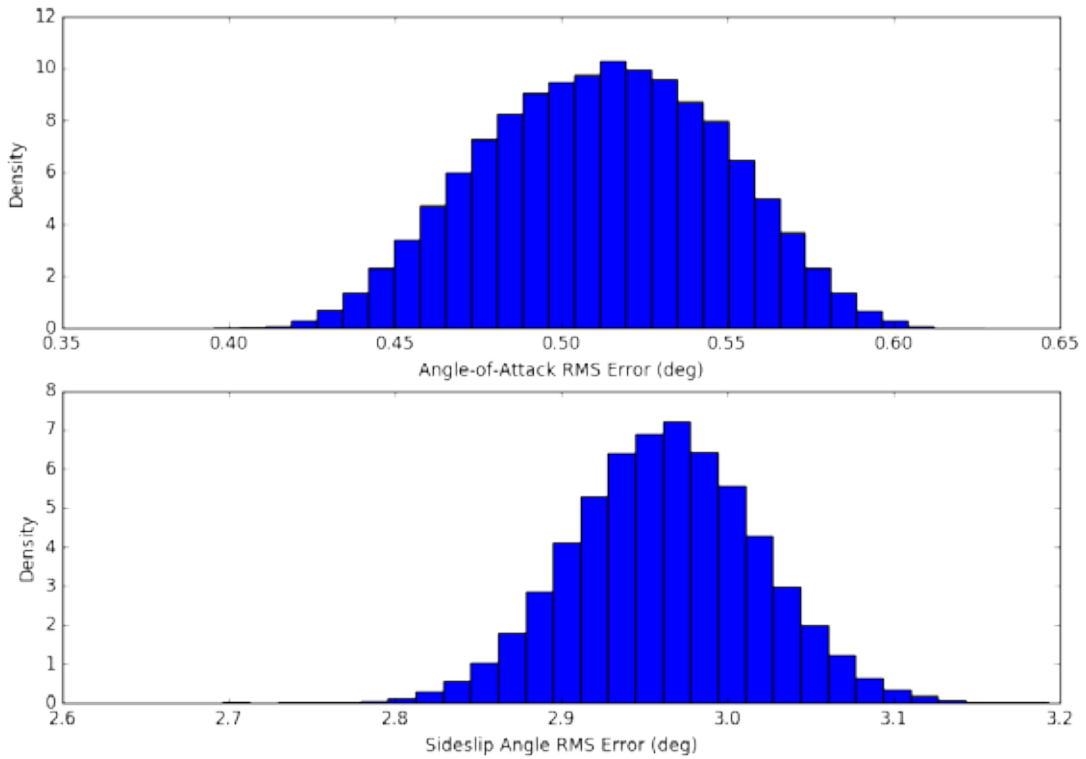
Figure C-8. RMS error histograms for Case 7

C.4.2 ANGLE-OF-ATTACK

For the derived AoA:

- 0.0000 % of runs violated the display tolerance.
- 100.0000 % of runs violated the envelope-protection tolerance.
- 0.0000 % of runs violated the AFPC tolerance
- 0.0000 % of runs met all tolerances.

C.4.3 SIDESLIP ANGLE

For the derived sideslip angle:

- 100.0000 % of runs violated the display tolerance.
- 0.0000 % of runs violated the envelope-protection tolerance.
- 0.0000 % of runs violated the AFPC tolerance.
- 0.0000 % of runs met all tolerances.

C.5 CASE 8: HIGH SENSOR NOISE, 10,000 RUNS

C.5.1 OVERVIEW

Case 8 consisted of 10,000 Monte Carlo iterations with noise added to the signals used to calculate the derived AoA and sideslip angle. The characteristics of a high-noise-level sensor package were used.
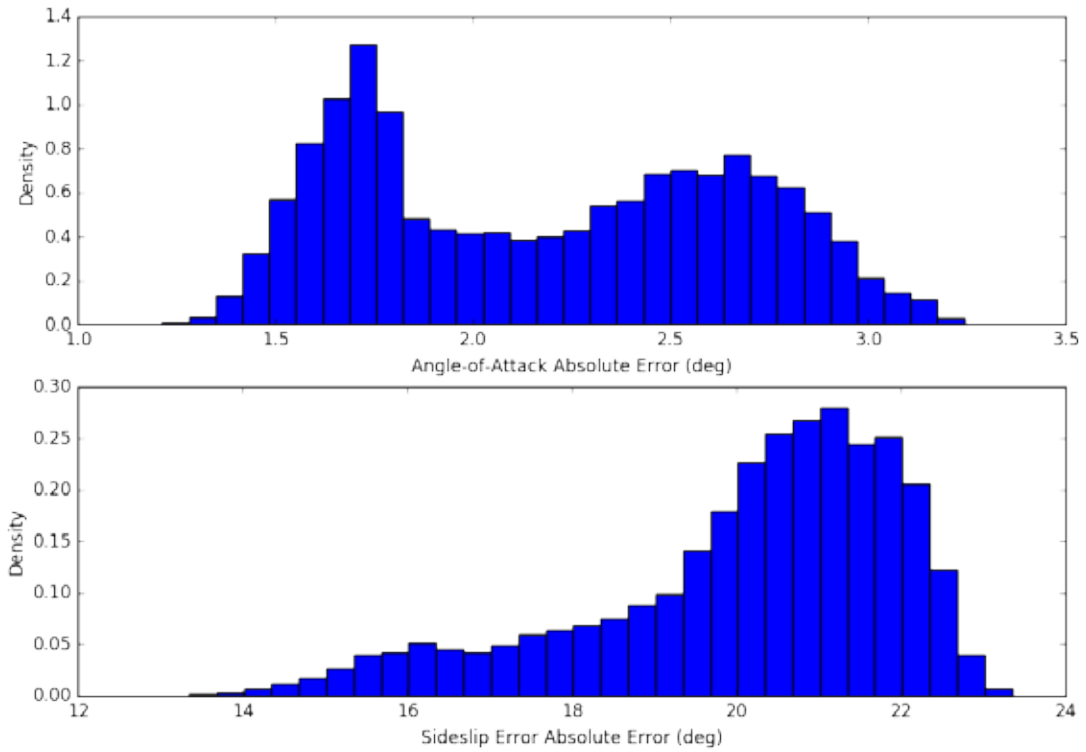
Figure C-9. Error histograms for Case 8
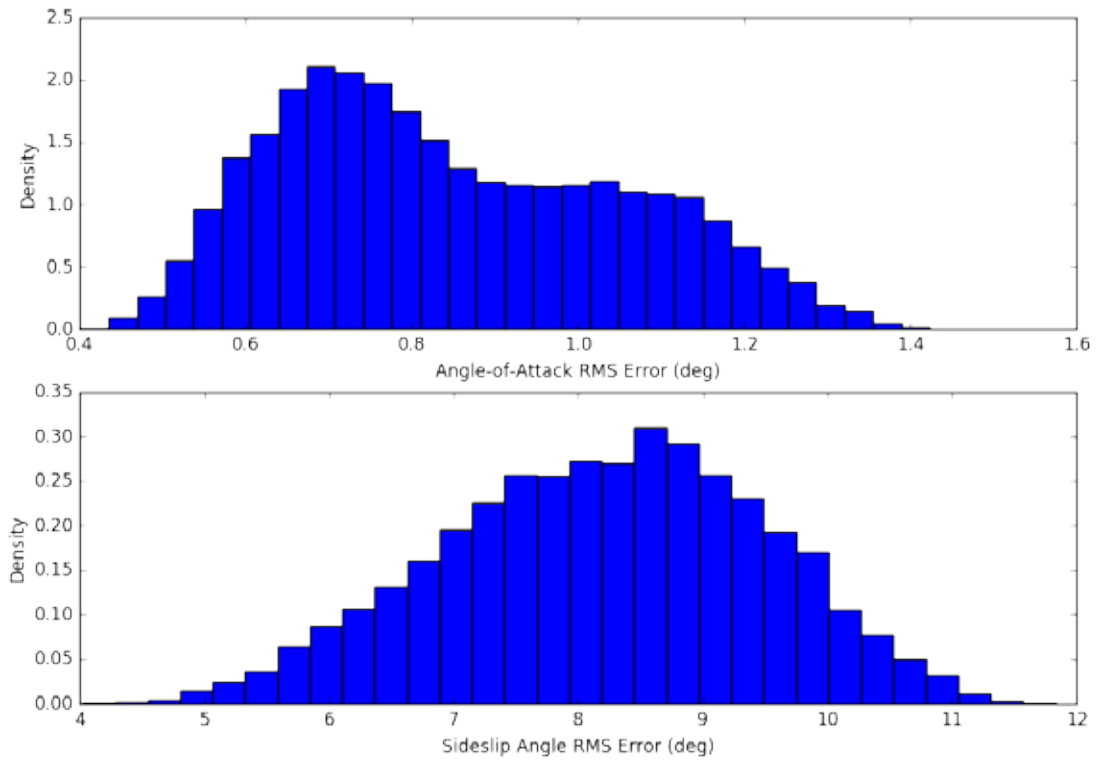
Figure C-10. RMS error histograms for Case 8

C.5.2 ANGLE-OF-ATTACK

For the derived AoA:

· 57.0300 % of runs violated the display tolerance.
· 42.9700 % of runs violated the envelope-protection tolerance.
· 0.0000 % of runs violated the AFPC tolerance.
· 0.0000 % of runs met all tolerances.

C.5.3 SIDESLIP ANGLE

For the derived sideslip angle:

· 100.0000 % of runs violated the display tolerance.
· 0.0000 % of runs violated the envelope-protection tolerance.
· 0.0000 % of runs violated the AFPC tolerance.
· 0.0000 % of runs met all tolerances.

C.6 CASE 9: HIGH SENSOR NOISE, 100,000 RUNS

C.6.1 OVERVIEW

Case 9 repeated Case 8 with 100,000 runs.
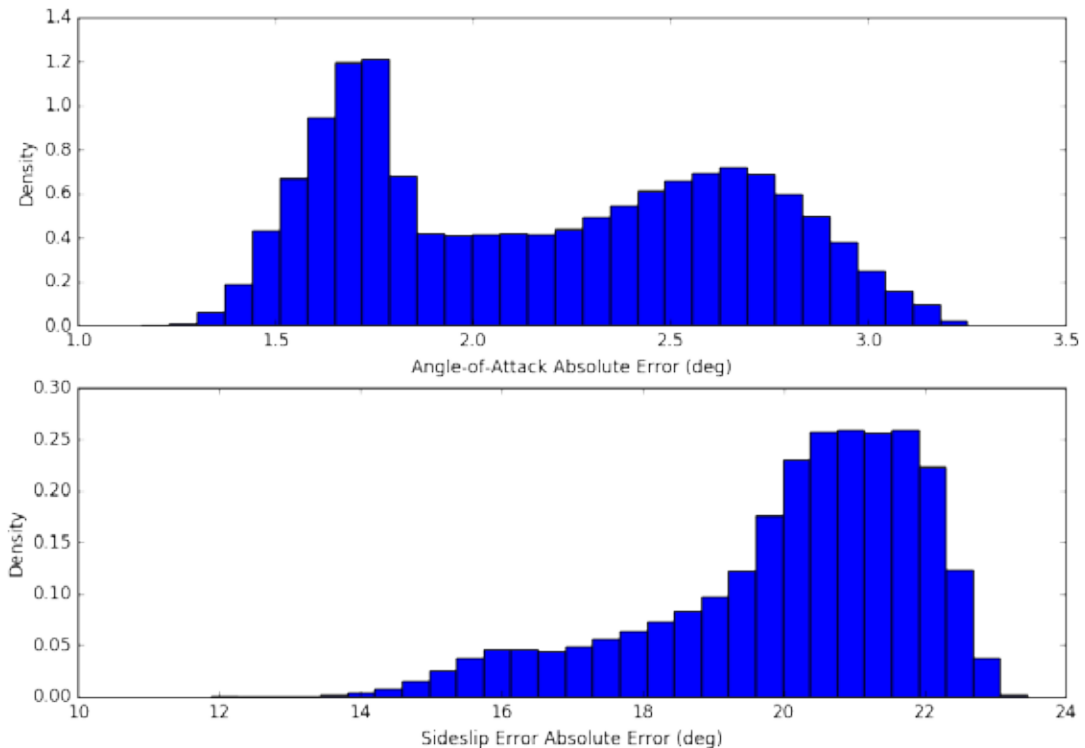
Figure C-11. Error histograms for Case 9
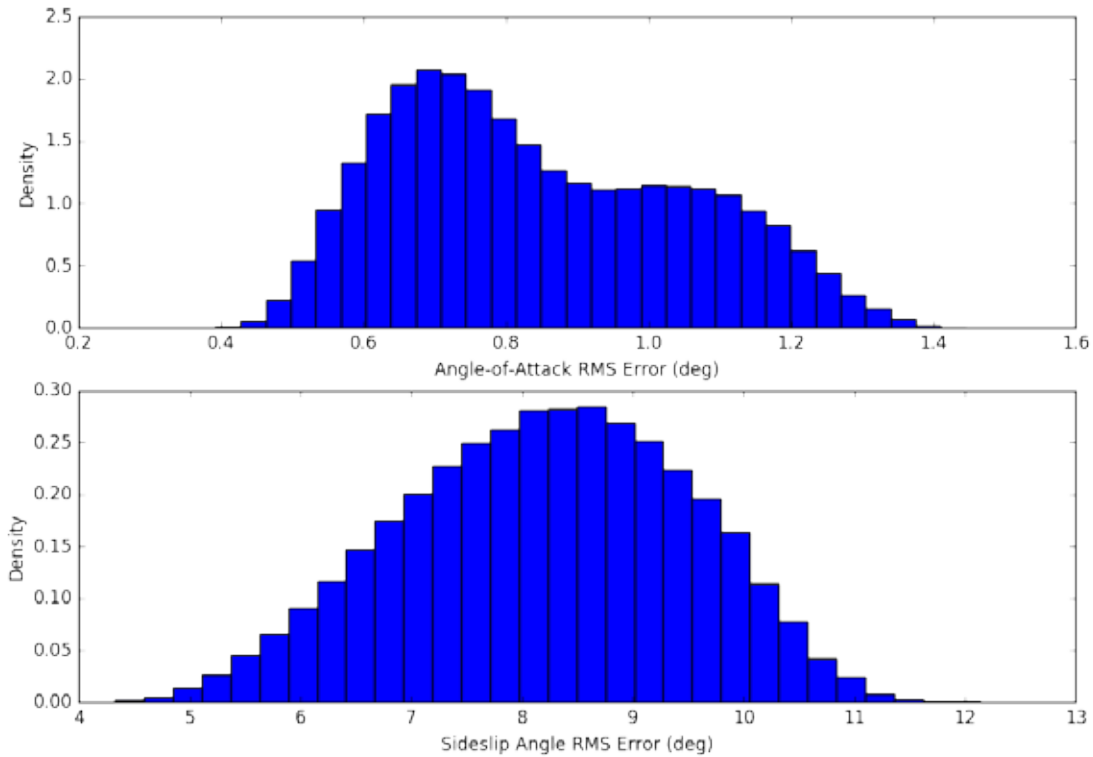
Figure C-12. RMS error histograms for Case 9

C.6.2 ANGLE-OF-ATTACK

For the derived AoA:

- 56.4450 % of runs violated the display tolerance.
- 43.5550 % of runs violated the envelope-protection tolerance.
- 0.0000 % of runs violated the AFPC tolerance.
- 0.0000 % of runs met all tolerances.

C.6.3 SIDESLIP ANGLE

For the derived sideslip angle:

- 100.0000 % of runs violated the display tolerance.
- 0.0000 % of runs violated the envelope-protection tolerance.
- 0.0000 % of runs violated the AFPC tolerance.
- 0.0000 % of runs met all tolerances.

C.7 CASE 10: UNCERTAIN S&C DERIVATIVES, LOW SENSOR NOISE, 10,000 RUNS

C.7.1 OVERVIEW

Case 10 consisted of randomized S&C derivatives simulating modeling errors, with added low-level sensor noise. Ten thousand iterations were run.
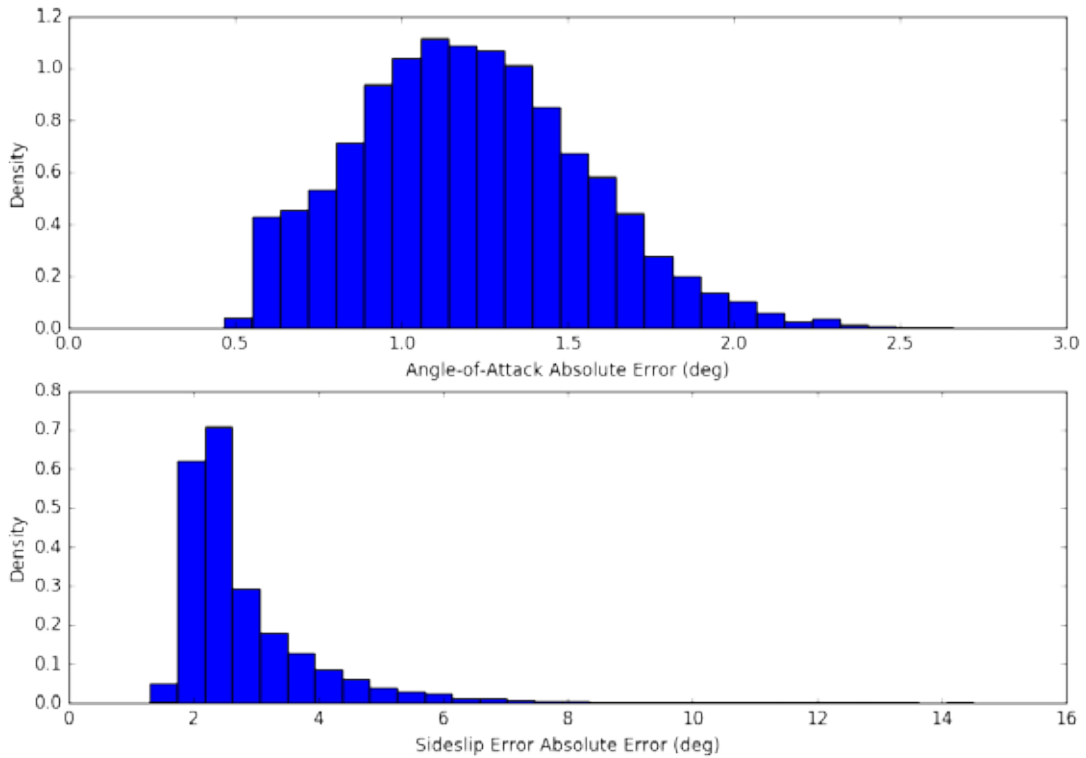
Figure C-13. Case 10 error histograms
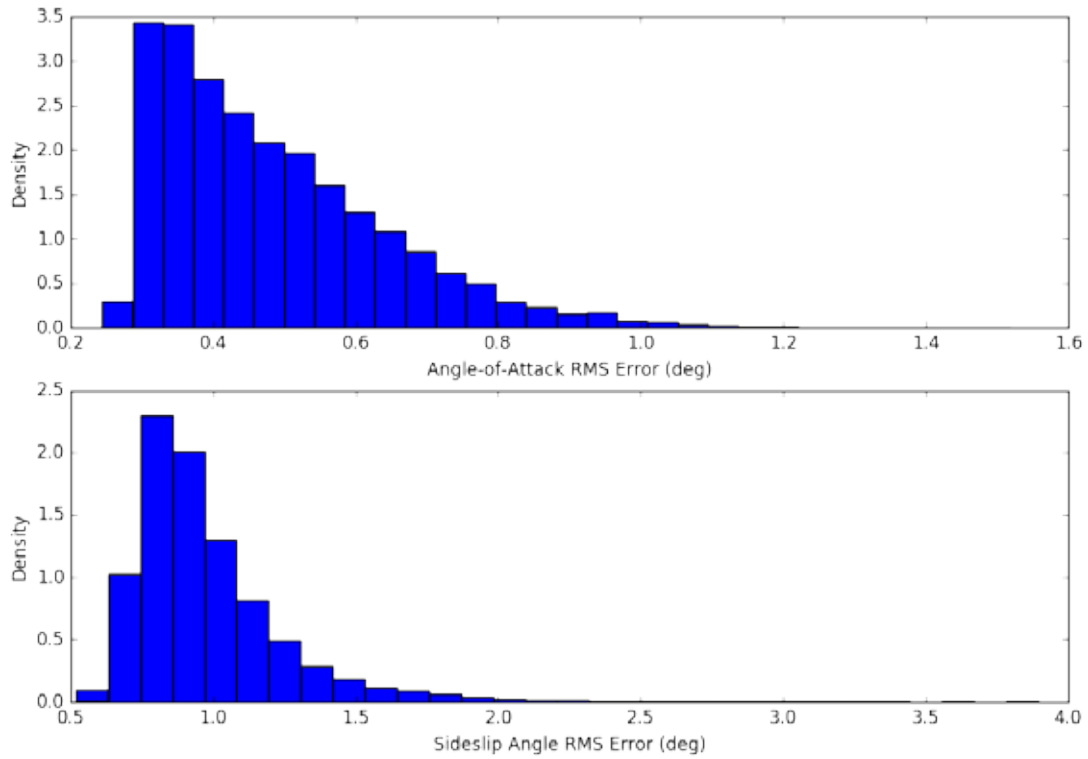
Figure C-14. Case 10 RMS error histograms

C.7.2 ANGLE-OF-ATTACK

For the derived AoA,

· 2.0500 % of runs violated the display tolerance.
· 69.1100 % of runs violated the envelope-protection tolerance.
· 28.8300 % of runs violated the AFPC tolerance.
· 0.0100 % of runs met all tolerances.
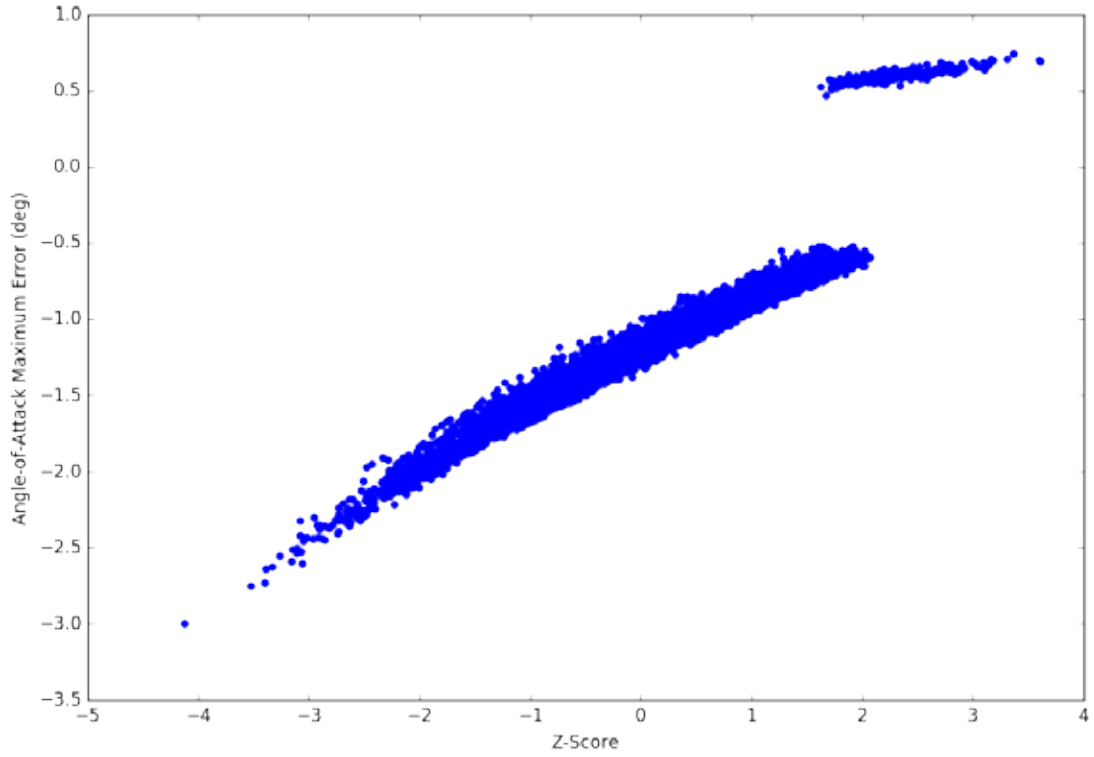
Figure C-15. C_{L_α} **scatter plot for Case 10**

Figure C-16. C_{L_α} **RMS error scatter plot for Case 10**

C-14
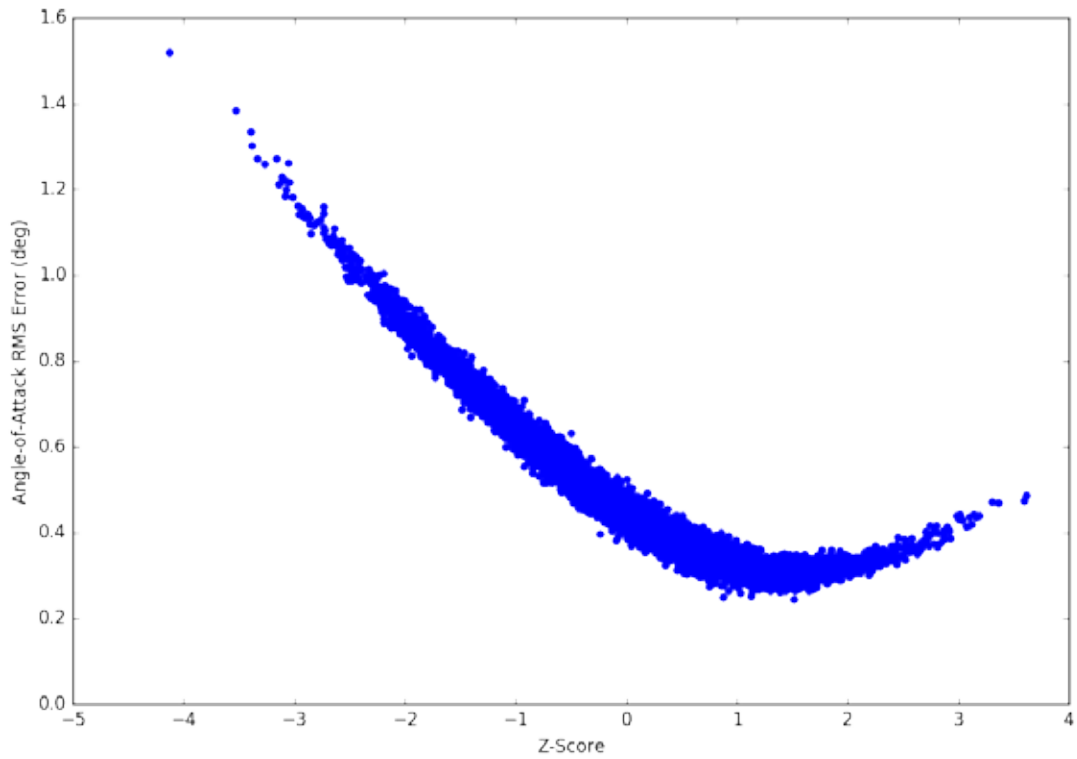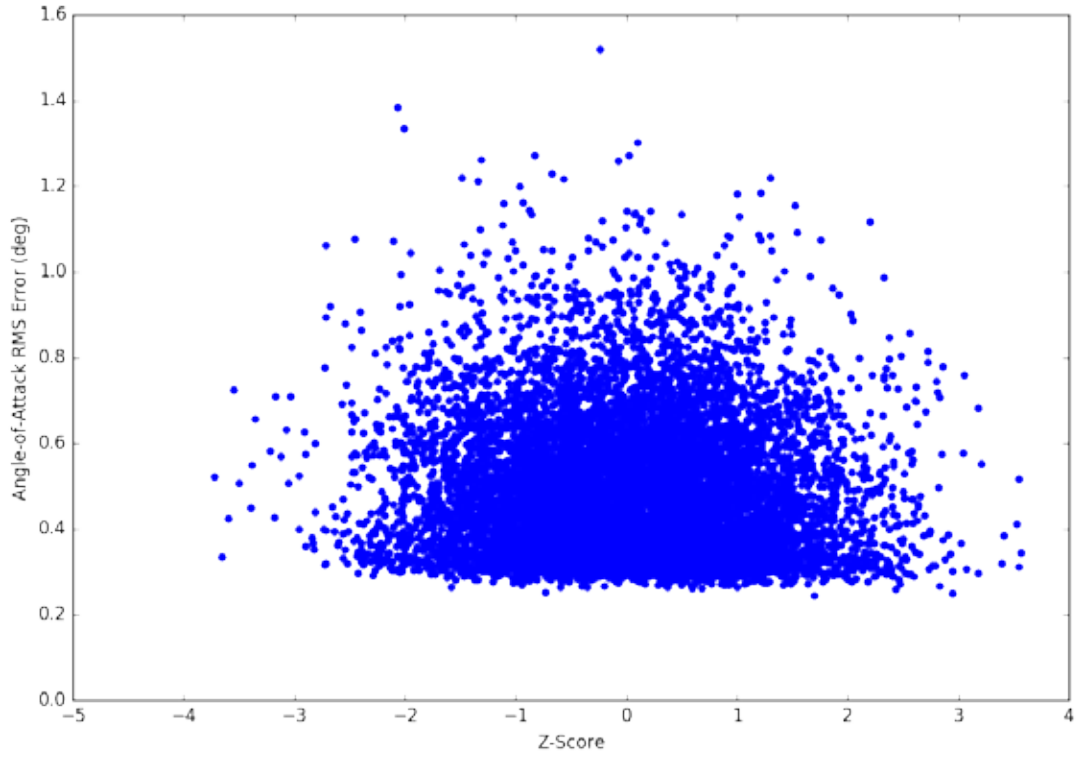
Figure C-17. C_{L_q} **RMS error scatter plot for Case 10**
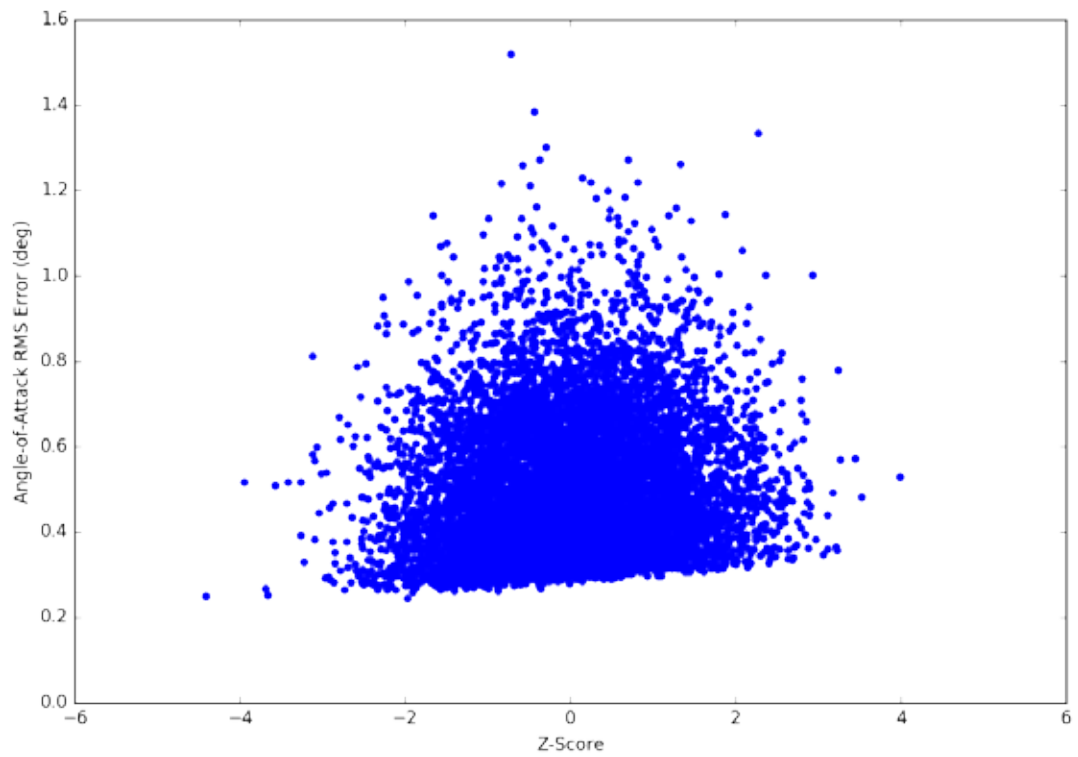
Figure C-18. $C_{L_{\delta_E}}$ **RMS error scatter plot for Case 10**

C-15

The simulated modeling error from the variation of S&C derivatives appears to dominate the low level of sensor noise based on the above figures.

C.7.3 SIDESLIP ANGLE

For the derived sideslip angle:

· 86.2900 % of runs violated the display tolerance.
· 13.7100 % of runs violated the envelope-protection tolerance.
· 0.0000 % of runs violated the AFPC tolerance.
· 0.0000 % of runs met all tolerances.
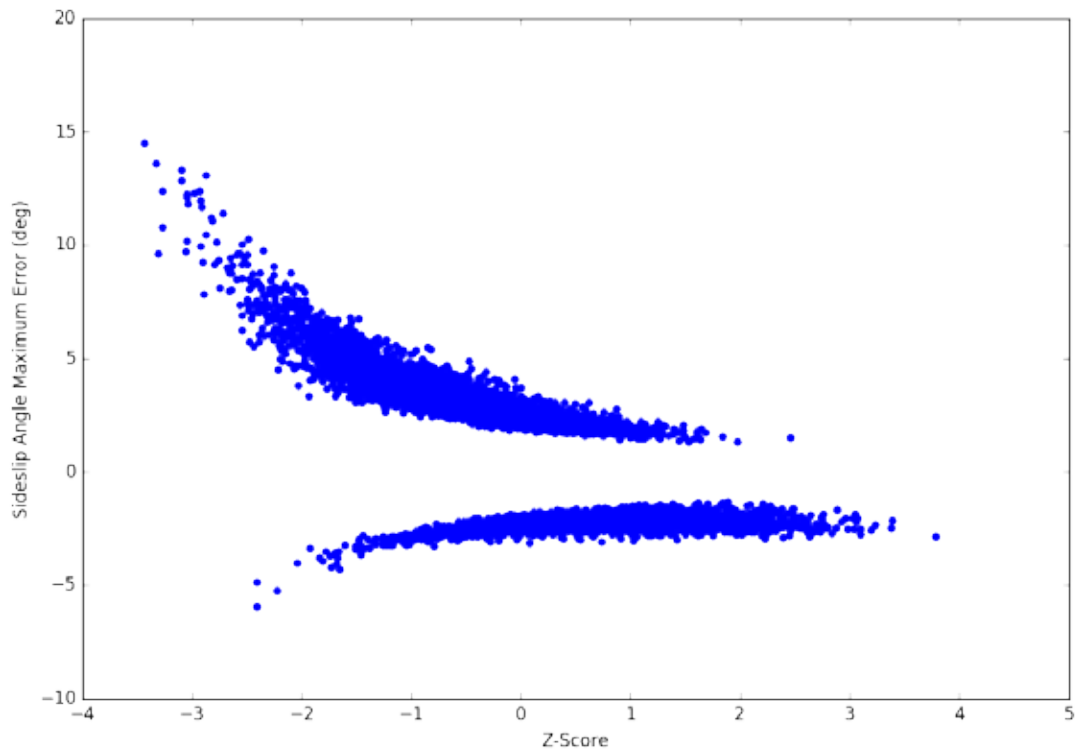
Figure C-19. C_{y_β} scatter plot for Case 10
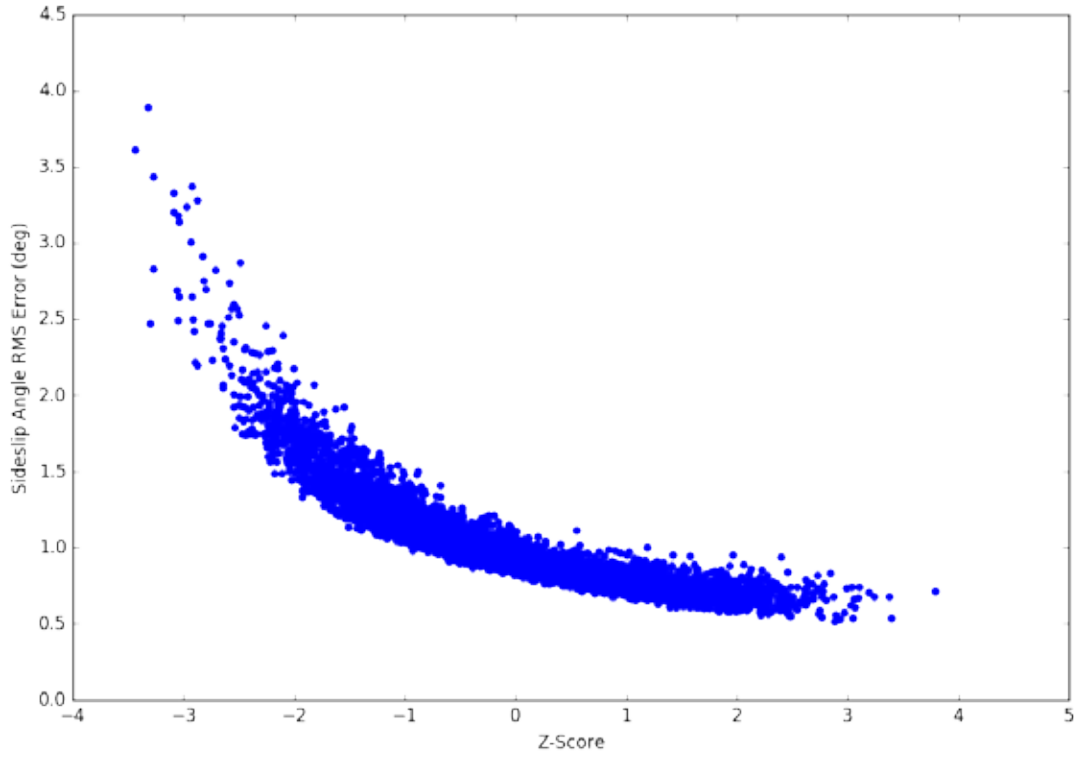
Figure C-20. C_{y_β} RMS error scatter plot for Case 10
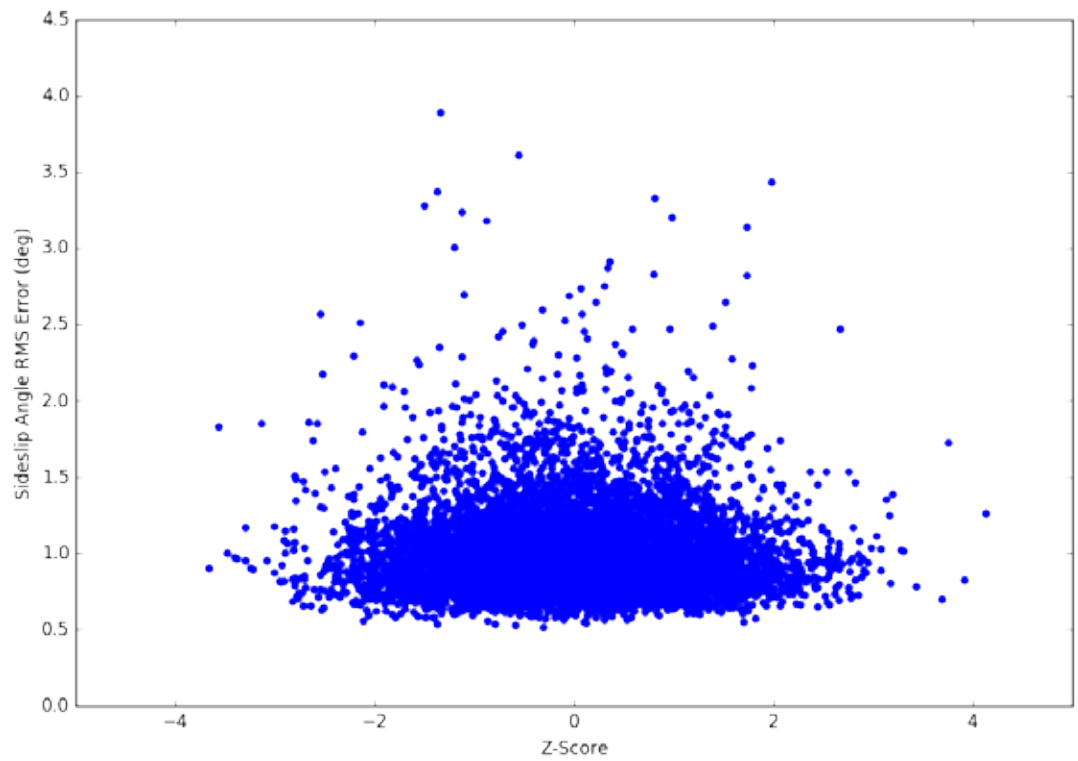
Figure C-21. C_{y_p} RMS error scatter plot for Case 10
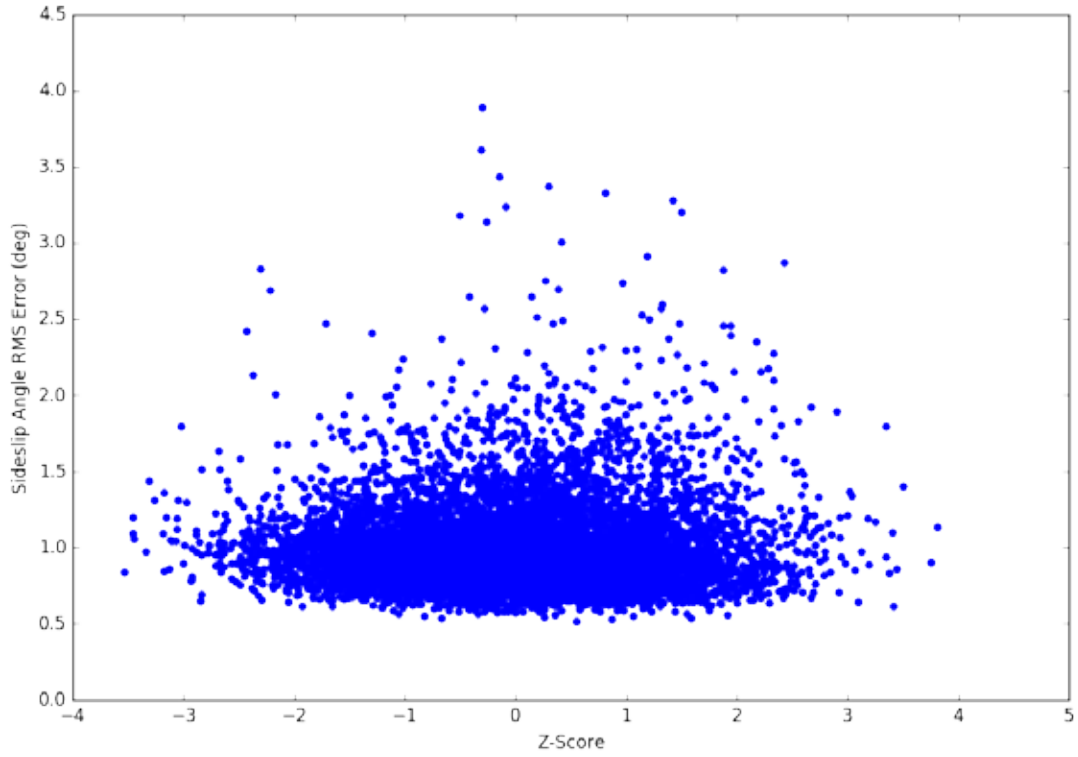
Figure C-22. C_{y_r} RMS error scatter plot for Case 10
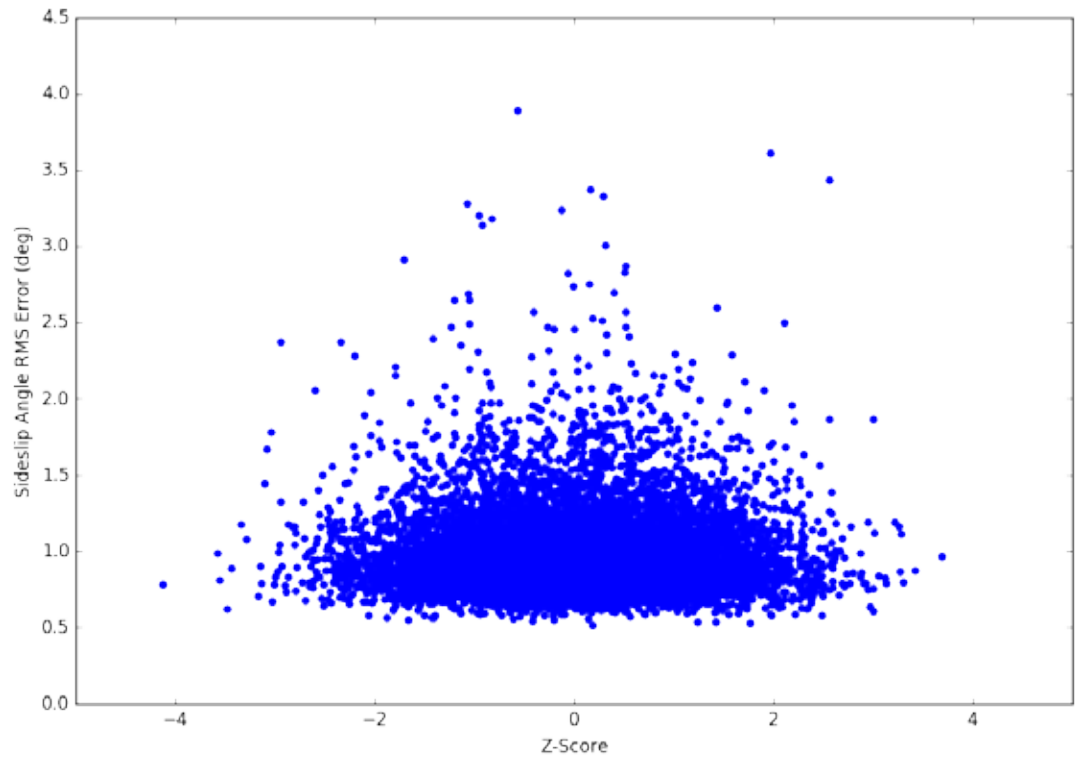
Figure C-23. $C_{y_{\delta_R}}$ RMS error scatter plot for Case 10

C.8 CASE 11: UNCERTAIN S&C DERIVATIVES, MEDIUM SENSOR NOISE, 10,000 RUNS

C.8.1 OVERVIEW

Case 11 consisted of randomized S&C derivatives simulating modeling errors, with added medium-level sensor noise. Again, 10,000 iterations were run.
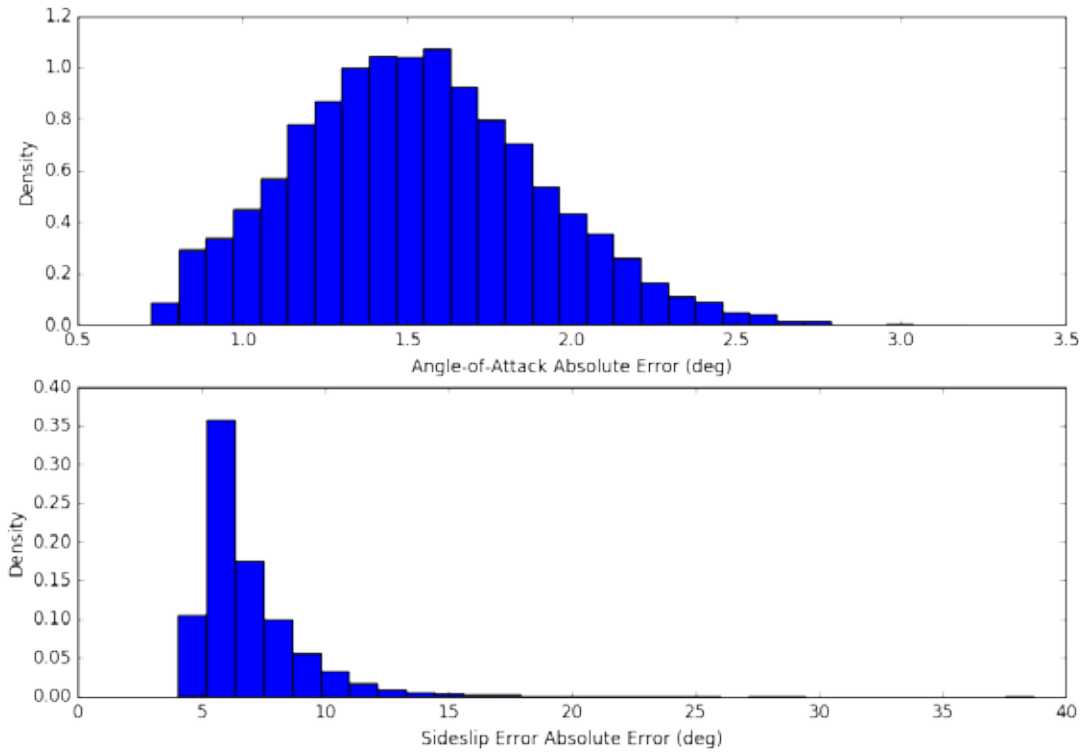
Figure C-24. Case 11 error histograms
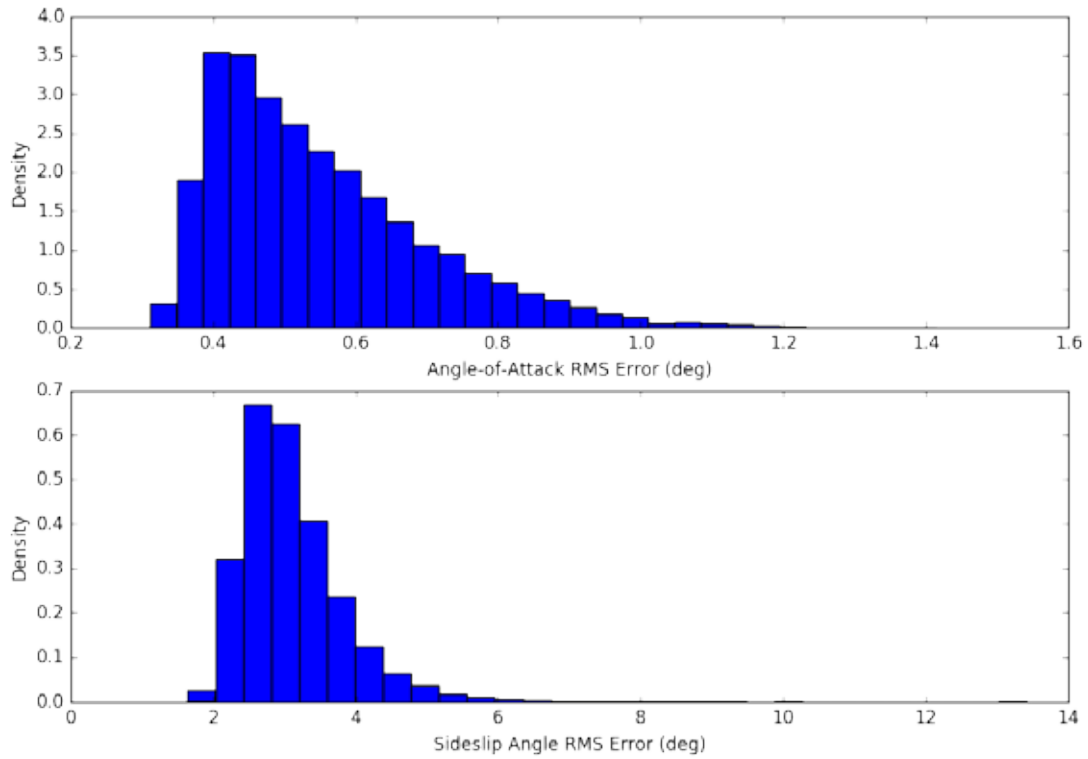
Figure C-25. Case 11 error histograms

C.8.2 ANGLE-OF-ATTACK

For the derived AoA:

·   11.3000 % of runs violated the display tolerance.
·   81.4700 % of runs violated the envelope-protection tolerance.
·   7.2300 % of runs violated the AFPC tolerance.
·   0.0000 % of runs met all tolerances.
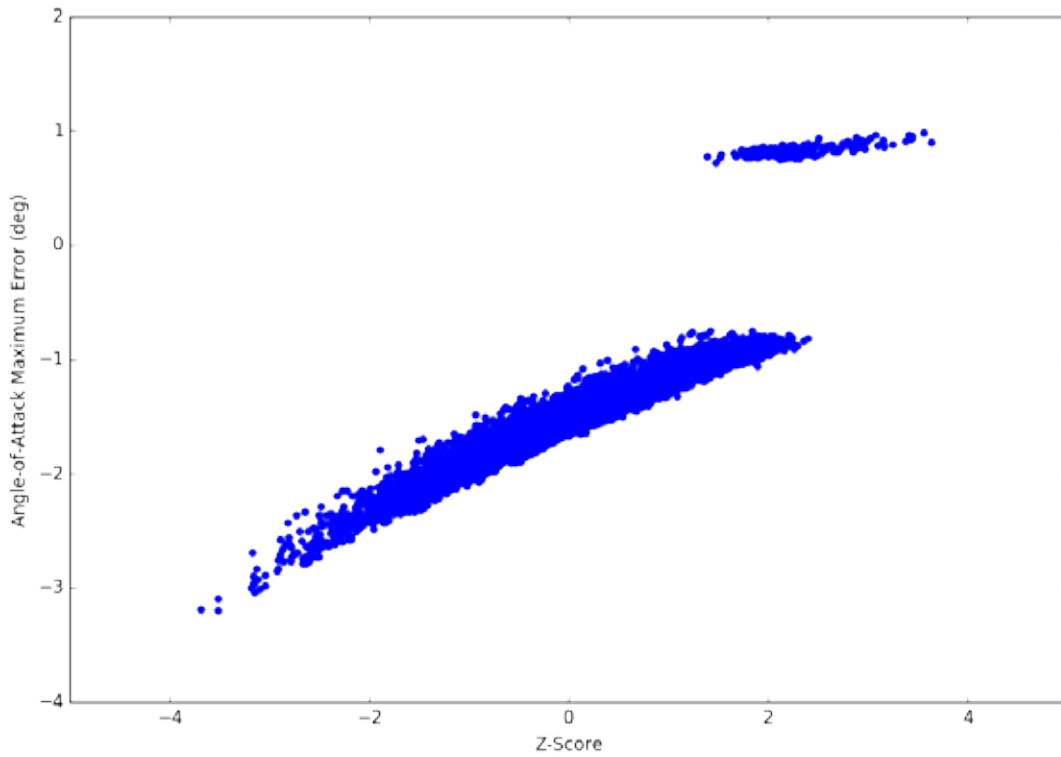
Figure C-26. C_{L_α} **scatter plot for Case 11**
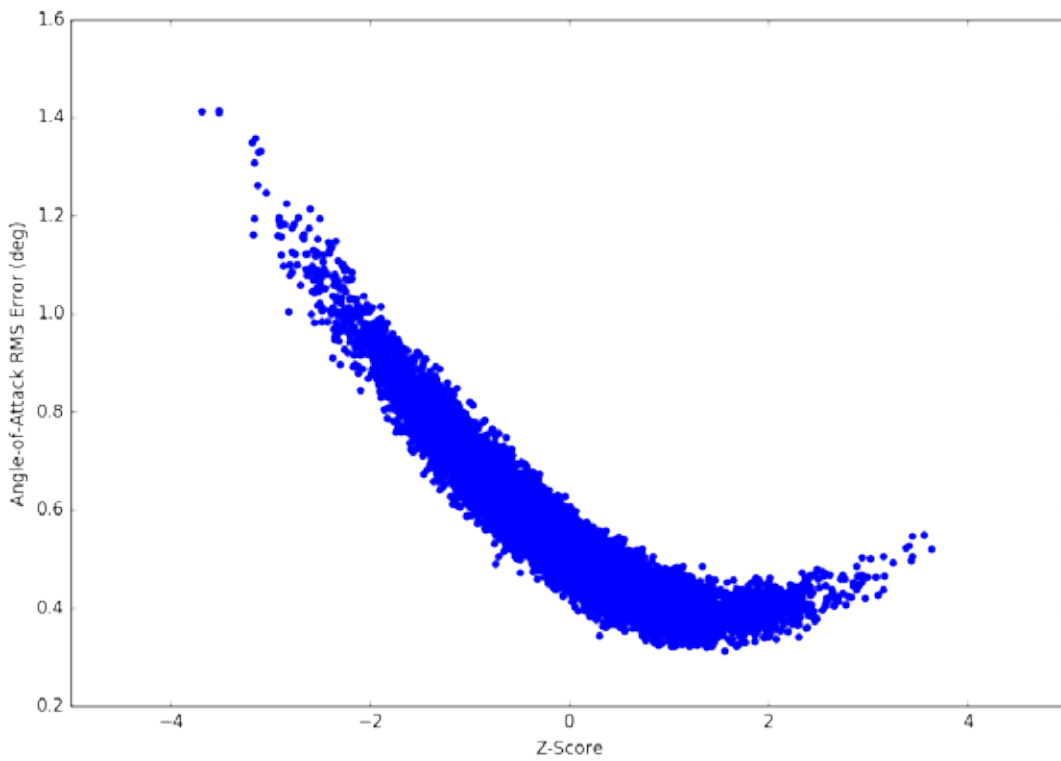
Figure C-27. C_{L_α} **RMS error scatter plot for Case 11**
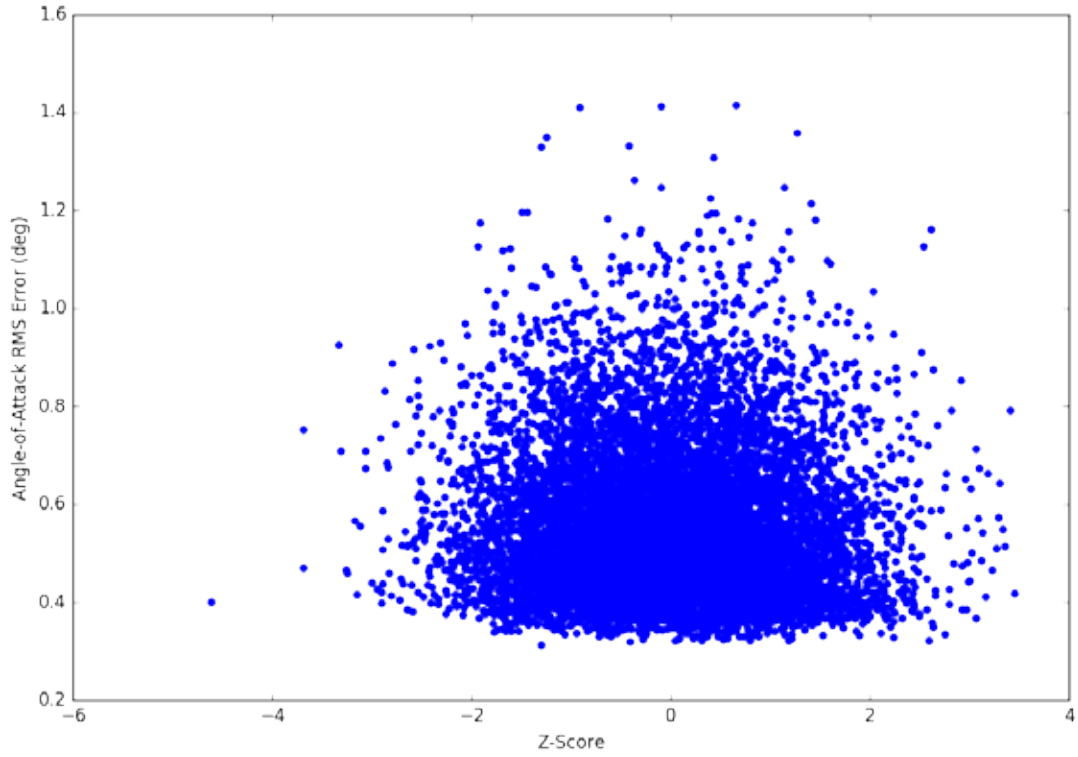
Figure C-28. C_{L_q} **RMS error scatter plot for Case 11**
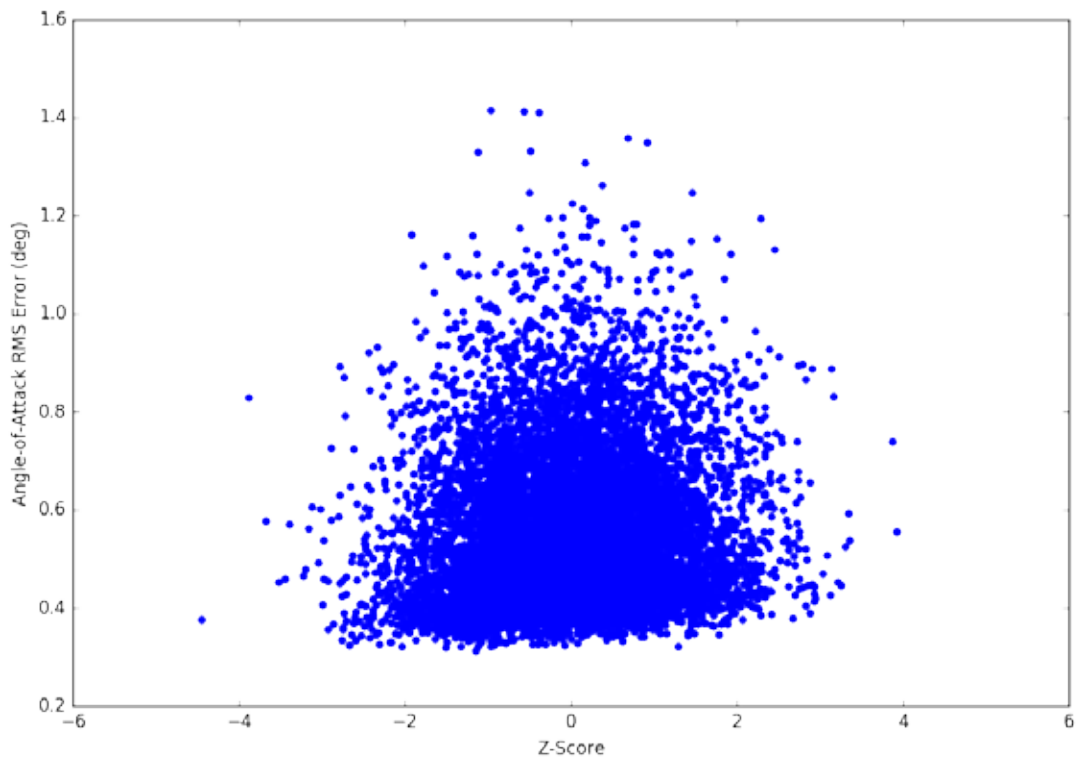
Figure C-29. $C_{L_{\delta_E}}$ **RMS error scatter plot for Case 11**

C.8.3 SIDESLIP ANGLE

For the derived sideslip angle:

- 100.0000 % of runs violated the display tolerance.
- 0.0000 % of runs violated the envelope-protection tolerance.
- 0.0000 % of runs violated the AFPC tolerance.
- 0.0000 % of runs met all tolerances.
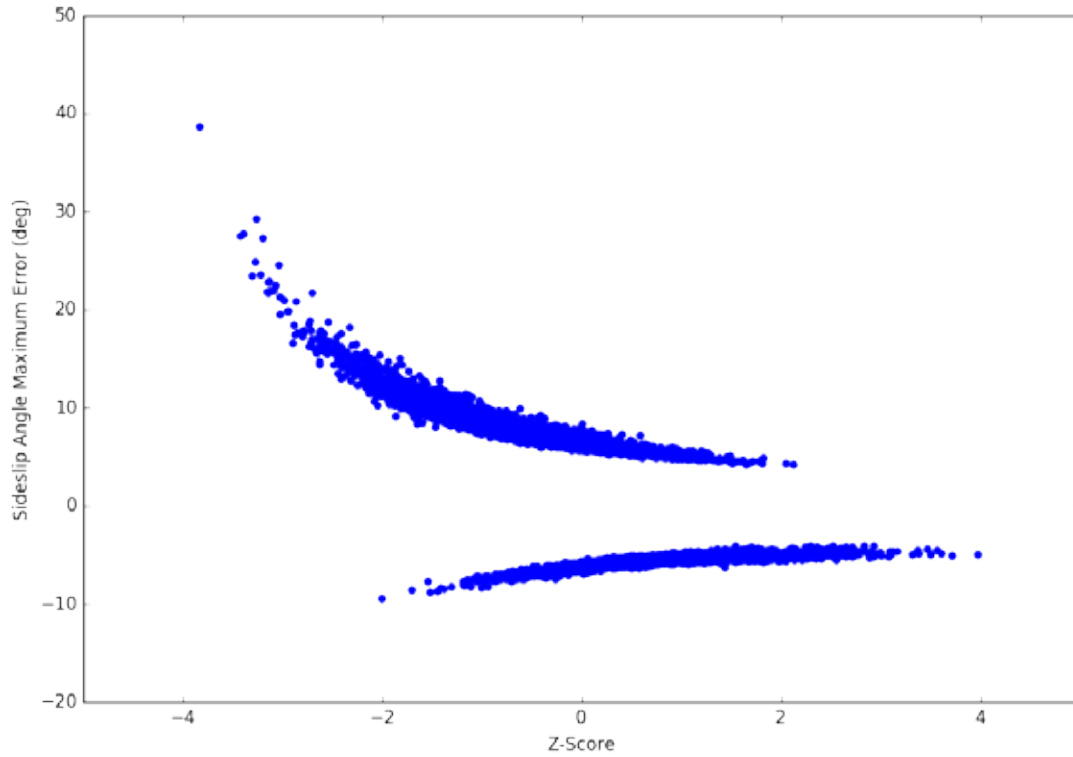
Figure C-30. C_{y_β} scatter plot for Case 11
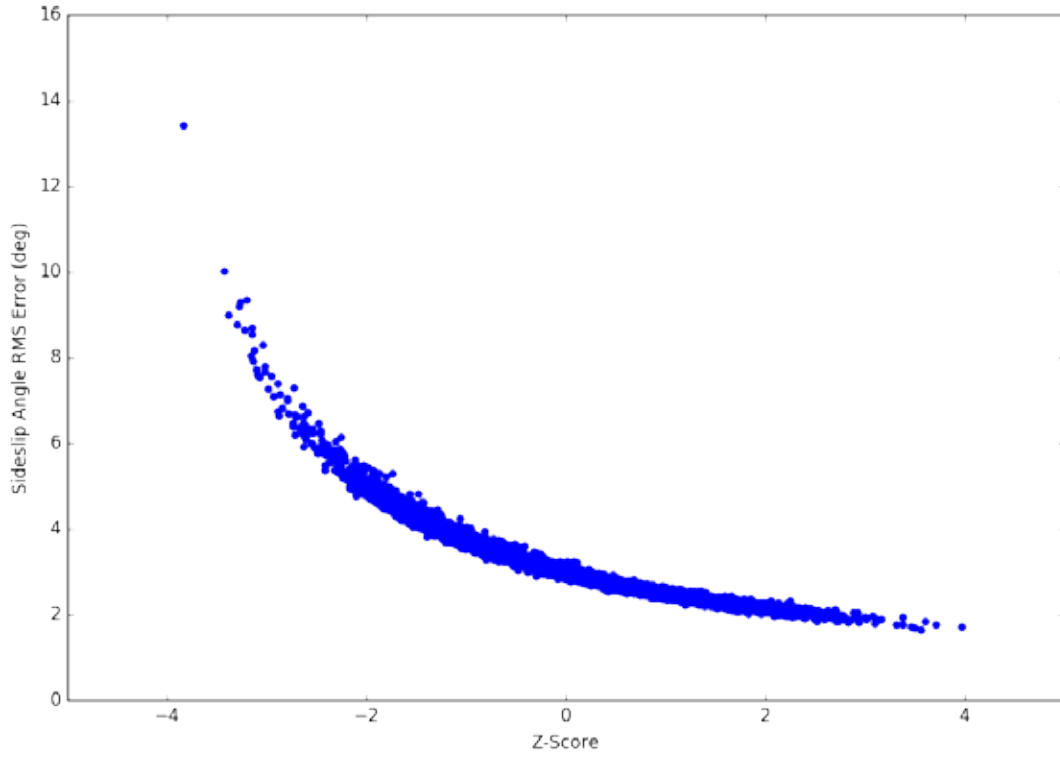
Figure C-31. C_{y_β} **RMS error scatter plot for Case 11**
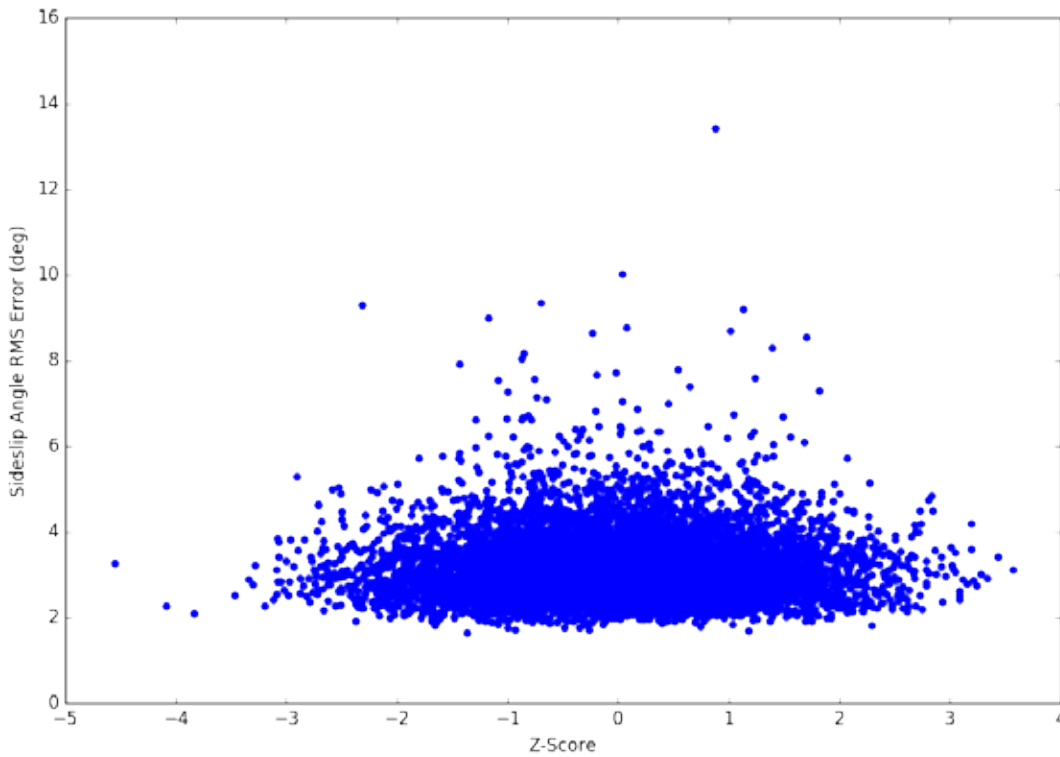
Figure C-32. C_{y_p} **RMS error scatter plot for Case 11**
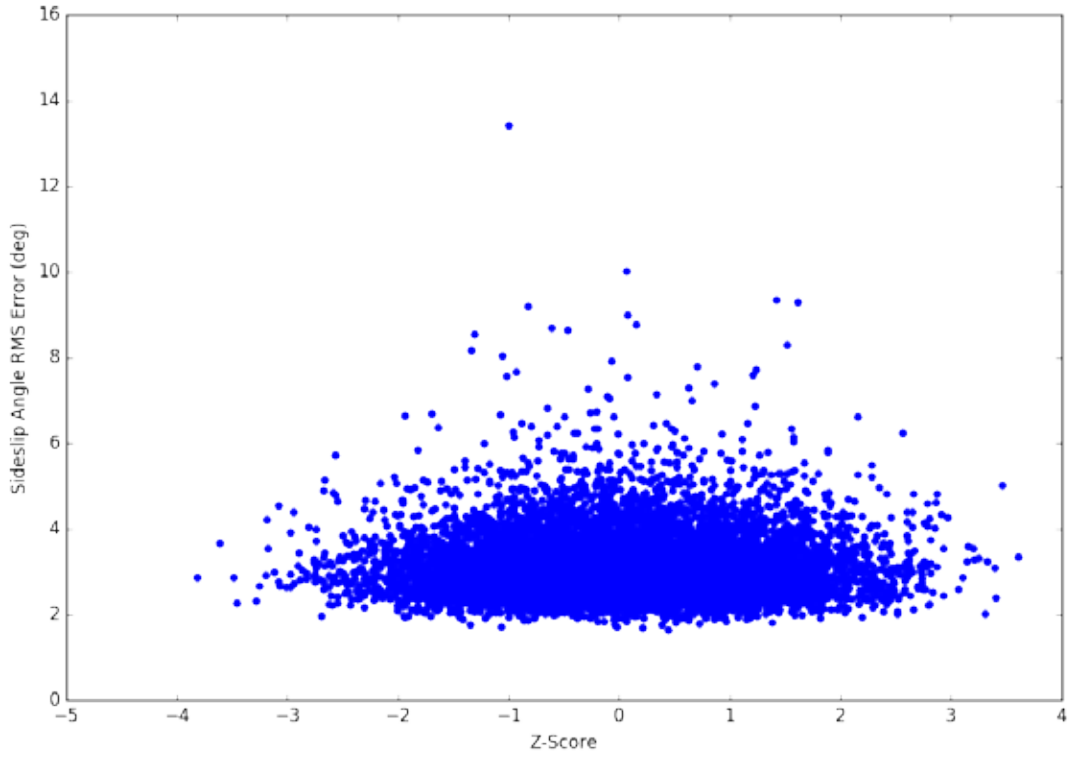
Figure C-33. C_{y_r} **RMS error scatter plot for Case 11**
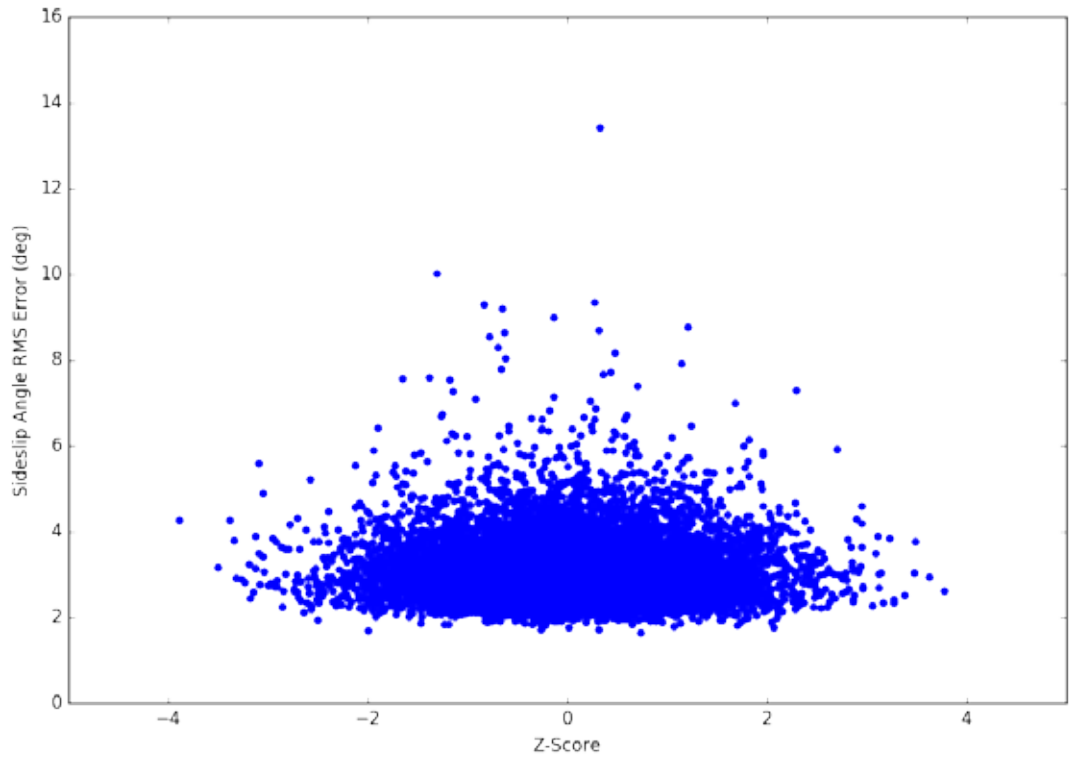
Figure C-34. $C_{y_{\delta_R}}$ **RMS error scatter plot for Case 11**

C-25

C.9 CASE 12: UNCERTAIN S&C DERIVATIVES, HIGH SENSOR NOISE, 10,000 RUNS

C.9.1 OVERVIEW

Case 12 consisted of randomized S&C derivatives simulating modeling errors, with added high-level sensor noise. Again, 10,000 iterations were run.
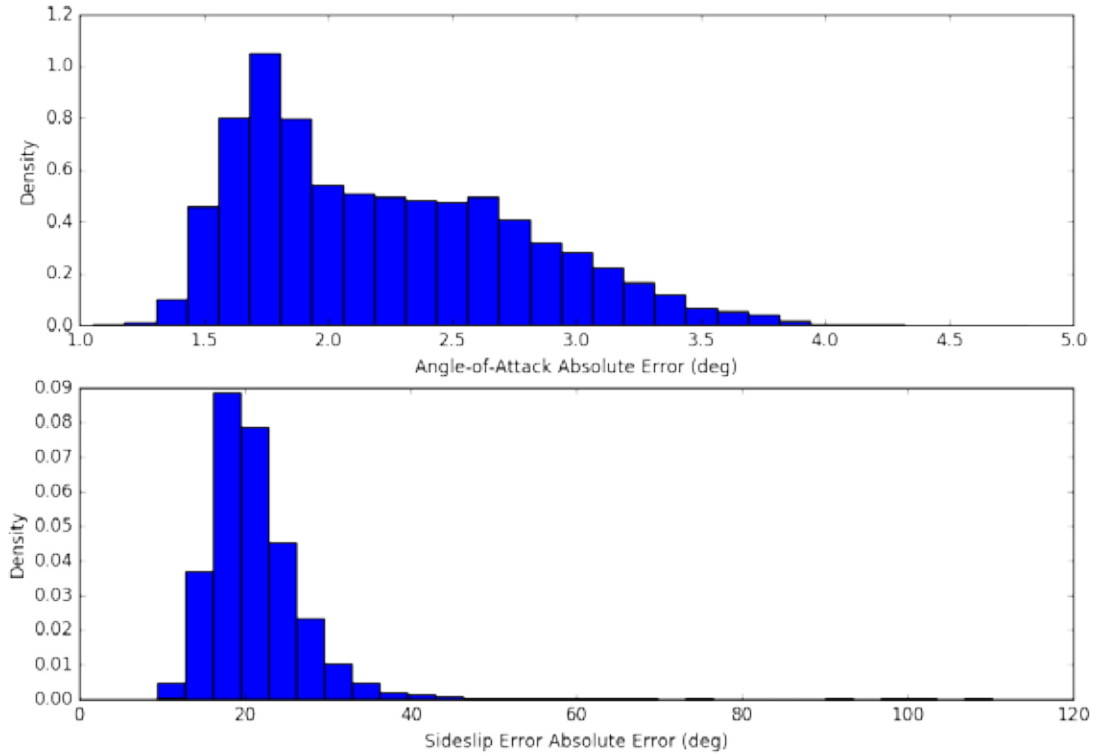
Figure C-35. Case 12 error histograms
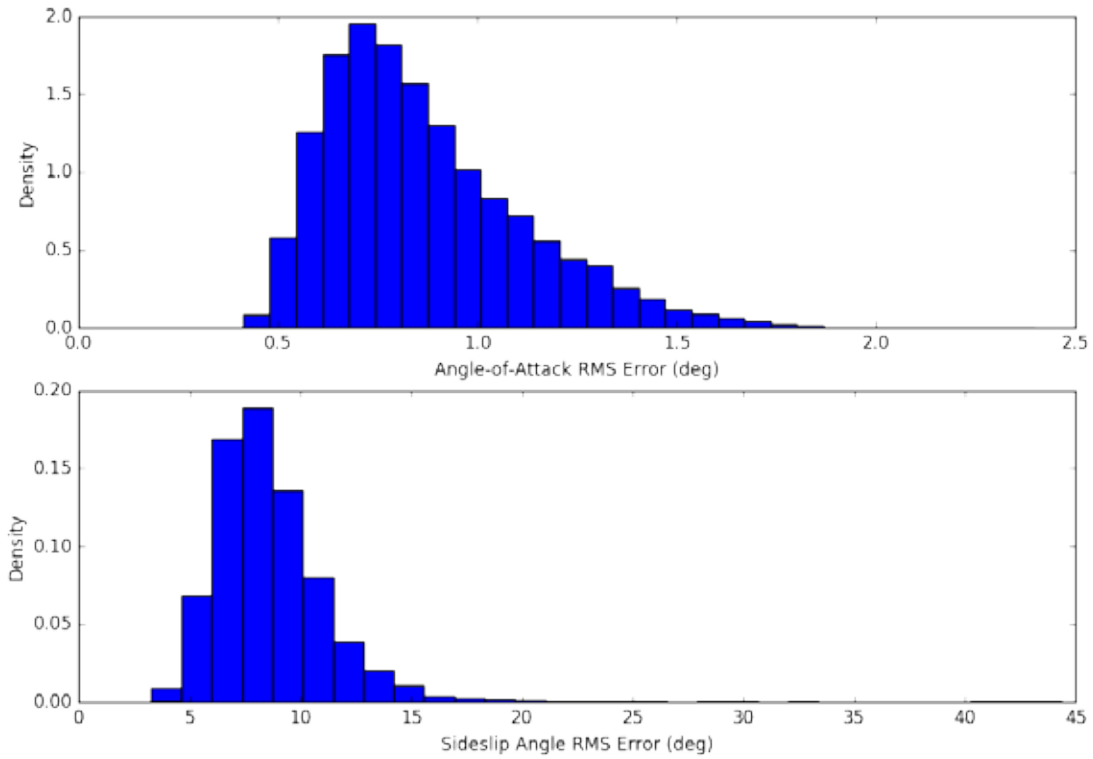
Figure C-36. Case 12 RMS error histograms

C.9.2 ANGLE-OF-ATTACK

For the derived AoA:

- 55.5200 % of runs violated the display tolerance.
- 44.4800 % of runs violated the envelope-protection tolerance.
- 0.0000 % of runs violated the AFPC tolerance.
- 0.0000 % of runs met all tolerances.

Observing figures 81–82, the effect of the sensor noise dominates the modeling errors.
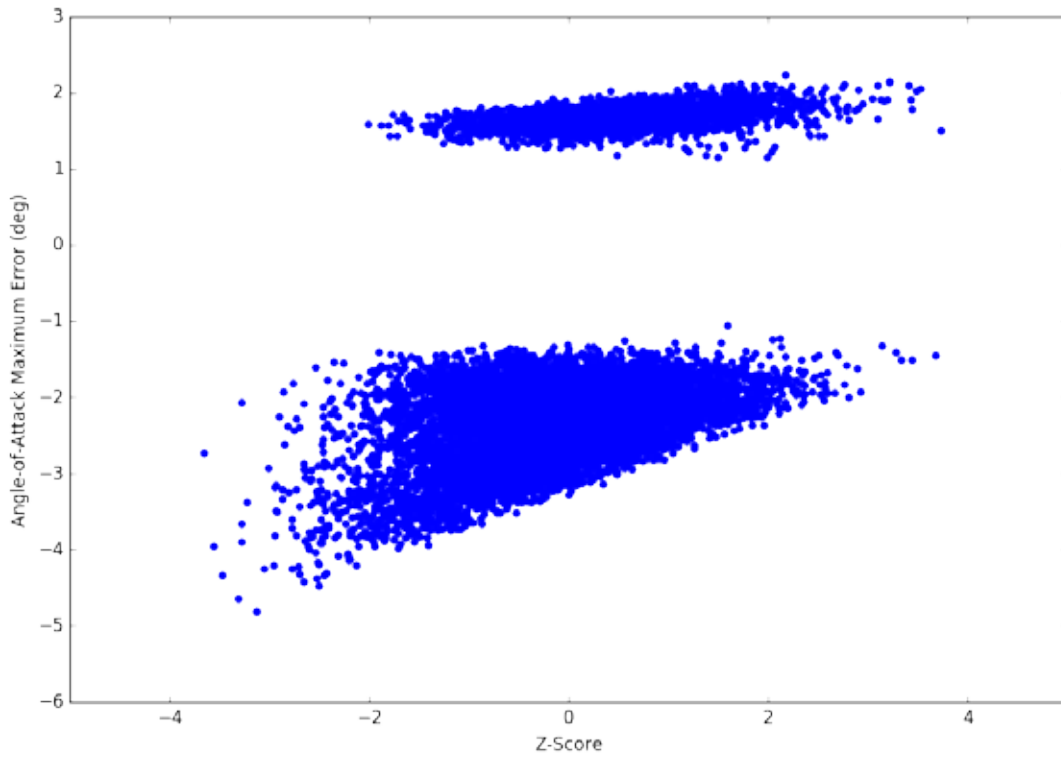
Figure C-37. C_{L_α} **scatter plot for Case 12**

Figure C-38. C_{L_α} **RMS error scatter plot for Case 12**

C-28
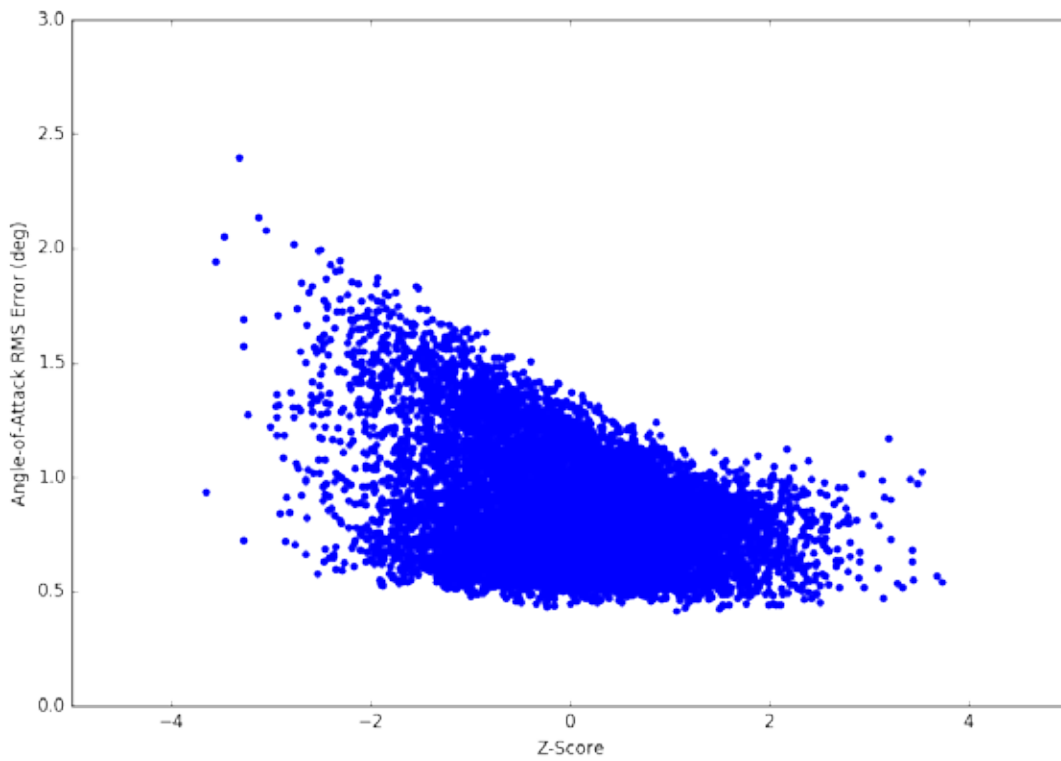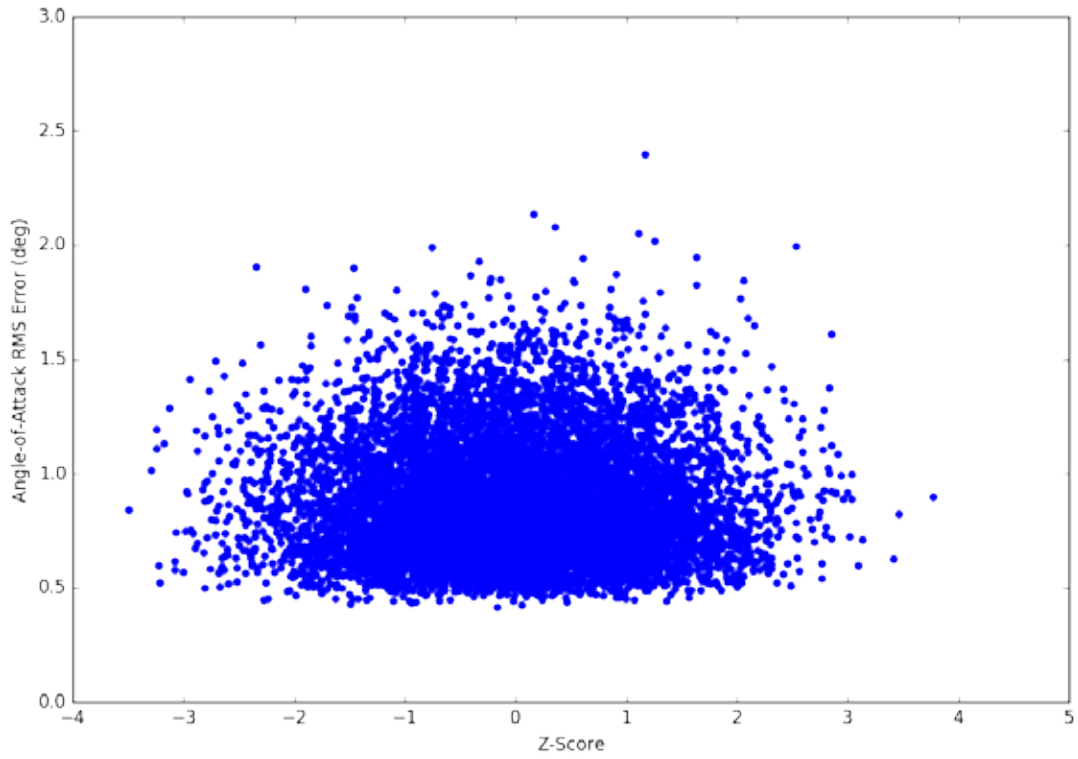
Figure C-39. C_{L_q} **RMS error scatter plot for Case 12**
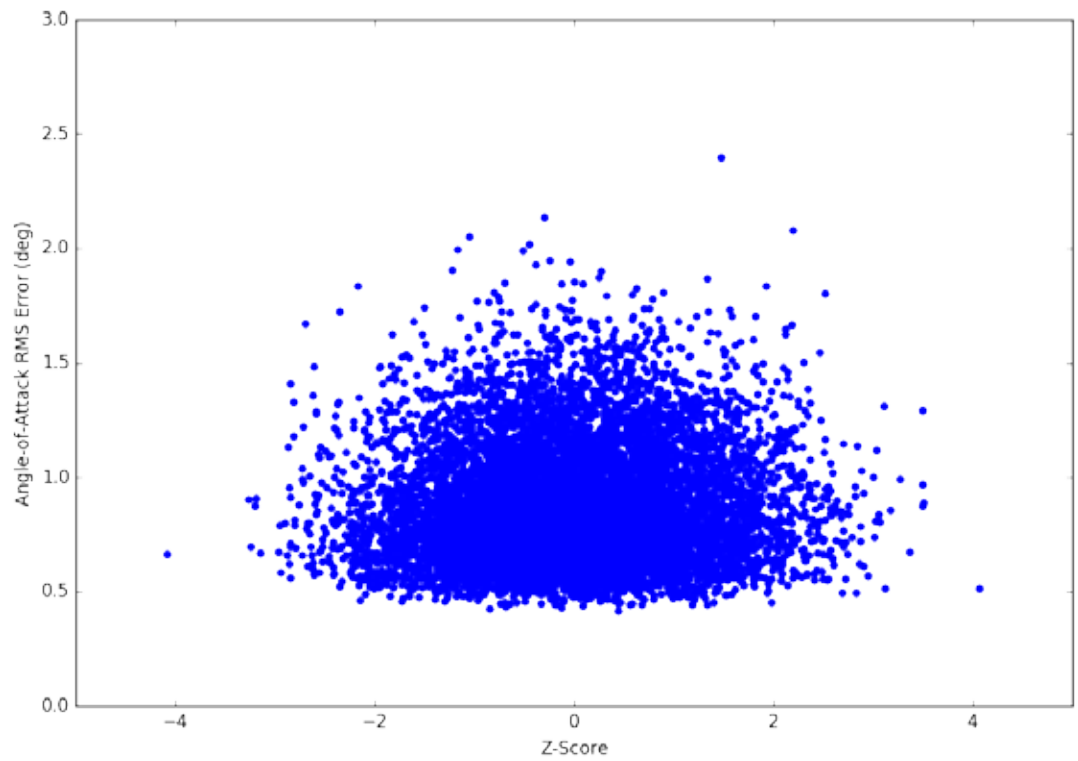
Figure C-40. $C_{L_{\delta_E}}$ **RMS error scatter plot for Case 12**

C.9.3 SIDESLIP ANGLE

For the derived sideslip angle:

-         100.0000 % of runs violated the display tolerance.
-         0.0000 % of runs violated the envelope-protection tolerance.
-         0.0000 % of runs violated the AFPC tolerance.
-         0.0000 % of runs met all tolerances.
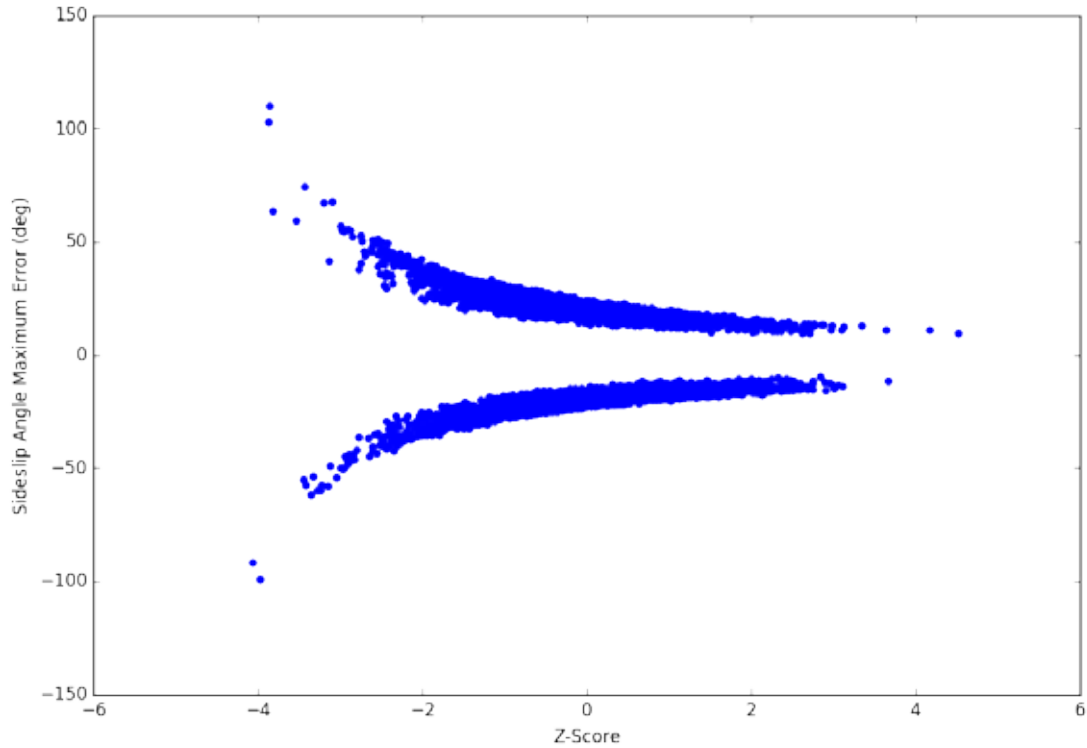
Figure C-41. C_{y_β} scatter plot for Case 12
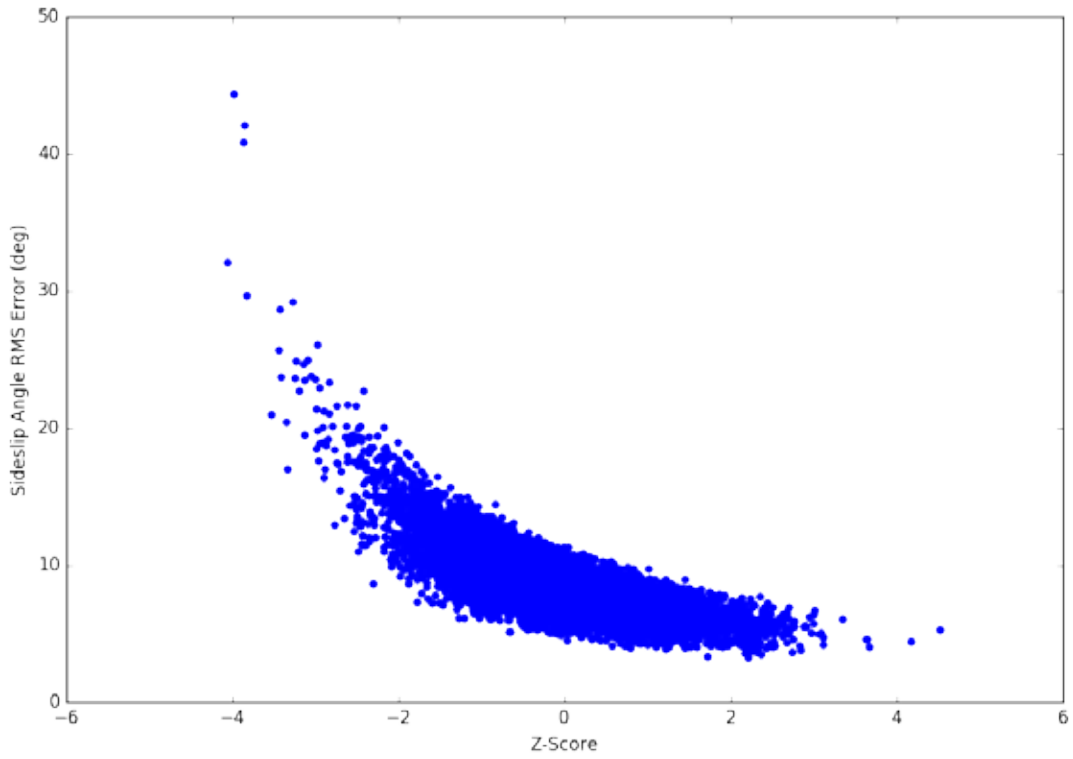
Figure C-42. C_{y_β} RMS error scatter plot for Case 12
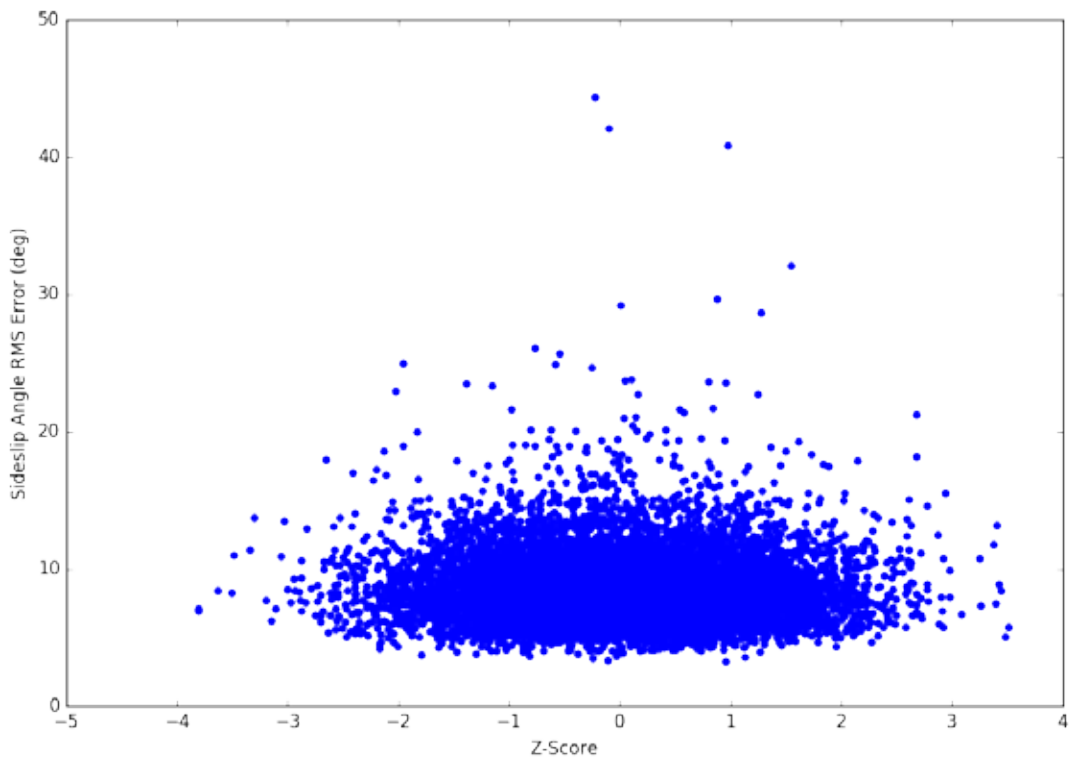
Figure C-43. C_{y_p} RMS error scatter plot for Case 12
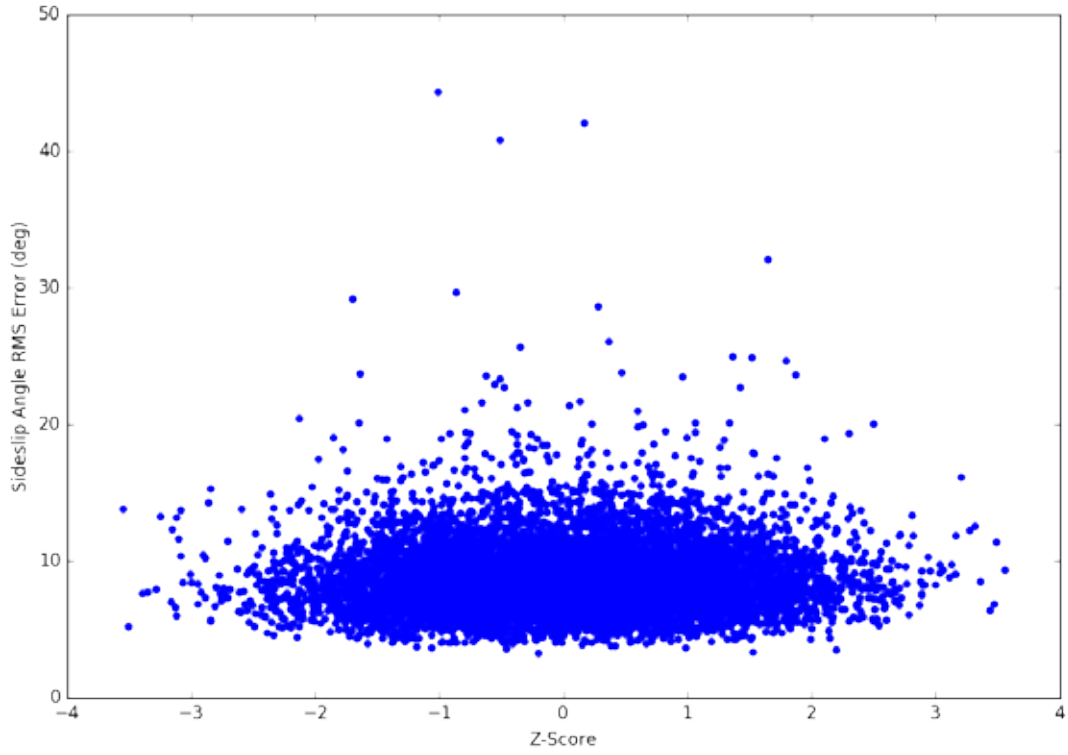
Figure C-44. C_{y_r} **RMS error scatter plot for Case 12**
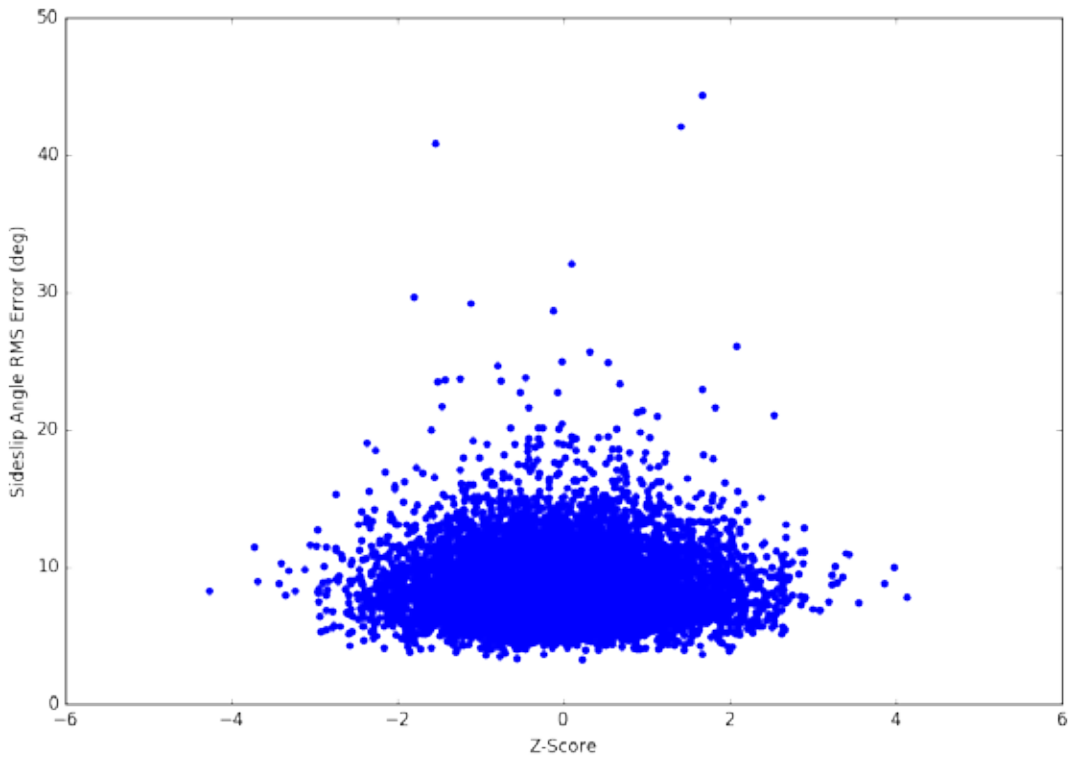
Figure C-45. $C_{y_{\delta_R}}$ **RMS error scatter plot for Case 12**

C.10 CASE 13: UNCERTAIN S&C DERIVATIVES, DOUBLET INPUTS, 10,000 RUNS

C.10.1 OVERVIEW

Case 13 consisted of randomized S&C derivatives simulating modeling errors with doublet inputs for each control. Again, 10,000 iterations were run.
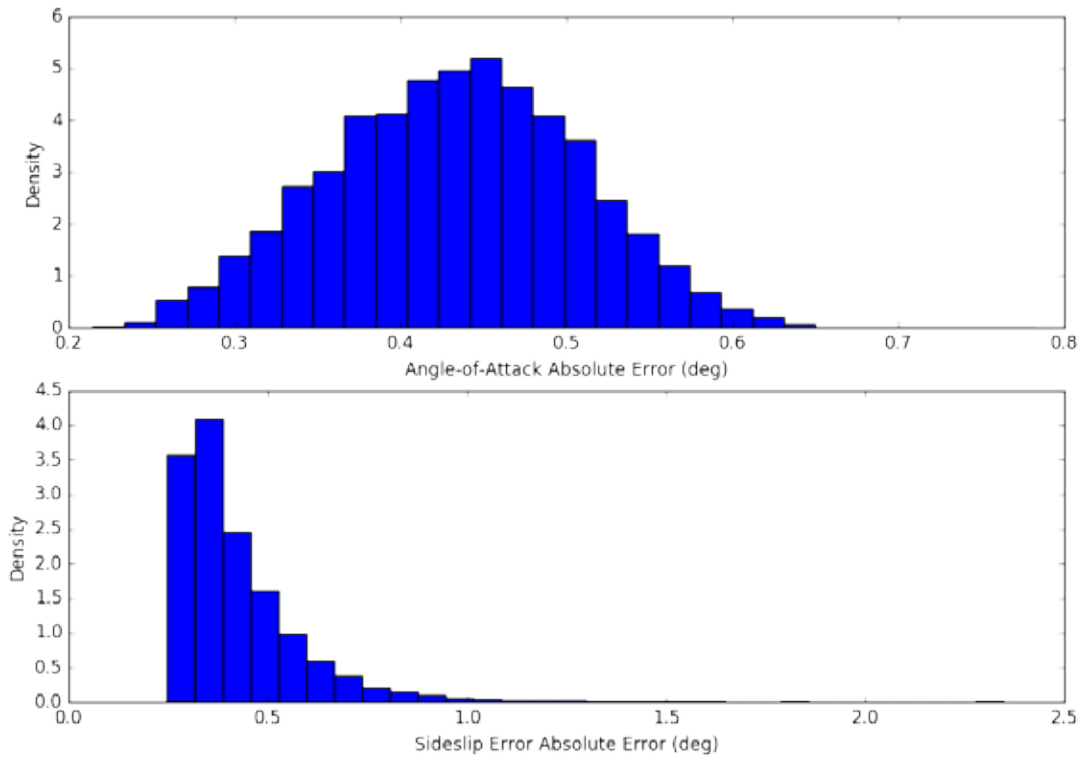
Figure C-46. Case 13 absolute error histograms
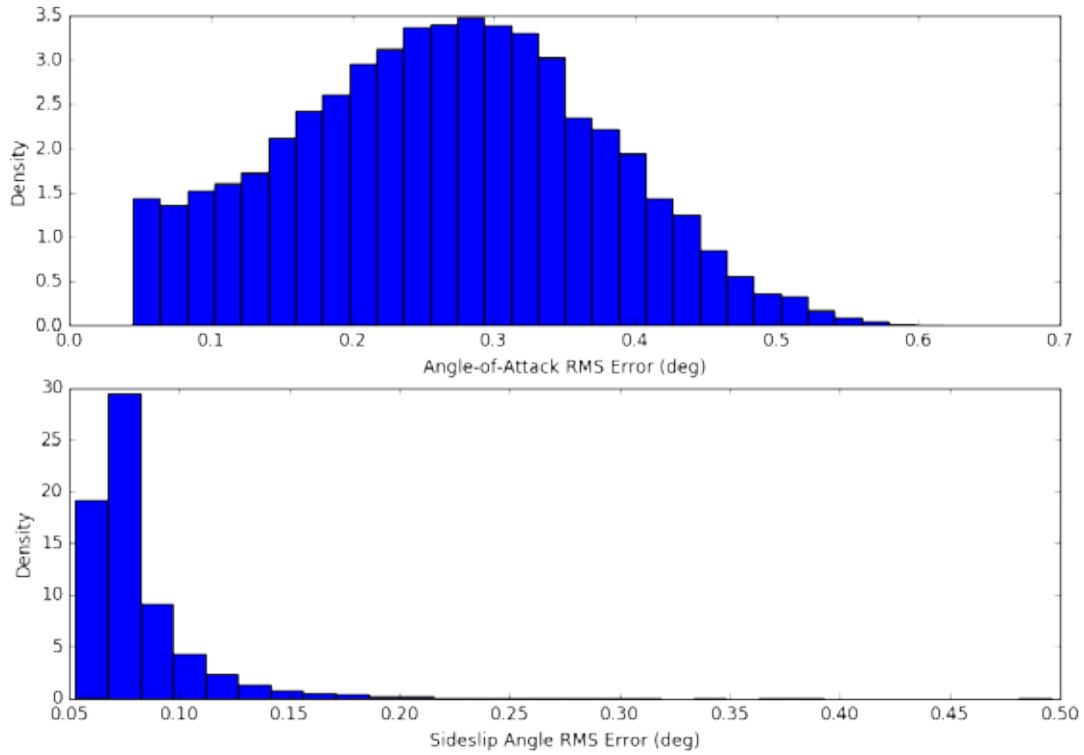
Figure C-47. Case 13 RMS error histograms

C.10.2 ANGLE-OF-ATTACK

For the derived AoA:

- 0.0000 % of runs violated the display tolerance.
- 0.0000 % of runs violated the envelope-protection tolerance.
- 19.3600 % of runs violated the AFPC tolerance.
- 80.6400 % of runs met all tolerances.
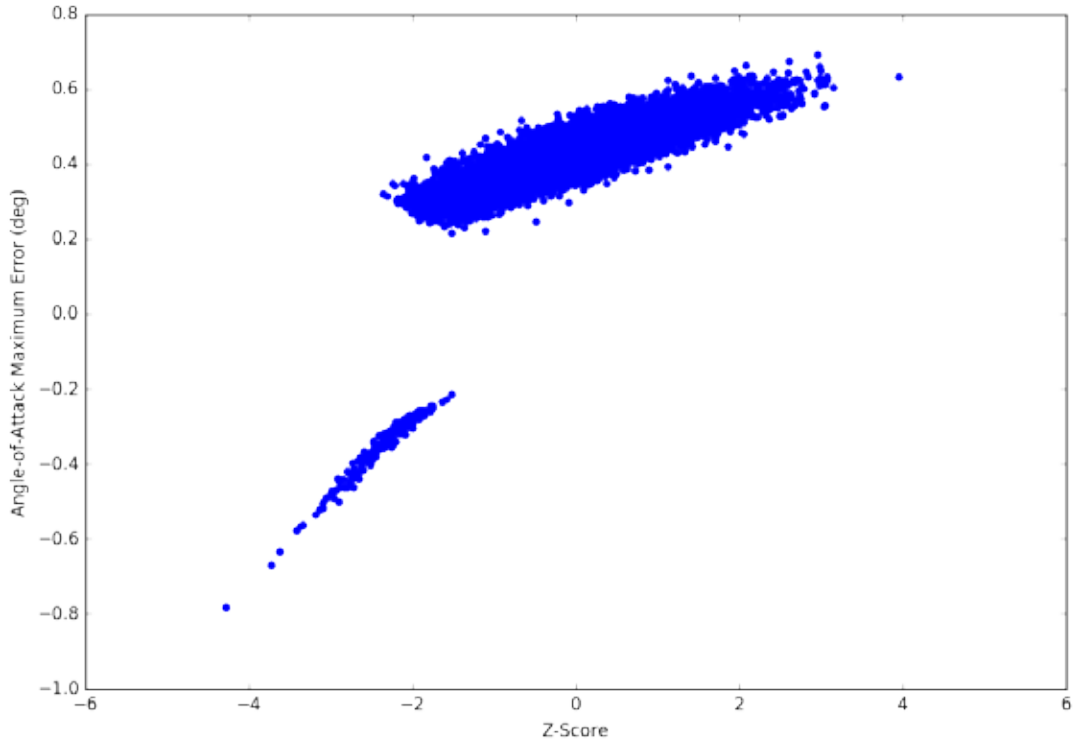
Figure C-48. C_{L_α} **scatter plot for Case 13**
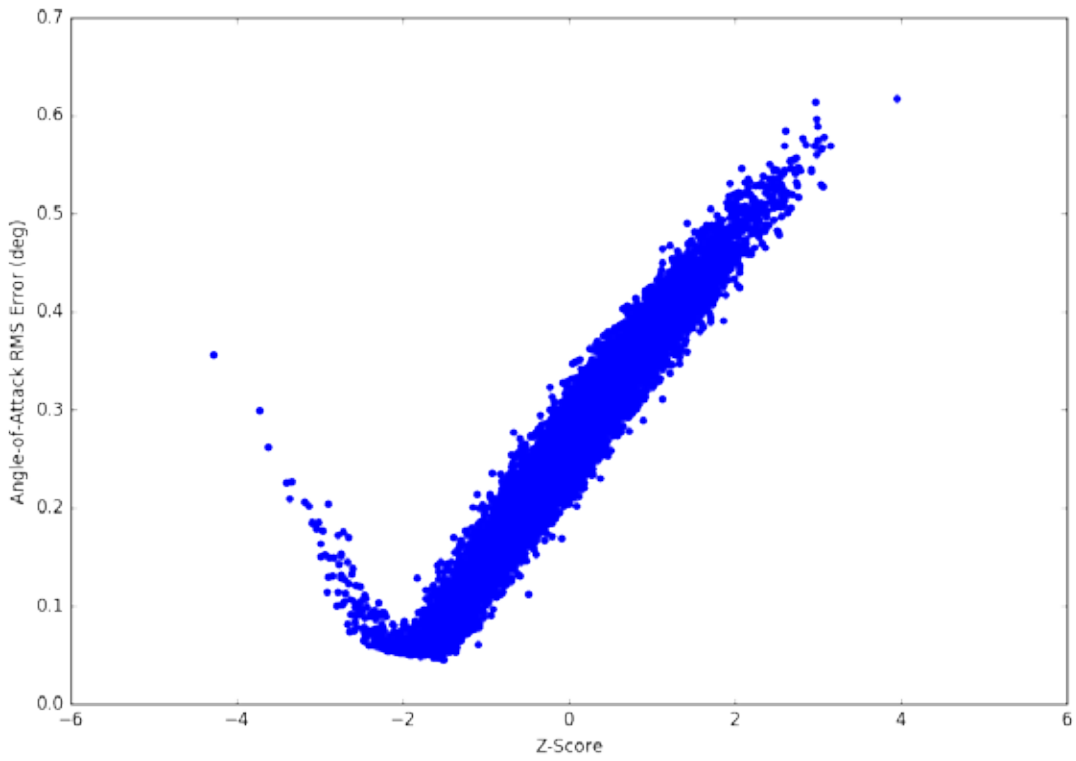
Figure C-49. C_{L_α} **RMS error scatter plot for Case 13**
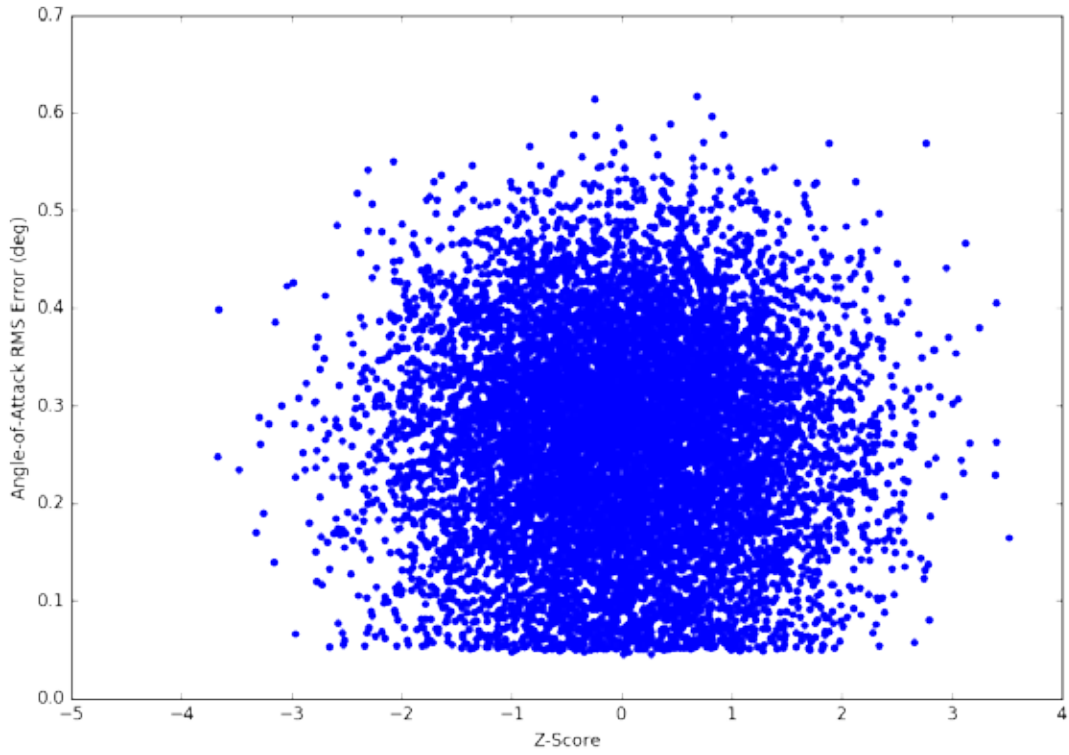
Figure C-50. C_{L_q} **RMS error scatter plot for Case 13**
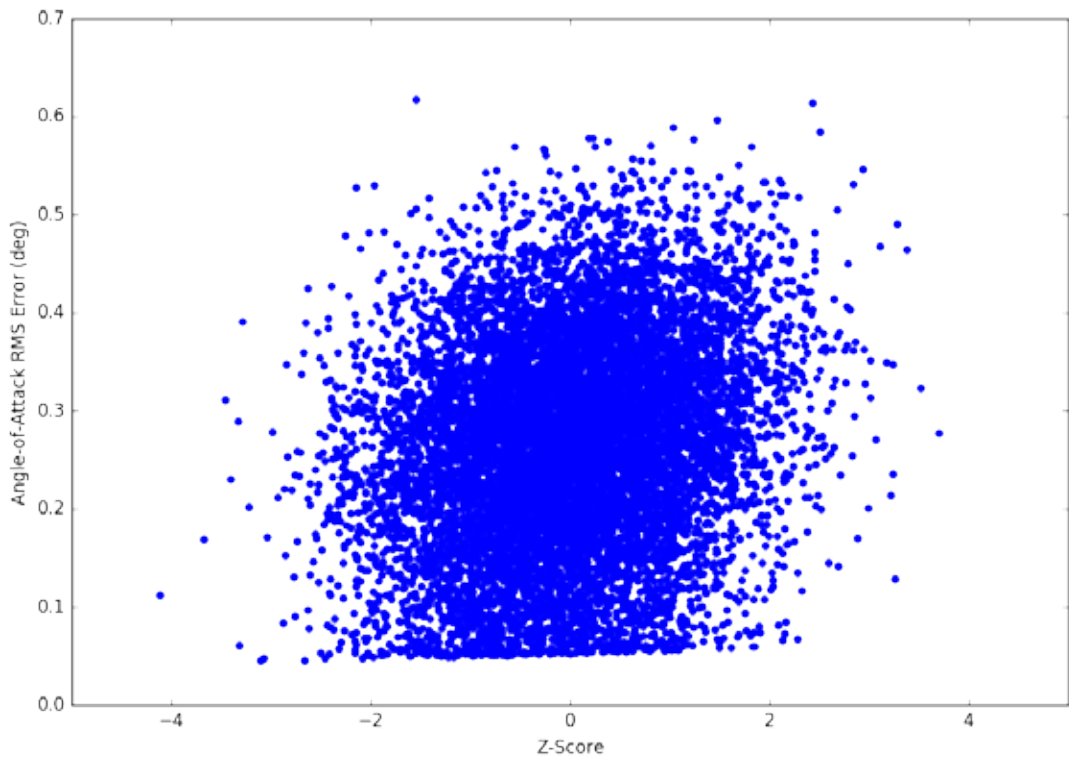
Figure C-51. $C_{L_{\delta_E}}$ **RMS error scatter plot for Case 13**

C.10.3 SIDESLIP ANGLE

For the derived sideslip angle:

- 0.0100 % of runs violated the display tolerance.
- 0.9300 % of runs violated the envelope-protection tolerance.
- 20.9600 % of runs violated the AFPC tolerance.
- 78.1000 % of runs met all tolerances.
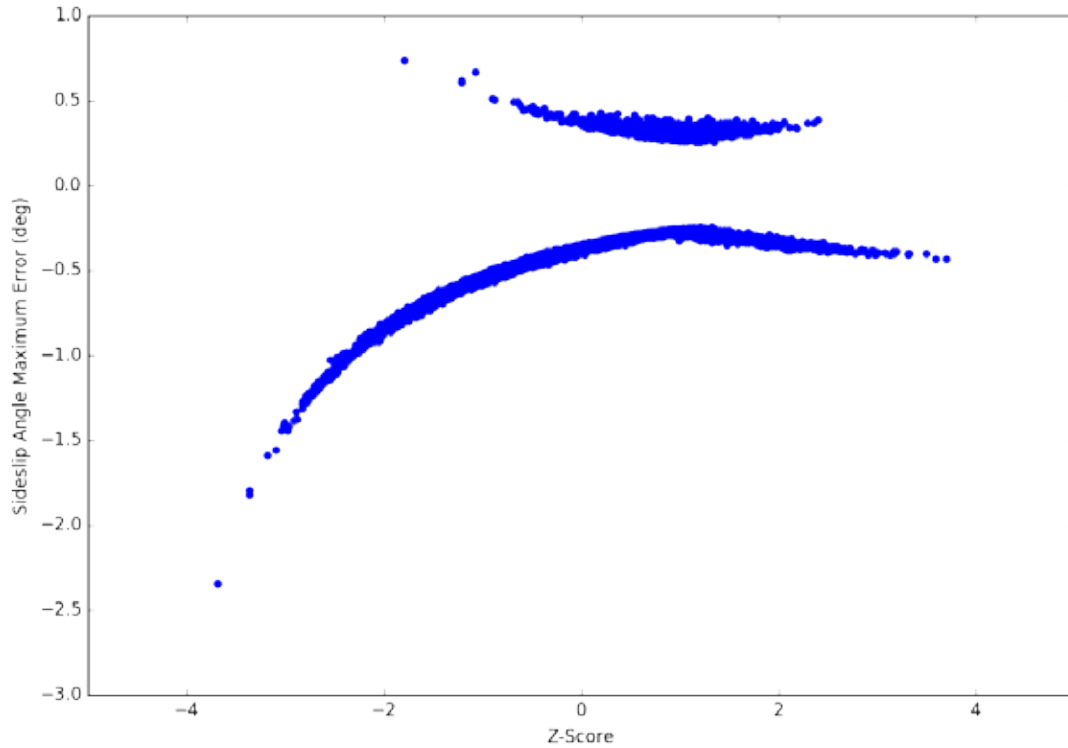
Figure C-52. C_{y_β} scatter plot for Case 13
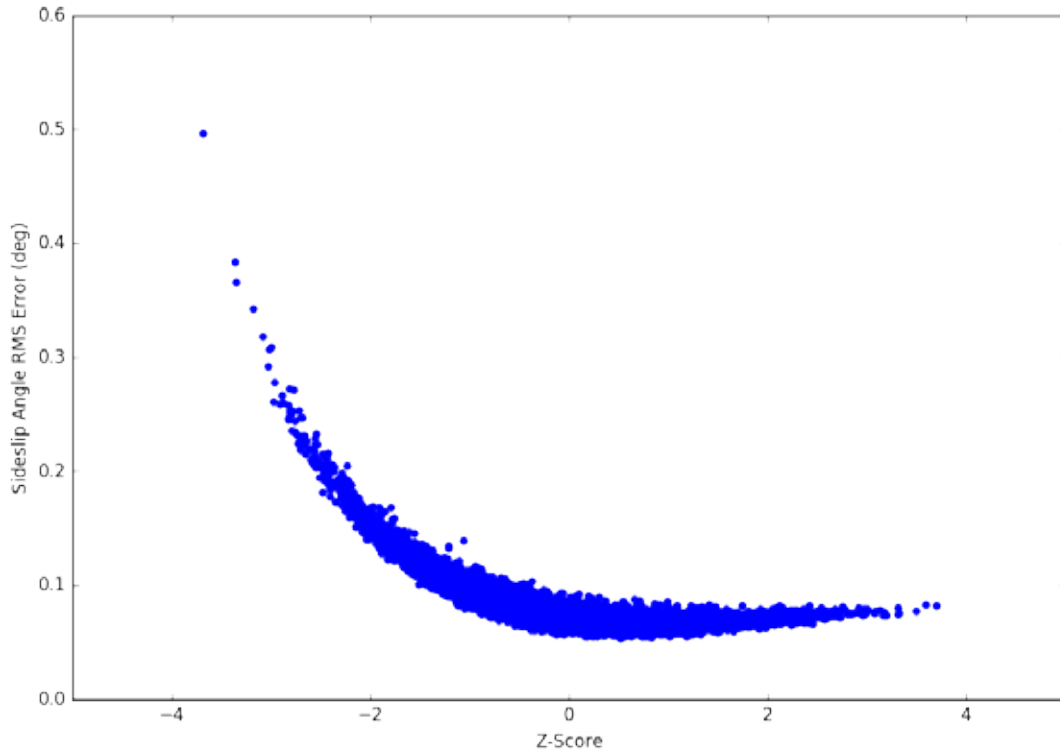
Figure C-53. C_{y_β} **RMS error scatter plot for Case 13**
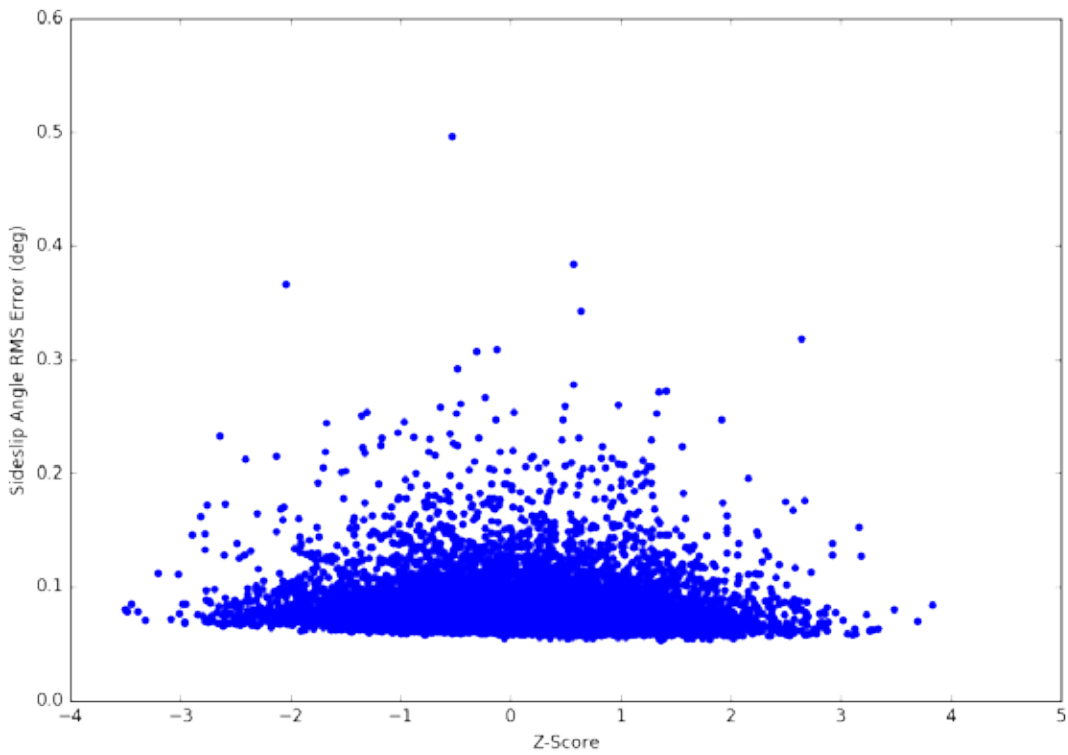
Figure C-54. C_{y_p} **RMS error scatter plot for Case 13**
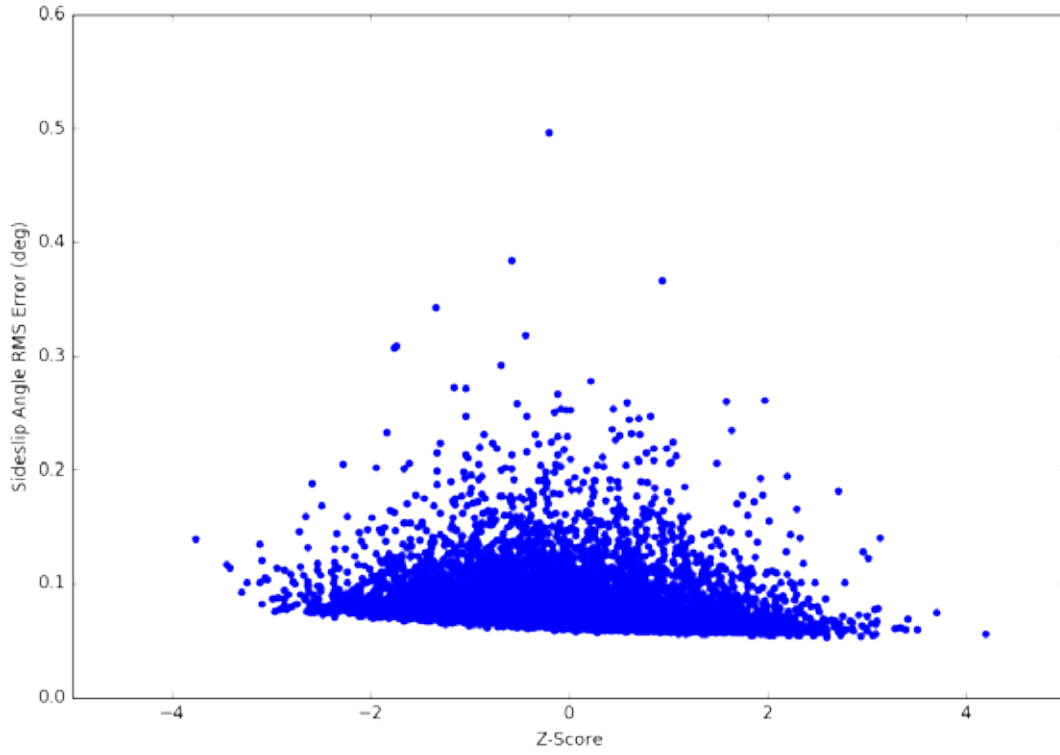
Figure C-55. C_{y_r} **RMS error scatter plot for Case 13**
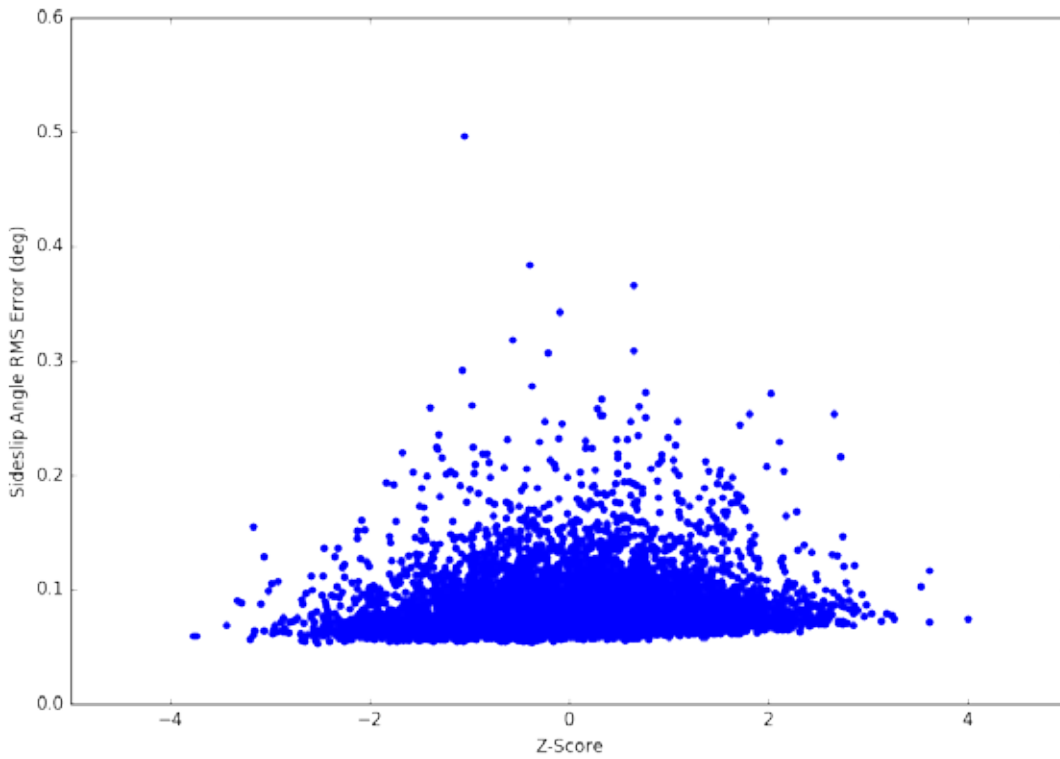
Figure C-56. $C_{y_{\delta_R}}$ **RMS error scatter plot for Case 13**

C.11 CASE 14: LOW SENSOR NOISE, DOUBLET INPUTS, 10,000 RUNS

C.11.1 OVERVIEW

Case 14 consisted of added low-level sensor noise and doublet inputs for each control. Again, 10,000 iterations were run.
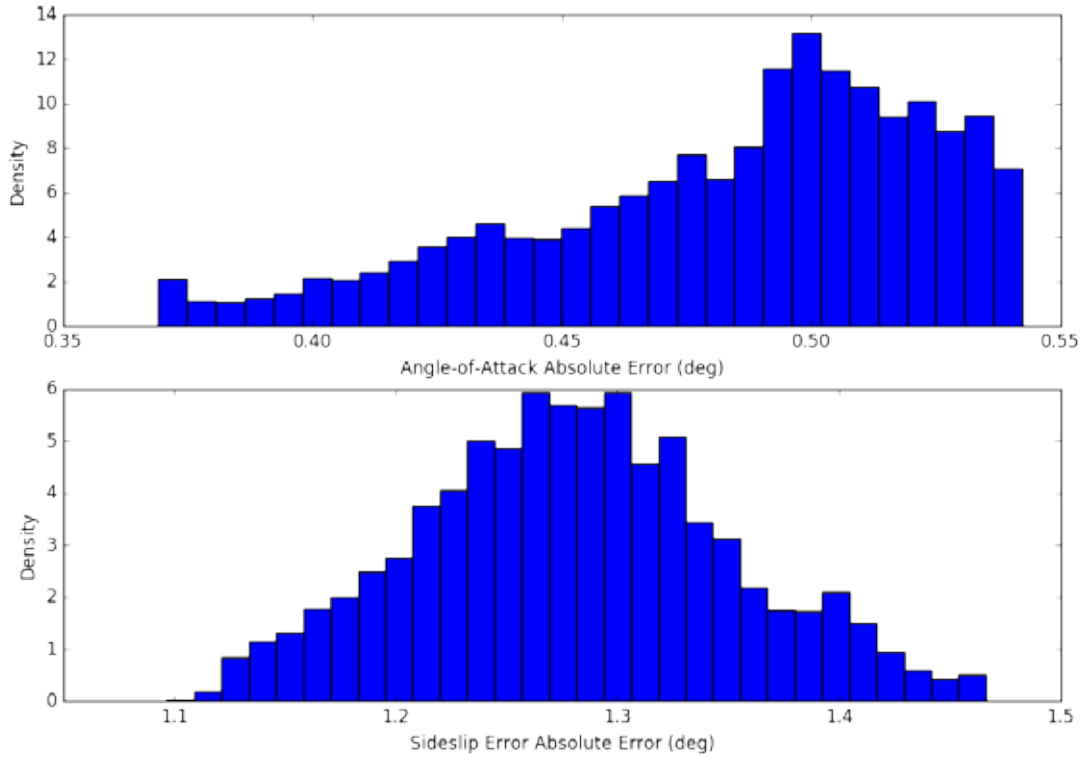
Figure C-57. Case 14 error histograms
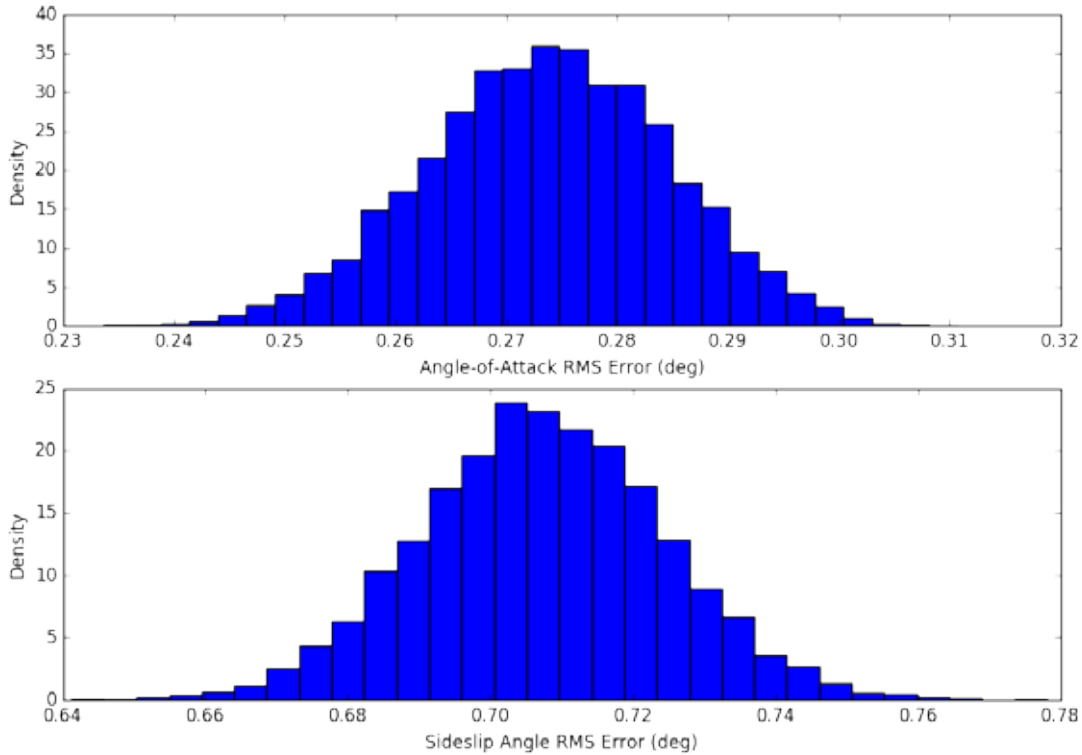
Figure C-58. Case 14 RMS error histograms

<u>C.11.2 ANGLE-OF-ATTACK</u>

For the derived AoA:

- 0.0000 % of runs violated the display tolerance.
- 0.0000 % of runs violated the envelope-protection tolerance.
- 41.3100 % of runs violated the AFPC tolerance,
- 58.6900 % of runs met all tolerances.

<u>C.11.3 SIDESLIP ANGLE</u>

For the derived sideslip angle,

- 0.0000 % of runs violated the display tolerance.
- 100.0000 % of runs violated the envelope-protection tolerance.
- 0.0000 % of runs violated the AFPC tolerance.
- 0.0000 % of runs met all tolerances.

C.12.1 OVERVIEW

Case 15 consisted of added medium-level sensor noise and doublet inputs for each control. Again, 10,000 iterations were run.
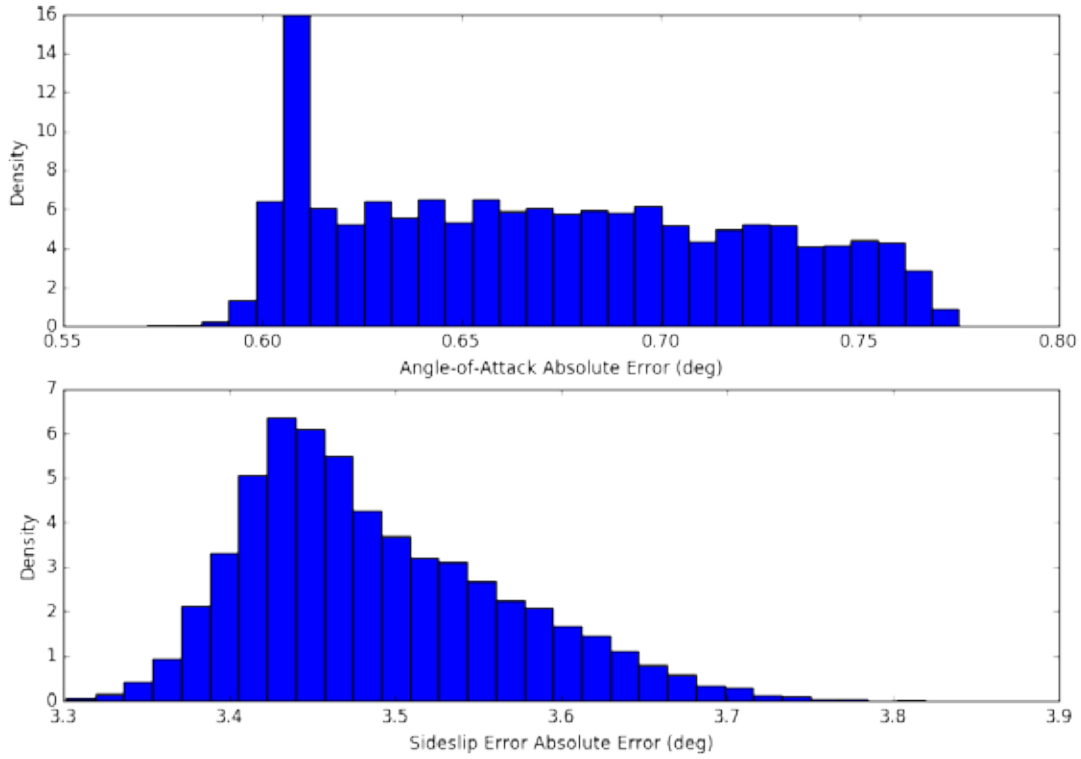
Figure C-59. Case 15 error histograms
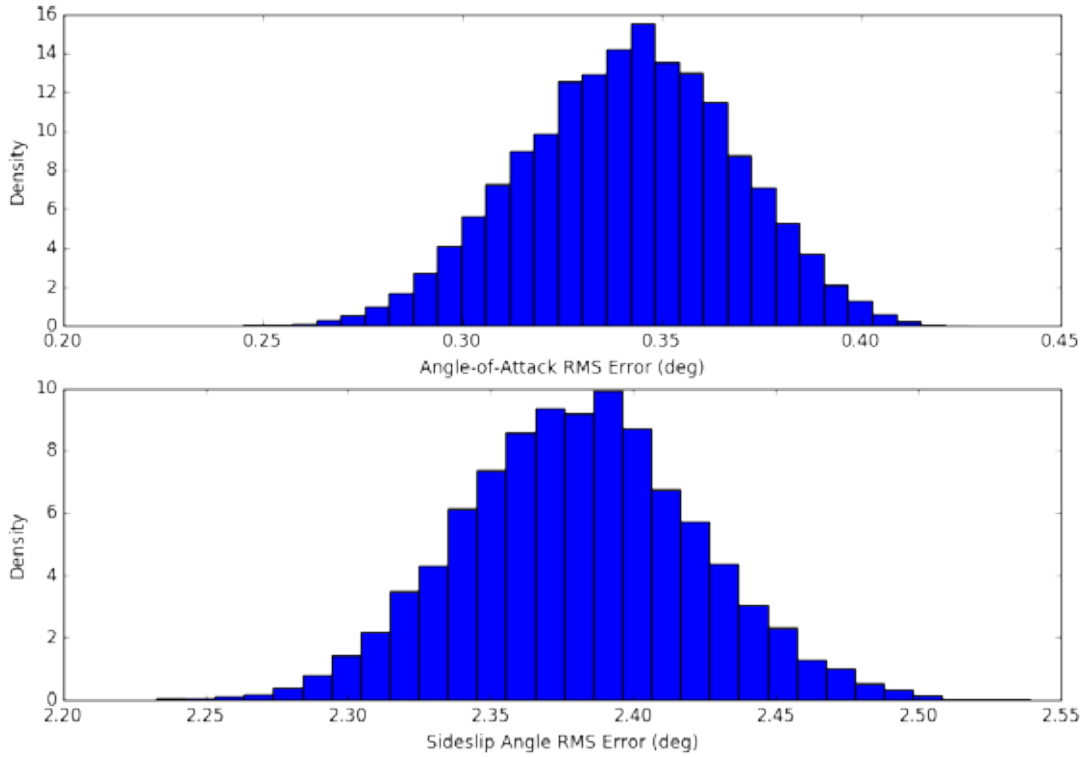
Figure C-60. Case 15 RMS error histograms

C.12.2 ANGLE-OF-ATTACK

For the derived AoA:

·   0.0000 % of runs violated the display tolerance.
·   0.0000 % of runs violated the envelope-protection tolerance.
·   100.0000 % of runs violated the AFPC tolerance.
·   0.0000 % of runs met all tolerances.

C.12.3 SIDESLIP ANGLE

For the derived sideslip angle:

·   100.0000 % of runs violated the display tolerance.
·   0.0000 % of runs violated the envelope-protection tolerance.
·   0.0000 % of runs violated the AFPC tolerance.
·   0.0000 % of runs met all tolerances.

C.13.1 OVERVIEW

Case 16 consisted of added high-level sensor noise and doublet inputs for each control. Again, 10,000 iterations were run.
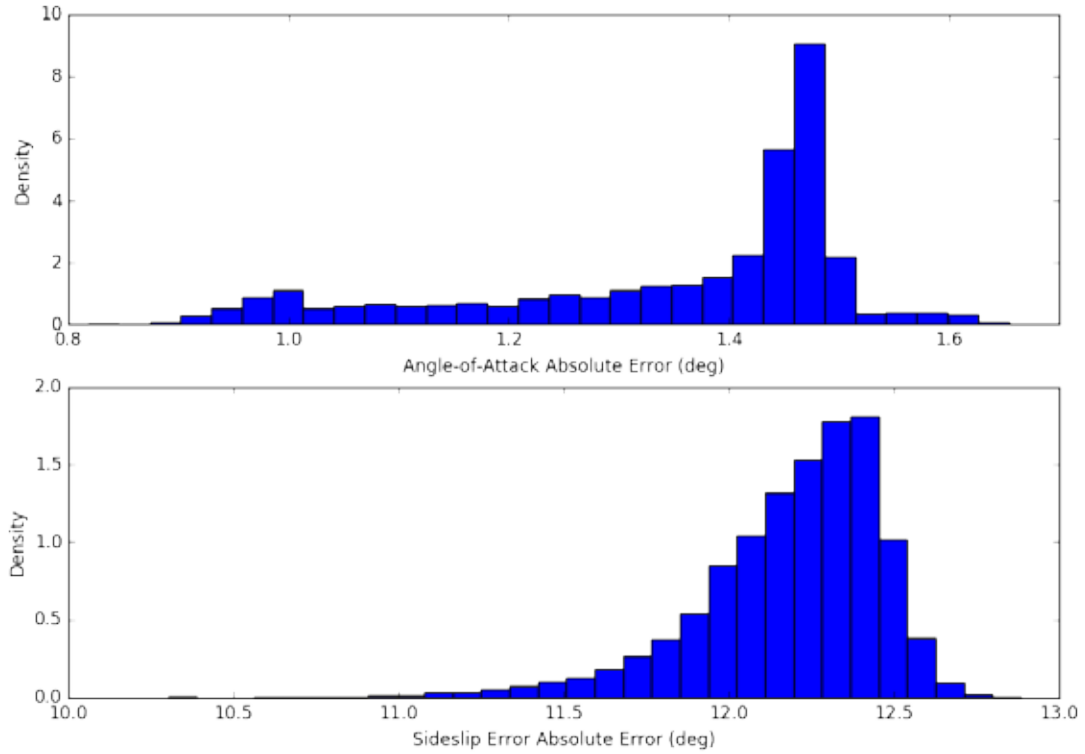
Figure C-61. Case 16 error histograms
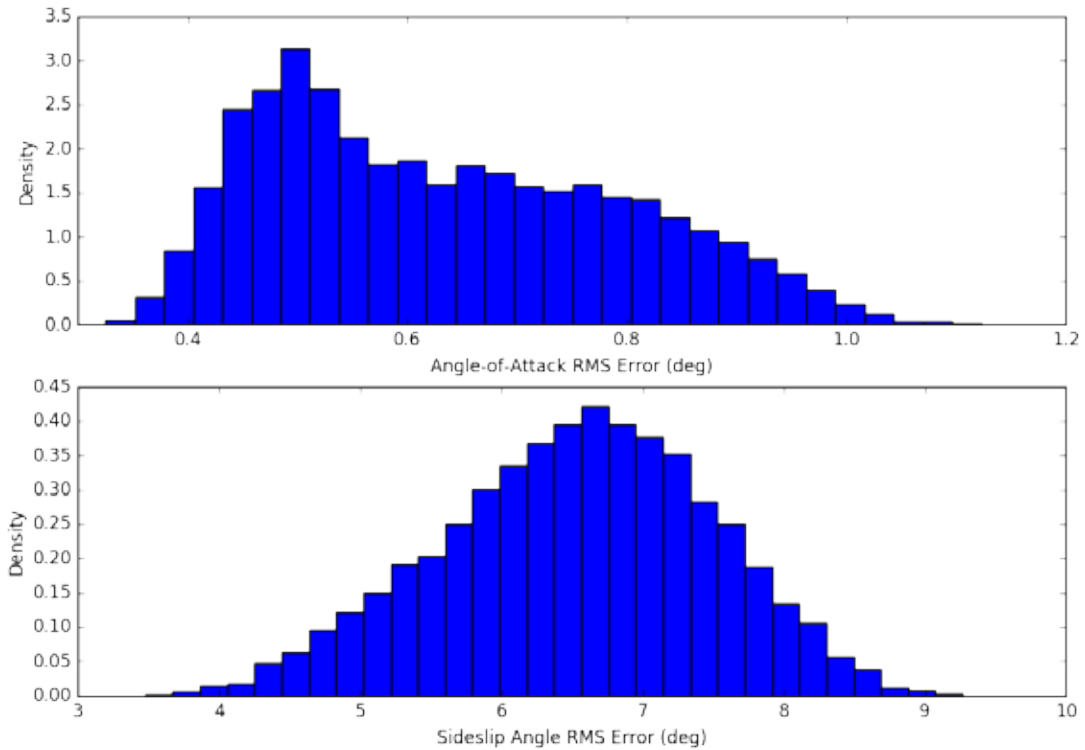
Figure C-62. Case 16 RMS error histograms

C.13.2 ANGLE-OF-ATTACK

For the derived AoA:

·   0.0000 % of runs violated the display tolerance.
·   92.9900 % of runs violated the envelope-protection tolerance.
·   7.0100 % of runs violated the AFPC tolerance.
·   0.0000 % of runs met all tolerances.

C.13.3 SIDESLIP ANGLE

For the derived sideslip angle:

·   100.0000 % of runs violated the display tolerance.
·   0.0000 % of runs violated the envelope-protection tolerance.
·   0.0000 % of runs violated the AFPC tolerance.
·   0.0000 % of runs met all tolerances.